UNIVERSITY OF CALIFORNIA SAN DIEGO

From the Deep Earth to the Atmosphere: New Geochemical Approaches to Address Marine Productivity, Long-term Climate, and Continental Rifting

A dissertation submitted in partial satisfaction of the requirements for the degree Doctor of Philosophy

in

Earth Sciences

by

Brian Morrison House

Committee in charge:

Professor Richard Norris, Chair
Professor Lihini Aluwihare
Professor Peter Franks
Professor Miriam Kastner
Professor Mark Thiemens

2019

The Dissertation of Brian Morrison House is approved, and it is acceptable in quality and form for publication on microfilm and electronically:

Chair

University of California San Diego

2019

DEDICATION

I wish to express my profound gratitude to my family and everyone else who supported me during these years.

And to all the others in the world for whom the “bipolar seesaw” is not only a climate phenomenon…

Oh, and to my cat, who helped me type by walking across my keyboard, and to whom I credit any remaining typos.

TABLE OF CONTENTS

LIST OF FIGURES

ACKNOWLEDGEMENTS

I wish to thank Professor Richard Norris, the chair of my committee for his support, his insight, and the scientific freedom he gave me to follow my intellectual curiosity.

Chapter 1 is in review for publication and is likely to appear in *Chemical Geology* as House, B. and Norris, R. D., 2019. The dissertation author was the primary investigator and author of this paper.

Chapter 2 has been submitted for publication and may appear in *Science* as House, B. and Norris, R. D. 2019. The dissertation author was the primary investigator and author of this paper.

Chapter 3, in full, is a reprint of the material as it appears in *Geology*: House, B.M., Bebout, G.E., Hilton, D.R., 2019. Carbon cycling at the Sunda margin, Indonesia: a regional study with global implications. Geology 47, 483–486. The dissertation author was the primary investigator and author of this paper.

Chapter 4 has been submitted for publication and may appear in *Earth and Planetary Science Letters* as House, B., Pickering, K., and Norris, R. D. 2019. The dissertation author was the primary investigator and author of this paper.

Chapter 5 is in revision for publication and will likely appear in *Nature Geoscience* as House, Brian M., Hammond, James, Keir, Derek, Gallacher, Ryan, Hilton, David R., Scarsi, Paolo, Abebe, Tsegaye, Halldórsson, Sæmundur A., and Castillo, Paterno R., 2019.

VITA

2011	Bachelor of Science, Stanford University
2011-2012	Post-Baccalaureate student, Georgetown University
2012-2013	Student researcher, Los Alamos National Laboratory
2013-2018	Research Assistant and Teaching Assistant, University of California San Diego
2018-2019	University of California President's Dissertation Year fellow, University of California San Diego
2019	Doctor of Philosophy, University of California San Diego

PUBLICATIONS

House, B.M., Bebout, G.E., Hilton, D.R., 2019. Carbon cycling at the Sunda margin, Indonesia: a regional study with global implications. Geology 47, 483–486.

ABSTRACT OF THE DISSERTATION

From the Deep Earth to the Atmosphere: New Geochemical Techniques to Address Marine Productivity, Long-term Climate, and Continental Rifting

by

Brian Morrison House

Doctor of Philosophy in Earth Sciences

University of California San Diego, 2019

Professor Richard Norris, Chair

This dissertation, as indicated by its title, is eclectic, but is united around the theme of developing and applying new geochemical approaches to answer large-scale questions in earth science. And it represents an interdisciplinary contribution, drawing on paleobiology, paleoclimate and paleoceanography as well as incorporating near surface and deep earth seismic models and signal analysis techniques to expand the range of conclusions that can be extracted from large geochemical datasets. The first two chapters focus on the marine biosphere in the geologic past. Chapter 1 presents a new high-throughput method for establishing paleo export productivity as well as evidence that increased supply of Southern Ocean water masses during glacial intervals stimulated productivity off the coast of East

Africa. The method presented in Chapter 1 enabled Chapter 2, in which an unprecedented global view of marine productivity reveals a global biological "heartbeat": marine productivity varies at the same frequencies as Earth's orbital obliquity and precession, indicating a fundamental link between astronomical and biological processes. Chapters 3 and 4 explore the information contained in the carbon in marine sediments to better constrain the amount and form of C subducting along the Sunda margin, Indonesia and to infer a multi-phased expansion of C_4 grasslands on the Indian subcontinent, indicating punctuated episodes of aridification. The final chapter traces the He isotope signature of a mantle plume from the core-mantle boundary to elucidate the processes involved in forming and sustaining continental rifting in Ethiopia and Afar. The breadth of topics covered here reflects the range of my own curiosity in pursuing what Nietzsche termed *fröliche wissenschaft* – joyful science.

CHAPTER 1

Unlocking the barite paleoproductivity proxy: a new high-throughput technique reveals glacial/interglacial productivity changes at the East African margin

Brian M. House[1], Richard D. Norris[1]

[1]Scripps Institution of Oceanography, University of California San Diego, La Jolla, CA 92037

Corresponding author: Brian M. House (bhouse@ucsd.edu)

Abstract

The accumulation rate of barite ($BaSO_4$) in marine sediments is a powerful tracer of paleo export productivity due to the refractory nature of barite in sediments and its ability to record ecosystem-wide productivity. Although it has been used to reconstruct past export productivity and infer the effects of ocean circulation and nutrient supply on ocean ecosystems, the complexity of and time needed for analyses has limited the usefulness of this proxy. We developed a new high-throughput method for quantifying barite in marine sediments, and using it in concert with X-Ray Fluorescence (XRF) core scans from IODP Site 1476 in the Mozambique Channel, we established a high-resolution record of export productivity since ~8 Ma. Focusing on the past 1 Myr., we find dramatically lower export productivity during glacial periods. We propose that diminished Antarctic Intermediate Water formation during glacial episodes may reduce nutrient availability at IODP Site 1476. This mechanism has been used to explain patterns of productivity in the high-latitude Southern Ocean and Benguela Current system, so our results expand this hypothesis to encompass the Indian Ocean as well.

1 Introduction

The accumulation rate of barite in marine sediments has proven to be one of the most useful tracers of paleo export productivity in the world's oceans (Dymond et al., 1992; Dymond & Collier, 1996; Francois et al., 1995; Gingele & Dahmke, 1994; Paytan & Kastner, 1996). Due to the strong correlation between organic C and particulate barite concentrations in sediment traps and surficial sediment samples, barite is hypothesized to form in the water

column as sinking organic matter is remineralized (Dehairs, et al., 1980; Dymond & Collier, 1996; Griffith & Paytan, 2012; Paytan & Griffith, 2007). Despite barite undersaturation in much of the world's oceans (Monnin et al., 1999), oxidation of organic matter may lead to "microenvironments" rich enough in Ba and sulfate that barite precipitates (Chow & Goldberg, 1960; Dehairs et al., 1980; Ganeshram et al., 2003). Marine barite is also highly refractory in sediments that lack pervasive sulfate reduction (e.g. Dymond et al., 1992). Furthermore, unlike many other proxies, the barite accumulation rate (BAR) reflects the export productivity of all species within an ecosystem that contribute to marine snow rather than tracing productivity of a subset of an ecosystem, such as calcifying organisms, or single microfossil species. For example, changes in ecological regime that alter the composition of biogenic sediments may appear as lulls in overall productivity if only a certain ecologic group or species is tracked (e.g. Calvert and Pedersen, 2007).

The potential of the BAR proxy has not, however, been fully realized due in large part to analytical challenges. Barite typically constitutes a small enough fraction of sediments that direct quantification with techniques like X-Ray Diffraction or electron microscopy is difficult and can lead to considerable uncertainty (Gingele and Dahmke, 1994; Robin et al., 2003). Instead, two broad schemes have been used to measure or estimate barite abundance in discrete samples: (1) the sequential barite extraction method, which involves quantification of barite following removal of silicate minerals and other Ba containing phases (Bains et al., 2000; Gonneea & Paytan, 2006; Ma et al., 2014; Paytan, 1995; Paytan et al., 1993; Paytan et al., 1996), and (2) estimation of barite abundance by measurement of total Ba and correction for non-barite Ba sources (Averyt and Paytan, 2004; Dehairs et al., 1980; Eagle et al., 2003; Gingele and Dahmke, 1994; Olivarez Lyle and Lyle, 2006; Reitz et al., 2004). We present a

new high-throughput method falls under the first scheme and directly quantifies barite in sediments without the need for correction. We also find that the commonly-used sequential barite extraction method of Paytan et al., (1993) and subsequently modified, is likely to underestimate true barite abundance and does not always produce repeatable results. Finally, the new method presented here can repeatably measure barite concentrations using less than one-tenth of the material needed for the sequential extraction method and is simple and uses non-hazardous chemicals, allowing it to be used during coring expeditions to measure barite concentrations in near real-time.

Non-destructive XRF core scanning is a particularly attractive method for estimating barite concentration due to the analytical rapidity that permits high-resolution records (e.g. Hull & Norris, 2011; Jaccard et al., 2010, 2013), but the results can be hard to interpret. The ratio of Ba to a predominantly terrigenous element like Al, Fe, Ti, or Zr is often interpreted to reflect Ba contributions from barite, but the analytical challenges in measuring barite in discrete samples have, in part, limited the rigorous evaluation of this assumption. For IODP Site 1476 in the Mozambique Channel, we find that discrete barite measurements showed no appreciable correlation with the previously-used XRF proxies of Ba/Al, Ba/Fe, and Ba/Ti. The ratio of Ba/Zr showed a mild correlation. However, normalizing Ba to Rh and Ag, which are present in the x-ray source and detector collimator respectively, showed a much more robust correlation with an R^2 for Ba/Ag of ~0.7 (n = 67). We therefore used Ba/Ag and discrete barite measurements from Site 1476 to "calibrate" the core scanning results and generate an envelope of estimated barite concentrations at cm-scale resolution. We chose to focus on the last ~1 Myr. of the ~8 Ma. record, and during this interval, the inferred barite concentration and accumulation rate (calculated as the product of barite concentration, bulk

dry density, and sedimentation rate) are at least twice as high during interglacial periods than during glacial intervals. While a relative paucity of paleceanographic data at Site 1476 prevents us from drawing definitive conclusions, changes in the supply of nutrient-rich Southern Ocean masses to this site are consistent with our observations.

The supply of nutrient-rich water from high southern latitudes has been implicated in sustaining productivity along the Antarctic margin and in the Benguela Upwelling System (Etourmeau et al., 2009; Jaccard et al., 2013), one of the most productive regions of the global ocean. Ventilation of deep waters and subduction to intermediate depths in the high-latitude Southern Ocean produces Antarctic Intermediate Water (AAIW), which spreads North and remains buoyant with respect to Antarctic Deep Water and North American Deep Water. The interaction of the South Equatorial Current with Madagascar makes the Mozambique Channel a region of exceptional eddy activity (José et al., 2014), and cyclonic eddies induce upwelling in their centers, which appears to cause the majority of productivity within the channel itself (e.g. Sætre and da Silva, 1984).

While this region has been the target of numerous hydrological and physical oceanographic studies, the origins of biological productivity and ultimate nutrient sources, both in the modern system and in the geologic past, have received significantly less attention. The glacial/interglacial productivity pattern we find since 1 Ma at Site 1476 mirrors the trends in the Southern Ocean and Benguela Upwelling System that are attributed to the diminution of AAIW production due to less vertical mixing during glacial periods (Etourmeau et al., 2009; Jaccard et al., 2013). This restricts the northern leakage of nutrients from the Southern Ocean and hence the productivity in regions that rely on Southern Ocean nutrient supply to sustain productivity. We propose a similar mechanism to explain the glacial/interglacial

export productivity trends within the Mozambique Channel, and our hypothesis would provide a unified framework for understanding productivity in regions that rely on high-latitude Southern Ocean water masses as a nutrient source.

2 Methods

2.1 Barite extraction and quantification procedure

Our novel method for quantifying barite in marine sediments relies on the well-documented ability of chelating carboxyl-amine ligands to bind Ba, thereby dissolving barite (Bao, 2006; Lea and Boyle, 1993; Paytan, 1995; Putnis et al., 2008). We used diethylenetriaminepentaacetic acid (DTPA), an octadentate analogue of ethylenediaminetetraacetic acid (EDTA), to quantitatively dissolve barite from a variety of test sediments and natural samples. Seven bulk test sediments were chosen to represent a range of lithologies, oceanographic settings, and expected export productivity levels (Table 1.1) to fully evaluate DTPA extraction of barite regardless of amount present or sediment matrix. Test sediments included predominantly biogenic material (INMD-12 105P CC and ANT-03 46G CC) as well as calcareous clays (Hessler-61 and IODP Site 1480E trimmings), all of which were expected to be rich in barite due to the abundance of foraminifera frustules. A red clay (ANT-13 201P CC) was included as well to evaluate the effects of transition metal oxyhydroxides deposits on Ba measurements, and a Mn-nodule from the same site was powdered to test the ability of reducing agents to liberate Ba, Fe, Mn, and S directly from metalliferous material. A sapropel was collected subaerially in Sicily, and a sample of terrestrially-sourced material from off the coast of La Jolla, California was included to test for interference from silicate-hosted Ba.

All sediments were dried at 50°C until the mass stabilized between two successive weighings, after which samples were ground with an agate mortar and pestle. Subsamples between 0.25 and 2 g were weighed and treated with 5 N acetic acid for 12 to 24 hours to remove carbonates that could contribute Ba; dissolving carbonates also removes Ca that would compete with Ba in DTPA complexation. Following acidification, samples were centrifuged, the supernatant was decanted, and samples were washed with DI water three times with centrifugation between each wash. A solution of 0.2 M DTPA was prepared by adding sufficient NaOH to an aqueous slurry of DTPA to dissolve the ligand and raise the pH to ~11.5-12. This ensures complete deprotonation of the pentaprotic DTPA, which is necessary to maximize Ba binding efficiency (Putnis et al., 2008). Samples were treated with 0.2 M DTPA solution in a ratio of 20 mL/g sediment and sonicated for 3 hours before being placed in a shaking water bath for at least 6 hours at 60°C. Aliquots of the resulting leachate were filtered through a 0.45 um membrane and archived for analysis. Table 1.2 summarizes the leaching method.

Approximately 50 uL of archived solution was added to 4 mL 2% v/v trace metal grade HNO_3/18.2 MΩ cm^{-1} water for analysis using a Perkin Elmer Optima 3000 Inductively Coupled Plasma-Optical Emission Spectrometer (ICP-OES) operating at 1300 W RF power, 15 L/min plasma Ar flow, 0.5 L/min auxiliary flow, and 0.8 mL/min through a concentric flow nebulizer. Samples were introduced at a flow rate of 1 mL/min, and a 40 second wash of 2% trace metal grade HNO_3 was conducted between samples. Measurements were made in axial view using the following emission peaks: Ba: 233.527 nm; Ca: 317.933 nm; Sr: 421.552 nm; Mn: 257.610 nm; Fe: 238.204 nm; S: 180.669 nm; and Al: 394.401 nm. A four-point calibration curve was constructed using a multi-element standard in a solution of 50 uL 0.2 M

DTPA/4 mL 2% HNO_3. Check standards were run every 15 samples to correct for instrumental drift. Counts obtained from five replicate spectroscopic measurements were averaged and converted to concentration values, and the precision on these replicates was better than 1% for most Ba analyses and was no greater than 4% for analyses presented in Table S1. Full procedural replicates of sample splits indicate an average one-sigma uncertainty of ~ 0.11-4.8% (Table S1) for Ba analyses. While instrumental replicates of S measurements gave a Relative Standard Deviation (RSD) of ~4%, S concentrations in leachate aliquots used for Ba standard addition experiments – which should contain identical amounts of S – differed by up to nearly a factor of two (978 ppb versus 519 ppb measured) for the PLDS 81 Bx-1 0-5 cm sample.

The effects of a pre-extraction reduction step – designed to minimize Ba contributions from Fe-Mn oxyhydroxides – were evaluated by treating samples with 20 mL/g sediment of a 0.2 M ascorbic acid solution in 5 N acetic acid. Bulk sediment samples for ascorbic acid reduction were collected from the same archived sediment as those used for sequential barite addition tests (Section 2.2), but due to sample depletion, we sometimes had to use new samples of the original cores.

2.2 Method verification and quality control tests

Synthetic barite was prepared by addition of $NaSO_4$ to $BaCl_2$; the resulting barite had impurities (including Sr levels) below the detection limit of ICP-OES. We conducted sequential barite addition experiments – in which progressively increasing amounts of synthetic barite were added to sediment aliquots –to ensure that added barite could be accurately quantified and as a check on possible interferences in measurement using ICP-OES. For these experiments, one sample aliquot with no added barite and at least four

aliquots with different masses of added barite were submitted to the DTPA leaching procedure. Separate Ba standard addition experiments were also conducted on individual samples to evaluate non-spectral ICP-OES interferences that could not be corrected by matrix-matching of calibration standards. In this case, at least two different masses of a Ba standard prepared by dilution of 100ppm Ba standard were added to sample aliquots, and the instrumental response was compared to the added Ba amount to determine the extent of "rotational" matrix effects and establish a correction factor to account for suppression of the Ba signal in complex matrices.

Sequential barite addition and Ba standard addition experiments were conducted on each of the seven bulk test sediments (Table 1). In addition, we obtained seven samples from the same cores and intervals previously analyzed using the sequential barite extraction method of Eagle et al. (2003) and analyzed them using the DTPA leaching method. These samples are not strict duplicates of what was previously analyzed, but we expect them to record similar compositions to published results.

Finally, quantitative leaching of barite was verified by doping an aliquot of decarbonated Hessler-61 material with synthetic barite representing >20 times the natural barite abundance. High-resolution Scanning Electron Microscope (SEM) images of unleached and leached aliquots were acquired by digitally mixing images from in-column (T1) and standard backscatter detectors on an Apreo SEM. Elemental analyses of individual grains and elemental maps of Ba, S, O, Si, Al, and Fe were produced using quantitative Energy Dispersive X-Ray Spectroscopy (EDS) with an XFlash detector on a Quanta 600 SEM. Additional tests designed to verify quantitative leaching were conducted by adding known

amounts of synthetic barite to a barite-free matrix of ground kaolinite and subjecting these samples to the DTPA leaching procedure.

2.2.1 Calculation of barite dissolution at low pH

To estimate the amount of barite dissolved during the acid dissolution steps of the sequential extraction method, we calculated the expected solubility of barite at low pH values. This calculation assumed a liquid of zero ionic strength such that all activity coefficients were one, and therefore it is likely to represent a lower bound on the true solubility. Using the definition of the solubility product (Rumble, 2018):

$$k_{sp} = \frac{[Ba^{2+}]}{[SO_4^{2-}]} \approx 10^{-9.97}$$

along with the second dissociation equation for H_2SO_4 (Rumble, 2018):

$$k_{a_2} = \frac{[H^+]}{[SO_4^{2-}]} \approx 10^{-1.99}$$

we calculated dissolved Ba^{2+}, HSO_4^-, and SO_4^{2-} concentrations for low pH values (Figure 1.4). To further investigate the potential effects of HF and non-zero activity coefficients, we used the PHREEQC geochemical modeling program to determine speciation and barite solubility under the reaction conditions presented in Eagle et al. (2003), which employed a set of three distinct HF/HNO_3 digestion steps with different reagent concentrations. We used the included wateq4f thermodynamic database to predict the amount of barite that would dissolve in 30 mL of (1) 2:1 1M HNO_3:HF, (2) 1:1 1M HNO_3:HF, and (3) 1:2 1M HNO_3:HF while maintaining equilibrium with a great excess (10 mole) of barite and allowing the formation of BaF_2 should it be thermodynamically favored. The results from these calculations are shown in Figure 1.4, and we find that for all steps, BaF_2 never reaches saturation (maximum saturation index ~10^{-3}), indicating that the addition of HF will have minimal additional effect on barite solubility at

low pH. For all pH conditions, however, the expected barite solubility calculated with PHREEQC (which accounts for ionic strength effects) was higher than what we calculated assuming activity coefficients of one. In total, the PHREEQC results suggest that if barite dissolution proceeds to thermodynamic equilibrium during each of the acid digestion steps of Eagle et al. (2003), a total of ~6 mg of barite will dissolve.

2.3 Discrete sample XRF measurements of total Ba

Sample preparation and analysis was carried out in the Peter Hooper Geoanalytical Laboratory at Washington State University. Samples were re-ground to ensure adequate homogeneity for XRF analysis and were mixed with $Li_2B_4O_7$ in a 1:2 sample:flux ratio. Sample beads were formed by fusion at 1000 ºC in graphite crucibles, and the resulting beads were ground and re-fused to ensure sample homogeneity. Sample surfaces were polished and elemental abundance measured on a ThermoARL Advant'XP wavelength-dispersive XRF spectrometer. Reproducibility of Ba between repeated duplicates and multiple calibration cycles was within 1.6%.

2.4 Comparison between discrete barite measurements and core scanning XRF

To establish a correlation between discrete barite concentration and XRF core scanning Ba records, 67 samples from IODP Site 1476 were analyzed by DTPA extraction and the results were compared with XRF core scans conducted at the Scripps Institution of Oceanography core repository. Core scans were conducted on an Avaatech XRF core scanner equipped with a 100 W Rh target x-ray tube from Oxford Instruments and a Canberra X-PIPS energy-dispersive detector with Ag collimator. Prior to analysis, the core surface was scraped gently to remove oxidized material and was covered in 4 μm SPEXCertiPrep Ultralene foil. All scans were conducted at 1 cm resolution with a footprint of 10 x 12 mm with scanning

gaps added to accommodate cracks or significant surface irregularities in the core. Scans were taken at 10, 30 and 50 kV with count times of 10, 20, and 30 seconds respectively. An x-ray tube current of 500 μA and no filter was used for 10 kV scans while currents of 2000 μA were used for both 30 and 50 kV scans with a Pd filter for 30 kV and Cu filter for 50 kV scans. Data processing followed the procedure detailed in Addison et al. (2013). One-sigma uncertainties averaged ~3% for Ba, ~4% for Zr and Rh, and 0.2% for Ag. The overall uncertainties for elemental ratios were estimated by summing the individual elemental uncertainties in quadrature.

For samples from IODP Site 1476, standard addition experiments were conducted on three samples to monitor for changes in non-spectral interference affecting measured Ba concentrations. Due to the paucity of material available from the stratigraphic splice for which XRF measurements exist, samples from IODP Site 1476A were analyzed and sample depths were correlated to along-splice XRF measurements using shipboard magnetic susceptibility measurements from the Special-Task Multisensor Logger "Fast Track" (STMSL; Hall et al., 2017).

2.4.1 Construction of age model

For the samples from IODP Site 1476, we modified the shipboard biostratigraphy age model to assign ages to samples and calculate a mass accumulation rate that was multiplied by the measured sediment barite concentration to obtain the Barite Accumulation Rate (BAR). A third-order polynomial was found to fit the biostratigraphic datums well (R^2 >0.99), and this polynomial was not constrained to zero age at zero depth (i.e. a non-zero intercept was permitted) as imposing zero age at the core top could propagate mathematical artifacts through the rest of the age model. Instead, we assumed a linear sedimentation rate between

the youngest biostratigraphic datum and the top of the core at zero age to minimize the assumptions inherent in this section of the age model.

3 Results and Discussion

3.1 Method verification and comparison

3.1.1 Sequential barite addition experiments

A wide variety of sediment compositions were used for these tests to ensure that leaching with DTPA reliably extracts barite regardless of sediment matrix. The results from sequential barite addition experiments for each of the seven bulk sediments (Table 1) were used to define lines of best fit using an ordinary least-squares regression (Figure 1.1). The y-intercept of this line gives the amount of Ba in sediment with no added barite, while the slope of the line gives an estimate of barite recovery with a slope of one indicating 100% full recovery. However, we found that apparent matrix effects during ICP-OES measurement confounded accurate determination of barite content. Matrix matching and internal standards were unable to resolve these effects to our satisfaction, and substantially increasing sample dilution was impractical for samples with low starting Ba concentrations. Instead, we conducted Ba standard addition experiments (distinct from sequential barite addition experiments), which, while more time consuming, better mitigated the presumed matrix effects that were particularly prominent for the Fe- and Mn-rich sapropel test sediment. Without such corrections, barite recovery varied between 89% for the sapropel and 99% for the terrigenous test sediment (Table S1). While the corrections indicated by standard addition experiments were small (0-9%; Table S1), applying them led to estimated recoveries of between 94 and 101%, and regressions for all sediments produced R^2 values > 0.99 (Table S1; Figure 1.1). Furthermore, the agreement between the y-intercepts of the linear fits and the Ba

contents of sediments with no additional barite indicates that single measurements of natural sediment provide results of comparable quality to those of sequential barite addition experiments. Finally, the high R^2 values indicate that our method gives repeatable results, and replicates of Hessler-61 sediment (n=6) along with replicates of previously analyzed samples (n= 3-7; Section 3.2) reveal a total procedural precision of 0.7-4% over an order of magnitude of barite content.

3.1.2 Verification of leaching effectiveness and other potential Ba sources

To verify that all barite dissolves during the DTPA extraction procedure and to establish whether the morphology of barite grains was likely to influence dissolution, we doped an aliquot of decarbonated Hessler-61 sediment with an additional 100 mg barite/g sediment, representing over 20 times the inferred natural barite content and up to three orders of magnitude more barite than we measured in other test sediments. Backscattered electron images and elemental mapping using Energy-Dispersive X-Ray Spectroscopy (EDS; Figure 1.2) confirm the presence of abundant barite in the doped sediment. A portion of this sediment was leached with DTPA, and subsequent SEM images and EDS elemental maps confirm the absence of detectable barite, providing strong evidence that all barite was removed (Figure 1.2). For all tests, we used laboratory-made barite, which tends to have a smaller grain size (~0.25-1 μm) than natural marine barite (~1-5 μm), and we might therefore expect our dissolution experiments with synthetic barite to proceed more rapidly than dissolution of natural barite would. However, because our method can dissolve the abundant natural barite from doped Hessler-61 sediments as well as 20 times more synthetic barite, we are confident that our procedure can dissolve all natural marine barite from even the most barite-rich sediments.

Indeed, we find that the total Ba measured by quantitative discrete sample XRF agrees well with the inferred amount of Ba from barite for five of the six samples analyzed (Figure 1.3), so any remaining marine barite must be minimal. Furthermore, Putnis et al. (2008) show that the dimensions of dissolution pits formed by DTPA treatment of barite surfaces exceed the size of marine barite grains after 30 minutes at 80°C and less optimal reagent concentrations. As a final test of leaching efficiency and reproducibility, we added known amounts of barite to a barite-free ground kaolinite matrix to produce test sediments with similar barite concentrations to those of natural samples. Subjecting these sediments to the DTPA leaching procedure confirmed that our method can measure barite concentrations to within 4% of the expected value (Figure 1.1; Table S1), which is not the case for other proposed barite quantification methods (Robin et al., 2003; Rutten and de Lange, 2002).

Because carbonates and any associated Ba are removed during acetic acid treatment, Ba associated with organic matter and that in hydrothermal Fe-Mn oxyhydroxides are likely to be the only remaining sources of DTPA-extractable Ba aside from barite (Gonneea and Paytan, 2006). We tested the contribution of organic matter-hosted Ba by degrading organic matter in samples with 15 mL 10% H_2O_2 per gram for 12 hours at room temperature prior to DTPA leaching. The samples evolved considerable gas when exposed to H_2O_2 but did not give appreciably different Ba yields compared to untreated samples for any test sediments (Table S1), even when the pH of the H_2O_2 solution was raised from 7 to 12 to increase reactivity. This step was not designed to completely remove organic matter but rather to degrade it sufficiently that Ba bound to it would be released. We therefore conclude that the amount of leachable Ba associated with organic matter is within the range of analytical uncertainty and treatment with H_2O_2 is unnecessary.

Previous work (e.g. Dymond et al., 1992) has noted the potential for Ba to be present in hydrothermally-sourced Fe-Mn oxyhydroxides, which at least partially dissolve during treatment with DTPA, but are efficiently removed by prior chemical reduction. However, because H_3NOHCl, the most commonly used reducing agent, is capable of partially dissolving barite (Table S1), the Ba contribution from Fe-Mn oxyhydroxides could be overestimated in previous studies (e.g. Dymond et al. 1992) and the barite concentration underestimated. Additionally, hydrothermal Fe-Mn deposits are thought to be a quantitatively minor component of sediments away from ridge crests (Calvert & Pedersen, 2007; Dymond et al., 1992), so sediments from most oceanographic settings are unlikely to incorporate significant hydrothermal Ba, either in Fe-Mn deposits or in abiotic hydrothermal barite. To avoid partial dissolution of barite during chemical reduction, we instead used ascorbic acid, a milder reducing agent. Because ascorbic acid is most reactive under acidic conditions, this reduction step was combined with sample decarbonation by using a solution of 0.2 M ascorbic acid in 5 N acetic acid. Doing so means that no separate reduction step is necessary, streamlining sample analysis.

In our experiments, ascorbic acid reduction liberated a similar amount of Fe, Mn, and S from both powdered Mn nodules and the red clay test sediment as treatment with H_3NOHCl did, but it does not dissolve barite, even at elevated temperatures (Table S1). To directly test the effect of ascorbic acid pre-treatment on DTPA leaching results, we subjected aliquots of five bulk test sediments and all seven samples previously analyzed by Eagle et al. (2003) to the reduction step prior to DTPA extraction. Due to sample depletion during sequential barite addition experiments, the aliquots of bulk test sediment used for ascorbic acid reduction tests were not strictly identical to those used in the first round of sequential barite addition

experiments, but they nonetheless gave Ba concentrations at or above those of samples that did not undergo the reduction step (Table S1). This suggests that reduction with ascorbic acid did not remove significant Ba from hydrothermal deposits, but it should be conducted as it may help minimize any ICP-OES matrix effects arising from solutions rich in Fe, Mn, and other metals rendered soluble by reduction.

Finally, because the unique utility of the DTPA leaching method extraction rests on its ability to selectively dissolve barite without releasing non-barite Ba from silicate phases, we monitored Al concentrations during ICP-OES analyses. Aluminum remained below the practical detection limit of 5 ppb for all analyses, corresponding to less than 200 ppb Al in the undiluted leachates. Using a Ba/Al ratio of 0.0075 for terrigenous sediments (Dymond et al., 1992), silicate dissolution is likely to contribute no more than 60 ng Ba/g sediment, which is well within analytical uncertainty for all samples.

3.1.3 Comparison with previous discrete barite measurements

Seven samples from sediment cores previously analyzed for barite concentration by Eagle et al. (2003) were re-analyzed to test agreement with the DTPA extraction method. For all samples, DTPA extraction gave higher Ba concentrations, and the Ba liberated during DTPA extraction is between 57 and 101% of the total Ba determined by quantitative XRF for six samples (Figure 1.3). While this is higher than for many samples from previous studies, it is not unreasonable given prior results that suggest that barite is often the dominant Ba-containing phase in marine sediments, particularly for samples in which barite is abundant (Dymond et al., 1992; Gonneea & Paytan, 2006). We cannot categorically rule out the possibility that DTPA extraction liberates Ba from non-barite phases, but chemical treatments designed to minimize Ba contributions from organic matter and Fe-Mn oxyhydroxides –

thought to be the main non-silicate Ba phases aside from barite and carbonate (Dymond and Collier, 1996; Gonneea and Paytan, 2006) – have a minor impact on our results (Table S1; Section 3.3).

Partial barite dissolution during the sequential extraction method of Eagle et al. (2003) may account for the difference in barite concentrations presented therein and what we measured. At least two steps in the sequential extraction procedure were shown to partially dissolve pure barite (Gonneea and Paytan, 2006), and our results indicate substantial barite dissolution during treatment with hydroxylammonium chloride (H_3NOHCl) and subsequent digestion using HF/HNO_3. Hydroxylammonium chloride, also known as hydroxylamine hydrochloride, is a reducing agent used to remove Fe-Mn oxyhydroxides that harbor Ba (Dymond et al., 1992). However, 0.2 M H_3NOHCl solution is also capable of partially dissolving barite (Table S1), presumably by reduction of sulfate or increasing barite solubility by raising ionic strength (Monnin and Galinier, 1988). Results from the treatment of pure barite indicate that the H_3NOHCl treatment of Gonneea and Paytan (2006) can mobilize at least 0.1 mg of barite (Table S1), which may represent a substantial fraction of the barite in natural samples.

However, enhanced dissolution of pure barite at low pH presents an even larger problem. While sulfate is only weakly basic (pK_a of $HSO_4^- \approx 2$), it will be protonated at low pH conditions, reducing the activity of sulfate, and thereby increasing barite solubility (Figure 1.4). Ignoring the effects of ionic strength (i.e. using activity coefficients of one), treatment of barite with 1 N HNO_3 (pH = 0) should protonate barite-derived SO_4^{2-} to such a degree that barite becomes approximately 10 times more soluble than it is at pH ≥ 2 (see Section 2.2.1; Figure 1.4). Results from the PHREEQC geochemical modeling program indicate that the

addition of HF will not greatly influence barite solubility because pH is only modestly affected, and BaF_2 remains undersaturated at the reaction conditions in Eagle et al. (2003) (see Section 2.2.1). Model results suggest that at equilibrium, a total of ~6 mg of barite would dissolve during the three acid digestion steps of the Eagle et al. (2003) procedure (see Section 2.2.1; Figure 1.4), but empirical tests suggest that slightly less may dissolve (Table S1) during the 12-hour reaction time (Table S1). Nevertheless, the amount of barite that is likely to be dissolved during this step exceeds the amount present in many aliquots of natural samples analyzed in this study. Paytan (1995) and Eagle et al. (2003) suggest approximately 5-10% of marine barite dissolves during the full sequential barite extraction procedure while Markovic et al. (2016) find that up to 50% dissolves. Therefore, the degree of partial dissolution prior to quantification is unclear, and indeed, the sequential extraction method of Eagle et al. (2013) recovered less than 50% of the barite we infer using the DTPA leaching method on samples from the same sediment cores and core depths (Figure 1.3). While the samples we compared with those of Eagle et al. (1993) are not strict replicates, it is striking that the DTPA leaching method always recovered higher amounts of barite than the sequential barite extraction method, including in samples for which barite was previously undetectable. Finally, barite contents of nominally identical samples analyzed by Eagle et al. (2003) and Gonneea and Paytan (2006) do not always show good agreement (Figure 1.3). For some samples, this may be due in part to the multiple HNO_3/HF digestion steps Eagle et al. (2003) employed to separate barite since each acid treatment is likely to dissolve progressively more barite. However, this is unlikely to account for the 30-fold difference in barite content for the JGOFS TT013-MC06 5-10 cm sample, and some analyses from Eagle et al. (2003) find higher barite

concentrations than re-analyses by Gonneea and Paytan (2006), which is contrary to expectations if repeated acid digestion steps are the sole source of discrepancy.

3.2 Paleo export productivity reconstruction using XRF core scans

3.2.1 Calibration of XRF core scan from IODP Site 1476

The ratio of Ba to a predominantly terrigenous element such as Al, Ti, Fe, or Zr measured by core scanning XRF has been employed as a paleoproductivity proxy (Hull and Norris, 2011; Jaccard et al., 2013, 2010, 2009), but the fidelity of this proxy has yet to be rigorously evaluated. Using the DTPA leaching method, we compared 67 discrete barite measurements from IODP Site 1476 with XRF core scanning results. The ratios of Ba/Al, Ba/Ti, and Ba/Fe show a poor correlation with our measurements of barite concentration ($R^2 < 0.1$) while Ba/Zr shows a reasonable correlation ($R^2 \approx 0.34$; Figure 1.5), indicating this better reflects the barite content of sediments. However normalizing Ba to an element whose flux may vary independently can be problematic since a change in the elemental ratio need not reflect a true change in Ba concentration (Anderson and Winckler, 2005). Therefore, we also tested the correlation of barite with Ba/Rh and Ba/Ag because Rh and Ag are present in the x-ray source and detector (see Methods Section) in much greater amounts than in sediments, so normalizing Ba to them should more accurately reflect true variations in Ba content by reducing the effects of sediment porosity, grainsize, sediment water content, and varying x-ray source intensity without requiring normalization to a separate lithogenic element. Indeed, the Ba/Rh and Ba/Ag ratios correlate better with barite concentration ($R^2 = 0.43$ and 0.55 respectively; Figure 1.5) than any other elemental ratios, indicating that they are better predictors of sediment barite content – at least for Site 1476 – than traditional proxies derived from XRF core scans.

We therefore chose to calibrate the Ba/Ag ratio throughout the core by using the relationship between Ba/Ag and discrete sample barite measurements. To reduce the influence of potential inaccuracies in the XRF scanning results and correlation between discrete sample and XRF measurement depths (see Section 2.3), we removed the four points for which the (ordinary) linear regression residual was more than two standard deviations away from the mean residual. This improved the correlation (R^2 =0.70) while still retaining 63 calibration points. Using this linear relationship and 95% confidence levels for the slope and intercept, we converted the Ba/Ag XRF record into an envelope of inferred barite concentrations for the entirety of the ~8 Myr. Site 1476 record (Figure 1.6). This record shows a secular trend toward higher barite concentrations from ~4.3 to 3.5 Ma, after which concentrations remained relatively constant until approximately 0.9 Ma – roughly contemporaneous with the shift to ~100 kyr. glacial/interglacial cycles – when the mean barite concentration fell by nearly 30% and cyclic variation about the mean became more extreme. Long period (~200-400 kyr.) cyclicity is apparent in inferred barite concentrations between about 6 and 2.5 Ma, suggesting that low frequency orbital variations may help modulate export productivity in addition to the ~40 kyr. obliquity cycles apparent from 2.5 to ~1.3 Ma. Barite accumulation rates, calculated as the barite concentration multiplied by the mass accumulation rate, record a similar long-term trend as the calibrated Ba/Ag record with the exception of a more pronounced peak around 3.5 Ma, when sedimentation rates increased substantially. Because sedimentation rates were approximately constant since 1 Ma, the time period we examine in detail, barite concentrations and accumulation rates show nearly identical trends.

3.2.2 Interpreting glacial/interglacial productivity cycles since 1 Ma

One of the most notable features of the barite record from Site 1476 is the pronounced relationship between export productivity and the global benthic $\delta^{18}O$ stack (Lisiecki and Raymo, 2005) within the last 1 Myr., indicating that export productivity was regularly two to three times greater during interglacial periods than during glacial intervals. Despite the hydrographic complexity of the Mozambique Channel (De Ruijter et al., 2002; Sætre and da Silva, 1984; Schouten et al., 2003; J F Ternon et al., 2014), decreased supply of Antarctic Intermediate Water (AAIW) and Subantarctic Mode Water (SAMW) during glacial periods is consistent with export productivity trends at Site 1476 and has been hypothesized to underlie similar productivity trends in other locations (Jaccard et al., 2013). Here we focus on the influence of AAIW (which may, in the strictest sense, represent a combination of AAIW and SAMW and potential mixing with overlying Indian Ocean water) in the Mozambique Channel because it clearly appears as a distinct water mass in hydrographic surveys due to its characteristic low salinity and temperature.

The present mechanism stimulating productivity in the center of the Mozambique Channel appears to be upwelling associated with mesoscale eddies induced by the interaction of the South Equatorial Current with Madagascar (e.g. Sætre & da Silva, 1984). The Mozambique Channel represents one of the most energetic eddy systems in the world (José et al., 2014), and eddy currents have been detected reaching the seafloor at ~2 km water depth (De Ruijter et al., 2002; Schouten et al., 2003), so while AAIW appears to reside mainly between 500-1000 m within the Mozambique Channel (De Ruijter et al., 2002), eddy-induced upwelling of it into the mixed layer seems plausible. Indeed, eddy cores have been shown to retain the AAIW temperature and salinity signatures to depths shallower than 500 m (Sætre and da Silva, 1984). Furthermore, the South Indian Common Water that upwells and drives

productivity near the Natal Bight, South of Site 1476, appears to acquire nutrients from mixing with AAIW (Meyer et al., 2002), so AAIW rather than the overriding Red Sea outflow or an Indian Ocean-sourced water mass is likely the ultimate nutrient source to the Mozambique Channel. Therefore, decreasing the supply of AAIW during glacial periods would be expected to limit the nutrient supply and hence productivity in the interior of the Mozambique Channel, assuming no major oceanographic rearrangements. Fluctuations in AAIW production have also been linked to productivity trends in the Benguela Current system off southwestern Africa (Etourmeau et al., 2009) and ODP Site 1094, South of Africa in the high-latitude Southern Ocean, though at this site, productivity is inferred from XRF Ba/Fe ratios (Jaccard et al., 2013). Opposing trends of greater productivity during glacial periods in the sub-Antarctic Zone are likely due to local Fe fertilization, which intensifies during glacial periods (Jaccard et al., 2013). Therefore, linking changes in AAIW supply to export productivity at Site 1476 would help provide a unifying framework for understanding productivity during glacial and interglacial periods in regions that are influenced by Antarctic water mass production.

The fraction of pre-formed versus recycled nutrients currently sustaining primary production in the Mozambique Channel is unclear as are possible changes in circulation or nutrient supply in the geologic past, so we cannot definitively link AAIW production to export productivity trends at Site 1476. The region remains poorly studied in general (J. F. Ternon et al., 2014), and no studies have yet constrained the origin of upwelled nutrients that stimulate primary productivity in the cores of cyclonic eddies in the Mozambique Channel, so at least some portion could be locally recycled rather than upwelled from an advected water mass like the AAIW. However, because cyclonic eddies produce regions of elevated

productivity, a widespread nutrient reservoir must exist below the mixed layer, and because productivity is otherwise low in the channel, nutrient recycling seems an unlikely explanation.

Alternatively, it is possible that sea level changes associated with glacial/interglacial cycles may have exposed or inundated portions of the continental margin either of East Africa or Madagascar, altering upwelling behavior and/or continental nutrient supply. At the moment, though, no evidence exists for changes in nutrient supply due to possible sea level fluctuations. Finally, because the barite paleoproductivity proxy only reflects export productivity, we also cannot rule out the possibility that primary productivity behaved differently, possibly even increasing during glacial periods while dramatic changes in ecosystem regime substantially altered the ratio of primary to export productivity. Indeed, alternation between layers of foraminifera-rich nanno fossil ooze and nanno fossil-rich foraminifera ooze in Site 1476 cores have been interpreted to reflect glacial/interglacial changes in ecological regime that could imply variation in organic matter ballasting and hence the fraction of primary productivity represented in the export productivity record (Hall et al., 2017a). The magnitude of difference in barite concentrations would seem to require a major change in the ballasting potential of organic matter rather than a small relative shift in ecosystem abundance. Altogether, the repeated switching between barite concentrations of ~0.6 mg/g during interglacial periods and ~0.3 mg/g during glacial periods (Figure 1.6) implies that the process(es) causing the glacial/interglacial productivity fluctuations were almost perfectly reversible, suggesting a regular and predictable mechanism such as nutrient supply via AAIW.

4 Conclusions

We have developed and verified a new method for the quantification of barite in marine sediments that relies on selective extraction of barite rather than either inference of barite content based on overall elemental abundances or sequential extraction followed by measurement of residual barite. Our method, involving complexation of Ba with the organic chelating ligand DTPA, promises a substantial improvement in sample throughput and recovery of barite. Furthermore, we have shown that previous barite quantification methods likely underestimate true barite content due to partial dissolution of barite prior to quantification. The rapidity of the DTPA leaching method allowed us to compare numerous discrete barite concentrations with XRF core scanning results to test the suitability of various elemental ratios in reconstructing paleo export productivity. We find that traditional XRF-derived proxies of Ba/Al, Ba/Fe, and Ba/Ti show no appreciable correlation with true barite concentrations at IODP Site 1476. Instead, we propose Ba/Ag as a far more reliable export productivity proxy as long as Ag is present in the XRF detector, leading to a far greater detector-driven Ag response than sediments alone would produce. Using discrete barite measurements to calibrate the Ba/Ag record for Site 1476 reveals that export productivity was regularly and up to nearly three times higher during interglacial periods compared to glacial intervals, particularly during the period of intense glacial/interglacial variation following the Mid-Pleistocene Transition at ~1 Ma. We propose that diminished upwelling in the Antarctic Zone during glacial periods reduced the supply of AAIW available to upwell in the Mozambique Channel, thereby reducing primary and ultimately export productivity. Our results therefore support a unified global model in which lowered AAIW production during glacial periods reduces productivity in the Antarctic Zone as well as other areas as geographically dispersed as the Indian Ocean and North Pacific. Our results show the unique

promise of the new DTPA extraction method of quantifying barite in marine sediments, a technique that will enable production of the large paleoproductivity datasets necessary to answer previously inaccessible questions regarding the global biological system of the oceans.

Acknowledgments

Many thanks to Miriam Kastner for productive comments and Paterno Castillo for analytical assistance. Katrina Cantu, Jacques Lyakov, and Alex Hangsterfer performed the XRF core scanning, and SEM and EDS analyses were conducted in the UCSD Nanoengineering and Materials Research Center. This work was made possible by Scripps Institution of Oceanography departmental funding and Norris group lab funds.

Chapter 1 is in review for publication and is likely to appear in *Chemical Geology* as House, B. and Norris, R. D., 2019. The dissertation author was the primary investigator and author of this paper.

References

Addison, J.A., Finney, B.P., Jaeger, J.M., Stoner, J.S., Norris, R.D., Hangsterfer, A., 2013. Integrating satellite observations and modern climate measurements with the recent sedimentary record: An example from Southeast Alaska. J. Geophys. Res. Ocean. 118, 3444–3461. https://doi.org/10.1002/jgrc.20243

Anderson, R.F., Winckler, G., 2005. Problems with paleoproductivity proxies. Paleoceanography 20. https://doi.org/10.1029/2004pa001107

Averyt, K.B., Paytan, A., 2004. A comparison of multiple proxies for export production in the equatorial Pacific. Paleoceanography 19. https://doi.org/10.1029/2004pa001005

Bains, S., Norris, R.D., Corfield, R., Faul, K.L., 2000. Termination of global warmth at the Palaeocene/Eocene boundary through productivity feedback. Nature 407, 171–174.

Bao, H., 2006. Purifying barite for oxygen isotope measurement by dissolution and reprecipitation in a chelating solution. Anal. Chem. 78, 304–309. https://doi.org/10.1021/ac051568z

Calvert, S.E., Pedersen, T.F., 2007. Elemental Proxies for Palaeoclimatic and Palaeoceanographic Variability in Marine Sediments: Interpretation and Application, in: Hillaire-Marcel, C., De Vernal, A. (Eds.), Developments in Marine Geology. Elsevier, pp. 567–644. https://doi.org/10.1016/s1572-5480(07)01019-6

Chow, T., Goldberg, E.D., 1960. On the marine geochemistry of barium. Geochim. Cosmochim. Acta 20, 192–198.

De Ruijter, W.P.M., Ridderinkhof, H., Lutjeharms, J.R.E., Schouten, M.W., Veth, C., 2002. Observations of the flow in the Mozambique Channel. Geophys. Res. Lett. 29. https://doi.org/10.1002/oby.20584/epdf

Dehairs, F., Chesselet, R., Jedwab, J., 1980. Discrete suspended paricles of barite and the barium cycle in the open ocean. Earth Planet. Sci. Lett. 49, 528–550.

Dymond, J., Collier, R., 1996. Particulate barium fluxes and their relationships to biological productivity. Deep Sea Res. Part II Top. Stud. Oceanogr. 43, 1283–1308.

Dymond, J., Suess, E., Lyle, M., 1992. Barium in deep-sea sediment: a geochemical proxy for paleoproductivity. Paleoceanography 7, 163–181.

Eagle, M., Paytan, A., Arrigo, K.R., van Dijken, G., Murray, R.W., 2003. A comparison between excess barium and barite as indicators of carbon export. Paleoceanography 18. https://doi.org/10.1029/2002pa000793

Etourmeau, J., Martinez, P., Blanz, T., Schneider, R., 2009. Pliocene – Pleistocene variability of upwelling activity, productivity, and nutrient cycling in the Benguela region. Geology 37, 871–874.

Francois, R., Honjo, S., Manganini, S., Ravizza, G., 1995. Biogenic barium fluxes to the deep sea: implications for paleoproductivity reconstruction. Global Biogeochem. Cycles 9, 289–303.

Ganeshram, R.S., François, R., Commeau, J., Brown-Leger, S.L., 2003. An experimental investigation of barite formation in seawater. Geochim. Cosmochim. Acta 67, 2599–2605. https://doi.org/10.1016/S0016-7037(03)00164-9

Gingele, F., Dahmke, A., 1994. Discrete barite particles and barium as tracers of paleoproductivity in South Atlantic sediments. Paleoceanography 9, 151–168.

Gonneea, M., Paytan, A., 2006. Phase associations of barium in marine sediments. Mar. Chem. 100. https://doi.org/10.1016/j.marchem.2005.12.003

Griffith, E., Paytan, A., 2012. Barite in the ocean -- occurrence, geochemistry and palaeoceanographic applications. Sedimentology 59, 1817–1835. https://doi.org/10.1111/j.1365-3091.2012.01327.x

Hall, I.R., Hemming, S.R., LeVay, L.J., Barker, S., Berke, M.A., Brentegani, L., Caley, T., Cartagena-Sierra, A., Charles, C.D., Coenen, J.J., Crespin, J.G., Franzese, A.M., Gruetzner, J., Han, X., Hines, S.K.V., Jimenez Espejo, F.J., Just, J., Koutsodendris, A., Kubota, K., Lathika, N., Norris, R.D., Periera dos Santos, T., Robinson, R., Rolinson, J.M., Simon, M.H., Tangunan, D., van der Lubbe, J.J.L., Yamane, M., Zhang, H., 2017a. Site U1476. Proc. Int. Ocean Discov. Progr. 361. https://doi.org/10.14379/iodp.proc.361.105.2017

Hall, I.R., Hemming, S.R., LeVay, L.J., Expedition 361 Scientists, 2017b. South African Climates (Agulhas LGM Density Profile), in: Proceedings of the Ocean Drilling Program. International Ocean Discovery Program, College Station, TX. https://doi.org/http://dx.doi.org/10.14379/iodp.proc.361.2017

Hull, P.M., Norris, R.D., 2011. Diverse patterns of ocean export productivity change across the Cretaceous-Paleogene boundary: New insights from biogenic barium. Paleoceanography 26. https://doi.org/10.1029/2010pa002082

Jaccard, S.L., Galbraith, E.D., Sigman, D.M., Haug, G.H., 2010. A pervasive link between Antarctic ice core and subarctic Pacific sediment records over the past 800 kyrs. Quat. Sci. Rev. 29, 206–212. https://doi.org/10.1016/j.quascirev.2009.10.007

Jaccard, S.L., Galbraith, E.D., Sigman, D.M., Haug, G.H., Francois, R., Pedersen, T.F., Dulski, P., Thierstein, H.R., 2009. Subarctic Pacific evidence for a glacial deepening of

the oceanic respired carbon pool. Earth Planet. Sci. Lett. 277, 156–165. https://doi.org/10.1016/j.epsl.2008.10.017

Jaccard, S.L., Hayes, C.T., Martinez-Garcia, A., Hodell, D.A., Anderson, R.F., Sigman, D.M., Haug, G.H., 2013. Two modes of change in Southern Ocean productivity of the past millions of years. Science (80). 339, 1419–1423.

José, Y.S., Aumont, O., Machu, E., Penven, P., Moloney, C.L., Maury, O., 2014. Influence of mesoscale eddies on biological production in the Mozambique Channel : Several contrasted examples from a coupled ocean-biogeochemistry model. Deep Sea Res. Part II 100, 79–93.

Lea, D.W., Boyle, E.A., 1993. Determination of carbonate-bound barium in corals and foraminifera by isotope dilution plasma mass spectrometry. Chem. Geol. 103, 73–84.

Lisiecki, L.E., Raymo, M.E., 2005. A Pliocene-Pleistocene stack of 57 globally distributed benthic δ18O records. Paleoceanography 20. https://doi.org/10.1029/2004pa001071

Ma, Z., Gray, E., Thomas, E., Murphy, B., Zachos, J., Paytan, A., 2014. Carbon sequestration during the Palaeocene–Eocene Thermal Maximum by an efficient biological pump. Nat. Geosci. 7, 382–388. https://doi.org/10.1038/ngeo2139

Meyer, A.A., Lutjeharms, J.R.E., De Villiers, S., 2002. The nutrient characteristics of the Natal Bight, South Africa. J. Mar. Syst. 35, 11–37. https://doi.org/10.1016/S0924-7963(02)00043-X

Monnin, C., Galinier, C., 1988. The solubility of celestite and barite in electrolyte solutions and natural waters at 25°C: a thermodynamic study. Chem. Geol. 71, 283–296.

Monnin, C., Jeandel, C., Cattaldo, T., Dehairs, F., 1999. The marine barite saturation state of the world's oceans. Mar. Chem. 65, 253–261.

Olivarez Lyle, A., Lyle, M.W., 2006. Missing organic carbon in Eocene marine sediments: Is metabolism the biological feedback that maintains end-member climates? Paleoceanography 21. https://doi.org/10.1029/2005pa001230

Paytan, A., 1995. Marine barite, a recorder of oceanic chemistry, productivity, and circulation. University of California San Diego.

Paytan, A., Griffith, E.M., 2007. Marine barite: Recorder of variations in ocean export productivity. Deep Sea Res. Part II Top. Stud. Oceanogr. 54, 687–705. https://doi.org/10.1016/j.dsr2.2007.01.007

Paytan, A., Kastner, M., 1996. Glacial to interglacial fluctuations in productivity in the Equatorial Pacific as indicated by marine barite. Science (80-.). 274, 1355–1357.

Paytan, A., Kastner, M., Chavez, F.P., 1996. Glacial to interglacial fluctutation in productivity in the Equitorial Pacific as indicated by marine barite. Science (80-.). 274, 1355–1357.

Paytan, A., Kastner, M., Martin, E.E., Macdougall, J.D., Herbert, T., 1993. Marine barite as a monitor of seawater strontium isotope composition. Nature 366, 445–449.

Putnis, C. V, Kowacz, M., Putnis, A., 2008. The mechanism and kinetics of DTPA-promoted dissolution of barite. Appl. Geochemistry 23, 2778–2788. https://doi.org/10.1016/j.apgeochem.2008.07.006

Reitz, A., Pfeifer, K., de Lange, G.J., Klump, J., 2004. Biogenic barium and the detrital Ba/Al ratio: a comparison of their direct and indirect determination. Mar. Geol. 204, 289–300. https://doi.org/10.1016/s0025-3227(04)00004-0

Robin, E., Rabouille, C., Martinez, G., Lefevre, I., Reyss, J.., van Beek, P., Jeandel, C., 2003. Direct barite determination using SEM/EDS-ACC system: implication for constraining barium carriers and barite preservation in marine sediments. Mar. Chem. 82, 289–306. https://doi.org/10.1016/S0304-4203(03)00075-6

Rumble, J.R. (Ed.), 2018. CRC Handbook of Chemistry and Physics, 99th ed. Taylor and Francis Group.

Rutten, A., de Lange, G., 2002. A novel selective extraction of barite, and its application to eastern Mediterranean sediments. Earth Planet. Sci. Lett. 198, 11–24.

Sætre, R., da Silva, A.J., 1984. The circulation of the Mozambique Channel. Deep Sea Res. Part II 31, 485–508.

Schouten, M.W., De Ruijter, W.P.M., Van Leeuwen, P.J., Ridderinkhof, H., 2003. Eddies and variability in the Mozambique Channel. Deep. Res. Part II Top. Stud. Oceanogr. 50, 1987–2003. https://doi.org/10.1016/S0967-0645(03)00042-0

Ternon, J.F., Bach, P., Barlow, R., Huggett, J., Jaquemet, S., Marsac, F., Ménard, F., Penven, P., Potier, M., Roberts, M.J., 2014. The Mozambique Channel : From physics to upper trophic levels. Deep Sea Drill. Proj. Site Reports 100, 1–9.

Ternon, J.F., Roberts, M.J., Morris, T., Hancke, L., Backeberg, B., 2014. In situ measured current structures of the eddy fi eld in the Mozambique Channel. Deep Sea Res. Part II 100, 10–26.

Tables

Table 1.1 Test sediment sources and compositions used for sequential barite addition experiments

Material type	Sample source	Oceanographic setting
Calcareous clay	Hessler-61	Equatorial Pacific, 4225 m water depth
Carbonate ooze	INMD-12 105P CC	Equatorial Atlantic, pelagic, 3200-4700 m water depth[a]
Terrigenous	Surficial sediment from 32° 40.324' N 117° 29.139' W	Continental shelf near La Jolla, California terrigenous with identifiable mineral grains, 488 m water depth
Calcareous clay	Trimmings from interstitial water whole round samples, IODP Site 1480E	Indian Ocean near Sumatra, hemi-pelagic to pelagic, 4100 m water depth
Red clay	ANT-13 201P CC	Western Pacific, pelagic, 5721 m water depth
Sapropel	Mediterranean Cycle 107 sapropel	Punta Grande, Sicily, Subaerial but originally pelagic with water depth of ~1000 m
Siliceous ooze	ANT-03 46G CC	Northwest Pacific, pelagic, 5736 m water depth

[a] Sample is not in SIO database, so exact water depth is unknown

Table 1.2 Summary of DTPA leaching method for barite extraction

Step		Reagent to sample ratio
1.	Dry sample at 50° C or freeze dry and homogenize	N/A
2.	Treat with 5 N acetic acid or 0.2 M ascorbic acid in 5 N acetic acid for 12 hours at room temperature or ≤ 60° C after initial CO_2 evolution[a]	20 mL/g
3.	Centrifuge and wash 3x with DI water	15 mL/g
4.	Treat with 0.2 M DTPA at pH 11.5-12 with sonication for 3 hours and agitation at 60° C for at least 6 hours[b]	20 mL/g

[a]Ascorbic acid can be included during this step to remove Ba associated with Fe-Mn oxyhydroxides if necessary
[b]Tests with only sonication and no additional heating revealed poor barite recovery

Figures

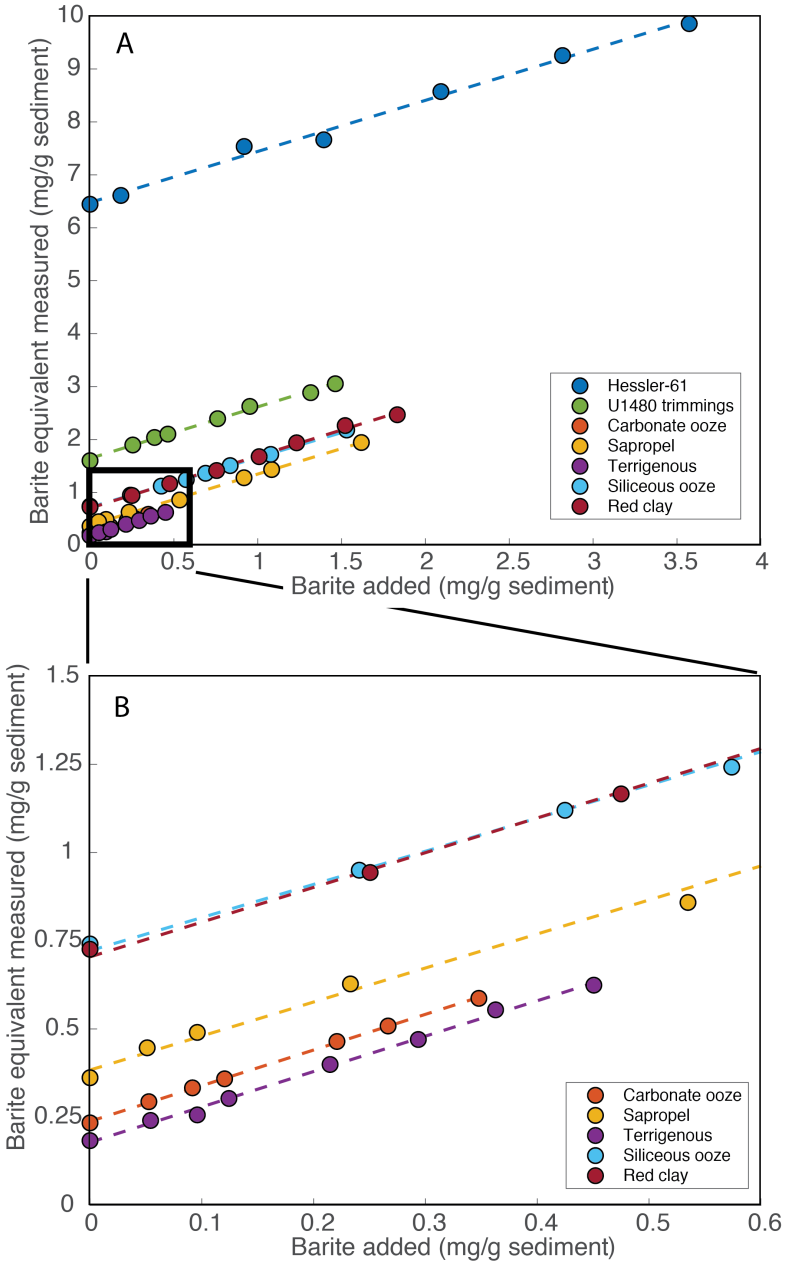

Figure 1.1 (a) results of all sequential barite addition experiments for seven compositions of bulk test sediments (Table 1) and (b) enlargement of region in (a) to show results for low barite samples. Barite equivalent is the amount of barite in the sample assuming all measured Ba derives from barite. After correction for matrix effects by standard addition experiments, all test sediments produced lines with slopes between 0.94 and 1.01 and R^2 values of ≥ 0.99. Dotted lines are results of ordinary least-squares linear regression.

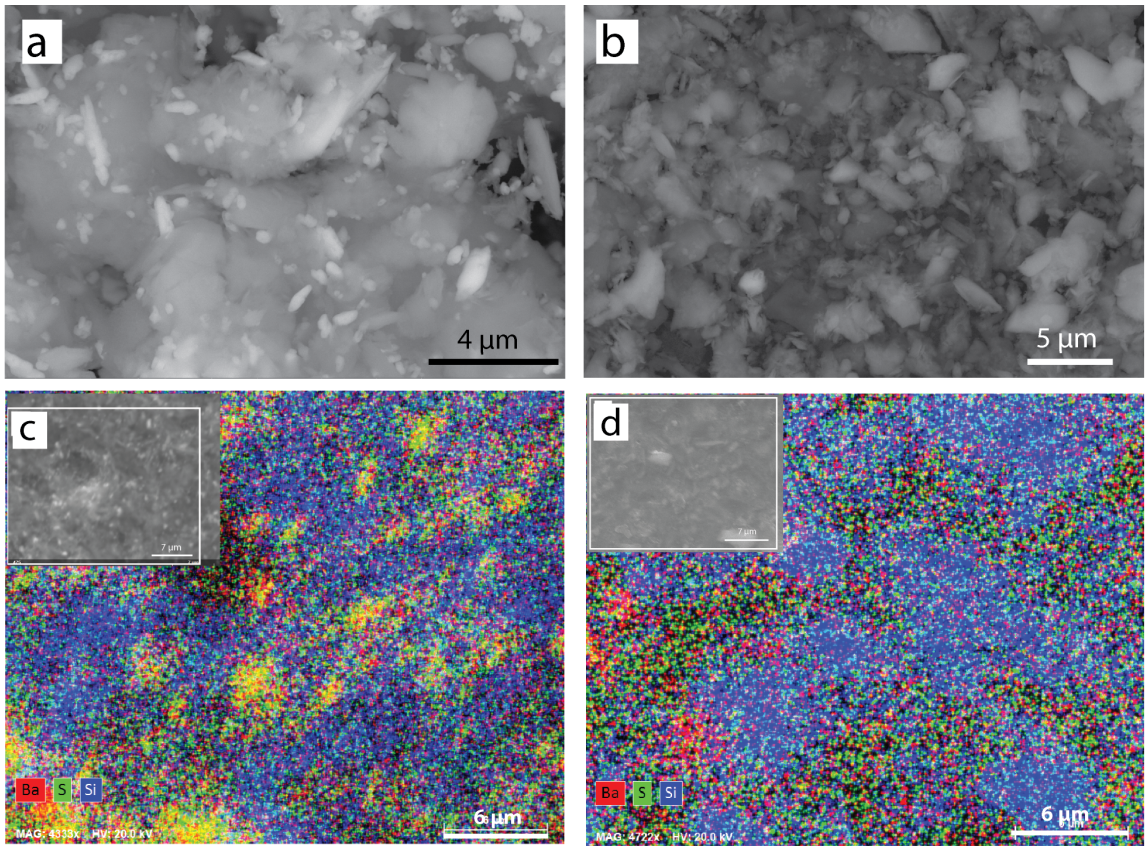

Figure 1.2. (a) backscatter SEM images of Hessler-61 test material doped with 100 mg synthetic barite/g sediment prior to leaching with DTPA, (b) after leaching, (c) overlaid Energy-dispersive X-Ray Spectroscopy (EDS) map of Ba (red), S (green), and Si (blue) for doped H-61 sediment prior to leaching, and (d) after leaching. In (a), barite grains appear as bright regions, while their absence is conspicuous in (b). In (c) and (d), insets show backscatter SEM image with white rectangle showing region of EDS elemental maps. Regions of collocated Ba and S without Si appear yellow and were confirmed to be barite grains with point analyses. Barite grains are abundant prior to DTPA leaching in (c) and none are apparent after leaching in (d).

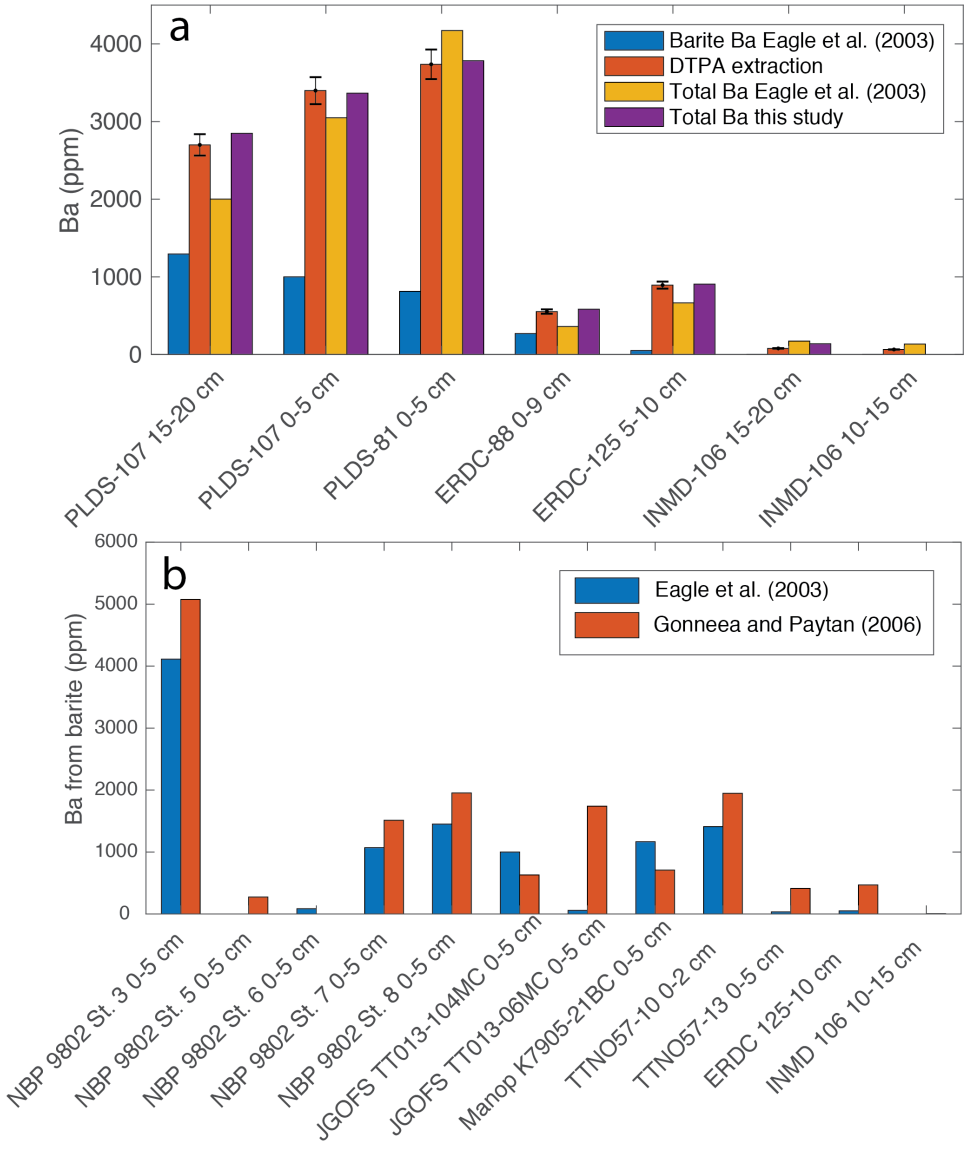

Figure 1.3. (a) Comparison of standard barite separation method and DTPA leaching method for previously analyzed samples as well as total Ba concentrations determined by sample digestion (Eagle et al. 2003) and quantitative XRF (this study). The DTPA leaching method consistently gives higher values than the sequential extraction procedure, and the putative barite Ba liberated during DTPA treatment closely matches total Ba for five of the six samples with high enough Ba to measure by quantitative XRF. Error bars on DTPA Ba indicate the maximum estimated 4% one-sigma uncertainty (see Methods Section). (b) Comparison of values from Eagle et al. (2003) and Gonneea and Paytan (2006) for samples analyzed in both. Values often agree to within 30%, but for JGOFS TT013-06MC 0-5 cm, the two values differ by nearly a factor of 30.

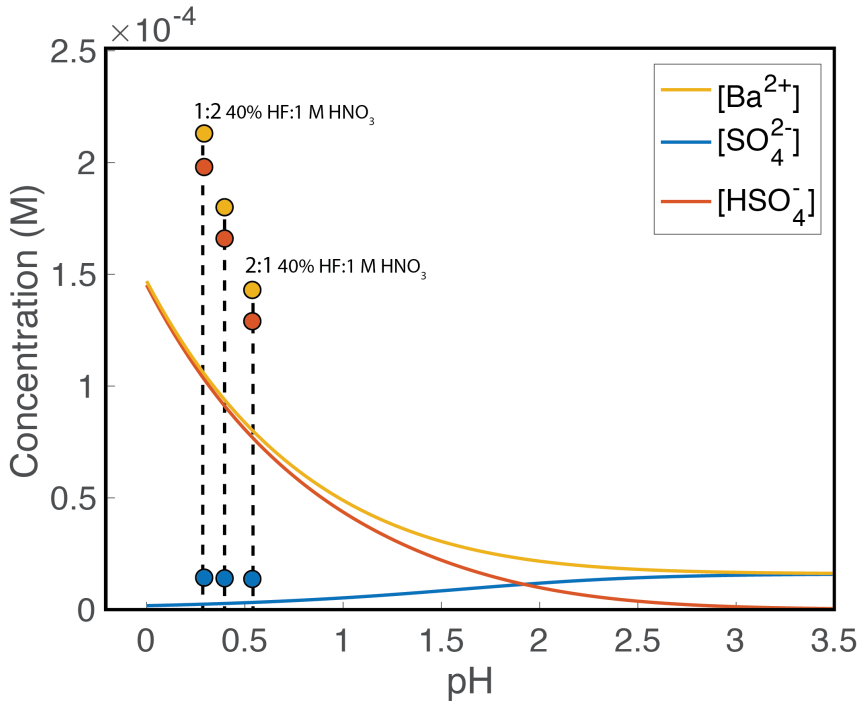

Figure 1.4. Modeled solubility of barite under acidic conditions. Calculations without considering ionic strength are shown as solid curves, and the outputs of the PHREEQC model results for the three acid digestions of Eagle et al. (2003) are shown as discrete points. The two models agree reasonably well considering that high ionic strength increases barite solubility. Model results suggest that the three acid digestion steps of Eagle et al. (2003) could dissolve up to ~6 mg barite, more than is in most sediment aliquots analyzed for this study.

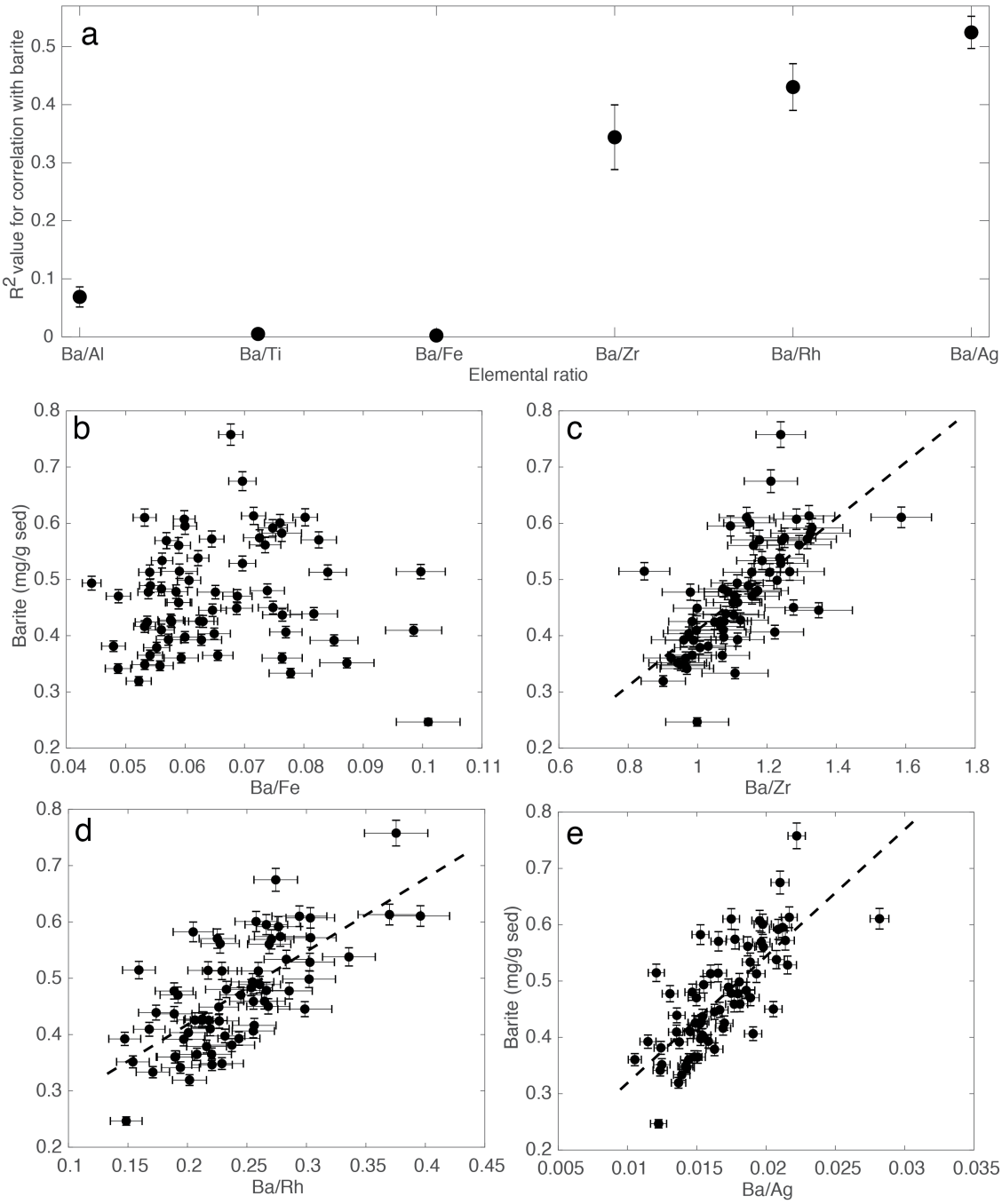

Figure 1.5. Correlation between XRF core scanning elemental ratios and barite concentrations measured on discrete samples for IODP Site 1476. (a) R^2 values for correlation between various element ratios and measured barite values with uncertainty estimated by simulated addition of random, normally distributed error and subsequent recalculation of R^2. (b) Ba/Fe shows no apparent correlation with barite concentration while the correlation is statistically significant for (c) Ba/Zr ($R^2 = 0.47$; $p \approx 10^{-10}$), (d) Ba/Rh ($R^2 = 0.48$; $p < 10^{-10}$), and (e) Ba/Ag

($R^2 = 0.55$; $p < 10^{-12}$). For b-e, Error bars show estimated 1σ uncertainty given by error propagation of XRF measurement uncertainty and assuming an extremely conservative 4% uncertainty in discrete barite measurements. These results indicate that the ratio of Ba to terrigenous elements like Fe may not be reliable paleoproductivity proxies, but the ratio of Ba to minor terrigenous elements like Zr much better reflects true barite content. The abundance of Ag and Rh in the x-ray source and paucity in natural sediments means Ba/Ag and Ba/Rh ratios will reflect true variations in Ba content more reliably than other elemental ratios.

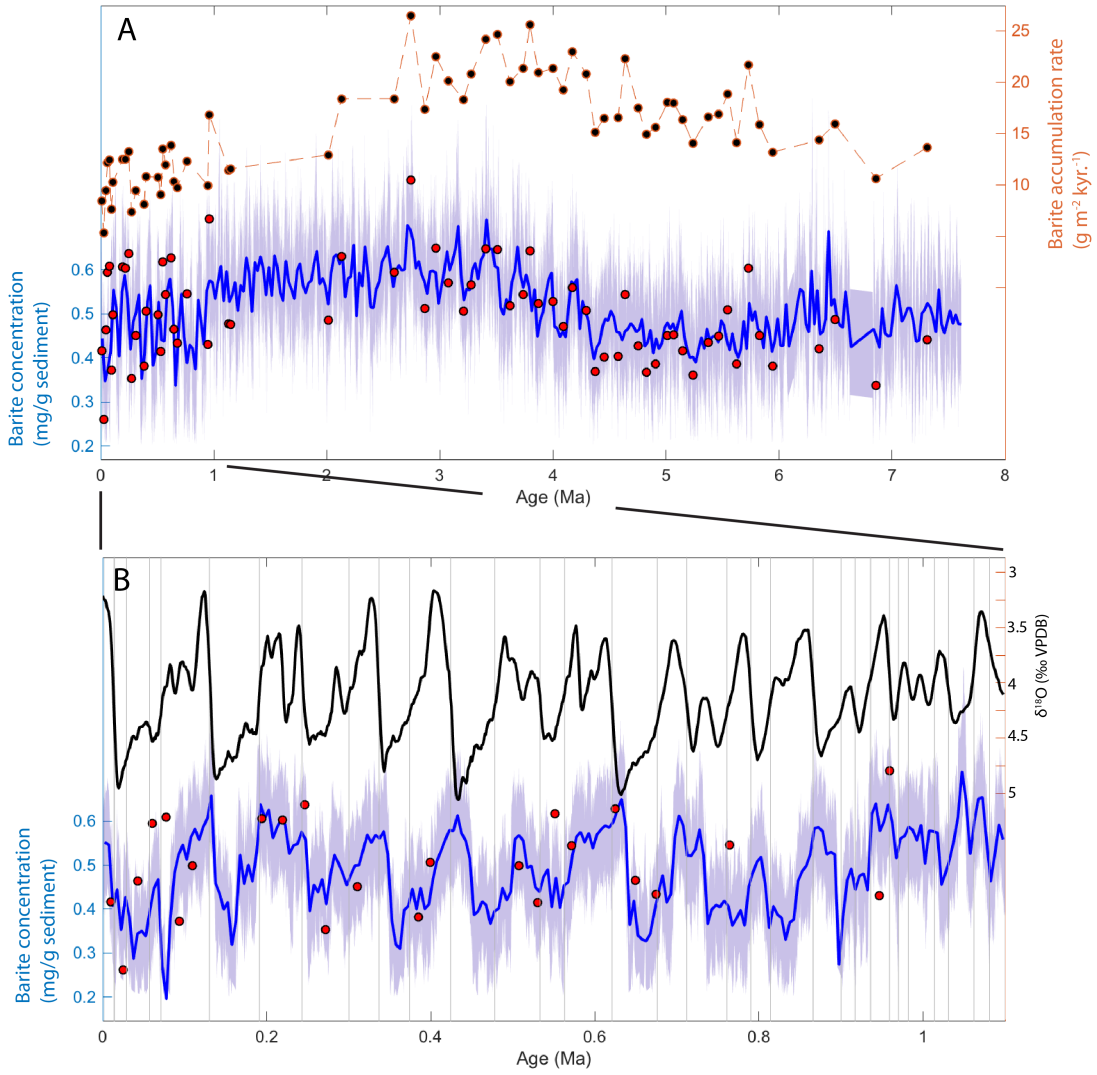

Figure 1.6. Ba/Ag from core scanning XRF calibrated into an inferred barite concentration using the linear relationship in Figure 1.5. (a) the full ~7.5 Myr. record of barite accumulation rate is shown in the top curve, and barite concentrations calculated from Ba/Ag are on the bottom as a curve averaged in 5 kyr. bins (blue) and a 95% confidence envelope (purple). Red points on the bottom curve show barite concentrations of discrete samples used to construct the Ba/Ag to barite calibration. (b) enlargement of the interval from the present to 1 Ma. Black curve is 5-point moving average of LR04 benthic foraminifera $\delta^{18}O$ stack (Lisiecki and Raymo, 2005), and barite concentration data are the same as in panel a (5 kyr. binned average in blue, 95% confidence envelope in purple, and discrete measurements in red). Light grey lines indicate boundaries between marine isotope stages. Site 1476 shipboard biostratigraphic age model was used for barite depth to age conversion, so slight misalignments between the $\delta^{18}O$ and barite curves are likely to be an artifact of the age model rather than true asynchronicity.

Chapter 1 Appendix

Table S1. Data generated and/or used in this study

Test sediments

Sample	Barite added (mg/g sed)	Barite equivalent[a] measured (mg/g sed)	Standard addition correction factor[b]	Corrected barite equivalent[c] (mg/g)	Recovery (%)	R^2	S:Ba molar ratio	Replicate 1σ uncertainty (%)
Hessler-61-1	0	6.07	1.06	6.445	97	0.99	1.15	
H-2	0.184	6.227		6.611				
H-3	0.919	7.098		7.536				
H-4	1.394	7.217		7.662				
H-5	2.092	8.075		8.573				
H-6	2.817	8.716		9.254				
H-7	3.573	9.284		9.857				
HR-1	0	5.877		6.24				1.61
HR-2	0	5.796		6.154				
HR-3	0	5.896		6.259				
HR-4	0	5.992		6.362				
HR-5	0	5.95		6.317				
H-H_2O_2	0	4.776	–	–	–	–	–	
H-ascorbic[d]	0	5.304	–	–	–	–	1.23	
Red clay-1	0	0.676	1.07	0.726	98	0.99	4.08	
R-2	0.251	0.878		0.943				
R-3	0.475	1.085		1.166				
R-4	0.755	1.316		1.414				
R-5	1.008	1.56		1.676				

Table S1 (cont'd)

Sample	Barite added (mg/g sed)	Barite equivalent[a] measured (mg/g sed)	Standard addition correction factor[b]	Corrected barite equivalent[c] (mg/g)	Recovery (%)	R^2	S:Ba molar ratio	Replicate 1σ uncertainty (%)
R-6	1.232	1.804		1.938				
R-7	1.521	2.107		2.264				
R-8	1.832	2.297		2.468				
R-H_2O_2	0	0.687	–	–	–	–	–	
R-ascorbic[d]	0	0.893	–	–	–	–	1.44	
U1480-1	0	1.517	1.06	1.6	97	0.99	1.32	
U1480-2	0.255	1.798		1.897				
U1480-3	0.385	1.933		2.039				
U1480-4	0.464	1.993		2.103				
U1480-5	0.761	2.269		2.394				
U1480-6	0.953	2.489		2.626				
U1480-7	1.316	2.735		2.886				
U1480-8	1.463	2.895		3.054				
Terrigenous-1	0	0.182	1.01	0.184	100	0.99	17.4	
T-2	0.054	0.239		0.241				
T-3	0.096	0.254		0.257				
T-4	0.124	0.3		0.303				
T-5	0.215	0.396		0.4				
T-6	0.294	0.467		0.471				
T-7	0.363	0.547		0.552				
T-8	0.451	0.616		0.622				
T-H_2O_2	0	0.143	–		–	–	–	

Table S1 (cont'd)

Sample	Barite added (mg/g sed)	Barite equivalent[a] measured (mg/g sed)	Standard addition correction factor[b]	Corrected barite equivalent[c] (mg/g)	Recovery (%)	R^2	S:Ba molar ratio	Replicate 1σ uncertainty (%)
T-ascorbic[d]	0	0.18	–		–	–	10.14	
Siliceous ooze-1	0	0.738	1	0.741	94	0.99	0.95	
Si-2	0.241	0.946		0.95				
Si-3	0.425	1.115		1.12				
Si-4	0.574	1.237		1.242				
Si-5	0.689	1.357		1.363				
Si-6	0.836	1.501		1.507				
Si-7	1.077	1.712		1.719				
Si-8	1.53	2.171		2.18				
Carbonate ooze-1	0	0.218	1.07	0.234	101	0.99	3.96	
C-2	0.053	0.274		0.294				
C-3	0.092	0.31		0.333				
C-4	0.12	0.334		0.359				
C-5	0.221	0.432		0.465				
C-6	0.267	0.473		0.508				
C-7	0.348	0.546		0.587				
C-8	0.505	1.36		1.461				
C-ascorbic	0	0.218	–	–	–	–	7.08	
Sapropel-1	0	0.337	1.08	0.362	96	0.99	9.34	

Table S1 (cont'd)

Sample	Barite added (mg/g sed)	Barite equivalent[a] measured (mg/g sed)	Standard addition correction factor[b]	Corrected barite equivalent[c] (mg/g)	Recovery (%)	R^2	S:Ba molar ratio	Replicate 1σ uncertainty (%)
Sa-2	0.051	0.416		0.447				
Sa-3	0.096	0.457		0.491				
Sa-4	0.233	0.584		0.628				
Sa-5	0.535	0.799		0.859				
Sa-6	0.918	1.19		1.279				
Sa-7	1.083	1.334		1.434				
Sa-8	1.618	1.81		1.945				
Sa-H_2O_2	0	0.362	–	–	–	–	–	
Sa-ascorbic[d]	0	0.488	–	–	–	–	4.51	
Barite-free kaolinite-1	0	0.04	–	–	97	0.99		
K-2	0.548	0.533	–	–			1.66	
K-3	0.844	0.811	–	–			1.03	
K-4	1.286	1.288	–	–			1.45	
K-5	1.529	1.496	–	–			0.97	

Method comparison

Sample	Barite equivalent[a] measured (mg/g sed)	Standard addition correction factor[b]	Corrected barite equivalent[c] (mg/g)	S:Ba molar ratio	Replicate 1σ uncertainty (%)	Total Ba from quantitative XRF (ppm)
PLDS 107 Bx-1 15-20 cm	4.346	1.06	4.586	1.16	0.11	2848

Table S1 (cont'd)

Sample	Barite equivalent[a] measured (mg/g sed)	Standard addition correction factor[b]	Corrected barite equivalent[c] (mg/g)	S:Ba molar ratio	Replicate 1σ uncertainty (%)	Total Ba from quantitative XRF (ppm)
Replicate 1	4.354		4.594			
Replicate 2	4.346		4.585			
With ascorbic acid reduction	4.523	–	–	1.15	–	
ERDC 88 Bx-1 0-9 cm	0.919	1.05	0.964	2.28	2.94	583.1
Replicate 1	0.865		0.908			
Replicate 2	0.877		0.921			
Replicate 3	0.928		0.974			
Replicate 4	0.923		0.969			
Replicate 5	0.917		0.963			
With ascorbic acid reduction	0.884	–	–	1.49	–	
PLDS 81 Bx-1 0-5 cm	6.052	1.05	6.355	2.03	0.23	3784
Replicate 1	6.029		6.33			
Replicate 2	6.027		6.328			
With ascorbic acid reduction	6.149	–	–	1.22	–	
INMD 106 Bx-5	0.098	1.05	0.103	5.95	4.84	*n.d.*

Table S1 (cont'd)

Sample	Barite equivalent[a] measured (mg/g sed)	Standard addition correction factor[b]	Corrected barite equivalent[c] (mg/g)	S:Ba molar ratio	Replicate 1σ uncertainty (%)	Total Ba from quantitative XRF (ppm)
10-15 cm						
Replicate 1	0.107		0.112			
Replicate 2	0.107		0.112			
With ascorbic acid reduction	0.116	–	–	8.48	–	
ERDC 125 Bx-2 5-10 cm	1.392	1.05	1.458	2.35	2.95	906.7
Replicate 1	1.419		1.486			
Replicate 2	1.479		1.549			
Replicate 3	1.502		1.573			
Replicate 4	1.488		1.559			
Replicate 5	1.461		1.53			
With ascorbic acid reduction	1.442	–	–	1.36	–	
INMD 106 Bx-5 15-20 cm	0.129	1.07	0.138	3.26	2.14	137.2
Replicate 1	0.124		0.133			
Replicate 2	0.125		0.133			
With ascorbic acid reduction	0.138	–	–	6.79	–	

Table S1 (cont'd)

Sample	Barite equivalent[a] measured (mg/g sed)	Standard addition correction factor[b]	Corrected barite equivalent[c] (mg/g)	S:Ba molar ratio	Replicate 1σ uncertainty (%)	Total Ba from quantitative XRF (ppm)
PLDS 107 Bx-1 0-5 cm	5.539	1.04	5.784	1.54	0.78	3366
Replicate 1	5.534		5.778			
Replicate 2	5.463		5.704			
With ascorbic acid reduction	5.426	–	–	1.17	–	

IODP 1476 Hole A

Core, section, interval (cm)	Depth (m CSF-A)	Barite equivalent[a] measured (mg/g sed)	Standard addition correction factor[b]	Corrected barite equivalent[e] (mg/g)	S:Ba molar ratio	Ba/Al	Ba/Ti	Ba/Fe	Ba/Zr	Ba/Rh	Ba/Ag
1H-1 30-33	0.315	0.392	1.05	0.412	1.96	3.91	0.83	0.063	0.96	0.147	0.0115
1H-1 80-83	0.815	0.247		0.263	1.32	11.86	1.29	0.101	1.00	0.149	0.0122
1H-1 130-133	1.315	0.437		0.466	1.43	3.66	0.98	0.076	1.10	0.189	0.0154
1H-2 30-33	1.815	0.562		0.6	1.69	2.18	0.86	0.074	1.29	0.228	0.0187
1H-2 80-83	2.315	0.574		0.613	1.06	2.05	0.87	0.073	1.25	0.278	0.0178
1H-2 130-133	2.815	0.352		0.375	1.56	5.49	1.13	0.087	0.94	0.154	0.0125
1H-3 30-33	3.315	0.47		0.502	1.49	2.69	0.78	0.049	1.11	0.192	0.0150
1H-3 80-83	3.815	0.572		0.611	1.56	1.58	0.69	0.065	1.32	0.304	0.0214
1H-3 130-133	4.315	0.569		0.608	2.06	1.40	0.66	0.057	1.24	0.271	0.0197
1H-4 30-33	4.815	0.601		0.641	1.87	1.72	0.83	0.076	1.15	0.258	0.0198

Table S1 (cont'd)

Core, section, interval (cm)	Depth (m CSF-A)	Barite equivalent[a] measured (mg/g sed)	Standard addition correction factor[b]	Corrected barite equivalent[e] (mg/g)	S:Ba molar ratio	Ba/Al	Ba/Ti	Ba/Fe	Ba/Zr	Ba/Rh	Ba/Ag
1H-4 80-83	5.315	0.333	1.08	0.36	4.54	2.35	0.81	0.078	1.11	0.171	0.0139
2H-1 30-33	6.015	0.425		0.454	2.35	1.36	0.70	0.058	0.98	0.212	0.0170
2H-2 30-33	7.515	0.36		0.385	3.81	1.64	0.78	0.076	0.97	0.190	0.0144
2H-3 30-33	9.015	0.478		0.51	1.57	1.64	0.72	0.065	0.98	0.189	0.0131
2H-3 130-133	10.015	0.47		0.502	1.63	2.29	0.83	0.069	1.16	0.245	0.0189
2H-4 30-33	10.515	0.392		0.418	2	3.47	1.07	0.085	0.99	0.197	0.0137
2H-4 80-83	11.015	0.582		0.622	1.64	3.64	1.13	0.076	1.33	0.205	0.0153
2H-4 130-133	11.515	0.514		0.549	2.26	3.53	1.11	0.100	1.27	0.217	0.0165
2H-5 80-83	12.515	0.592		0.632	1.56	1.69	0.86	0.075	1.33	0.277	0.0209
2H-5 130-133	13.015	0.439		0.469	1.1	2.90	0.94	0.082	1.08	0.174	0.0136
2H-6 30-33	13.515	0.409	1.07	0.44	2.15	2.79	1.00	0.099	1.00	0.168	0.0135
3H-1 30-33	15.515	0.515		0.55	2.06	1.34	0.68	0.059	0.85	0.159	0.0121
3H-2 80-83	17.515	0.406		0.434	2.73	1.66	0.86	0.077	1.22	0.255	0.0191
3H-4 30-33	20.015	0.675		0.721	1.91	1.63	0.80	0.070	1.21	0.274	0.0210
3H-7 30-33	24.515	0.45		0.481	1.86	1.50	0.82	0.075	1.28	0.268	0.0205
4H-1 30-33	25.015	0.449		0.479	2.07	1.39	0.74	0.069	1.00	0.226	0.0167
6H-3 80-83	46.42	0.459		0.49	3.41	1.40	0.69	0.059	1.10	0.256	0.0177
6H-5 130-133	49.76	0.595		0.636	3.18	1.21	0.72	0.060	1.09	0.266	0.0212
8H-3 30-33	66.29	0.561		0.599	2.8	1.23	0.65	0.059	1.16	0.269	0.0198
8H-5 80-83	69.76	0.758		0.809	2.88	1.29	0.73	0.068	1.24	0.375	0.0222
9H-1 80-83	74.37	0.483		0.516	5.33	1.36	0.66	0.056	1.07	0.254	0.0186
9H-3 80-83	76.38	0.613		0.655	3.26	1.71	0.83	0.072	1.32	0.370	0.0217

Table S1 (cont'd)

Core, section, interval (cm)	Depth (m CSF-A)	Barite equivalent[a] measured (mg/g sed)	Standard addition correction factor[b]	Corrected barite equivalent[e] (mg/g)	S:Ba molar ratio	Ba/Al	Ba/Ti	Ba/Fe	Ba/Zr	Ba/Rh	Ba/Ag
9H-6 130-133	80.4	0.538		0.575	2.78	1.49	0.74	0.062	1.24	0.336	0.0207
10H-2 30-33	85	0.478		0.51	3.01	1.20	0.63	0.054	1.17	0.286	0.0180
10H-4 80-83	87.6	0.534		0.57	3.85	1.23	0.65	0.056	1.19	0.283	0.0189
10H-6 130-133	91.7	0.611		0.652	2.26	1.68	0.89	0.080	1.59	0.396	0.0282
11H-2 130-133	95.5	0.61		0.652	14.55	1.18	0.62	0.053	1.14	0.294	0.0175
11H-5 130-133	100.48	0.489		0.522	3.67	1.38	0.64	0.054	1.15	0.261	0.0173
12H-1 130-133	102.85	0.513		0.548	3.09	1.15	0.62	0.054	1.21	0.260	0.0193
12H-3 80-83	105.8	0.607		0.648	2.82	1.44	0.76	0.060	1.29	0.303	0.0195
12H-5 80-83	108.74	0.493		0.527	3.56	0.88	0.50	0.044	1.11	0.255	0.0155
13H-1 130-133	113.61	0.498		0.532	3.98	1.35	0.80	0.061	1.23	0.302	0.0181
13H-4 30-33	117.2	0.445		0.475	3.05	1.50	0.85	0.065	1.35	0.299	0.0163
13H-6 80-83	118.52	0.528		0.564	3.34	1.59	0.82	0.070	1.24	0.303	0.0216
14H-2 130-133	124.15	0.478		0.511	4.27	1.22	0.73	0.059	1.09	0.266	0.0175
14H-4 130-133	127.27	0.349		0.372	4.52	1.19	0.66	0.053	0.95	0.229	0.0142
14H-7 30-33	129.14	0.379		0.405	3.44	1.25	0.71	0.055	1.01	0.216	0.0163
15H-3 130-133	134.67	0.381		0.407	4.3	1.00	0.57	0.048	1.03	0.237	0.0124

Table S1 (cont'd)

Core, section, interval (cm)	Depth (m CSF-A)	Barite equivalent[a] measured (mg/g sed)	Standard addition correction factor[b]	Corrected barite equivalent[e] (mg/g)	S:Ba molar ratio	Ba/Al	Ba/Ti	Ba/Fe	Ba/Zr	Ba/Rh	Ba/Ag
15H-5 80-83	137.22	0.513		0.548	2.61	2.07	1.10	0.084	1.16	0.229	0.0160
16H-1 130-133	140.92	0.404		0.431	4.25	1.40	0.84	0.065	0.97	0.201	0.0154
16H-3 130-133	143.42	0.346		0.37	4.59	1.24	0.71	0.056	0.96	0.221	0.0143
16H-6 30-33	147	0.365		0.39	3.33	1.19	0.69	0.054	0.98	0.220	0.0148
17H-2 80-83	151.22	0.426		0.455	3.2	1.38	0.84	0.062	1.07	0.206	0.0149
17H-4 30-33	153.44	0.428		0.457	3.13	1.21	0.69	0.058	1.12	0.213	0.0153
17H-6 30-33	156.49	0.393		0.42	3.99	1.29	0.75	0.057	1.12	0.243	0.0158
18H-2 30-33	159.62	0.342		0.365	4.32	1.14	0.69	0.049	0.97	0.194	0.0124
18H-5 130-133	164.16	0.41		0.438	3.45	1.13	0.67	0.056	1.07	0.219	0.0145
19H-1 130-133	168.84	0.424		0.453	3.28	1.12	0.70	0.054	1.05	0.227	0.0152
19H-3 130-133	170.61	0.48		0.513	6.04	1.73	0.90	0.074	1.17	0.233	0.0147
19H-5 80-83	173.49	0.365		0.39	37.03	1.46	0.77	0.066	1.07	0.208	0.0151
20H-1 130-133	178.37	0.57		0.609	3.48	1.73	1.04	0.083	1.18	0.225	0.0166
20H-4 30-33	179.74	0.425		0.454	3.22	1.34	0.76	0.063	1.08	0.218	0.0149
20H-6 80-83	183.8	0.36		0.385	4.79	1.27	0.70	0.059	0.92	0.190	0.0105
22H-3 30-33	199.73	0.397		0.424	3.35	1.32	0.76	0.060	1.08	0.232	0.0153

Table S1 (cont'd)

Core, section, interval (cm)	Depth (m CSF-A)	Barite equivalent[a] measured (mg/g sed)	Standard addition correction factor[b]	Corrected barite equivalent[e] (mg/g)	S:Ba molar ratio	Ba/Al	Ba/Ti	Ba/Fe	Ba/Zr	Ba/Rh	Ba/Ag
22H-5 130-133	202.08	0.459		0.49	3.48	1.18	0.69	0.059	1.12	0.265	0.0181
23H-6 30-33	213.59	0.319		0.341	5.15	1.09	0.62	0.052	0.90	0.202	0.0137
24H-7 30-33	224.29	0.416		0.445	3.84	1.08	0.70	0.053	1.07	0.256	0.0169

Barite dissolution tests

Treatment	Barite added (mg)	Barite dissolved (mg)
1 N HNO_3, 12 hours at room temperature	2.424	1.04
	5.675	1.15
	13.365	1.18
0.2 M NH_3OCl in 4 N acetic acid, 12 hours 80°C	10.714	0.11
0.2 M ascorbic acid in 5 N acetic acid, 12 hours at room temperature	10.803	0.01
0.2 M ascorbic acid in 5 N acetic acid, 12 hours at 60°C	10.13	*b.d.l.*

Reduction tests

Table S1 (cont'd)

	Ba (ug/g sample)	Ca (mg/g sample)	Fe (mg/g sample)	Mn (mg/g sample)	Sr (ug/g sample)	S (mg/g sample)
Red clay NH_3OHCl	15.8	2.91	6.05	7.79	53.86	1.53
Red clay ascorbic acid	2.4	2.1	10.94	7.21	2.5	1.52
Mn-nodule NH_3OHCl	783.9	11.69	129.64	169.06	685.67	3.9
Mn-nodule ascorbic acid	753.2	10.61	149.15	153.2	612.41	3.78

[a]Amount of barite assuming no other sources of Ba

[b]Defined as the reciprocal of the slope of line of best fit on a plot of added Ba (from standard) against measured Ba

[c]Measured barite equivalent multiplied by the standard addition correction factor

[d]Samples were depleted during sequential addition experiments so these aliquots are not precisely the same as others of the same type of test sediment

[e]Due to the agreement of standard addition correction factors for IODP 1476A samples, an average correction factor of 1.07 was used for samples that were not subjected to standard addition experiments

b.d.l.: below detection limit

n.d.: no data

CHAPTER 2

Earth's "heartbeat": A global link between marine productivity and astronomical cycles

Brian House[1] and Richard D. Norris[1]

[1]Scripps Institution of Oceanography, University of California San Diego La Jolla CA 92037

Corresponding author: Brian M. House (bhouse@ucsd.edu)

Abstract

Marine productivity shows orbital pacing in individual sediment records, but whether this reflects orbital control of the size of the global biosphere remains unknown. We produced high resolution productivity records from eight sediment core locations to make the first global "stack" of marine productivity. Both the individual records and the stack show cycles that coincide in frequency with the major variations in Earth's orbit, suggesting productivity in the global ocean has an astronomically-paced "heartbeat".

Main text

Periodic variations the Earth's orbital eccentricity (how non-circular the orbit is), obliquity (the inclination of the orbit), and the position in the orbit at which solstices occur lead to mathematically predictable cycles in the intensity of incoming sunlight, termed solar insolation. These long-term changes in solar insolation could conceivably affect marine productivity directly by altering the intensity of sunlight available for photosynthetic primary production, which we would expect to be reflected in sediment core paleoproductivity proxies that reflect the amount of biological production in the overlying water column. Such trends have been identified over different time intervals at various locations (Jaccard et al., 2013; Paytan and Kastner, 1996; Rickaby et al., 2007), but to systematically address this question, we generated early Pleistocene records of the accumulation rate of barite ($BaSO_4$) in marine sediments, which is a powerful proxy for export productivity (Averyt and Paytan, 2004; Dehairs et al., 1980; Eagle et al., 2003; Griffith and Paytan, 2012), at eight sediment core locations (Figure 1). For each site, we measured the barite concentration of ~100 samples, giving an average sampling interval of ~5 kyr. from 2.5-2 Ma., which was only feasible with a

high-throughput analytical method (House and Norris, n.d.), and which provides the necessary temporal resolution and record length to identify precession (~19 and 23 kyr.), obliquity (41 kyr.), and the more minor eccentricity cycles (~100 kyr. period; Table S1). Using either published (Bickert et al., 1997; Chen et al., 1995; Gorgas et al., 2017; Harris, 2002; Lisiecki and Raymo, 2005; Mix et al., 1995; Raymo et al., 1989; Shackleton et al., 1990; Tiedemann et al., 1994; Tiedemann and Haug, 1995) or re-aligned age models to convert sample depth to age, we constructed Barite Accumulation Rates (BARs), which show widespread coherence with solar insolation at precession and obliquity frequencies (Figure 1) despite a range of effects such as variations in phytoplankton ecological communities, upwelling intensity, and seafloor carbonate dissolution that may affect the fidelity of productivity records. We also normalized and mathematically "stacked" the BAR records to look for more global trends while minimizing the effects of geographically localized processes and uncertainty in age models at individual sites (Figure 2). Our productivity stack – the first of its kind – reveals strong coherence with precession and obliquity insolation cycles, and the phase lag between it and orbital obliquity suggests glacial periods tended to be more productive during the early Pleistocene.

We find pronounced coherence at ~40 kyr. periods, reflecting the obliquity cycle underlying early Pleistocene glacial and interglacial intervals (Figure 1; Supplement). Obliquity cycles are especially notable at Site 607 (Figure 1), which is consistent with substantial glacial/interglacial reorganization of intermediate and deep water in the North Atlantic (Curry and Oppo, 2005). We note that while barite in carbonate-rich sediments could be concentrated during glacial periods when increased deep water acidity leads to carbonate dissolution (Curry and Oppo, 2005), but the five-fold increase in barite concentration during

glacial periods at North Atlantic Site 607 during an interval of relatively constant carbonate content (Leg 94 Shipboard Scientific Party, 1983) suggests that the barite signal represents variations in biological production rather than carbonate dissolution. The difference in phase lag between BAR and insolation at the summer and winter solstices implies that glacial periods are gnerally more productive than interglacial intervals (Figure 3), which accords with the coherence and phase lags at Site 882 in the North Pacific (Figure 1) as well as previous localized studies (Paytan and Kastner, 1996). Previous results suggest spatial heterogeneity in whether glacial or interglacial periods are more productive, particularly in areas influenced by nutrient-rich water masses produced in the high latitude Southern Ocean (Etourmeau et al., 2009; Jaccard et al., 2013), so local effects may cause deviations from the large scale trends apparent in our data. However, coherence peaks at ~40 kyr. periods for the lower latitude sites 677, 849, and 758 suggest that the productivity response to orbital obliquity is not relegated to the high latitude regions most affected by obliquity variations (Figure 1).

Precession has the greatest effect on low-latitude insolation, and indeed we see the greatest evidence for coherence at ~23 kyr. periods at tropical ODP Sites 758 (Indian Ocean), 849 (Pacific), 659, and 927 (eastern and western Atlantic, respectively). While productivity variations between glacial and interglacial periods have been noted before (House and Norris, n.d.; Jaccard et al., 2013; Paytan et al., 1996), this is the first time that precessional frequencies have been identified in productivity records, suggesting that orbital variations affect productivity on a more fundamental level than previously thought. Localized phenomena such as the Indian Ocean Monsoon (Site 758) or tropical rainfall and terrigenous runoff (Site 927, near the Amazon fan), may modulate productivity at precessional frequencies more than insolation does directly (see Supplement).

To deemphasize local effects and magnify global trends, we normalized and summed the site-specific BAR records to form the first global marine productivity stack (Figure 3; Supplement). We compare the stack to boreal summer insolation from North Pacific Site 882 (Figure 2) since it most closely represents the canonical 65º N summer insolation curve. Insolation records from other sites and times of year produce similar results (see Supplement). Coherence spectra show peaks at ~150, ~40, ~23, and ~17-18 kyr. periods using both published and re-aligned age models (Figure 2). The peaks associated with obliquity and precession frequencies produce coherence magnitudes that are highly unlikely to emerge from random signals (Figure 4; Supplement) and the associated phase lags are largely unchanged by age model adjustments (Figure 3). The exceptionally strong ~40 kyr. BAR cyclicity is out of phase with Northern Hemisphere summer insolation and orbital obliquity (Figure 2), which accords with the interpretation from site-specific results that glacial periods tend to be more productive during the early Pleistocene. The phase lag at precessional frequencies is less easily interpreted and would benefit from further study, but may support the conclusion from (Rickaby et al., 2007) that both insolation intensity and growing season length contribute to intervals of high productivity (see Supplement).

This is the first work to present contemporaneous high-resolution productivity records from globally-dispersed core locations. There have been hints of an astronomical cycle in carbon burial based on carbon isotope records form the deep Pacific (e.g. *22*), which, as the largest ocean basin, is expected to reflect a global signal. Biotic evolution, including the appearance of species (Dam et al., 2006) and abundance of C3 and C4 plants (An et al., 2005), may also respond to orbital cycles that change terrestrial aridity and productivity. Our results support this suggestion that evolutionary opportunity, reflected by marine productivity,

varies with an orbital rhythm. While uncertainty is unavoidable in extrapolating isolated sediment core analyses to the global ocean, our data nevertheless cover a large geographic area and strongly suggest that the oceans, the largest global ecosystem by biomass, have an astronomically-paced biological "heartbeat".

Acknowledgements

Analytical support was provided by Paterno Castillo and Christopher McIsaac, and Sara Gile and Christopher Charles (all at Scripps Institution of Oceanography) contributed insight into data analysis and interpretation. Funding: Scripps Institution of Oceanography and Norris group laboratory funding supported analytical costs, and BMH was supported by a University of California President's Dissertation Year Fellowship.

Chapter 2 has been submitted for publication and may appear in *Science* as House, B. and Norris, R. D. 2019. The dissertation author was the primary investigator and author of this paper.

References

An, Z., Huang, Y., Liu, W., Guo, Z., Clemens, S., Li, L., Prell, W., Ning, Y., Cai, Y., Zhou, W., Lin, B., Zhang, Q., Cao, Y., Qiang, X., Chang, H., Wu, Z., 2005. Multiple expansions of C4 plant biomass in East Asia since 7 Ma coupled with strengthened monsoon circulation. Geology 33, 705–708. https://doi.org/10.1130/G21423.1

Averyt, K.B., Paytan, A., 2004. A comparison of multiple proxies for export production in the equatorial Pacific. Paleoceanography 19, 1–14. https://doi.org/10.1029/2004PA001005

Bickert, T., Curry, W.B., Wefer, G., 1997. Late Pliocene to Holocene (2.6-0 Ma) western Equatorial Atlantic deep-water circulation: Inferences from benthic stable isotopes, in: Proceedings of the Ocean Drilling Program, Scientific Results. pp. 239–254.

Chen, J., Farrell, W., Murray, W., Prell, L., 1995. Timescale and paloceanographic implications of a 3.6 m.y. oxygen isotope record from the northeast Indian Ocean (Ocean Drilling Program site 758). Paleo 10, 21–47.

Curry, W.B., Oppo, D.W., 2005. Glacial water mass geometry and the distribution of δ13C of ΣCO_2 in the western Atlantic Ocean.pdf. Paleoceanography 20. https://doi.org/10.1029/2004

Dam, J.A. Van, Aziz, H.A., Ostende, L.W.V.D.H., Lourens, L.J., Mein, P., Meulen, A.J. Van Der, Pelaez-campomanes, P., 2006. Long-period astronomical forcing of mammal turnover. Nature 443, 687–691. https://doi.org/10.1038/nature05163

Dehairs, F., Chesselet, R., Jedwab, J., 1980. Discrete suspended particles of barite and the barium cycle in the open ocean. Earth Planet. Sci. Lett. 49, 528–550.

Eagle, M., Paytan, A., Arrigo, K.R., van Dijken, G., Murray, R.W., 2003. A comparison between excess barium and barite as indicators of carbon export. Paleoceanography 18. https://doi.org/10.1029/2002pa000793

Etourmeau, J., Martinez, P., Blanz, T., Schneider, R., 2009. Pliocene – Pleistocene variability of upwelling activity, productivity, and nutrient cycling in the Benguela region. Geology 37, 871–874.

Gorgas, T., Lyle, M., Wilkens, R.H., Westerhold, T., Tian, J., Drury, A.J., 2017. Revisiting the Ceara Rise, equatorial Atlantic Ocean: isotope stratigraphy of ODP Leg 154 from 0 to 5 Ma. Clim. Past 13, 779–793. https://doi.org/10.5194/cp-13-779-2017

Griffith, E.M., Paytan, A., 2012. Barite in the ocean - occurrence, geochemistry and palaeoceanographic applications. Sedimentology 59, 1817–1835. https://doi.org/10.1111/j.1365-3091.2012.01327.x

Harris, S.E., 2002. Data Report: Later Pliocene-Pleistocene carbon and oxygen stable isotopes from benthic Foraminifers at Ocean Drilling Program Site 1123 in the Southwest Pacific, in: Richter, C. (Ed.), Proceedings of the Ocean Drilling Program, Scientific Results.

House, B.M., Norris, R.D., *in review* Unlocking the barite paleoproductivity proxy: a new high-throughput technique reveals glacial/interglacial productivity changes at the East African margin. Chem. Geol.

Jaccard, S.L., Hayes, C.T., Martinez-Garcia, A., Hodell, D.A., Anderson, R.F., Sigman, D.M., Haug, G.H., 2013. Two modes of change in Southern Ocean productivity of the past millions of years. Science (80-.). 339, 1419–1423.

Leg 94 Shipboard Scientific Party, 1983. Site 607. Proc. Deep Sea Drill. Proj. Initial Reports 94, 75–143.

Lisiecki, L.E., Raymo, M.E., 2005. A Pliocene-Pleistocene stack of 57 globally distributed benthic $\delta^{18}O$ records. Paleoceanography 20. https://doi.org/10.1029/2004pa001071

Mix, A.C., Pisias, N.G., Rugh, W., Wilson, J., Morey, A., Hagelberg, T.K., 1995. Benthic foraminifer stable isotope record from Site 849 (0-5 Ma): Local and global climate changes, in: Pisias, Nicklas G, Mayer, L.M., Janecek, T.R., Palmer-Julson, A., van Andel, T.H. (Eds.), Proceedings of the Ocean Drilling Program, Scientific Results. pp. 371–412.

Pälike, H., Norris, R.D., Herrle, J., Wilson, P.A., Coxall, H.K., Lear, C., Shackleton, N.J., Tripati, A., Wade, B.S., 2006. The heartbeat of the Oligocene climate system. Science (80). 314, 894–898.

Paytan, A., Kastner, M., 1996. Glacial to interglacial fluctuations in productivity in the Equatorial Pacific as indicated by marine barite. Science (80-.). 274, 1355–1357.

Paytan, A., Kastner, M., Chavez, F.P., 1996. Glacial to interglacial fluctutation in productivity in the Equitorial Pacific as indicated by marine barite. Science (80-.). 274, 1355–1357.

Raymo, M.E., Ruddiman, W.F., Backman, J., Clement, B.M., Martinson, D.G., 1989. Late Pliocene variation in northern hemisphere ice sheets and North Atlantic deep water circulation. Paleoceanography 4, 413–446.

Rickaby, R.E.M., Bard, E., Sonzogni, C., Rostek, F., Beaufort, L., Barker, S., Rees, G., Schrag, D.P., 2007. Coccolith chemistry reveals secular variations in the global ocean carbon cycle? Earth Planet. Sci. Lett. 253, 83–95. https://doi.org/10.1016/j.epsl.2006.10.016

Shackleton, N.J., Berger, W., Peltier, W.R., 1990. An alternative astronomical calibration of the lower Pleistocene timescale based on ODP 677. Trans. R. Soc. Edinb. Earth Sci. 81,

251–261.

Tiedemann, R., Haug, G.H., 1995. Astronomical calibration of cycle stratigraphy for Site 882 in the Northwest Pacific. Proc. Ocean Drill. Progr. Sci. Results1 145, 283–292.

Tiedemann, R., Sarnthein, M., Shackleton, N.J., 1994. Astronomic timescale for the Pliocene Atlantic $\delta^{18}O$ and dust flux records of Ocean Drilling Program site 659. Paleoceanography 9, 619–638.

Figures

Figure 2.1. (following page) Overview map of site locations and coherence magnitude and phase lag between BAR and local summer solstice insolation at each site shown in polar form. For each site, the color of point(s) on the polar graph represents the frequency of a coherence peak deemed significant. The radial distance of these points represents the magnitude of the associated coherence peak while the angle from the positive x-axis represents the phase lag between the BAR and insolation signals (clockwise rotation indicates BAR lags insolation, counterclockwise indicates insolation lags BAR). The shaded areas on the plots represent the estimated interquartile range in coherence magnitude and phase lag based on Monte Carlo simulations of age model uncertainty (see Supplement).

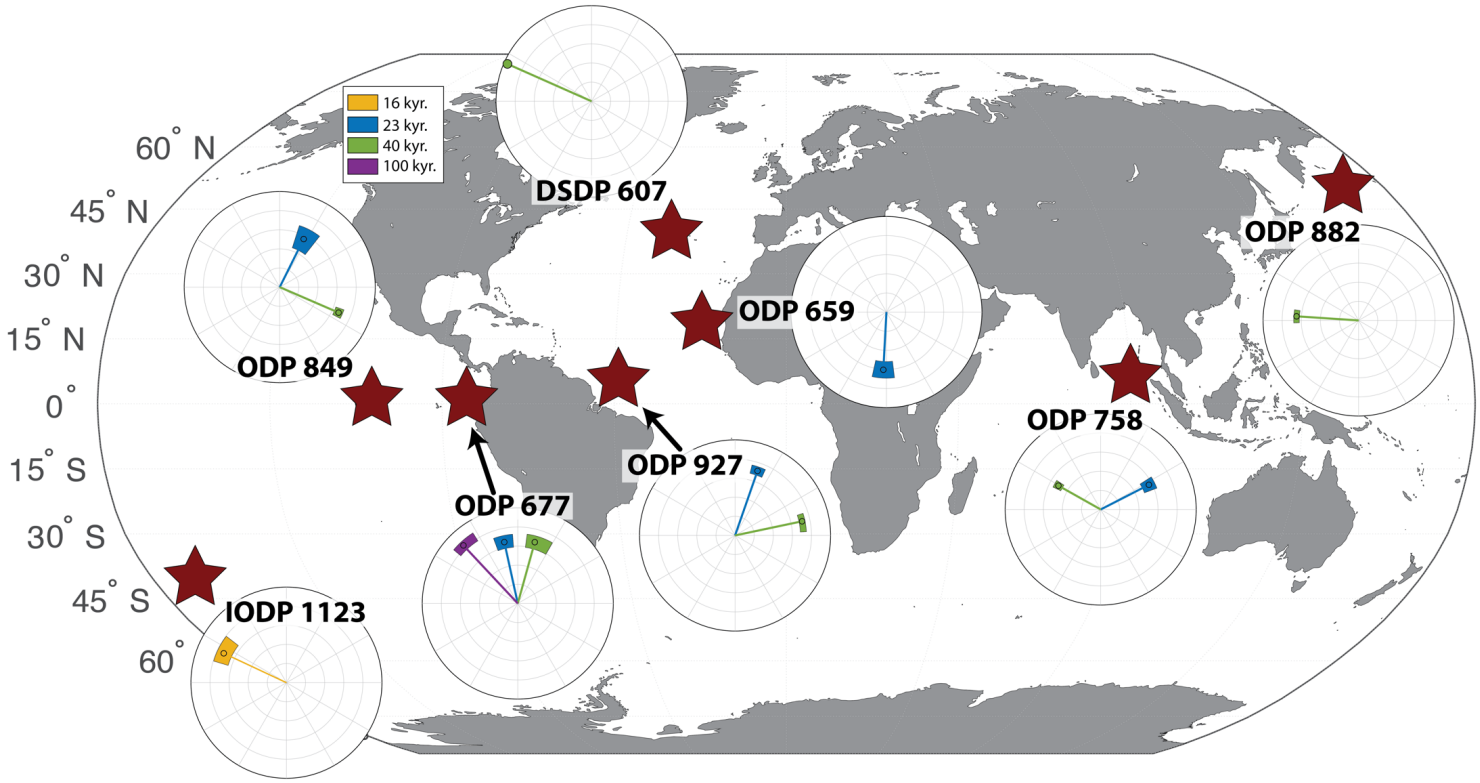
16 kyr.
23 kyr.
40 kyr.
100 kyr.
60° N
45° N
30° N
15° N
0°
15° S
30° S
45° S
60°
DSDP 607
ODP 882
ODP 659
ODP 849
ODP 758
ODP 927
ODP 677
IODP 1123

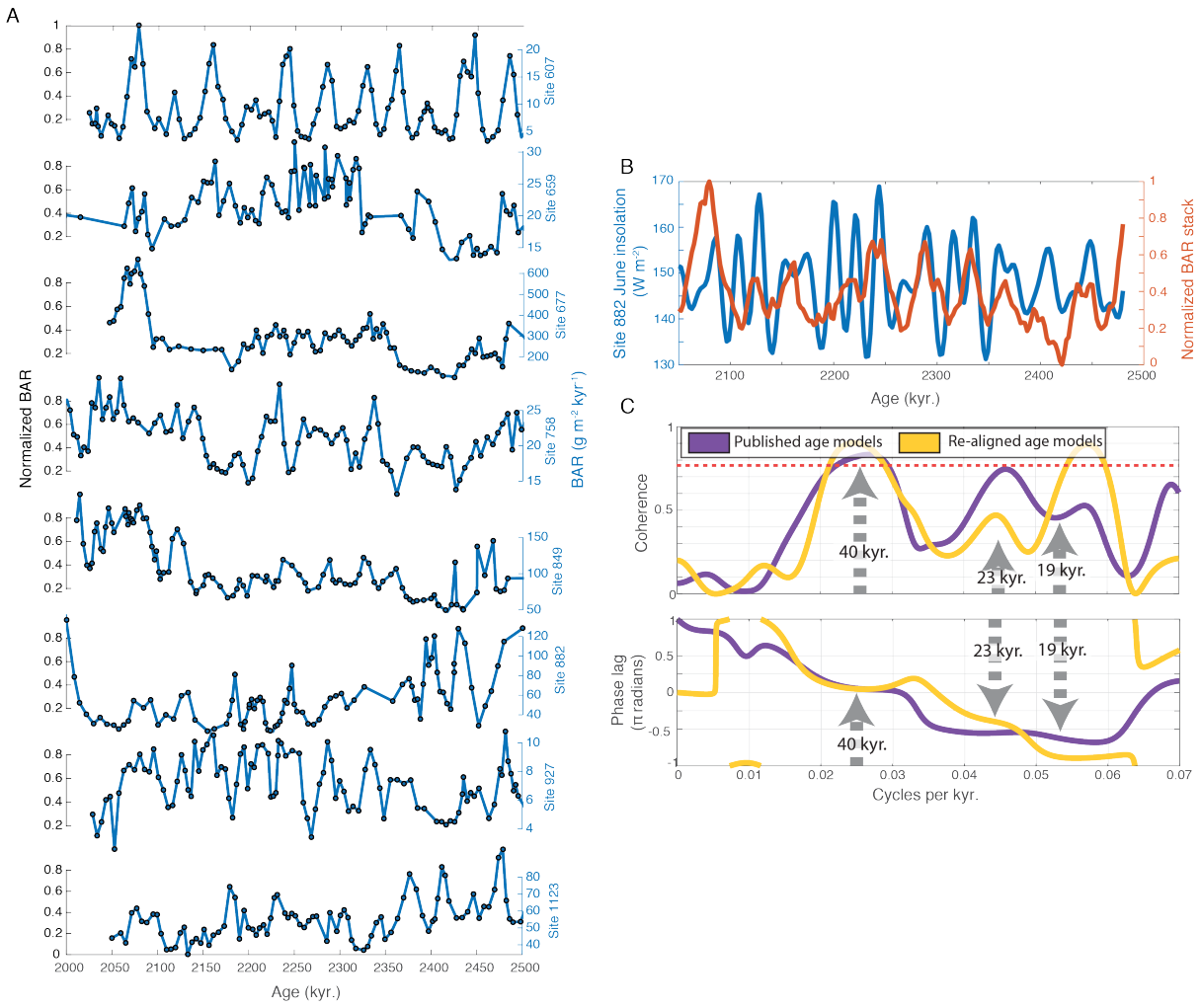

Figure 2.2. (A) BAR records for individual sites, and (B) global BAR stack that shows visual similarities with boreal summer insolation at Site 882, which best represents the frequently-used June insolation curves from 65º N. (C) the coherence spectra between the BAR stack and Site 882 insolation show peaks at obliquity and precessional frequencies that remain regardless of which age models are used for individual sites. The red dotted line indicates the formal 95% confidence level (see Supplement), though we also employed Monte Carlo simulations as an additional test of robustness (Figure 4). The robustness and physical meaning of the ~150 kyr. peaks are unclear from this study. Phase lags associated with the coherence peaks imply more productive glacial periods (Figure 2), in accordance with site-specific results, and a more complex relationship at precessional frequencies.

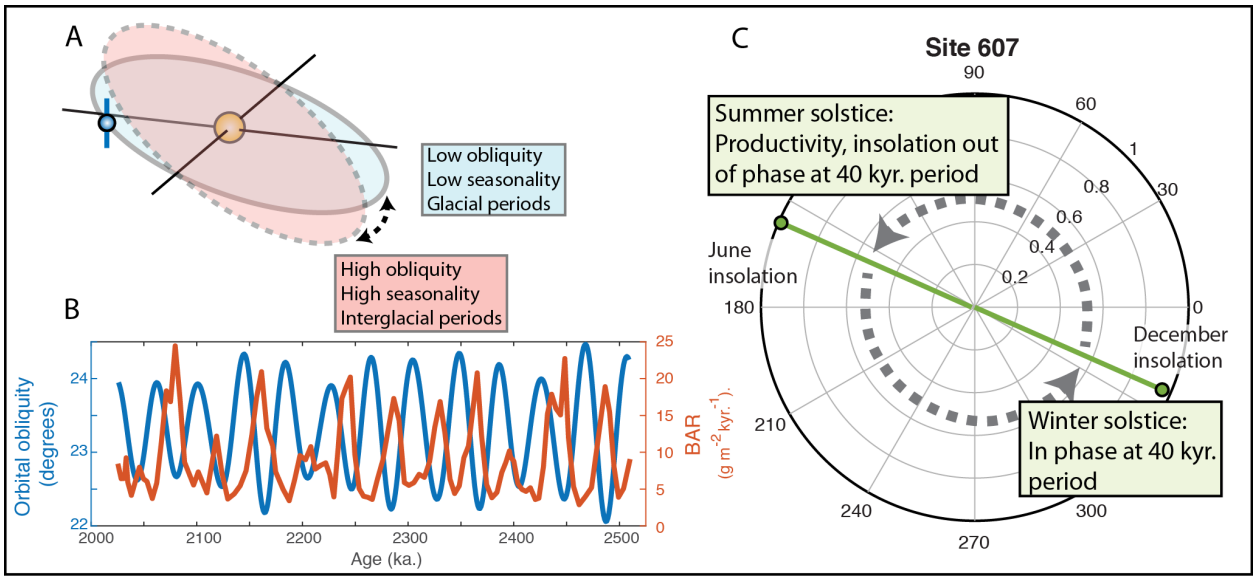

Figure 2.3. Interpretation of the physical meaning behind phase lags of ~40 kyr. cycles at different seasons. (A) Extremes in orbital obliquity lead to extremes in seasonality as the insolation difference between opposing seasons is greatest, (B) shows the BAR record (red) for Site 607 in the North Atlantic, where ~40 kyr. coherence is particularly prominent and orbital obliquity (blue). As indicated in (C), BAR is out of phase with ~40 kyr. insolation cycles at the summer solstice and in phase at the winter solstice indicating periods of lower obliquity, which correspond to intervals of decreased seasonality and hence glacial periods, tend to be more productive.

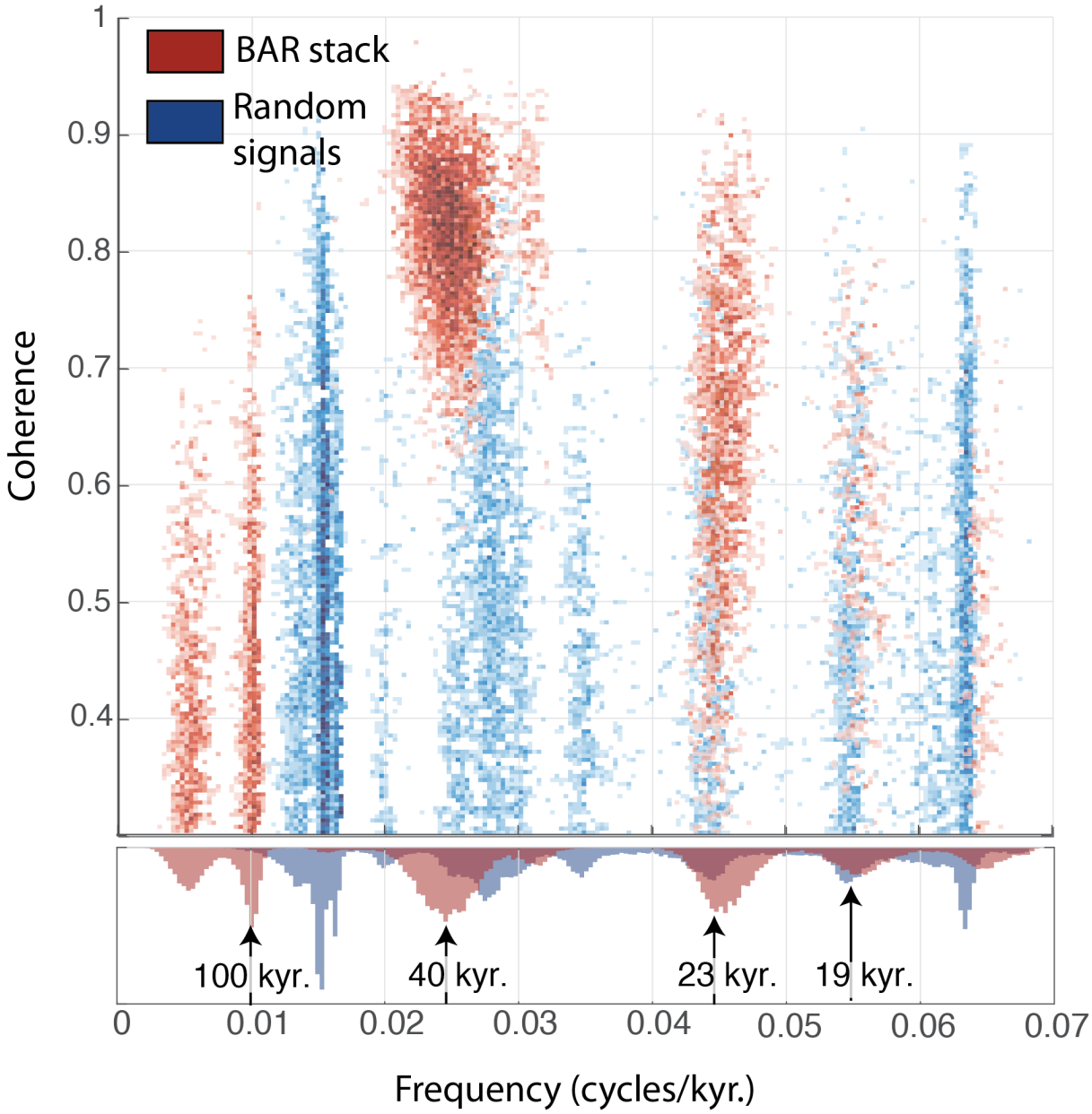

Figure 2.4. Univariate and bivariate histograms showing the coherence magnitudes at different frequencies produced by simulated perturbations of the ages of stacked BAR data (red) and random white-noise signals (blue). Both the BAR stack (based on the published age models) and random signals were compared with June insolation at Site 882. All peaks in the coherence spectra with magnitude greater than 0.3 and a minimum prominence of 0.1 above the surrounding spectrum were identified and discretized into frequency and coherence magnitude bins. More intense colors indicate higher bin counts, and the marginal histogram below the frequency axis shows the distribution of the frequencies of coherence peaks

detected along with the frequencies of obliquity and precession cycles. The ~40 kyr. and ~23 kyr. peaks occurred more frequently and generally at greater magnitude for the BAR stack than for random signals, leading us to conclude that these peaks in the coherence spectrum of the BAR stack are likely to represent true processes linking cycles in obliquity and precession to export productivity.

Chapter 2 Appendix

1 Materials and methods

1.1 Barite quantification

Barite concentrations in discrete sediment samples were determined using the method of House and Norris (2019), which involves selectively dissolving barite from sediments using a chelating organic ligand. Barium in solution was quantified according to the detailed methods in House and Norris (2019): briefly, Ba concentrations in leachate solutions were measured with Inductively Coupled Plasma Optical Emission Spectroscopy (ICP-OES) using the 233.527 nm Ba emission peak viewed axially. House and Norris (2019) note the potential for ~5-10% diminution of Ba emission intensity, likely due to the complex sample matrices, so we conducted standard addition experiments in which increasing amounts of a Ba standard (CertiSpex, 100 ppm Ba) were added to at least three sample splits, and the slope of the resulting line of added versus measured Ba concentrations was used to correct for matrix effects that could not be overcome with matrix matching of standards. This procedure suggested a small correction of ~5% for samples from all sites. We also conducted sets of sequential barite addition experiments in which progressively increasing amounts of synthetic barite were added to splits of the same sediment samples to verify that recovery, when corrected for matrix effects using standard addition experiments, was sufficiently close to 100%. Check standards were run every 15 analyses to correct for instrumental drift.

1.2 Age models and mass accumulation rate

Original age models came from comparing benthic foraminifera $\delta^{18}O$ records to (Lisiecki and Raymo, 2005) for all sites except Site 882 at which cyclicity in the magnetic susceptibility and Gamma Ray Attenuation Porosity Evaluator (GRAPE) records were

orbitally tuned to the 41 kyr. obliquity cycle (Tiedemann and Haug, 1995). We note, however, that filtering these records with a slightly wider (40-42 kyr.) bandpass filter or very narrow filters centered at either 40 or 42 kyr. produced a number of cycles that was either greater or less than the number of obliquity cycles between 2.5 and 2 Ma., so we are uncertain of how physically meaningful the apparent cyclicity is.

The ~10 cm sample spacing for $\delta^{18}O$ measurements necessary to minimize sediment bioturbation effects means that the $\delta^{18}O$ record at all sites is an aliased version of the global stack, which leads to slight ambiguity in aligning the two records. Estimated sedimentation rates for the sites we used were on the order of several cm/kyr., so a ~10 cm sample spacing would represent a temporal resolution of ~1 sample per 2-5 kyr. While this uncertainty is small relative to the age resolution needed for many purposes, it can be significant when testing for cyclicity at the precessional frequencies of ~19 and 23 kyr. We tested the potential effects of aliasing in the $\delta^{18}O$ (and the Site 882 magnetic susceptibility/GRAPE signals) used to create age models by fitting smoothing splines through the age/depth data and re-aligning them with obliquity cycles. This process typically led to minor adjustments in the age models. These re-aligned age models generally, however, produced small changes in the results. Ages of discrete samples generated from published and realigned age models are presented in Table S1.

Sedimentation rates were calculated from age models by smoothing apparent sedimentation rates from adjacent age/depth tie points with a 25-point moving median filter to avoid spurious extrema. Dry bulk densities were taken from shipboard values presented in the relevant site reports (Leg 108 Shipboard Scientific Party, 1988; Leg 111 Shipboard Scientific Party, 1988; Leg 121 Shipboard Scientific Party, 1989; Leg 138 Shipboard Scientific Party,

1992; Leg 145 Shipboard Scientific Party, 1993; Leg 154 Shipboard Scientific Party, 1995; Leg 94 Shipboard Scientific Party, 1983; Party, 1999), and the barite accumulation rate was calculated as the product of the sedimentation rate, the dry bulk density, and the sediment barite concentration.

1.3 Data treatment

We primarily used spectral coherence between our BAR records and either local insolation (for individual sites) or a combination of local insolation and global orbital parameters (for the stacked data; see below) to establish whether cyclicity in export productivity occurs at similar frequencies as those of orbital variations. Coherence consists of two parts: the magnitude of similarity between two datasets at different frequencies and the phase lag between cycles in the two datasets as a function of frequency. Because the magnitude of coherence reflects the normalized magnitude of the Fourier transform of the cross-correlation function between the BAR and insolation/orbital parameter timeseries, it is only sensitive to linear relationships between the two datasets. More complex non-linear relationships cannot be detected, so less direct effect of insolation variations such as potential changes in wind patterns or cloud cover, could conceivably affect productivity in complicated ways that would be exceedingly difficult to identify unambiguously.

For analysis of the coherence at individual sites, we compared the BAR records with local insolation averaged over the 30-day periods centered on the solstices and the March equinox to better understand the influences of seasonality based on the changes in phase lags between BAR and insolation at different seasons (Figures 2 and 3). Because of the relatively short length of BAR signals, we used three Hamming windows with 50% overlap to estimate coherence for both the individual and stacked BAR records (see below), which means that

coherence of ~0.77 corresponds to a confidence level of 0.05 according to the formal definition of statistical significance.

Uncertainty in the age model complicates analysis of coherence as it also leads to uncertainty in BAR, which is calculated as the product of barite concentration, dry bulk sediment density, and sediment accumulation rate. Because of the difficulties in quantifying age model uncertainty, which was nevertheless likely to introduce greater uncertainty than the <4% associated with the barite measurement procedure (House and Norris, n.d.), we used Monte Carlo simulations in which we perturbed the age of each individual sample by an amount randomly drawn from a normal distribution with a relatively large standard deviation of 2.5 kyr. We note that searching only within specified frequency windows for coherence peaks could bias results by ignoring peaks at non-orbital frequencies, but the coherence spectra for all sites and the global stack were quite clean with few unexpected peaks (Figure S1), so peak detection within prescribed frequency windows seems reasonable. The peak detection algorithm we used only picked coherence peaks with an absolute magnitude above 0.3 and prominence of at least 0.1 above the surrounding spectrum. Using 10^3 simulations for each site/season combination and 10^4 simulations for the global stack, we established distributions for coherence magnitudes at the frequencies of orbital parameter variations (Figure S2).

To produce a null model to compare our data against, we conducted similar Monte Carlo simulations using 500 random white-noise signals (the color of the noise we used had minimal effect on our results), each subjected to 10^3 random age perturbations using the same parameters as for our BAR signals. The difference between the distributions of coherence peak magnitudes from our data and those from the random signals was visually distinct for

certain frequencies at certain sites (Figure S2). One-tailed Kolmogorov-Smirnov statistical tests supported the conclusion that in these cases, the level of coherence associated with the true age model for our data was extremely unlikely to arise from a random signal, even when p-values for confidence intervals were adjusted to account for multiple hypothesis testing by the conservative Bonferroni method ($p < \sim 5 \times 10^{-4}$ for $\alpha=0.05$; $p < \sim 10^{-5}$ for $\alpha=0.01$; see Table S2). Because of the potentially large influence of age model uncertainty on coherence magnitude, we feel this approach is more reasonable than relying solely on the formal confidence intervals for the magnitude of coherence peaks.

We additionally tested the effects of the magnitude of age model perturbations and the potential for noise in a signal to degrade coherence given age model uncertainty. The age model perturbations used for Monte Carlo simulations were drawn from a normal distribution of random numbers with a standard deviation of 2.5 kyr. for individual sites and 1.5 kyr. for the global stack to reflect the decrease in uncertainty magnitude associated with producing a data stack. At sedimentation rates of several cm per kyr., this age uncertainty would correspond to a substantial "uncertainty" of centimeters in sample depths, which is already likely to be unrealistically large. However, we also tried increasing the standard deviation of the age model perturbation distribution to 10 kyr., and while the magnitude and phase lags of precession-frequency peaks were understandably altered greatly, neither the coherence magnitude nor phase lags for the ~40 kyr. period coherence peaks were changed greatly, indicating they are a robust feature. Finally, to test the combined coherence effects of signal noise and age model uncertainty, we estimated coherence between two identical insolation signals, one with added age uncertainty (simulated in the same way as in earlier tests) and signal noise to simulate non-linear relationships between insolation and BAR. When the

standard deviation of the normally-distributed random noise reached ~30% of the insolation signal, the 2.5 kyr. standard deviation age model perturbations reduced the coherence of these two originally identical signals substantially (Figure S3). This indicates that the procedure we use to evaluate coherence between BAR and insolation records is reasonably sensitive to non-linear "noise" in the BAR-insolation relationship, and therefore that the observed levels of coherence are likely to be physically meaningful.

To assemble a more globally representative view of periodicity in export productivity and to minimize the potential influence of phenomena localized at individual sites, we stacked the data by normalizing each site's BAR record to have a magnitude between zero and one, interpolating the records onto a finer scale, and binning the resulting records. Interpolating the BAR of individual sites onto a common timescale yielded similar results. Comparing the stack with the individual orbital parameters of eccentricity, obliquity, and precession index (Laskar et al., 2004), which are invariant with respect to location, presented reasonably different results than estimating the coherence between the global stack and insolation at individual sample sites. However, the location of the insolation record we used made only a small difference in both the coherence spectrum and phase lags. Insolation was calculated from the Laskar (2004) orbital parameters using the Palinsol package for R (Crucifix, 2016).

References

Crucifix, M., 2016. Palinsol package.

Gorgas, T., Lyle, M., Wilkens, R.H., Westerhold, T., Tian, J., Drury, A.J., 2017. Revisiting the Ceara Rise, equatorial Atlantic Ocean: isotope stratigraphy of ODP Leg 154 from 0 to 5 Ma. Clim. Past 13, 779–793. https://doi.org/10.5194/cp-13-779-2017

House, B.M., Norris, R.D., *in review*. Unlocking the barite paleoproductivity proxy: a new high-throughput technique reveals glacial/interglacial productivity changes at the East African margin. Chem. Geol.

Laskar, J., Robutel, P., Joutel, F., Gastineau, M., Correia, A.C.M., Levrard, B., 2004. A long-term numerical solution for the insolation quantities of the Earth. Astron. Astrophys. https://doi.org/10.1051/0004-6361:20041335

Leg 108 Shipboard Scientific Party, 1988. Site 659. Proc. Ocean Drill. Progr. Initial Reports 108.

Leg 111 Shipboard Scientific Party, 1988. Sites 677 and 678. Proc. Ocean Drill. Progr. Initial Reports 11.

Leg 121 Shipboard Scientific Party, 1989. Site 758. Proc. Ocean Drill. Progr. Initial Reports 121.

Leg 138 Shipboard Scientific Party, 1992. Site 849. Proc. Ocean Drill. Progr. Initial Reports 138.

Leg 145 Shipboard Scientific Party, 1993. Site 882. Proc. Ocean Drill. Progr. Initial Reports 145.

Leg 154 Shipboard Scientific Party, 1995. Site 927. Proc. Ocean Drill. Progr. Initial Reports 154.

Leg 94 Shipboard Scientific Party, 1983. Site 607. Proc. Deep Sea Drill. Proj. Initial Reports 94, 75–143.

Lisiecki, L.E., Raymo, M.E., 2005. A Pliocene-Pleistocene stack of 57 globally distributed benthic $\delta^{18}O$ records. Paleoceanography 20. https://doi.org/10.1029/2004pa001071

Party, L. 181 S.S., 1999. Site 1123: North Chatham drift -- a 20-Ma record of the Pacific deep western boundary current. Proc. Ocean Drill. Progr. Initial Reports 181.

Tiedemann, R., Haug, G.H., 1995. Astronomical calibration of cycle stratigraphy for Site 882 in the Northwest Pacific. Proc. Ocean Drill. Progr. Sci. Results1 145, 283–292.

Supplemental figures

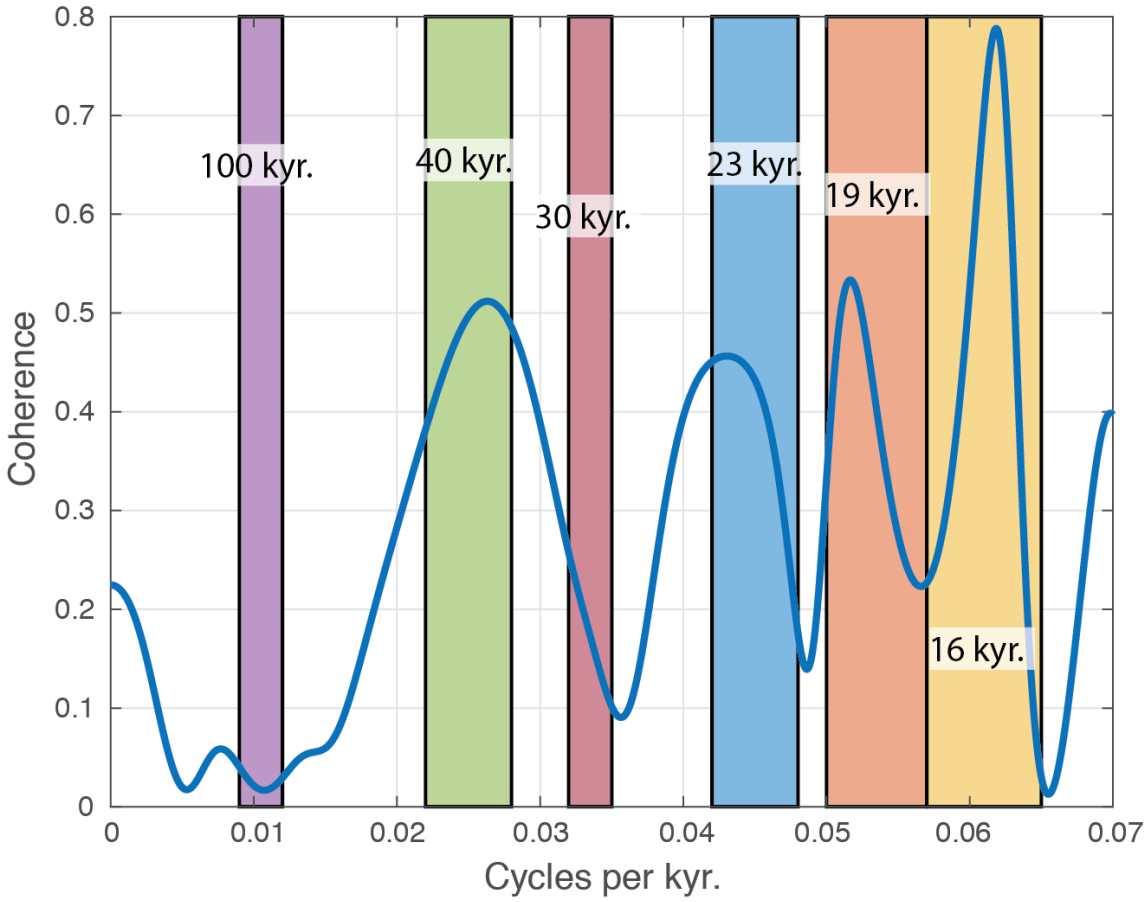

Figure 2.S1. Coherence spectrum between Site 1123 BAR and local summer insolation showing frequency windows used for peak picking in all spectra. The frequency windows are centered around the main eccentricity, obliquity, and precession frequencies as well as the minor 16 and 30 kyr. period variations in insolation. An automated algorithm was used to identify peaks that had a coherence of at least 0.3 and a prominence over the surrounding spectrum of at least 0.1. This technique of using only the magnitude of coherence peaks is justified because of the general lack of peaks outside the frequencies of astronomical variation; otherwise, if coherence spectra contained abundant additional peaks, choosing only those at the frequencies of interest could bias results.

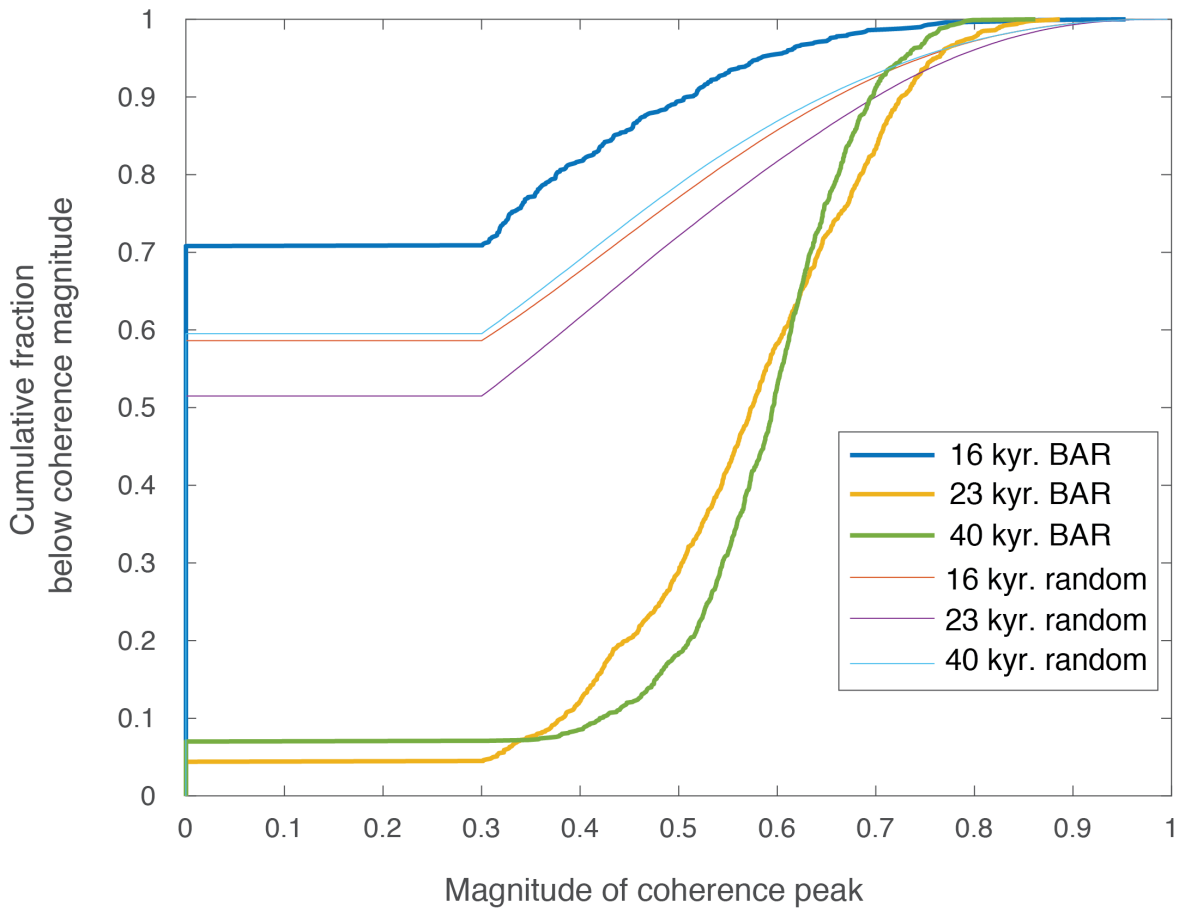

Figure 2.S2. Example empirical cumulative distribution functions of the magnitudes of coherence peaks at different frequencies following Monte Carlo simulations for winter insolation at Site 758. The distributions for the dataset were constructed from recalculating coherence and picking coherence peak magnitudes for 10^3 simulations in which sample ages were randomly perturbed. Distributions for random data are the compilation of coherence peak magnitudes of 500 samples, each of which was subjected to 10^3 random age perturbations using the same procedure as for BAR data. When no coherence peak was identified within a frequency window using the criteria described above, a value of 0 was assigned. For the coherence peak at ~16 kyr., random signals perform better (i.e. have higher coherence at all cumulative fractions) than the actual BAR data. This means that the true age model is likely to produce a coherence peak at ~16 kyr. that is of lesser magnitude than random signals do. However, for the ~40 and ~23 kyr. peaks, the data clearly produce a superior distribution of peak magnitudes, so the true age model is likely to give coherence peaks at these periods that are substantially greater in magnitude than random signals do. We therefore consider these peaks but not the peak at ~16 kyr. period in our interpretations.

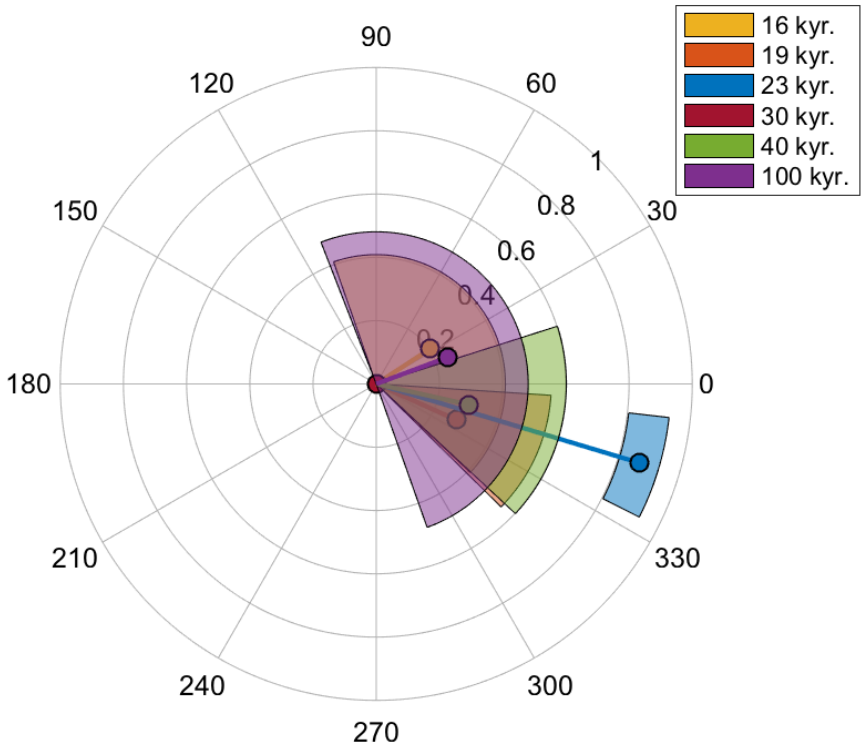

Figure 2.S3. Polar plot of magnitude and phase lags associated with coherence peaks between two copies of Site 1123 December insolation, one unaltered, and one with added white noise and simulated age perturbations treated using the same Monte Carlo process as for BAR signals.

The addition of white noise with maximum amplitude of 30% of the insolation signal simulates non-linear interactions between insolation and BAR signals. As in Figure 1, the magnitude of coherence peaks at different frequencies are represented by the radial distance while the phase lag between the signals at those frequencies are shown as an angle from the positive x-axis. For each frequency, the point represents the median magnitude and phase lag while the shaded region represents the inter-quartile range produced from 10^3 Monte Carlo simulations of age model uncertainty in one signal. The extreme decrease in coherence magnitude for all periods but ~23 kyr. suggests that age model uncertainty along with indirect insolation/productivity relationships could tremendously affect the observed coherence. This suggests that the strength of the coherence we detect between our data and insolation likely reflects a true physical link between productivity and orbital parameters.

Table S1 Data generated for and/or used in this study

Site 607

Sample ID	Hole	Core	Sect	Interval upper (cm)	Interval Lower (cm)	Average depth on splice (m)	Age, published age model (ka.)	Age, realigned age model (ka.)	Corrected barite (mg/g sediment)
5051305	607	10	2	16	17	84.21	2025		0.11
5051306	607	10	2	38	39	84.43	2029		0.09
5051307	607	10	2	60	61	84.65	2032		0.09
5051310	607	10	2	16	127	84.76	2033		0.13
5051308	607	10	2	82	83	84.87	2035		0.08
5051309	607	10	2	104	105	85.09	2038		0.07
5051311	607	10	2	148	149	85.53	2046		0.14
5051312	607	10	3	20	21	85.75	2050		0.11
5051313	607	10	3	39	40	85.94	2053		0.11
5051314	607	10	3	68	69	86.23	2058		0.07
5051315	607	10	3	92	93	86.47	2062		0.10
5051316	607	10	3	116	117	86.71	2067		0.21
5051317	607	10	3	140	141	86.95	2071		0.35
5051318	607	10	4	10	11	87.15	2075		0.33
5051319	607	10	4	32	33	87.37	2080		0.48
5051320	607	10	4	54	55	87.59	2084		0.35
5051321	607	10	4	76	77	87.81	2089		0.17
5051323	607	10	4	120	121	88.25	2097		0.11
5051324	607	10	4	142	143	88.47	2101		0.15
5051326	607	10	5	32	33	88.87	2110		0.09
5051328	607	10	5	76	77	89.31	2119		0.25
5051330	607	10	5	98	99	89.53	2124		0.16
5051331	607	10	5	120	121	89.75	2129		0.08

Table S1 (cont'd)

Sample ID	Hole	Core	Sect	Interval upper (cm)	Interval Lower (cm)	Average depth on splice (m)	Age, published age model (ka.)	Age, realigned age model (ka.)	Corrected barite (mg/g sediment)
5051332	607	10	5	142	143	89.97	2136		0.10
5051333	607	10	6	12	13	90.17	2141		0.13
5051334	607	10	6	34	35	90.39	2147		0.18
5051335	607	10	6	56	57	90.61	2152		0.30
5051336	607	10	6	78	79	90.83	2157		0.42
5051337	607	10	6	100	101	91.05	2161		0.51
5051338	607	10	6	122	123	91.27	2166		0.33
5051339	607	10	6	144	145	91.49	2172		0.27
5051340	607	10	7	4	5	91.59	2175		0.18
5051344	607	10	7	26	27	91.81	2182		0.12
5051428	607 A	11	4	20	21	92.01	2188		0.08
5051429	607 A	11	4	42	43	92.23	2193		0.15
5051430	607 A	11	4	64	65	92.45	2198		0.23
5051431	607 A	11	4	86	87	92.67	2203		0.21
5051432	607 A	11	4	104	105	92.85	2208		0.24
5051348	607	11	1	19	20	93.00	2212		0.17
5051350	607	11	1	42	43	93.23	2218		0.18
5051351	607	11	1	64	65	93.45	2222		0.18
5051352	607	11	1	86	87	93.67	2226		0.14
5051353	607	11	1	108	109	93.89	2230		0.08
5051354	607	11	1	130	131	94.11	2234		0.22
5051355	607	11	1	149	150	94.30	2237		0.36
5051356	607	11	2	20	21	94.51	2241		0.42
5051358	607	11	2	42	43	94.73	2245		0.45
5051359	607	11	2	64	65	94.95	2250		0.22

Table S1 (cont'd)

Sample ID	Hole	Core	Sect	Interval upper (cm)	Interval Lower (cm)	Average depth on splice (m)	Age, published age model (ka.)	Age, realigned age model (ka.)	Corrected barite (mg/g sediment)
5051361	607	11	2	86	87	95.17	2254		0.11
5051362	607	11	2	108	109	95.39	2258		0.09
5051363	607	11	2	130	131	95.61	2262		0.09
5051364	607	11	2	149	150	95.80	2266		0.08
5051365	607	11	3	20	21	96.01	2271		0.14
5051366	607	11	3	42	43	96.23	2276		0.20
5051367	607	11	3	64	65	96.45	2281		0.30
5051368	607	11	3	86	87	96.67	2286		0.39
5051369	607	11	3	108	109	96.89	2292		0.32
5051370	607	11	3	130	131	97.11	2297		0.13
5051371	607	11	3	149	150	97.30	2301		0.12
5051374	607	11	4	20	21	97.51	2306		0.13
5051375	607	11	4	42	43	97.73	2310		0.16
5051376	607	11	4	64	65	97.95	2315		0.15
5051377	607	11	4	86	87	98.17	2320		0.20
5051378	607	11	4	108	109	98.39	2325		0.30
5051379	607	11	4	130	131	98.61	2330		0.38
5051380	607	11	4	149	150	98.80	2335		0.28
5051381	607	11	5	20	21	99.01	2340		0.14
5051382	607	11	5	42	43	99.23	2344		0.10
5051383	607	11	5	64	65	99.45	2348		0.12
5051384	607	11	5	86	87	99.67	2353		0.20
5051385	607	11	5	108	109	99.89	2357		0.23
5051386	607	11	5	130	131	100.11	2362		0.33
5051387	607	11	5	149	150	100.30	2365		0.43

Table S1 (cont'd)

Sample ID	Hole	Core	Sect	Interval upper (cm)	Interval Lower (cm)	Average depth on splice (m)	Age, published age model (ka.)	Age, realigned age model (ka.)	Corrected barite (mg/g sediment)
5051388	607	11	6	20	21	100.51	2370		0.25
5051389	607	11	6	42	43	100.73	2374		0.11
5051390	607	11	6	64	65	100.95	2379		0.08
5051391	607	11	6	86	87	101.17	2384		0.09
5051392	607	11	6	108	109	101.39	2389		0.14
5051393	607	11	6	130	131	101.61	2393		0.17
5051394	607	11	6	149	150	101.80	2396		0.20
5051396	607	11	7	5	6	101.86	2397		0.19
5051433	607 A	12	3	120	121	102.04	2400		0.18
5051434	607 A	12	3	142	143	102.26	2404		0.11
5051435	607 A	12	4	15	16	102.49	2408		0.10
5051436	607 A	12	4	37	38	102.71	2412		0.09
5051437	607 A	12	4	59	60	102.93	2416		0.10
5051438	607 A	12	4	81	82	103.15	2420		0.07
5051406	607	12	1	10	11	103.30	2424		0.07
5051407	607	12	1	32	33	103.52	2428		0.15
5051408	607	12	1	54	55	103.74	2432		0.28
5051409	607	12	1	76	77	103.96	2436		0.34
5051410	607	12	1	98	99	104.18	2440		0.30
5051411	607	12	1	120	121	104.40	2444		0.29
5051412	607	12	1	142	143	104.62	2448		0.44
5051413	607	12	2	10	11	104.80	2452		0.23
5051414	607	12	2	32	33	105.02	2457		0.10
5051415	607	12	2	54	55	105.24	2462		0.06
5051416	607	12	2	76	77	105.46	2468		0.08

Table S1 (cont'd)

Sample ID	Hole	Core	Sect	Interval upper (cm)	Interval Lower (cm)	Average depth on splice (m)	Age, published age model (ka.)	Age, realigned age model (ka.)	Corrected barite (mg/g sediment)
5051417	607	12	2	98	99	105.68	2474		0.10
5051418	607	12	2	120	121	105.90	2479		0.21
5051420	607	12	3	10	11	106.30	2486		0.37
5051421	607	12	3	32	33	106.52	2491		0.31
5051422	607	12	3	54	55	106.74	2495		0.17
5051423	607	12	3	76	77	106.96	2499		0.08
5051424	607	12	3	98	99	107.18	2504		0.11
5051425	607	12	3	120	121	107.40	2510		0.20

Site 659

Sample ID	Hole	Core	Sect	Interval upper (cm)	Interval Lower (cm)	Average depth on splice (m)	Age, published age model (ka.)	Age, realigned age model (ka.)	Corrected barite (mg/g sediment)
5051546	B	6	6	130	131	57.17	1985	NaN	0.61
5051547	B	6	6	144	145	57.31	1993	NaN	0.49
5051548	B	6	7	10	11	57.47	1998	NaN	0.60
5051442	A	7	1	45	46	57.52	1999	NaN	0.64
5051550	B	7	1	14	15	58.14	2015	2013.50	0.63
5051443	A	7	1	60	61	59.67	2063	2069.10	0.51
5051444	A	7	1	75	76	59.82	2068	2077.40	0.61
5051445	A	7	1	90	91	59.97	2072	2083.10	0.67
5051446	A	7	1	105	106	60.12	2076	2087.00	0.49
5051447	A	7	1	120	121	60.27	2079	2090.70	0.55
5051448	A	7	1	135	136	60.42	2083	2094.20	0.58
5051449	A	7	1	149	150	60.56	2086	2097.50	0.66
5051450	A	7	2	14	15	60.71	2089	2101.20	0.48
5051451	A	7	2	29	30	60.86	2094	2106.10	0.41

Table S1 (cont'd)

Sample ID	Hole	Core	Sect	Interval upper (cm)	Interval Lower (cm)	Average depth on splice (m)	Age, published age model (ka.)	Age, realigned age model (ka.)	Corrected barite (mg/g sediment)
5051453	A	7	2	59	60	61.16	2107	2120.50	0.54
5051454	A	7	2	74	75	61.31	2115	2127.30	0.51
5051455	A	7	2	89	90	61.46	2122	2133.40	0.52
5051456	A	7	2	104	105	61.61	2130	2139.40	0.54
5051457	A	7	2	119	120	61.76	2137	2145.60	0.64
5051458	A	7	2	134	135	61.91	2144	2152.90	0.62
5051459	A	7	2	149	150	62.06	2150	2159.00	0.71
5051461	A	7	3	14	15	62.21	2155	2163.30	0.70
5051462	A	7	3	29	30	62.36	2159	2167.10	0.69
5051465	A	7	3	44	45	62.51	2163	2170.70	0.79
5051467	A	7	3	59	60	62.66	2167	2174.30	0.56
5051468	A	7	3	74	75	62.81	2172	2178.50	0.62
5051469	A	7	3	89	90	62.96	2179	2184.10	0.70
5051470	A	7	3	104	105	63.11	2185	2190.90	0.60
5051471	A	7	3	119	120	63.26	2191	2196.50	0.53
5051472	A	7	3	134	135	63.41	2195	2201.10	0.60
5051473	A	7	3	148	149	63.55	2199	2205.10	0.57
5051474	A	7	4	14	15	63.71	2203	2209.30	0.60
5051475	A	7	4	29	30	63.86	2207	2213.10	0.55
5051476	A	7	4	44	45	64.01	2211	2216.80	0.54
5051477	A	7	4	59	60	64.16	2215	2220.40	0.69
5051478	A	7	4	74	75	64.31	2220	2224.60	0.78
5051483	A	7	4	89	90	64.46	2225	2229.90	0.74
5051479	A	7	4	104	105	64.61	2231	2235.50	0.64
5051480	A	7	4	119	120	64.76	2236	2240.30	0.60

Table S1 (cont'd)

Sample ID	Hole	Core	Sect	Interval upper (cm)	Interval Lower (cm)	Average depth on splice (m)	Age, published age model (ka.)	Age, realigned age model (ka.)	Corrected barite (mg/g sediment)
5051481	A	7	4	134	135	64.91	2240	2244.00	0.59
5051482	A	7	4	149	150	65.06	2243	2246.90	0.55
5051485	A	7	5	14	15	65.21	2246	2250.70	0.75
5051552	B	7	5	148	149	65.35	2250	2254.70	0.75
5051486	A	7	5	29	30	65.36	2250	2255.00	0.87
5051487	A	7	5	44	45	65.51	2255	2260.60	0.57
5051554	B	7	6	27	28	65.64	2260	2266.40	0.76
5051488	A	7	5	59	60	65.66	2261	2267.10	0.75
5051555	B	7	6	42	43	65.79	2267	2271.40	0.59
5051489	A	7	5	74	75	65.81	2267	2272.10	0.77
5051556	B	7	6	57	58	65.94	2273	2276.40	0.59
5051490	A	7	5	89	90	65.96	2274	2277.10	0.72
5051558	B	7	6	87	88	66.24	2283	2284.10	0.61
5051492	A	7	5	119	120	66.26	2283	2284.60	0.83
5051559	B	7	6	102	103	66.39	2287	2288.70	0.61
5051493	A	7	5	134	135	66.41	2287	2289.40	0.69
5051560	B	7	6	117	118	66.54	2291	2293.70	0.69
5051494	A	7	5	149	150	66.56	2292	2294.40	0.66
5051495	A	7	6	14	15	66.71	2297	2301.00	0.80
5051563	B	7	7	12	13	66.99	2306	2311.10	0.70
5051497	A	7	6	44	45	67.01	2307	2311.60	0.59
5051564	B	7	7	27	28	67.14	2310	2315.20	0.68
5051498	A	7	6	59	60	67.16	2311	2315.70	0.61
5051499	A	7	6	74	75	67.31	2314	2319.50	0.74
5051500	A	7	6	89	90	67.46	2317	2323.10	0.79

Table S1 (cont'd)

Sample ID	Hole	Core	Sect	Interval upper (cm)	Interval Lower (cm)	Average depth on splice (m)	Age, published age model (ka.)	Age, realigned age model (ka.)	Corrected barite (mg/g sediment)
5051501	A	7	6	104	105	67.61	2321	2326.60	0.74
5051502	A	7	6	119	120	67.76	2324	2330.10	0.47
5051503	A	7	6	134	135	67.91	2327	2333.70	0.51
5051504	A	7	6	149	150	68.06	2331	2337.50	0.55
5051506	A	8	1	42	43	68.15	2333	2340.00	0.59
5051507	A	8	1	58	59	69.15	2367	2375.10	0.56
5051511	A	8	1	87	88	69.44	2375	2381.50	0.54
5051512	A	8	1	102	103	69.59	2380	2385.10	0.50
5051513	A	8	1	117	118	69.74	2384	2391.80	0.73
5051515	A	8	2	14	15	70.21	2397	2409.90	0.68
5051516	A	8	2	29	30	70.36	2404	2415.90	0.61
5051517	A	8	2	44	45	70.51	2412	2422.30	0.48
5051514	A	8	2	59	60	70.66	2420	2429.10	0.43
5051518	A	8	2	74	75	70.81	2427	2435.30	0.44
5051519	A	8	2	89	90	70.96	2433	2440.00	0.53
5051521	A	8	2	119	120	71.26	2442	2447.40	0.56
5051522	A	8	2	134	135	71.41	2446	2450.90	0.46
5051523	A	8	2	149	150	71.56	2450	2454.50	0.50
5051524	A	8	3	13	14	71.70	2454	2457.90	0.46
5051525	A	8	3	29	30	71.86	2459	2462.40	0.48
5051526	A	8	3	44	45	72.01	2465	2468.20	0.51
5051527	A	8	3	59	60	72.16	2472	2473.70	0.48
5051528	A	8	3	74	75	72.31	2477	2478.60	0.79
5051529	A	8	3	89	90	72.46	2482	2482.40	0.70
5051530	A	8	3	104	105	72.61	2486	2485.80	0.68

Table S1 (cont'd)

Sample ID	Hole	Core	Sect	Interval upper (cm)	Interval Lower (cm)	Average depth on splice (m)	Age, published age model (ka.)	Age, realigned age model (ka.)	Corrected barite (mg/g sediment)
5051531	A	8	3	119	120	72.76	2490	2489.90	0.73
5051532	A	8	3	134	135	72.91	2495	2496.70	0.59
5051533	A	8	3	149	150	73.06	2500	2504.10	0.62
5051535	A	8	4	14	15	73.21	2507	2511.10	0.56
5051534	A	8	4	29	30	73.36	2513	2516.90	0.48
5051536	A	8	4	44	45	73.51	2518	2521.40	0.62
5051537	A	8	4	59	60	73.66	2522	2525.20	0.70
5051539	A	8	4	89	90	73.96	2531	2532.80	0.63
5051540	A	8	4	104	105	74.11	2537	2537.40	0.63
5051541	A	8	4	119	120	74.26	2542	2542.00	0.62
5051542	A	8	4	134	135	74.41	2549	2547.70	0.60
5051543	A	8	4	149	150	74.56	2556	2553.90	0.61
5051544	A	8	5	14	15	74.71	2563	2560.00	0.64
5051545	A	8	5	29	30	74.86	2567	2564.00	0.77

Site 677

Sample ID	Hole	Core	Sect	Interval upper (cm)	Interval Lower (cm)	Average depth on splice (m)	Age, published age model (ka.)	Age, realigned age model (ka.)	Corrected barite (mg/g sediment)
17049092	A	10	1	1	2	86.21	2047	2041	6.4
17049102	A	10	1	25	26	86.46	2052	2046	6.5
17049112	A	10	1	47	48	86.68	2056	2050	7.5
17049122	A	10	1	70	71	86.91	2060	2054	7.7
17049132	A	10	1	93	94	87.14	2063	2059	9.0
17049142	A	10	1	116	117	87.37	2067	2062	9.7
17049152	A	10	1	139	140	87.60	2070	2066	8.5
17049222	A	10	2	1	2	87.72	2071	2068	9.3

Table S1 (cont'd)

Sample ID	Hole	Core	Sect	Interval upper (cm)	Interval Lower (cm)	Average depth on splice (m)	Age, published age model (ka.)	Age, realigned age model (ka.)	Corrected barite (mg/g sediment)
17049232	A	10	2	24	25	87.95	2075	2071	9.5
17049242	A	10	2	47	48	88.18	2078	2075	10.4
17049252	A	10	2	70	71	88.41	2081	2079	9.3
17049262	A	10	2	93	94	88.64	2085	2083	9.7
17049272	A	10	2	116	117	88.87	2090	2088	7.9
17049282	A	10	2	139	140	89.10	2095	2094	6.6
17049332	A	10	3	1	2	89.22	2098	2098	8.0
17049342	A	10	3	24	25	89.45	2105	2107	8.4
17049352	A	10	3	47	48	89.68	2113	2117	8.6
17049362	A	10	3	70	71	89.91	2123	2131	9.6
17049372	A	10	3	93	94	90.14	2136	2148	9.1
17049382	A	10	3	116	117	90.37	2150	2159	8.9
17049392	A	10	3	139	140	90.60	2163	2169	9.1
17049452	A	10	4	1	2	90.72	2170	2175	9.0
17049462	A	10	4	24	25	90.95	2181	2183	5.4
17049472	A	10	4	47	48	91.18	2188	2193	5.3
17049482	A	10	4	70	71	91.41	2194	2200	5.5
17049492	A	10	4	93	94	91.64	2198	2206	4.9
17049502	A	10	4	116	117	91.87	2203	2210	5.1
17049512	A	10	4	139	140	92.10	2208	2214	6.7
17049522	A	10	5	0	2	92.21	2210	2216	6.0
17049532	A	10	5	24	25	92.45	2215	2220	4.5
17049542	A	10	5	47	48	92.68	2220	2224	6.1
17049552	A	10	5	70	71	92.91	2224	2228	6.3
17049562	A	10	5	93	94	93.14	2229	2234	7.2

Table S1 (cont'd)

Sample ID	Hole	Core	Sect	Interval upper (cm)	Interval Lower (cm)	Average depth on splice (m)	Age, published age model (ka.)	Age, realigned age model (ka.)	Corrected barite (mg/g sediment)
17049572	A	10	5	116	117	93.37	2233	2239	6.1
17049582	A	10	5	139	140	93.60	2238	2244	6.7
17056122	A	10	6	1	2	93.72	2240	2246	6.1
17056142	A	10	6	24	25	93.95	2245	2250	4.3
17056152	A	10	6	47	48	94.18	2249	2253	5.5
17056162	A	10	6	70	71	94.41	2254	2256	6.6
17056172	A	10	6	93	94	94.64	2259	2260	6.8
17056192	A	10	6	116	117	94.87	2264	2264	7.5
17056202	A	10	6	139	140	95.10	2270	2270	5.9
17067962	A	10	7	1	2	95.22	2272	2273	5.3
17067972	A	10	7	24	25	95.45	2278	2280	5.4
17067982	A	10	7	46	47	95.67	2283	2286	7.3
17070712	A	11	1	17	18	95.90	2288	2292	6.7
17070722	A	11	1	40	41	96.13	2293	2298	6.5
17070732	A	11	1	63	64	96.36	2298	2303	6.7
17070742	A	11	1	86	87	96.59	2303	2309	6.1
17070752	A	11	1	109	110	96.82	2307	2314	5.6
17070762	A	11	1	132	133	97.05	2312	2319	5.0
17070772	A	11	2	5	6	97.28	2316	2324	5.4
17070782	A	11	2	28	29	97.51	2321	2330	5.6
17070792	A	11	2	51	52	97.74	2325	2335	5.9
17070802	A	11	2	74	75	97.97	2329	2339	5.3
17070812	A	11	2	97	98	98.20	2332	2344	6.3
17070822	A	11	2	120	121	98.43	2336	2348	4.5
17070832	A	11	2	143	144	98.66	2339	2353	5.2

Table S1 (cont'd)

Sample ID	Hole	Core	Sect	Interval upper (cm)	Interval Lower (cm)	Average depth on splice (m)	Age, published age model (ka.)	Age, realigned age model (ka.)	Corrected barite (mg/g sediment)
17070842	A	11	3	16	17	98.89	2343	2357	4.6
17070852	A	11	3	39	40	99.12	2346	2361	5.6
17070862	A	11	3	62	63	99.35	2350	2366	5.2
17070872	A	11	3	85	86	99.58	2354	2371	4.6
17070882	A	11	3	108	109	99.81	2359	2376	4.8
17070892	A	11	3	131	132	100.04	2364	2383	4.5
17070902	A	11	4	2	3	100.25	2370	2389	4.2
17070912	A	11	4	25	26	100.48	2377	2395	3.9
17070922	A	11	4	48	49	100.71	2384	2401	3.7
17070932	A	11	4	71	72	100.94	2391	2408	3.6
17070942	A	11	4	94	95	101.17	2399	2414	4.4
17070952	A	11	4	117	118	101.40	2405	2420	3.9
17070962	A	11	4	140	141	101.63	2412	2425	3.1
17070972	A	11	5	13	14	101.86	2418	2431	3.0
17070982	A	11	5	36	37	102.09	2424	2438	2.8
17070992	A	11	5	59	60	102.32	2430	2443	3.3
17071002	A	11	5	82	83	102.55	2434	2448	3.3
17071012	A	11	5	105	106	102.78	2439	2451	3.8
17071022	A	11	5	128	129	103.01	2443	2454	4.6
17071032	A	11	5	149	150	103.22	2447	2456	4.1
17071042	A	11	6	22	23	103.45	2451	2459	5.4
17071052	A	11	6	45	46	103.68	2456	2461	3.7
17071062	A	11	6	68	69	103.91	2460	2464	3.8
17071072	A	11	6	91	92	104.14	2464	2466	3.9
17071082	A	11	6	114	115	104.37	2469	2470	4.1

Table S1 (cont'd)

Sample ID	Hole	Core	Sect	Interval upper (cm)	Interval Lower (cm)	Average depth on splice (m)	Age, published age model (ka.)	Age, realigned age model (ka.)	Corrected barite (mg/g sediment)
17071092	A	11	6	137	168	104.60	2473	2474	3.5
17103042	A	11	7	10	11	104.83	2477	2478	2.7
17103052	A	11	7	33	34	105.06	2481	2482	4.4
17103062	A	11	7	56	57	105.29	2484	2486	5.5
17103072	A	12	1	20	21	107.41	2513	2512	3.7
17103082	A	12	1	43	44	107.64	2517	2518	4.3
17103092	A	12	1	66	67	107.87	2520	2524	5.0
17103102	A	12	1	89	90	108.10	2523	2530	6.5
17103112	A	12	1	112	113	108.33	2527	2538	6.6
17103122	A	12	1	135	136	108.56	2531	2548	6.6
17103132	A	12	2	8	9	108.79	2535	2558	6.4
17103142	A	12	2	31	32	109.02	2540	2569	6.3
17103152	A	12	2	54	55	109.25	2544	2580	6.3
17103162	A	12	2	77	78	109.48	2549	2591	5.7
17103172	A	12	2	100	101	109.71	2554	2604	5.4
17103182	A	12	2	123	124	109.94	2559	2617	5.6
17103192	A	12	2	146	147	110.17	2565	2629	5.0
17103202	A	12	3	19	20	110.40	2570	2642	5.3
17103212	A	12	3	42	43	110.63	2575	2655	5.9
17103222	A	12	3	65	66	110.86	2581	2668	6.9
17103232	A	12	3	88	89	111.09	2586	2681	3.9
17103242	A	12	3	111	112	111.32	2591	2694	4.3
17103252	A	12	3	134	135	111.55	2597	2707	4.2

Site 758

Table S1 (cont'd)

Sample ID	Hole	Core	Sect	Interval upper (cm)	Interval Lower (cm)	Average depth on splice (m)	Age, published age model (ka.)	Age, realigned age model (ka.)	Corrected barite (mg/g sediment)
5863701	A	4	1	71	72	30.25	1992	NaN	1.6
5863801	A	4	1	78	79	30.32	1996	NaN	1.6
5863901	A	4	1	86	87	30.40	2001	NaN	1.7
5864001	A	4	1	92	93	30.46	2004	2005	1.6
5864101	A	4	1	99	100	30.53	2008	2009	1.4
5864201	A	4	1	106	107	30.60	2012	2013	1.4
5864301	A	4	1	113	114	30.67	2016	2018	1.2
5864401	A	4	1	119	120	30.73	2019	2022	1.3
5864501	A	4	1	127	128	30.81	2024	2027	1.2
5864601	A	4	1	134	135	30.88	2028	2031	1.7
5864701	A	4	1	141	142	30.95	2032	2036	1.6
5864801	A	4	1	148	149	31.02	2036	2040	1.9
5864901	A	4	2	5	6	31.09	2040	2044	1.5
5865001	A	4	2	12	13	31.16	2044	2049	1.6
5865101	A	4	2	19	20	31.23	2047	2053	1.7
5865201	A	4	2	26	27	31.30	2051	2058	1.5
5865301	A	4	2	33	34	31.37	2055	2062	1.6
5865401	A	4	2	40	41	31.44	2059	2067	1.9
5865501	A	4	2	46	47	31.50	2063	2071	1.5
5865601	A	4	2	54	55	31.58	2068	2078	1.3
5865701	A	4	2	61	62	31.65	2073	2083	1.3
5865801	A	4	2	68	69	31.72	2079	2087	1.3
5865901	A	4	2	82	83	31.86	2091	2096	1.4
5866001	A	4	2	89	90	31.93	2097	2100	1.5
5866101	A	4	2	96	97	32.00	2103	2113	1.6

Table S1 (cont'd)

Sample ID	Hole	Core	Sect	Interval upper (cm)	Interval Lower (cm)	Average depth on splice (m)	Age, published age model (ka.)	Age, realigned age model (ka.)	Corrected barite (mg/g sediment)
5866201	A	4	2	103	104	32.07	2109	2126	1.5
5866301	A	4	2	109	110	32.13	2114	2130	1.5
5866401	A	4	2	117	118	32.21	2121	2136	1.8
5866501	A	4	2	124	125	32.28	2128	2141	1.5
5866601	A	4	2	131	132	32.35	2134	2146	1.6
5866701	A	4	2	138	139	32.42	2140	2151	1.8
5866801	A	4	2	145	146	32.49	2145	2155	1.7
5866901	A	4	3	2	3	32.56	2149	2159	1.5
5867001	A	4	3	9	10	32.63	2153	2162	1.3
5867101	A	4	3	16	17	32.70	2157	2165	1.2
5867201	A	4	3	23	24	32.77	2161	2168	1.2
5867301	A	4	3	30	31	32.84	2165	2170	1.2
5867401	A	4	3	38	39	32.92	2170	2174	1.2
5867501	A	4	3	44	45	32.98	2174	2176	1.1
5867601	A	4	3	52	53	33.06	2180	2180	1.2
5867701	A	4	3	58	59	33.12	2184	2182	1.3
5867801	A	4	3	65	66	33.19	2189	2190	1.3
5867901	A	4	3	71	72	33.25	2193	2200	1.2
5868001	A	4	3	79	80	33.33	2199	2212	1.0
5868101	A	4	3	86	87	33.40	2204	2222	1.1
5868201	A	4	3	94	95	33.48	2210	2229	1.4
5868301	A	4	3	100	101	33.54	2214	2231	1.5
5868401	A	4	3	107.5	108.5	33.61	2219	2234	1.7
5868501	A	4	3	114	115	33.68	2224	2237	1.7
5868601	A	4	3	121	122	33.75	2229	2239	1.7

Table S1 (cont'd)

Sample ID	Hole	Core	Sect	Interval upper (cm)	Interval Lower (cm)	Average depth on splice (m)	Age, published age model (ka.)	Age, realigned age model (ka.)	Corrected barite (mg/g sediment)
5868701	A	4	3	128	129	33.82	2234	2242	2.0
5868801	A	4	3	135	136	33.89	2238	2244	1.4
5868901	A	4	3	142	143	33.96	2243	2247	1.1
5869001	A	4	3	149	150	34.03	2248	2252	1.2
5869101	A	4	4	6	7	34.10	2254	2257	1.4
5869201	A	4	4	13	14	34.17	2260	2263	1.7
5869301	A	4	4	20	21	34.24	2266	2270	1.5
5869401	A	4	4	27	28	34.31	2272	2277	1.6
5869501	A	4	4	34	35	34.38	2278	2284	1.6
5869601	A	4	4	41	42	34.45	2284	2291	1.5
5869701	A	4	4	48	49	34.52	2291	2298	1.4
5869801	A	4	4	55	56	34.59	2296	2305	1.5
5869901	A	4	4	63	64	34.67	2303	2313	1.6
5870001	A	4	4	69	70	34.73	2307	2318	1.5
5870101	A	4	4	76	77	34.80	2312	2324	1.2
5870201	A	4	4	83	84	34.87	2317	2330	1.3
5870301	A	4	4	89	90	34.93	2321	2334	1.2
5870401	A	4	4	97	98	35.01	2327	2339	1.5
5870501	A	4	4	104	105	35.08	2332	2343	1.6
5870601	A	4	4	112	113	35.16	2337	2349	1.9
5870701	A	4	4	118	119	35.22	2341	2353	1.6
5870801	A	4	4	125	126	35.29	2346	2358	1.3
5870901	A	4	4	132	133	35.36	2351	2363	1.2
5871001	A	4	4	138	139	35.42	2356	2368	1.2
5871101	A	4	4	146	147	35.50	2362	2372	0.9

Table S1 (cont'd)

Sample ID	Hole	Core	Sect	Interval upper (cm)	Interval Lower (cm)	Average depth on splice (m)	Age, published age model (ka.)	Age, realigned age model (ka.)	Corrected barite (mg/g sediment)
5871301	A	4	5	9	10	35.63	2373	2380	1.3
5871401	A	4	5	17	18	35.71	2380	2385	1.4
5871501	A	4	5	23	24	35.77	2385	2390	1.4
5871601	A	4	5	30	31	35.84	2391	2396	1.3
5871701	A	4	5	38	39	35.92	2396	2402	1.2
5871801	A	4	5	45	46	35.99	2401	2408	1.2
5871901	A	4	5	52	53	36.06	2406	2414	1.2
5872001	A	4	5	59	60	36.13	2411	2421	1.2
5872101	A	4	5	66	67	36.20	2416	2427	1.4
5872201	A	4	5	73	74	36.27	2421	2432	1.3
5872301	A	4	5	81	82	36.35	2427	2437	1.0
5872401	A	4	5	87	88	36.41	2431	2441	1.1
5872501	A	4	5	94	95	36.48	2436	2446	1.2
5872601	A	4	5	102	103	36.56	2443	2452	1.3
5872701	A	4	5	108	109	36.62	2449	2456	1.5
5872801	A	4	5	114	115	36.68	2454	2461	1.3
5872901	A	4	5	122	123	36.76	2461	2466	1.5
5873001	A	4	5	129	130	36.83	2467	2471	1.4
5873101	A	4	5	136	137	36.90	2473	2476	1.5
5873201	A	4	5	143	144	36.97	2478	2480	1.6
5873301	A	4	6	1	2	37.05	2483	2485	1.7
5873401	A	4	6	8	9	37.12	2488	2489	1.4
5873501	A	4	6	15	16	37.19	2493	2495	1.7
5873601	A	4	6	22.5	23.5	37.26	2499	2501	1.6
5873701	A	4	6	29	30	37.33	2503	2506	1.7

Table S1 (cont'd)

Sample ID	Hole	Core	Sect	Interval upper (cm)	Interval Lower (cm)	Average depth on splice (m)	Age, published age model (ka.)	Age, realigned age model (ka.)	Corrected barite (mg/g sediment)
5873801	A	4	6	36	37	37.40	2508	2512	1.7
5873901	A	4	6	43	44	37.47	2513	2517	1.6
5874001	A	4	6	49	50	37.53	2517	2522	1.4

Site 849

Sample ID	Hole	Core	Sect	Interval upper (cm)	Interval Lower (cm)	Average depth on splice (m)	Age, published age model (ka.)	Age, realigned age model (ka.)	Corrected barite (mg/g sediment)
17112832	D	5	5	108	109	57.52	2011	2007	4.6
17112842	D	5	5	119	121	57.63	2014	2010	5.6
17112852	D	5	5	132	133	57.79	2019	2014	3.8
17112862	D	5	5	147	148	57.94	2023	2017	3.0
17122722	D	5	6	7	8	58.06	2026	2020	2.9
17122732	D	5	6	18	19	58.15	2028	2023	3.0
17122742	D	5	6	30	31	58.26	2031	2026	4.0
17122752	D	5	6	42	43	58.37	2033	2030	3.6
17122772	D	5	6	66	67	58.58	2038	2037	2.9
17122782	D	5	6	78	79	58.70	2040	2041	2.8
17122792	D	5	6	90	91	58.82	2043	2045	3.5
17122802	D	5	6	102	103	58.97	2046	2049	4.1
17122812	D	5	6	117	118	59.14	2050	2053	3.6
17122842	D	5	6	126	128	59.24	2052	2056	3.4
17122862	D	5	7	35	37	59.81	2064	2071	4.3
17103332	C	6	2	55	56	59.85	2065	2072	4.3
17122872	D	5	7	48	49	59.94	2068	2075	4.4
17103342	C	6	2	68	69	59.98	2069	2077	4.9
17122882	D	5	7	60	61	60.06	2071	2079	5.0

Table S1 (cont'd)

Sample ID	Hole	Core	Sect	Interval upper (cm)	Interval Lower (cm)	Average depth on splice (m)	Age, published age model (ka.)	Age, realigned age model (ka.)	Corrected barite (mg/g sediment)
17103352	C	6	2	80	81	60.11	2072	2081	4.9
17122902	D	5	7	70	71	60.16	2074	2082	4.8
17103362	C	6	2	92	93	60.28	2077	2085	5.5
17103372	C	6	2	104	105	60.39	2080	2088	5.8
17103382	C	6	2	117	118	60.52	2084	2091	5.5
17103392	C	6	2	128	129	60.63	2088	2093	5.5
17103402	C	6	2	140	141	60.75	2092	2096	5.3
17129562	D	6	1	4	5	60.80	2094	2098	5.2
17103412	C	6	3	2	3	60.87	2097	2100	4.7
17129582	D	6	1	16	17	60.92	2099	2102	5.3
17103422	C	6	3	14	15	60.99	2102	2105	4.2
17129602	D	6	1	28	29	61.02	2103	2106	3.8
17103432	C	6	3	25	26	61.11	2107	2110	4.3
17129622	D	6	1	40	41	61.24	2112	2116	4.4
17129632	D	6	1	52	53	61.33	2116	2120	6.3
17129652	D	6	1	64	65	61.46	2122	2126	6.9
17129672	D	6	1	76	77	61.62	2128	2133	6.0
17129682	D	6	1	88	89	61.80	2136	2142	3.8
17129722	D	6	1	112	113	61.94	2142	2149	3.1
17129702	D	6	1	100	101	61.95	2143	2150	3.3
17129732	D	6	1	124	125	62.13	2150	2162	3.6
17129752	D	6	1	136	137	62.18	2152	2165	4.2
17129772	D	6	1	148	149	62.26	2156	2168	4.2
17150632	D	6	2	11	12	62.37	2160	2172	4.0
17146222	D	6	2	24	25	62.56	2169	2178	3.5

Table S1 (cont'd)

Sample ID	Hole	Core	Sect	Interval upper (cm)	Interval Lower (cm)	Average depth on splice (m)	Age, published age model (ka.)	Age, realigned age model (ka.)	Corrected barite (mg/g sediment)
17146242	D	6	2	37	38	62.75	2177	2185	2.9
17146262	D	6	2	48	49	62.89	2183	2190	3.0
17146272	D	6	2	59	60	62.99	2187	2194	3.4
17146282	D	6	2	72	73	63.05	2189	2196	3.9
17146302	D	6	2	84	85	63.15	2194	2200	3.6
17146312	D	6	2	96	97	63.25	2198	2204	3.0
17146332	D	6	2	108	109	63.38	2204	2209	4.1
17146342	D	6	2	120	121	63.51	2209	2214	4.1
17194662	D	6	3	78	79	63.72	2218	2222	3.8
17146362	D	6	2	132	133	63.75	2219	2223	4.1
17194732	D	6	3	6	7	63.93	2227	2231	3.5
17194612	D	6	3	18	19	63.99	2230	2235	3.8
17194622	D	6	3	30	31	64.05	2232	2239	3.8
17194632	D	6	3	42	43	64.17	2237	2246	5.1
17194642	D	6	3	54	55	64.40	2247	2253	4.8
17194652	D	6	3	65	67	64.58	2255	2257	4.2
17194672	D	6	3	90	91	64.74	2262	2261	3.7
17194682	D	6	3	102	103	64.81	2265	2263	3.3
17194692	D	6	3	114	115	65.08	2276	2276	3.5
17194702	D	6	3	126	127	65.20	2281	2282	4.2
17194722	D	6	3	148	149	65.37	2289	2293	5.1
17194742	D	6	4	10	11	65.45	2292	2299	3.9
17194752	D	6	4	24	25	65.52	2295	2303	3.7
17194762	D	6	4	36	37	65.62	2299	2308	3.9
17194772	D	6	4	48	49	65.76	2305	2314	3.7

Table S1 (cont'd)

Sample ID	Hole	Core	Sect	Interval upper (cm)	Interval Lower (cm)	Average depth on splice (m)	Age, published age model (ka.)	Age, realigned age model (ka.)	Corrected barite (mg/g sediment)
17194782	D	6	4	59	60	65.89	2311	2320	3.6
17194792	D	6	4	72	73	66.02	2316	2325	3.7
17194802	D	6	4	84	85	66.13	2321	2330	4.2
17194812	D	6	4	96	98	66.23	2326	2335	5.2
17194822	D	6	4	108	109	66.37	2331	2340	4.9
17194832	D	6	4	120	121	66.51	2337	2347	3.8
17194842	D	6	4	132	133	66.62	2342	2351	3.4
17194852	D	6	4	144	145	66.73	2347	2355	3.8
17203662	D	6	5	18	19	66.94	2356	2363	4.2
17203672	D	6	5	30	31	67.07	2361	2367	4.6
17203682	D	6	5	42	43	67.23	2368	2375	3.4
17203692	D	6	5	54	55	67.33	2372	2379	2.9
17203702	D	6	5	66	68	67.42	2376	2384	2.7
17203712	D	6	5	78	79	67.51	2380	2388	2.5
17203722	D	6	5	90	91	67.61	2384	2392	2.5
17203732	D	6	5	101	103	67.79	2391	2401	2.6
17203742	D	6	5	117	119	67.99	2399	2410	2.7
17203752	D	6	5	127	128	68.08	2403	2414	2.9
17203762	D	6	5	137	138	68.18	2407	2418	2.3
17203772	D	6	5	145	146	68.20	2408	2419	2.3
17204052	D	6	6	23	25	68.38	2415	2427	2.0
17204062	D	6	6	33	35	68.43	2417	2428	1.8
17204132	D	6	6	47	49	68.56	2422	2432	2.0
17204042	D	6	5	6	8	68.67	2426	2434	4.1
17204072	D	6	6	59	61	68.72	2428	2436	2.0

Table S1 (cont'd)

Sample ID	Hole	Core	Sect	Interval upper (cm)	Interval Lower (cm)	Average depth on splice (m)	Age, published age model (ka.)	Age, realigned age model (ka.)	Corrected barite (mg/g sediment)
17204082	D	6	6	71	73	68.90	2434	2440	1.8
17204122	D	6	6	73	75	68.92	2435	2441	1.8
17204092	D	6	6	118	120	69.34	2450	2452	2.6
17204102	D	6	6	132	134	69.35	2450	2453	4.9
17204112	D	6	6	142	144	69.58	2458	2461	3.5
17103442	C	7	1	87	89	69.84	2467	2470	5.2
17103452	C	7	1	98	100	69.93	2471	2473	2.8
17103462	C	7	1	110	112	70.06	2475	2477	2.7
17103472	C	7	1	122	124	70.18	2480	2481	2.7
17103482	C	7	1	133	135	70.29	2483	2485	3.3
17218942	D	7	1	18	20	70.80	2502	2502	3.3
17223942	D	7	1	33	35	70.89	2505	2507	3.4
17223962	D	7	1	51	54	71.07	2511	2516	3.2

Site 882

Sample ID	Hole	Core	Sect	Interval upper (cm)	Interval Lower (cm)	Average depth on splice (m)	Age, published age model (ka.)	Age, realigned age model (ka.)	Corrected barite (mg/g sediment)
17233832	A	9	3	45	46	85.00	1967	2024	0.8
17233842	A	9	3	63	64	85.18	1971	2028	2.7
17233852	A	9	3	81	82	85.35	1975	2032	1.2
17233862	A	9	3	99	100	85.53	1980	2036	1.7
17233872	A	9	3	117	118	85.70	1985	2041	1.5
17233882	A	9	3	135	136	85.87	1989	2045	1.7
17237402	A	9	4	3	4	86.05	1994	2049	1.9
17237412	A	9	4	21	22	86.22	1999	2053	4.9
17237442	A	9	4	57	58	86.57	2009	2061	2.8

Table S1 (cont'd)

Sample ID	Hole	Core	Sect	Interval upper (cm)	Interval Lower (cm)	Average depth on splice (m)	Age, published age model (ka.)	Age, realigned age model (ka.)	Corrected barite (mg/g sediment)
17237452	A	9	4	75	76	86.75	2014	2065	1.9
17237462	A	9	4	93	94	86.92	2022	2070	1.5
17237482	A	9	4	112	113	87.11	2030	2074	1.2
17237492	A	9	4	129	130	87.27	2037	2078	1.4
17237502	A	9	4	147	148	87.44	2045	2082	1.2
17283122	A	9	5	15	16	87.62	2052	2086	1.2
17283132	A	9	5	33	34	87.79	2057	2090	1.0
17283142	A	9	5	51	52	87.97	2063	2095	1.2
17283162	A	9	5	68	69	88.13	2068	2098	1.4
17283172	A	9	5	87	88	88.32	2074	2103	2.3
17283192	A	9	5	123	124	88.67	2085	2111	2.0
17283212	A	9	5	141	142	88.84	2092	2115	2.3
17290242	A	9	6	8	9	89.00	2100	2119	1.2
17290252	A	9	6	26	27	89.18	2109	2123	1.7
17290262	A	9	6	44	45	89.35	2118	2128	1.5
17290272	A	9	6	62	63	89.53	2126	2132	2.5
17290282	A	9	6	79	80	89.69	2133	2136	2.6
17290292	A	9	6	98	99	89.88	2141	2140	1.4
17290312	A	9	6	134	135	90.23	2155	2148	1.0
17299352	A	9	7	2	3	90.40	2162	2152	1.1
17303962	B	10	3	111	112	90.89	2176	2164	1.3
17303972	B	10	3	129	130	91.07	2179	2168	1.7
17303982	B	10	3	147	148	91.25	2182	2173	2.3
17303992	B	10	4	15	16	91.43	2185	2177	3.4
17304012	B	10	4	51	52	91.79	2191	2185	1.3

Table S1 (cont'd)

Sample ID	Hole	Core	Sect	Interval upper (cm)	Interval Lower (cm)	Average depth on splice (m)	Age, published age model (ka.)	Age, realigned age model (ka.)	Corrected barite (mg/g sediment)
17304022	B	10	4	69	70	91.97	2194	2190	1.1
17304032	B	10	4	78	79	92.06	2196	2192	1.4
17304042	B	10	4	103	104	92.31	2200	2198	2.0
17300272	A	10	1	25	26	92.32	2200	2198	2.1
17300282	A	10	1	39	40	92.45	2203	2201	2.3
17300292	A	10	1	57	58	92.62	2206	2205	1.9
17300302	A	10	1	75	76	92.80	2209	2209	2.2
17300312	A	10	1	93	94	92.97	2212	2214	2.4
17300322	A	10	1	111	112	93.14	2215	2218	2.2
17300332	A	10	1	129	130	93.31	2218	2222	1.3
17300342	A	10	1	147	148	93.49	2221	2226	1.0
17300352	A	10	2	15	16	93.66	2223	2230	0.9
17300362	A	10	2	33	34	93.83	2226	2234	0.9
17300372	A	10	2	52	53	94.02	2229	2239	1.1
17300382	A	10	2	68	69	94.17	2231	2242	1.1
17300392	A	10	2	87	88	94.35	2234	2247	1.3
17300402	A	10	2	105	106	94.53	2237	2251	1.6
17300412	A	10	2	123	124	94.70	2239	2255	2.0
17300422	A	10	2	141	142	94.87	2242	2259	1.9
17303512	A	10	3	8	9	95.04	2244	2263	2.4
17303522	A	10	3	26	27	95.21	2247	2267	3.2
17303532	A	10	3	44	45	95.38	2250	2271	1.8
17303542	A	10	3	62	63	95.56	2253	2275	1.5
17303552	A	10	3	80	81	95.73	2259	2279	1.5
17303562	A	10	3	98	99	95.90	2265	2283	1.1

Table S1 (cont'd)

Sample ID	Hole	Core	Sect	Interval upper (cm)	Interval Lower (cm)	Average depth on splice (m)	Age, published age model (ka.)	Age, realigned age model (ka.)	Corrected barite (mg/g sediment)
17303572	A	10	3	116	117	96.07	2271	2288	1.0
17303582	A	10	3	134	135	96.25	2277	2292	1.2
17303592	A	10	4	2	3	96.42	2283	2296	1.7
17303602	A	10	4	20	21	96.59	2289	2300	2.0
17303612	A	10	4	38	39	96.77	2295	2304	2.0
17303622	A	10	4	56	57	96.94	2301	2308	2.1
17303632	A	10	4	74	75	97.11	2307	2312	1.6
17303642	A	10	4	92	93	97.29	2315	2316	1.9
17303652	A	10	4	111	112	97.47	2326	2321	2.3
17303682	A	10	5	14	15	97.98	2357	2333	1.8
17303692	A	10	5	32	33	98.15	2368	2337	2.3
17303702	A	10	5	50	51	98.33	2375	2341	2.5
17303712	A	10	5	68	69	98.50	2378	2345	2.2
17303722	A	10	5	86	87	98.67	2382	2349	1.8
17303732	A	10	5	104	105	98.84	2385	2353	1.8
17303742	A	10	5	122	123	99.02	2388	2358	1.1
17303752	A	10	5	140	142	99.20	2391	2362	2.3
17303762	A	10	6	8	9	99.36	2394	2366	3.7
17303772	A	10	6	25	26	99.53	2397	2370	2.9
17303782	A	10	6	44	45	99.71	2400	2374	3.1
17303792	A	10	6	62	63	99.88	2403	2378	3.8
17303802	A	10	6	80	81	100.06	2406	2382	2.6
17303812	A	10	6	98	99	100.23	2409	2386	2.0
17303822	A	10	6	116	117	100.40	2413	2391	1.9
17303832	A	10	6	134	135	100.58	2417	2395	1.5

Table S1 (cont'd)

Sample ID	Hole	Core	Sect	Interval upper (cm)	Interval Lower (cm)	Average depth on splice (m)	Age, published age model (ka.)	Age, realigned age model (ka.)	Corrected barite (mg/g sediment)
17303842	A	10	7	2	3	100.75	2421	2399	1.3
17303852	A	10	7	19	20	100.91	2425	2403	2.4
17304052	B	11	3	28	29	100.91	2425	2403	2.6
17304062	B	11	3	48	49	101.10	2429	2407	3.6
17304072	B	11	3	66	67	101.27	2437	2411	3.1
17304082	B	11	3	84	85	101.44	2444	2415	1.9
17304092	B	11	3	103	104	101.62	2452	2420	0.8
17304102	B	11	3	121	122	101.79	2459	2424	1.3
17304112	B	11	3	138	139	101.95	2465	2428	1.7
17304122	B	11	4	6	7	102.12	2473	2432	2.4
17304132	B	11	4	23	24	102.29	2479	2435	3.0
17303872	A	11	1	53	54	102.77	2502	2447	3.3
17303882	A	11	1	71	72	102.94	2511	2451	1.6
17303892	A	11	1	88	89	103.11	2520	2455	1.7
17303902	A	11	1	107	108	103.29	2529	2459	1.4
17303912	A	11	1	125	126	103.47	2537	2464	1.1
17303922	A	11	1	143	144	103.64	2542	2468	1.2
17303932	A	11	2	11	12	103.82	2548	2472	1.3
17303942	A	11	2	28	30	103.99	2554	2476	1.5

Site 927

Sample ID	Hole	Core	Sect	Interval upper (cm)	Interval Lower (cm)	Average depth on splice (m)	Age, published age model (ka.)	Age, realigned age model (ka.)	Corrected barite (mg/g sediment)
5051627	C	8	3	56	57	76.88	2029		0.14
5051628	C	8	3	74	75	77.06	2034		0.10
5051629	C	8	3	92	93	77.24	2039		0.13

Table S1 (cont'd)

Sample ID	Hole	Core	Sect	Interval upper (cm)	Interval Lower (cm)	Average depth on splice (m)	Age, published age model (ka.)	Age, realigned age model (ka.)	Corrected barite (mg/g sediment)
5051630	C	8	3	110	111	77.42	2043		0.17
5051631	C	8	3	128	129	77.60	2048		0.17
5051632	C	8	3	146	147	77.78	2053		0.07
5051633	C	8	4	14	15	77.96	2058		0.17
5051634	C	8	4	34	35	78.16	2063		0.22
5051635	C	8	4	54	55	78.36	2069		0.23
5051636	C	8	4	74	75	78.56	2075		0.22
5051637	C	8	4	94	95	78.76	2081		0.25
5051638	C	8	4	114	115	78.96	2086		0.22
5051639	C	8	4	134	135	79.16	2091		0.22
5051641	C	8	5	2	3	79.34	2096		0.26
5051640	C	8	5	20	21	79.52	2101		0.21
5051642	C	8	5	38	39	79.70	2107		0.19
5051643	C	8	5	56	57	79.88	2112		0.15
5051644	C	8	5	74	75	80.06	2117		0.15
5051645	C	8	5	92	93	80.24	2122		0.19
5051646	C	8	5	110	111	80.42	2126		0.23
5051647	C	8	5	128	129	80.60	2130		0.19
5051648	C	8	5	146	147	80.78	2134		0.15
5051649	C	8	6	14	15	80.96	2137		0.14
5051650	C	8	6	34	35	81.16	2141		0.23
5051651	C	8	6	54	55	81.36	2145		0.18
5051652	C	8	6	74	75	81.56	2150		0.21
5051653	C	8	6	94	95	81.76	2154		0.22
5051654	C	8	6	112	113	81.94	2159		0.24

Table S1 (cont'd)

Sample ID	Hole	Core	Sect	Interval upper (cm)	Interval Lower (cm)	Average depth on splice (m)	Age, published age model (ka.)	Age, realigned age model (ka.)	Corrected barite (mg/g sediment)
5051590	B	9	2	138	139	82.05	2162		0.24
5051591	B	9	3	6	7	82.23	2165		0.17
5051592	B	9	3	24	25	82.41	2170		0.19
5051593	B	9	3	42	43	82.59	2175		0.19
5051594	B	9	3	60	61	82.77	2178		0.14
5051595	B	9	3	78	79	82.95	2182		0.11
5051596	B	9	3	96	97	83.13	2187		0.16
5051597	B	9	3	114	115	83.31	2191		0.21
5051598	B	9	3	132	133	83.49	2195		0.22
5051599	B	9	3	149	150	83.66	2199		0.15
5051600	B	9	4	17	18	83.84	2203		0.18
5051601	B	9	4	35	36	84.02	2206		0.18
5051602	B	9	4	53	54	84.20	2210		0.22
5051603	B	9	4	71	72	84.38	2215		0.22
5051607	B	9	4	88	90	84.55	2222		0.20
5051604	B	9	4	107	108	84.74	2224		0.14
5051605	B	9	4	125	126	84.92	2227		0.14
5051606	B	9	4	143	144	85.10	2230		0.15
5051608	B	9	5	8	9	85.25	2232		0.21
5051565	A	9	3	90	91	85.28	2233		0.23
5051566	A	9	3	108	109	85.46	2236		0.24
5051567	A	9	3	126	127	85.64	2241		0.22
5051568	A	9	3	144	145	85.82	2248		0.23
5051569	A	9	4	14	15	86.02	2256		0.23
5051570	A	9	4	32	33	86.20	2260		0.14

Table S1 (cont'd)

Sample ID	Hole	Core	Sect	Interval upper (cm)	Interval Lower (cm)	Average depth on splice (m)	Age, published age model (ka.)	Age, realigned age model (ka.)	Corrected barite (mg/g sediment)
5051571	A	9	4	50	51	86.38	2264		0.12
5051572	A	9	4	68	69	86.56	2269		0.08
5051573	A	9	4	86	87	86.74	2273		0.13
5051574	A	9	4	104	105	86.92	2278		0.18
5051575	A	9	4	122	123	87.10	2282		0.19
5051576	A	9	4	140	141	87.28	2287		0.25
5051580	A	9	5	8	9	87.46	2291		0.22
5051581	A	9	5	26	27	87.64	2295		0.15
5051582	A	9	5	44	45	87.82	2300		0.18
5051583	A	9	5	62	63	88.00	2305		0.16
5051584	A	9	5	80	81	88.18	2310		0.13
5051585	A	9	5	98	99	88.36	2314		0.14
5051587	A	9	5	116	117	88.54	2321		0.13
5051586	A	9	5	136	137	88.74	2328		0.20
5051588	A	9	6	2	3	88.90	2334		0.23
5051589	A	9	6	20	21	89.08	2339		0.21
5051655	C	9	4	78	79	89.36	2344		0.17
5051656	C	9	4	96	97	89.54	2348		0.12
5051657	C	9	4	114	115	89.72	2356		0.19
5051658	C	9	4	132	133	89.90	2363		0.19
5051659	C	9	5	0	1	90.08	2370		0.18
5051660	C	9	5	18	19	90.26	2378		0.19
5051661	C	9	5	36	37	90.44	2385		0.14
5051662	C	9	5	54	55	90.62	2393		0.14
5051664	C	9	5	90	91	90.98	2406		0.12

Table S1 (cont'd)

Sample ID	Hole	Core	Sect	Interval upper (cm)	Interval Lower (cm)	Average depth on splice (m)	Age, published age model (ka.)	Age, realigned age model (ka.)	Corrected barite (mg/g sediment)
5051665	C	9	5	108	109	91.16	2412		0.12
5051666	C	9	5	126	127	91.34	2417		0.11
5051667	C	9	5	144	145	91.52	2421		0.12
5051668	C	9	6	12	13	91.70	2426		0.13
5051669	C	9	6	30	31	91.88	2431		0.15
5051670	C	9	6	48	49	92.06	2435		0.19
5051671	C	9	6	53	54	92.11	2436		0.23
5051609	B	10	2	118	119	92.30	2440		0.18
5051610	B	10	2	136	137	92.48	2444		0.19
5051611	B	10	3	4	5	92.66	2447		0.18
5051612	B	10	3	22	23	92.84	2453		0.19
5051614	B	10	3	58	59	93.20	2463		0.13
5051615	B	10	3	76	77	93.38	2470		0.16
5051616	B	10	3	94	95	93.56	2476		0.23
5051620	B	10	3	100	101	93.62	2478		0.22
5051617	B	10	3	112	113	93.74	2482		0.30
5051621	B	10	3	120	121	93.82	2485		0.24
5051618	B	10	3	130	131	93.92	2488		0.22
5051622	B	10	3	140	141	94.02	2491		0.19
5051619	B	10	3	148	149	94.10	2493		0.20
5051623	B	10	4	8	9	94.20	2496		0.18
5051624	B	10	4	36	37	94.48	2503		0.15
5051625	B	10	4	54	55	94.66	2508		0.14

Site 1123

Table S1 (cont'd)

Sample ID	Hole	Core	Sect	Interval upper (cm)	Interval Lower (cm)	Average depth on splice (m)	Age, published age model (ka.)	Age, realigned age model (ka.)	Corrected barite (mg/g sediment)
17304162	B	9	3	90	91	79.45	2050	NaN	0.92
17304172	B	9	3	105	106	79.60	2060	2069	0.98
17304182	B	9	3	114	115	79.69	2065	2080	0.86
17304192	B	9	3	127	128	79.82	2072	2085	1.23
17304202	B	9	3	138	139	79.93	2077	2088	1.28
17304212	B	9	3	149	150	80.04	2083	2092	1.12
17304222	B	9	4	10	11	80.15	2088	2096	1.11
17304232	B	9	4	25	26	80.30	2095	2100	1.21
17304242	B	9	4	35	36	80.40	2100	2105	1.20
17304252	B	9	4	45	46	80.50	2104	2110	0.97
17304262	B	9	4	59	60	80.64	2110	2117	0.77
17304272	B	9	4	70	71	80.75	2115	2123	0.78
17304282	B	9	4	82	83	80.87	2120	2128	0.80
17304292	B	9	4	95	96	81.00	2125	2133	0.98
17304302	B	9	4	108	109	81.13	2129	2137	1.05
17304312	B	9	4	119	120	81.24	2133	2141	0.71
17304322	B	9	4	131	132	81.36	2138	2146	0.87
17304332	B	9	4	142	143	81.47	2142	2150	0.91
17304342	B	9	5	5	7	81.60	2148	2155	0.85
17304352	B	9	5	15	16	81.70	2151	2158	1.02
17304362	B	9	5	29	30	81.84	2157	2164	0.83
17304372	B	9	5	40	41	81.95	2161	2168	0.95
17304382	B	9	5	52	53	82.07	2167	2172	0.99
17304392	B	9	5	65	66	82.20	2173	2177	1.05
17305372	C	9	2	141	142	82.32	2179	2182	1.51

Table S1 (cont'd)

Sample ID	Hole	Core	Sect	Interval upper (cm)	Interval Lower (cm)	Average depth on splice (m)	Age, published age model (ka.)	Age, realigned age model (ka.)	Corrected barite (mg/g sediment)
17305382	C	9	3	3	4	82.44	2185	2187	1.35
17305392	C	9	3	14	15	82.55	2190	2192	0.86
17305402	C	9	3	27	28	82.68	2195	2196	1.16
17305412	C	9	3	39	40	82.80	2200	2201	0.95
17305422	C	9	3	52	53	82.93	2204	2206	0.92
17305432	C	9	3	63	64	83.04	2208	2209	0.86
17305442	C	9	3	74	75	83.15	2212	2213	0.93
17305452	C	9	3	87	88	83.28	2216	2217	0.97
17305462	C	9	3	99	100	83.40	2220	2221	0.87
17305472	C	9	3	111	112	83.52	2224	2225	1.04
17305482	C	9	3	123	124	83.64	2228	2229	1.27
17305492	C	9	3	133	134	83.74	2231	2233	1.30
17305642	C	9	4	9	10	84.00	2240	2244	1.08
17305652	C	9	4	21	22	84.12	2243	2248	1.03
17305662	C	9	4	33	34	84.24	2247	2253	1.08
17305672	C	9	4	44	45	84.35	2251	2257	1.05
17305682	C	9	4	57	58	84.48	2256	2263	0.96
17305692	C	9	4	69	70	84.60	2261	2268	0.93
17305702	C	9	4	81	82	84.72	2266	2271	0.98
17305712	C	9	4	93	94	84.84	2270	2275	1.01
17305722	C	9	4	104	105	84.95	2274	2278	1.02
17305742	C	9	4	141	142	85.32	2286	2287	0.75
17305502	C	9	5	3	4	85.44	2289	2291	1.06
17305522	C	9	5	27	28	85.68	2297	2298	0.86
17305532	C	9	5	39	40	85.80	2301	2302	1.03

Table S1 (cont'd)

Sample ID	Hole	Core	Sect	Interval upper (cm)	Interval Lower (cm)	Average depth on splice (m)	Age, published age model (ka.)	Age, realigned age model (ka.)	Corrected barite (mg/g sediment)
17305542	C	9	5	51	52	85.92	2305	2307	1.09
17305552	C	9	5	63	64	86.04	2309	2312	1.01
17305562	C	9	5	74	75	86.15	2313	2317	0.77
17305572	C	9	5	87	88	86.28	2318	2323	0.68
17305582	C	9	5	111	112	86.52	2326	2332	0.66
17305592	C	9	5	123	124	86.64	2331	2337	0.70
17305602	C	9	5	134	135	86.75	2335	2341	0.81
17305622	C	9	5	148	149	86.89	2340	2346	0.95
17305632	C	9	6	11	13	87.02	2345	2351	1.01
17304402	B	10	2	22	23	87.13	2350	2355	0.77
17304412	B	10	2	39	40	87.30	2356	2360	0.85
17304422	B	10	2	57	58	87.48	2363	2367	1.00
17304432	B	10	2	74	76	87.65	2370	2372	1.22
17304442	B	10	2	93	94	87.84	2376	2378	1.47
17304452	B	10	2	112	113	88.03	2384	2384	1.31
17304462	B	10	2	129	130	88.20	2391	2392	1.03
17304472	B	10	2	147	148	88.38	2397	2399	0.86
17304602	B	10	3	12	13	88.53	2402	2405	0.97
17304612	B	10	3	21	23	88.62	2404	2408	0.99
17304622	B	10	3	32	33	88.73	2407	2411	1.21
17304632	B	10	3	46	47	88.87	2412	2417	1.54
17304642	B	10	3	57	58	88.98	2416	2422	1.45
17304652	B	10	3	69	70	89.10	2420	2427	1.18
17304672	B	10	3	92	93	89.33	2428	2437	1.00
17304682	B	10	3	106	107	89.47	2434	2445	1.00

Table S1 (cont'd)

Sample ID	Hole	Core	Sect	Interval upper (cm)	Interval Lower (cm)	Average depth on splice (m)	Age, published age model (ka.)	Age, realigned age model (ka.)	Corrected barite (mg/g sediment)
17304692	B	10	3	117	118	89.58	2440	2451	1.07
17304702	B	10	3	129	130	89.70	2447	2455	1.25
17304712	B	10	3	142	143	89.83	2453	2460	0.99
17305122	B	10	4	3	4	89.94	2458	2464	1.11
17305132	B	10	4	14	15	90.05	2463	2468	1.11
17305142	B	10	4	28	30	90.19	2470	2473	1.29
17305152	B	10	4	39	40	90.30	2474	2477	1.62
17305262	B	10	4	51	53	90.42	2479	2481	1.70
17305232	B	10	4	63	64	90.54	2483	2484	1.16
17305172	B	10	4	74	75	90.65	2486	2487	0.97
17305252	B	10	4	87	88	90.78	2490	2492	0.93
17305242	B	10	4	112	113	91.03	2498	2502	0.91
17305222	B	10	4	123	124	91.14	2502	2507	1.01
17305202	B	10	4	134	135	91.25	2507	2513	1.03
17305272	B	10	5	9	10	91.50	2516	2525	1.00
17305282	B	10	5	22	23	91.63	2520	2530	1.06
17305292	B	10	5	33	34	91.74	2523	2532	1.07
17305312	B	10	5	57	58	91.98	2532	2538	0.86
17305322	B	10	5	69	70	92.10	2536	2540	0.99
17305332	B	10	5	81	82	92.22	2540	2543	1.05
17305342	B	10	5	92	93	92.33	2543	2545	0.96
17305352	B	10	5	106	107	92.47	2546	2547	0.93
17305362	B	10	5	117	118	92.58	2548	2548	1.05

CHAPTER 3

Carbon cycling at the Sunda margin: Indonesia: a regional study with global implications

Brian M. House[1], Gray Bebout[2], David Hilton[1†]

[1]Scripps Institution of Oceanography, University of California San Diego, La Jolla, CA 92037

[2]Department of Earth and Environmental Sciences, Lehigh University, Bethlehem, PA 18015

[†]Deceased

Corresponding author: Brian M. House (bhouse@ucsd.edu)

GEOLOGY | THE GEOLOGICAL SOCIETY OF AMERICA®

https://doi.org/10.1130/G45830.1

Manuscript received 20 November 2018
Revised manuscript received 3 March 2019
Manuscript accepted 5 March 2019

Published online 22 March 2019

Carbon cycling at the Sunda margin, Indonesia: A regional study with global implications

Brian M. House[1]*, Gray E. Bebout[2], and David R. Hilton[1†]
[1]Scripps Institution of Oceanography, Vaughan Hall 434, 8675 Naga Lane, La Jolla, California 92037, USA
[2]Department of Earth and Environmental Sciences, Lehigh University, 1 West Packer Avenue, Bethlehem, Pennsylvania 18015, USA

ABSTRACT

The subduction and release of carbon at convergent margins is a primary mechanism by which tectonic processes influence atmospheric pCO_2, but the balance between the amount of carbon subducting and the CO_2 flux from volcanic arcs remains poorly constrained. Estimating CO_2 recycling efficiency in complex regions like the Sunda margin, Indonesia, is particularly difficult due to the lateral variability in sediment thickness, composition, and fraction subducted. We present a new approach for estimating sedimentary carbon flux that combines high-precision carbon content and isotope measurements with a regional sediment and unit thickness model we generated from seismic profiles to more accurately extrapolate compositional measurements from sediment core sites to the margin. Our results suggest that the subducting sedimentary carbon flux is up to an order of magnitude less than previous estimates and cannot alone account for the volume of CO_2 released along the volcanic arc. Together, this and the isotopic composition of subducting sedimentary carbon suggest that an additional isotopically heavy carbon source contributes to the released CO_2. Carbon from carbonate—likely from subducted altered oceanic crust and the overriding plate—can account for the discrepancy between both amount and isotopic composition of sedimentary carbon influx and those of volcanic CO_2 efflux. These results highlight the importance of considering the full range of subduction zone processes operating at individual margins in order to better understand the cycling of carbon and other elements. Similar scrutiny should be applied in the evaluation of carbon subduction inputs to other subduction margins to improve global estimates of tectonic carbon cycling.

INTRODUCTION

The flux of carbon into subduction zones has traditionally been estimated using measurements of C content in cored sedimentary sections that may be hundreds of kilometers outboard of the respective trench. Without models for the spatial variability of sediment and unit thicknesses, this technique can lead to situations in which few and potentially dubious shipboard measurements (Fig. DR1 in the GSA Data Repository[1]) are used to calculate a subducting C flux along thousands of kilometers of trench length. While this approach may work for subduction zones where no sediment is accreted (Li and Bebout, 2005), a more detailed approach is necessary for the commonly more complex subduction zones like the Sunda margin, Indonesia, where sediment thickness, lithology, and accretion efficiency vary along strike (McNeill and Henstock, 2014; Plank and Langmuir, 1998). Instead of assuming that sediments at core locations directly reflect what is present at the trench, we produced a sediment and unit thickness model from seismic profile picks, a technique which has not been previously utilized. Furthermore, sediment is actively accreting along most of the Sunda margin (e.g., McNeill and Henstock, 2014), which needs to be realistically accounted for.

The Sunda margin, which encompasses a part of the convergent boundary between the Sunda and Indoaustralian plates (Fig. 1), is notable for its sediment thickness (>5 km) at its northwestern extreme and a dramatic shift from the organic-rich sediments of the Nicobar Fan off Sumatra (McNeill et al., 2017) to a carbonate-dominated system off Java and the islands to the east (Shipboard Scientific Party, 1974, 1990). A wedge of organic-rich trench fill is present along the entire margin (Dean et al., 2010). Along eastern Java, subduction of the Roo Rise, an elevated region in the Australian plate, produces a local region of subduction erosion (Kopp et al., 2006), while east of this, the Australian continental shelf impinges upon the margin at what we define as the transition from the Sunda to the Banda margin.

METHODS

Sediment and unit thickness models were produced by digitizing single and multichannel seismic profiles (see the Data Repository). Unit boundaries were inferred based on seismic interpretations from site reports of nearby Deep Sea Drilling Project–Ocean Drilling Program–Integrated Ocean Drilling Program (DSDP-ODP-IODP) sites when other published interpretations were not available. When profiles were presented in two-way traveltime rather than depth, and no local sediment velocity model was available, velocities of 2 and 2.5 km s^{-1} were used to generate upper and lower bounds on sediment and unit thicknesses. Carbonate content and $\delta^{13}C$ were measured by acidification and analysis of evolved CO_2 using a dual-inlet isotope ratio mass spectrometer following the methodology of Li and Bebout (2005). Total organic C and $\delta^{13}C$ were measured by heating pre-acidified sample aliquots in evacuated quartz tubes to 910 °C in the presence of Cu and CuO_x and subsequently purifying and measuring CO_2 amount and $\delta^{13}C$ using a dual-inlet isotope ratio mass spectrometer (Li and Bebout, 2005). All analyses were carried out in the Bebout lab at Lehigh University (Pennsylvania, United States).

We estimated the total amount of C reaching the trench by integrating the organic and carbonate C of each operationally defined sediment unit (Fig. 2) over the estimated unit thicknesses at the points along the trench defined by the MORVEL

*E-mail: bhouse@ucsd.edu
†Deceased

[1]GSA Data Repository item 2019180, detailed methods, supplementary discussion, and supplemental figures DR1–DR3, is available online at http://www.geosociety.org/datarepository/2019/, or on request from editing@geosociety.org. Piston and gravity cores used to establish trench fill composition are archived at the Scripps Institution of Oceanography (La Jolla, California, USA) and Lamont-Doherty Earth Observatory (Palisades, New York, USA) core repositories. Data used in this study are archived in the PANGEA database, at https://doi.pangaea.de/10.1594/PANGAEA.899126.

CITATION: House, B.M., Bebout, G.E., and Hilton, D.R., 2019, Carbon cycling at the Sunda margin, Indonesia: A regional study with global implications: Geology, v. 47, p. 483–486, https://doi.org/10.1130/G45830.1

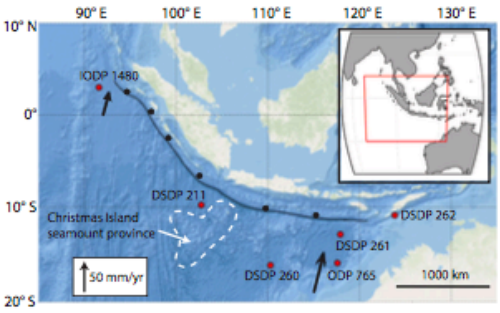

Figure 1. Overview of study area, Sunda margin, Indonesia, with Deep Sea Drilling Project–Ocean Drilling Program–Integrated Ocean Drilling Program (DSDP-ODP-IODP) core sites (red circles), locations of piston and gravity cores (black circles), and plate motion vectors (black arrows).

plate motion model (http://geoscience.wisc.edu/~chuck/MORVEL/; Argus et al., 2011). These values were converted into C fluxes in the intervals between each set of MORVEL points using relative plate motions (Argus et al., 2011). Estimates for the fraction of sediment subducting versus accreting came from previous work that imaged or estimated the thickness of the subduction channel using seismic profiles across the deformation front or mass balance estimates considering sediment thickness and accretionary complex volume and age (see the Data Repository for details). Upper- and lower-bound estimates for the flux of sedimentary C bypassing the deformation front (Fig. 3) were generated by integrating the C content only over those units or fractions of units thought to subduct. Overall C isotope compositions were calculated as the average of organic C and carbonate $\delta^{13}C$ weighted by the fractions of C from each source. When published dry bulk densities of sediments were not available, we used densities of 1.8 and 2.0 g cm^{-3} to calculate bounds on C flux.

IMPROVING SEDIMENTARY CARBON FLUX ESTIMATES

We used new C content and isotope data from cores taken at the three sites nearest the margin (DSDP Sites 211, 260, and 261) to constrain the quantity and form of C available for subduction. Combined with our sediment thickness model (Fig. 2; Fig. DR2), these results suggest a decrease in the amount of C reaching the trench from northern Sumatra southeastward to the Sunda Strait as the Nicobar Fan thins, and a relatively constant amount of total C, but a shift toward carbonate, farther to the southeast (Figs. 2 and 3). The amount of organic C reaching the deformation front is also strongly influenced by the organic-rich trench wedge, which reaches >1 wt% organic C (Fig. 2; Table DR1 in the Data Repository). Overall, our calculations indicate that ~5.5–6.5 Tg C yr^{-1}, 60%–75% of which is organic C, reaches the deformation front and is therefore available for subduction (see Methods herein, and the Data Repository). The magnitude of uncertainty in C reaching the trench is difficult to quantify, but large uncertainty in the proportion of sediment subducted (e.g., McNeill and Henstock, 2014) is likely to have a far greater effect on our calculated subducting C flux.

Using existing estimates for the fraction of sediment subducted (see Methods herein, and the Data Repository), we estimate that of the total sediment-hosted C reaching the trench, only ~480–1100 Gg yr^{-1} subducts past ~20 km depth (Fig. 3). This implies that only one-sixth to one-twelfth of the C reaching the trench actually subducts because ~85%–100% of the overall sediment reaching the deformation front is offscraped (McNeill and Henstock, 2014). Our estimate, which is the first to use a seismically constrained sediment thickness model, is as much as an order of magnitude less than previous estimates (Clift, 2016; Hilton et al., 2002; Plank and Langmuir, 1998), which we suggest is due to more realistic sediment accretion percentages. Furthermore, the composition of the subducting C is dramatically different from what is reaching the trench: organic C accounts for up to ~75% of the C reaching the trench, while it represents only ~10%–25% of what subducts. Organic C–rich Nicobar Fan material appears to be subducting over a short distance off North Sumatra, but otherwise, carbonate is the dominant C source along the entire margin largely due to offscraping of the organic-rich trench wedge.

REVISING THE CARBON CYCLING BUDGET

Estimates of CO_2 flux at volcanic centers are necessary to construct a C cycling budget, but both ground- and satellite-based gas flux measurements contain significant uncertainty that is compounded when assembling arc-wide estimates of CO_2 flux (e.g., Hilton et al., 2002). For the Sunda margin, estimates range from ~98 to ~2200 Gg C yr^{-1} (Nho et al., 1996; Pfeffer, 2007; Carn et al., 2017; Hilton et al., 2002), and ground-based CO_2 flux estimates exist only for seven of the ~95 historically active volcanoes in Indonesia (Aiuppa et al., 2015; Bani et al., 2015; Andres and Kasgnoc, 1998; Bluth et al., 1994; Pfeffer, 2007). Satellite-based CO_2 flux estimates—calculated from measured SO_2 loads and the C/S ratio of discrete gas samples—are particularly promising for determining CO_2 fluxes along an entire margin because they can incorporate decades of observations and obviate the need for extrapolating arc-wide fluxes from measurements at individual volcanoes (Carn et al., 2017).

Using a conservative C/S molar ratio of 4/1 (Hilton et al., 2002) along with the most recent satellite-derived arc-wide SO_2 fluxes (Carn et al., 2017), we derive a CO_2 flux of ~1700–2500 Gg C yr^{-1}, which is 1.5 to 5 times greater than our estimate for the amount of C subducting in sediments alone. The extent to which C is released from subducted sediments is still unclear, but exhumed metasediments suggest that a substantial fraction of subducted sedimentary C may be retained to inferred depths of ~80 km (Cook-Kollars et al., 2014). Therefore, even in the unlikely scenario of complete decarbonation, the subducted sedimentary C cannot alone account for the magnitude of volcanic CO_2 output of the Sunda arc (Mason et al., 2017). This observation contrasts with accounts of other arcs (e.g., de Leeuw et al., 2007), highlighting the need for detailed

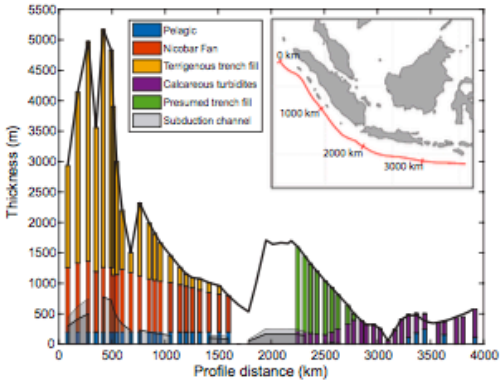

Figure 2. Overall sediment thickness (black line) along trench, Sunda margin, Indonesia. Distances along profile are shown in inset map. Colored bars indicate thicknesses of geochemically distinct units. Thickness of pelagic unit to ~1500 km profile distance is fixed at 200 m due to lack of clear seismic reflectors at interface between Nicobar Fan and pelagic units. Thickness of trench fill unit was calculated as difference between overall thickness and thicknesses of other units. While overall thickness is well constrained from ~1500 to ~2250 km, unit thicknesses are not. Gray regions indicate upper and lower estimates of sediment bypassing deformation front from McNeill and Henstock (2014).

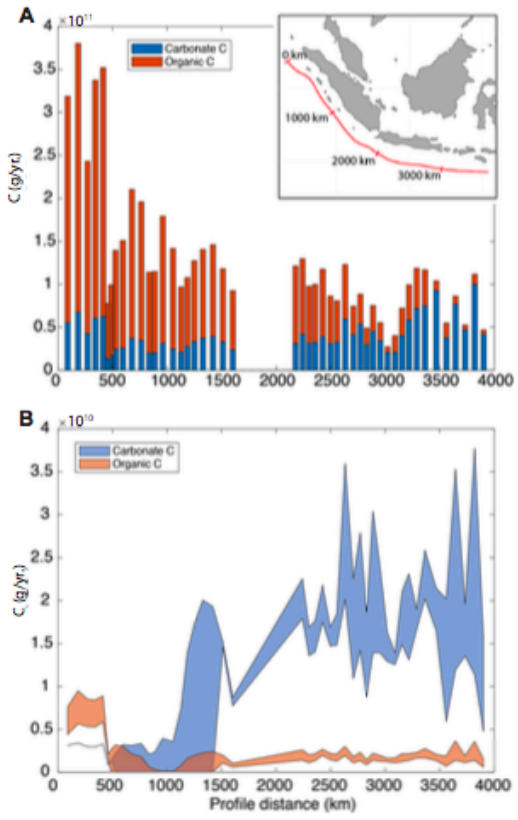

Figure 3. A: Organic and carbonate carbon reaching trench, Sunda margin, Indonesia. B: Organic and carbonate carbon subducting to ~20 km depth, with range in values representing range in estimates of fraction of accreting sediment. Distances along profile are shown in inset map. Organic carbon dominates where Nicobar Fan impinges on trench and organic-rich trench fill wedge is prominent, while carbonate is dominant carbon source along southeast of margin. All trench fill is offscraped along with most Nicobar Fan material, causing subducting flux of organic carbon to be far lower than what reaches trench. Region around 2000 km profile distance lacks reliable seismic profile constraints on sediment and unit thickness, so to calculate final subducting carbon fluxes, we assumed that carbon flux varied linearly over this interval.

margin-by-margin accounting of C cycling in order to reliably estimate global C (re)cycling efficiency at convergent margins.

ISOTOPIC COMPOSITION OF SUBDUCTING CARBON

To compare current sedimentary inputs with sediments subducting in the geologic past, we must assume that the overall subduction behavior, particularly accretion and erosion efficiency, has remained constant through time. Under these assumptions, Sano and Marty (1995) presented a mixing model to separate sedimentary organic, carbonate, and mantle C contributions to volcanic and hydrothermal CO_2 based on $\delta^{13}C$ and $CO_2/^3He$ ratios. However, the $CO_2/^3He$ ratio for the mantle wedge end member is not well constrained, and inferred CO_2 provenance may be highly sensitive to the end-member composition used (see the Data Repository). In addition, their model does not allow other C sources such as carbonate from altered oceanic crust (AOC) or the overlying crust to be resolved due to overlap between the isotopic compositions of these sources and that of carbonate in the sediment.

Instead, directly comparing the bulk $\delta^{13}C$ of subducting sediments with that of volcanic CO_2 suggests that additional C from a ^{13}C-rich source is involved. For example, we estimate that the bulk $\delta^{13}C$ of subducting sedimentary C is –14‰ to –17‰ along Sumatra, while CO_2 $\delta^{13}C$ values average –4‰. Mantle wedge–derived CO_2 with $\delta^{13}C$ of ~–6‰ ± 1‰ (Hilton et al., 2002) is insufficiently enriched in ^{13}C to account for this discrepancy, suggesting some combination of (1) isotopic fractionation during C release and migration and (2) incorporation of C from an isotopically heavier source. Forearc release of isotopically light C, perhaps as hydrocarbons from subducted organic matter, could help increase the $\delta^{13}C$ of the remaining C but would need to be substantial to account for volcanic CO_2 $\delta^{13}C$ values. Where measured, however, C flux in forearc regions is small (Füri et al., 2010). Furthermore, significant isotopic fractionation in the forearc appears unlikely due to the retention of organic C inferred from the study of forearc metamorphic suites (Cook-Kollars et al., 2014; see the Data Repository). While carbonate and organic C reservoirs may undergo some isotopic homogenization at forearc depths, these effects alone are unlikely to be large enough to explain the $\delta^{13}C$ of volcanic CO_2 (Cook-Kollars et al., 2014).

Therefore, incorporation of additional ^{13}C-rich C from a carbonate source is a more likely explanation. Southern Sumatra and Java in particular are underlain by substantial limestone deposits (Wilson, 2002), which have been shown to be a likely source of CO_2 released during recent eruptive periods at Merapi volcano (Troll et al., 2012; Deegan et al., 2010; Aiuppa et al., 2017). Such limestones may be a significant arc-wide CO_2 source; however, we observe the greatest discrepancy between the $\delta^{13}C$ of subducting sedimentary C and volcanic CO_2 in northern Sumatra, where the Nicobar Fan appears to supply ^{13}C-depleted C and carbonate platforms are thought to be small and localized (Wilson, 2002). We therefore suggest that release of isotopically heavy C from carbonate veins and matrix in brecciated AOC likely contributes to volcanic CO_2, at least in northern Sumatra and perhaps arc-wide. Along parts of the Sunda margin, the influx of C in AOC may be an order of magnitude greater than that in sediments (Hilton et al., 2002), but decarbonation of AOC can not be resolved using the mixing model of Sano and Marty (1995) (see the Data Repository).

Many studies of arc lava geochemistry invoke fluid-mediated addition of AOC signatures (Elliott et al., 1997; Jicha et al., 2004), so it is plausible that CO_2 is also liberated by decarbonation reactions in subducting crust and delivered to arc source regions (Aiuppa et al., 2017). Carbonate in AOC has been shown to "survive" transit through forearc regions to arc depths of ~80–120 km, at which point the subducting slab and sediments are heated by exposure to the convecting mantle wedge (Collins et al., 2015). Finally, we acknowledge that deep sediment underplating or diapiric sediment removal may further prevent the sediment currently subducting from being representative of what is currently at arc depths (Varekamp et al., 1992; Li and Bebout, 2005; Marschall and Schumacher, 2012). However, these processes would need to preferentially affect the subducting portion of the Nicobar Fan and not the underlying pelagic unit to have a substantial effect on the overall $\delta^{13}C$ of sedimentary C at arc depth along northern Sumatra, and sequestering C in the overriding plate would only increase the difference between subducting and volcanic C fluxes.

CONCLUSIONS

We present a new method for determining the flux of carbon subducting in marine sediments that reduces uncertainty due to the spatial variability of sediment thickness and composition by combining new geochemical results with a three-dimensional model of sediment and unit thickness. Doing so allows us to revise the flux of sedimentary C subducting at the Sunda margin down by an order of magnitude from

the previous estimates of Clift (2016). Satellite-based estimates of volcanic CO_2 fluxes exceed sedimentary C inputs by up to a factor of five, suggesting greater contributions from carbonate in the overlying crust and AOC than previously thought. While platform carbonate recycling is likely important in southern Sumatra and particularly in Java, the strong discrepancy between the $\delta^{13}C$ of subducting sedimentary C and that of volcanic CO_2 in northern Sumatra provides evidence for the release of AOC-hosted carbonate, a C reservoir of global significance. Our results emphasize the unique insight that margin-specific studies of C cycling provide, and applying similar methods to the world's major convergent margins will lead to greatly improved estimates of global C cycling.

ACKNOWLEDGMENTS

Timothy Henstock assisted with verifying seismic picks. Digitization of many archived single-channel seismic profiles was accomplished using GeoMapApp (http://www.geomapapp.org). Thanks to Terry Plank for providing the samples from the Deep Sea Drilling Project Site 211 and Ocean Drilling Program Site 765. Funding for the carbon and oxygen isotope analyses came from National Science Foundation grant EAR-1119264 (to Bebout), with additional support from Lehigh University (Department of Earth and Environmental Sciences, Pennsylvania, USA). We would like to thank Valentin Troll, Matthjis van Soest, and an anonymous reviewer for their comments, which greatly improved this work. We thank Lehigh University undergraduate students Brian Rodriguez, Kaylee Kraft, and Charlotte Malmborg for their participation in the stable isotope analyses.

REFERENCES CITED

Aiuppa, A., Bani, P., Moussallam, Y., Di Napoli, R., Allard, P., Gunawan, H., Hendrasto, M., and Tamburello, G., 2015, First determination of magma-derived gas emissions from Bromo volcano, eastern Java (Indonesia): Journal of Volcanology and Geothermal Research, v. 304, p. 206–213, https://doi.org/10.1016/j.jvolgeores.2015.09.008.

Aiuppa, A., Fischer, T.P., Plank, T., Robidoux, P., and Di Napoli, R., 2017, Along-arc, inter-arc and arc-to-arc variations in volcanic gas CO_2/S_T ratios reveal dual source of carbon in arc volcanism: Earth-Science Reviews, v. 168, p. 24–47, https://doi.org/10.1016/j.earscirev.2017.03.005.

Andres, R.J., and Kasgnoc, A.D., 1998, A time-averaged inventory of subaerial volcanic sulfur emissions: Journal of Geophysical Research, v. 103, p. 25,251–25,261, https://doi.org/10.1029/98JD02091.

Argus, D.F., Gordon, R.G., and DeMets, C., 2011, Geologically current motion of 56 plates relative to the no-net-rotation reference frame: Geochemistry Geophysics Geosystems, v. 12, Q11001, https://doi.org/10.1029/2011GC003751.

Bani, P., Normier, A., Bacri, C., Allard, P., Gunawan, H., Hendrasto, M., Surono, and Tsanev, V., 2015, First measurement of the volcanic gas output from Anak Krakatau, Indonesia: Journal of Volcanology and Geothermal Research, v. 302, p. 237–241, https://doi.org/10.1016/j.jvolgeores.2015.07.008.

Bluth, G.J.S., Casadevall, T.J., Schnetzler, C.C., Doiron, S.D., Walter, L.S., Krueger, A.J., and Badruddin, M., 1994, Evaluation of sulfur dioxide emissions from explosive volcanism: The 1982–1983 eruptions of Galunggung, Java, Indonesia: Journal of Volcanology and Geothermal Research, v. 63, p. 243–256, https://doi.org/10.1016/0377-0273(94)90077-9.

Carn, S.A., Fioletov, V.E., McLinden, C.A., Li, C., and Krotkov, N.A., 2017, A decade of global volcanic SO_2 emissions measured from space: Scientific Reports, v. 7, 44095, https://doi.org/10.1038/srep44095.

Clift, P.D., 2016, A revised budget for Cenozoic sedimentary carbon subduction: Reviews of Geophysics, v. 55, p. 97–125, https://doi.org/10.1002/2016rg000531.

Collins, N.C., Bebout, G.E., Angiboust, S., Agard, P., Scambelluri, M., Crispini, L., and John, T., 2015, Subduction zone metamorphic pathway for deep carbon cycling: II. Evidence from HP/UHP metabasaltic rocks and ophicarbonates: Chemical Geology, v. 412, p. 132–150, https://doi.org/10.1016/j.chemgeo.2015.06.012.

Cook-Kollars, J., Bebout, G.E., Collins, N.C., Angiboust, S., and Agard, P., 2014, Subduction zone metamorphic pathway for deep carbon cycling: I. Evidence from HP/UHP metasedimentary rocks, Italian Alps: Chemical Geology, v. 386, p. 31–48, https://doi.org/10.1016/j.chemgeo.2014.07.013.

Dean, S.M., McNeill, L.C., Henstock, T.J., Bull, J.M., Gulick, S.P., Austin, J.A., Bangs, N.L., Djajadihardja, Y.S., and Permana, H., 2010, Contrasting décollement and prism properties over the Sumatra 2004–2005 earthquake rupture boundary: Science, v. 329, p. 207–210, https://doi.org/10.1126/science.1189373.

Deegan, F.M., Troll, V.R., Freda, C., Misiti, V., Chadwick, J.P., McLeod, C.L., and Davidson, J.P., 2010, Magma-carbonate interaction processes and associated CO_2 release at Merapi volcano, Indonesia: Insights from experimental petrology: Journal of Petrology, v. 51, p. 1027–1051, https://doi.org/10.1093/petrology/egq010.

de Leeuw, G.A.M., Hilton, D.R., Fischer, T.P., and Walker, J.A., 2007, The He-CO_2 isotope and relative abundance characteristics of geothermal fluids in El Salvador and Honduras: New constraints on volatile mass balance of the Central American Volcanic Arc: Earth and Planetary Science Letters, v. 258, p. 132–146, https://doi.org/10.1016/j.epsl.2007.03.028.

Elliott, T., Plank, T., Zindler, A., White, W., and Bourdon, B., 1997, Element transport from slab to volcanic front at the Mariana arc: Journal of Geophysical Research, v. 102, p. 14,991–15,019, https://doi.org/10.1029/97JB00788.

Füri, E., Hilton, D.R., Tryon, M.D., Brown, K.M., McMurtry, G.M., Brückmann, W., and Wheat, C.G., 2010, Carbon release from submarine seeps at the Costa Rica fore arc: Implications for the volatile cycle at the Central America convergent margin: Geochemistry Geophysics Geosystems, v. 11, Q04S21, https://doi.org/10.1029/2009GC002810.

Hilton, D.R., Fischer, T.P., and Marty, B., 2002, Noble gases and volatile recycling at subduction zones, *in* Porcelli, D., et al.. eds., Noble Gases in Geochemistry and Cosmochemistry: Reviews in Mineralogy and Geochemistry, v. 47, p. 319–370, https://doi.org/10.1515/9781501509056-011.

Jicha, B.R., Singer, B.S., Brophy, J.G., Fournelle, J.H., Johnson, C.M., Beard, B.L., Lapen, T.J., and Mahlen, N.J., 2004, Variable impact of the subducted slab on Aleutian island arc magma sources: Evidence from Sr, Nd, Pb, and Hf isotopes and trace element abundances: Journal of Petrology, v. 45, p. 1845–1875, https://doi.org/10.1093/petrology/egh036.

Kopp, H., Flueh, E.R., Petersen, C.J., Weinrebe, W., Wittwer, A., and Meramex Scientists, 2006, The Java margin revisited: Evidence for subduction erosion off Java: Earth and Planetary Science Letters, v. 242, p. 130–142, https://doi.org/10.1016/j.epsl.2005.11.036.

Li, L., and Bebout, G.E., 2005, Carbon and nitrogen geochemistry of sediments in the Central American convergent margin: Insights regarding subduction input fluxes, diagenesis, and paleoproductivity: Journal of Geophysical Research, v. 110, B11202, https://doi.org/10.1029/2004JB003276.

Marschall, H.R., and Schumacher, J.C., 2012, Arc magmas sourced from mélange diapirs in subduction zones: Nature Geoscience, v. 5, p. 862–867, https://doi.org/10.1038/ngeo1634.

Mason, E., Edmonds, M., and Turchyn, A.V., 2017, Remobilization of crustal carbon may dominate volcanic arc emissions: Science, v. 357, p. 290–294, https://doi.org/10.1126/science.aan5049.

McNeill, L.C., and Henstock, T.J., 2014, Forearc structure and morphology along the Sumatra-Andaman subduction zone: Tectonics, v. 33, p. 112–134, https://doi.org/10.1002/2012TC003264.

McNeill, L.C., et al., 2017, Understanding Himalayan erosion and the significance of the Nicobar Fan: Earth and Planetary Science Letters, v. 475, p. 134–142, https://doi.org/10.1016/j.epsl.2017.07.019.

Nho, E.-Y., Le Cloarec, M.-F., Ardouin, B., and Tjetjep, W.S., 1996, Source strength assessment of volcanic trace elements emitted from the Indonesian arc: Journal of Volcanology and Geothermal Research, v. 74, p. 121–129, https://doi.org/10.1016/S0377-0273(96)00051-0.

Pfeffer, M.A., 2007, The relative influences of volcanic and anthropogenic emissions on air pollution in Indonesia as studied with a regional atmospheric chemistry and climate model: Max Planck Institute for Meteorology Report on Earth System Science 46, 119 p.

Plank, T., and Langmuir, C.H., 1998, The chemical composition of subducting sediment and its consequences for the crust and mantle: Chemical Geology, v. 145, p. 325–394, https://doi.org/10.1016/S0009-2541(97)00150-2.

Sano, Y., and Marty, B., 1995, Origin of carbon in fumarolic gas from island arcs: Chemical Geology, v. 119, p. 265–274, https://doi.org/10.1016/0009-2541(94)00097-R.

Shipboard Scientific Party, 1974, Site 211, *in* von der Borch, C.C, et al., eds., Initial Reports of the Deep Sea Drilling Project, Volume 22: Washington, D.C., U.S. Government Printing Office, p. 13–36, https://doi.org/10.2973/dsdp.proc.22.102.1974.

Shipboard Scientific Party, 1990, Site 765, *in* Ludden, J.N., et al., Proceedings of the Ocean Drilling Program, Initial Reports, Volume 123: College Station, Texas, Ocean Drilling Program, p. 63–267, https://doi.org/10.2973/odp.proc.ir.123.104.1990.

Troll, V.R., Hilton, D.R., Jolis, E.M., Chadwick, J.P., Blythe, L.S., Deegan, F.M., Schwarzkopf, L.M., and Zimmer, M., 2012, Crustal CO_2 liberation during the 2006 eruption and earthquake events at Merapi volcano, Indonesia: Geophysical Research Letters, v. 39, L11302, https://doi.org/10.1029/2012GL051307.

Varekamp, J.C., Kreulen, R., Poorter, R.P.E., and Van Bergen, M.J., 1992, Carbon sources in arc volcanism, with implications for the carbon cycle: Terra Nova, v. 4, p. 363–373, https://doi.org/10.1111/j.1365-3121.1992.tb00825.x.

Wilson, M.E.J., 2002, Cenozoic carbonates in Southeast Asia: Implications for equatorial carbonate development: Sedimentary Geology, v. 147, p. 295–428, https://doi.org/10.1016/S0037-0738(01)00228-7.

Printed in USA

Chapter 3, in full, is a reprint of the material as it appears in *Geology*: House, B.M., Bebout, G.E., Hilton, D.R., 2019. Carbon cycling at the Sunda margin, Indonesia: a regional study with global implications. Geology 47, 483–486. The dissertation author was the primary investigator and author of this paper.

Chapter 3 Appendix

1. Detailed methods

1.1 Sediment analyses

Sediment samples were obtained from archived DSDP, ODP, and piston cores from the Lamont-Doherty Earth Observatory (LDEO) core archive. Samples were dried at 50 °C, and sediment aliquots for Total Organic C (TOC) analysis were acidified using 1 N HCl for at least 12 hours or until effervescence ceased. Following acidification, samples were centrifuged and washed 3x with DI water and re-dried before homogenization in an agate mortar and pestle. Approximately 100 mg was combusted with Cu/CuO_x in an evacuated quartz tube at 910 °C overnight. Resulting CO_2 was purified and collected on a gas line. Sample aliquots for carbonate analysis were acidified with 100% phosphoric acid at 70 °C in a Finnigan Gas Bench CO_2 handling system. For all samples, CO_2 was quantified using manometry, and all isotope measurements were conducted on a Finnigan MAT 252 mass spectrometer operated in dual inlet mode. All $\delta^{13}C$ values are reported relative to VPDB C isotope standard. For measurements of C isotopic composition of carbonate within Altered Oceanic Crust (AOC), we used a microdrill to obtain samples of the carbonate veins and breccia matrix. These samples were then analyzed in an identical fashion to sedimentary C.

1.2 Sediment and unit thicknesses

Archived 3.5 kHz single channel seismic lines from the Lamont-Doherty Earth Observatory (LDEO) collection were used to determine overall sediment thickness and the thicknesses of geochemically distinct units outboard of the Sunda margin. Archived profiles from the following cruise tracks were used:

RC 1107

RC 1402

RC 1403

V 1909

V 2009

V 2410

V 2819

V 2901

V 3503

V 3616

Seafloor, basement, and unit boundary picks, made using the GeoMap App program for these profiles, were augmented with additional constraints from more recent published multichannel lines(Kopp and Kukowski, 2003; Lüschen et al., 2011; Kopp et al., 2006; Planert et al., 2010; Kopp, 2013; Kopp et al., 2009; McNeill et al., 2016; Dean et al., 2010). Geochemical unit boundaries (Nicobar Fan, terrigenous trenchfill, pelagic material, and calcareous turbidites) were defined by picks following the seismic interpretations in the Initial Report volumes of the appropriate DSDP/ODP sites and subsequent seismic studies. The terrigenous trenchfill unit is defined by reflectors that converge moving away from the trench, and the top of the Nicobar Fan was inferred to coincide with the base of this unit as reported elsewhere(Dean et al., 2010). The base of the Nicobar Fan lacks clear seismic reflectors, and as such, we assumed a uniform thickness of 200 m for the underlying pelagic unit (which is intermediate between results from DSDP 211 and IODP 1480) rather than using dubious seismic picks to constrain the thickness of the Nicobar Fan unit(Expedition 22 Scientific Party, 1974; McNeill et al., 2017). The lower extent of the unit of calcareous turbidites from the Exmouth

Plateau/Australian margin is defined by a distinct set of reflectors(Ludden and Gradstein, 1990), and since this unit is uppermost at Sites 261 and 765 where it is sampled, we infer that overlying sediment is likely to be quantitatively minimal throughout the margin. Therefore, constraining this unit's thickness – as well as that of the underlying pelagic sediments – was straightforward. The lack of a clear seismic boundary between the calcareous turbidite unit and the trenchfill wedge in seismic profiles along the southeastern portion of the margin led us to assign a thickness for the trenfill unit by subtracting the thickness of the other units outboard of the trench from the overall sediment thickness at the trench. This approach, while necessary to constrain overall sediment flux to the trench, is unlikely to substantially affect our estimates of subducting C because the entirety of the trench wedge appears to be off-scraped through much of the margin. While the Roo Rise is inducing localized subduction erosion along eastern Java, sediment cover on the rise is minimal, and sediments trenchward of it are difficult to interpret from seismic profiles. Indeed, East Java stands out as a region of low sediment cover (Figures S2 and 3), so while our estimates consider the subduction of the thin sediment veneer currently present, significantly more sediment and sedimentary C may have subducted in the recent past when the Roo Rise first impinged upon the margin.

When seismic velocity profiles reported two-way travel time rather than sediment thickness and sediment velocity models were not available, sediment velocities of 2 and 2.5 km/s were used to construct upper and lower bounds on sediment thickness respectively. While these velocities are greater than those determined for surficial sediments(Dean et al., 2010), they encapsulate the range of velocities expected for the deeper sediments that escape off-scraping at the deformation front along much of the margin. Therefore, these seismic velocity bounds are reasonable for estimating subducting C flux and may slightly overestimate the amount of

sediment – and hence C – present at the trench. A total of ~8000 picks were made, and additional unit and sediment thickness constraints from DSDP Sites 211, 213, 260, 261, ODP Site 765, and IODP Site 1480 were also incorporated. Using these data, surfaces were constructed to model unit and overall sediment thicknesses and extrapolate these from core sites to the trench. With these models and results from sediment analyses, we estimated the amount and types of C within the sediment column at the trench.

Plate motion models of the Indoaustralian plate relative to the stable Sunda core from McNeill et al. (2014) were used to convert C content into a C flux to the trench, calculated at points along the trench that correspond to the MORVEL plate boundary between the Indoaustralian and Sunda plates(Argus et al., 2011). Single and multichannel seismic profiles as well as velocity models across the trench (Lüschen et al., 2011; Kopp et al., 2009, 2006; Kopp and Kukowski, 2003; Kopp et al., 2001; Planert et al., 2010) were used to estimate the fraction of the overall sediment and C flux bypassing the deformation front and subducting past ~20 km, the maximum seismically-resolved depth. These estimates were combined with those from McNeill et al. (2014) to generate upper and lower bounds on the sediment subducting past the deformation front. This range in possible subduction channel thickness leads to the range in estimates for subducted C amount.

The thickness of Nicobar Fan deposits is difficult to establish definitively from seismic profiles as the bottom of the fan is not marked by any prominent reflector (e.g. DSDP 211 site report). This led us to define a uniform thickness of the underlying hemi-pelagic to pelagic unit (Unit 3 of Dean et al., 2010) of 200 m, consistent with interpretations from DSDP 211 and shipboard sedimentological evidence from IODP U1480. In contrast, the base of the calcareous turbidites from the Australian margin/Exmouth Plateau is marked by a series of

clear reflectors (DSDP 261, ODP 765 site reports), and while they infill bathymetric relief, where they do not fully account for total sediment thickness, they are underlain by a Cretaceous pelagic to hemipelagic unit. Sediment thickness off East Java is minimal as this region represents the impingement of the Roo Rise on the deformation front.

2. Comparing shipboard and shore-based organic C analyses

The tendency for disagreement between shipboard estimates of Total Organic C (TOC) made during coring expeditions and shorebased measurements has been previously documented (Olivarez Lyle and Lyle, 2006). Shipboard TOC is typically not measured directly but calculated as the difference between total C (measured by combustion elemental analysis) and carbonate C (measured by coulometry). However, this method can lead to substantial uncertainty. Several hundred replicate shipboard analyses conducted on a total of 5 samples from IODP Site 1480 give one-sigma uncertainties of 35 to 180%(McNeill et al., 2017). Furthermore, comparing the pool of shipboard data from DSDP Sites 211, 260, 261, 262, and ODP Site 765(Ludden and Gradstein, 1990; Plank and Ludden, 1992; Bode, 1974; Pimm, 1974) with our shore-based TOC results shows that we are unable to reproduce the highest shipboard TOC values and that the distribution of values is substantially different between ship- and shore-based analyses (Figure S1). While these analyses were not conducted on precisely the same samples, the large number of data compiled suggests a true difference between the two distributions, and indeed a one-tailed non-parametric unpaired t-test reveals that the mean of shipboard data is higher than that of shorebased data at a statistically significant level ($p < 10^{-10}$). This suggests that using shipboard data is likely to overestimate of the abundance of organic C and to overemphasize its importance in C-

cycling. Future studies of organic C cycling at convergent margins should therefore rely on shorebased reanalysis of shipboard samples.

3. Caveats in determining provenance of arc CO_2

The three endmember mixing model of Sano and Marty (1995) has been used previously to establish the provenance of volcanic and hydrothermal CO_2 released along Indonesia (Halldórsson et al., 2013; Fig. S3). In this model, the $\delta^{13}C$ and $CO_2/^3He$ composition of volcano or hydrothermal CO_2 are used to resolve contributions from subducting carbonate and organic C as well as C from the mantle wedge. While the $\delta^{13}C$ of organic C can be readily measured, the meaning of a $CO_2/^3He$ ratio for organic C is less clear. A value of $\sim10^{14}$ is typically used for this ratio, as well as for the $CO_2/^3He$ ratio of sedimentary carbonate (termed "limestone" in previous work; Marty et al., 1989; Hilton et al., 2002; Halldórsson et al., 2013). Because typical volcanic gases have a $CO_2/^3He$ ratio of $\sim10^{10}$, CO_2 provenance results from this mixing model are relatively insensitive to changes in these endmember compositions. However, the $CO_2/^3He$ composition of the mantle wedge endmember is also required for the mixing model, and small changes in this value can have enormous effects on inferred CO_2 provenance.

A value of $\sim2.7 \times 10^9$ is usually used for the $CO_2/^3He$ ratio of the mantle wedge(Hilton et al., 2002), but this value reflects the average of measurements of volatile concentrations in mid-ocean ridge glasses, which show significant variation (e.g. Graham, 2002), an may not represent the composition of the extensively flux-melted mantle wedge. When the $CO_2/^3He$ ratio in volcanic gas samples is relatively low, the precise $CO_2/^3He$ ratio used for the mantle wedge endmember becomes very important. Using data from Varekamp et al. (1992) for Sirung volcano, even a 25% deviation from 2.7×10^9 leads to a ~10-fold change in the ratio of

CO_2 from carbonate to CO_2 from organic C inferred from the mixing model. Therefore, results from this mixing model should be used with caution, which is why we consider the simple balance between the $\delta^{13}C$ of the subducting sedimentary C and the $\delta^{13}C$ of volcanic CO_2 to infer that an additional ^{13}C rich reservoir external to sedimentary C is likely contributing to the arc-released CO_2.

Other insight, potentially significant, regarding the mixing of C from multiple sources comes from study of deeply subducted metasedimentary rocks containing varying proportions of C in carbonate (oxidized) and C in carbonaceous matter (reduced). Cook-Kollars et al. (2014) and Kraft et al. (2017; manuscript in preparation) demonstrated extensive C isotope exchange between C in the two reservoirs as they attempted equilibration particularly at the higher temperatures represented in the suite. This exchange is most significant in pelite-carbonate mixed rocks inferred by Cook-Kollars et al. (2014) to have experienced the most C loss by decarbonation. Both the oxidized and the reduced C reservoirs were shifted in $\delta^{13}C$ from their starting/oceanic compositions toward the "mantle value" of -6‰. Depending on the relative abundances of carbonaceous matter and carbonate in the samples, the reduced C is shifted from $\delta^{13}C$ values near -22‰ for low-grade rocks in which there is little re-equilibration with carbonate near 0‰ to values as high as -8‰ at the higher grades (also see Kraft et al., 2017). Carbonate C is shifted from $\delta^{13}C$ values near +1‰ for low-grade rocks in which there is little re-equilibration with carbonate near 0‰ to values as low as -6‰ at the higher grades. Shift in the C isotope compositions of the two subducting C reservoirs would obviously have implications for the application of the three-component mixing model of Sano and Marty (1995). Yet unknown are the relative degrees of C release from each of these

reservoirs during the devolatilization and partial melting beneath arcs at the subduction interface and in subducting slabs.

References

Argus, D.F., Gordon, R.G., and DeMets, C., 2011, Geologically current motion of 56 plates relative to the no-net-rotation reference frame: Geochemistry, Geophysics, Geosystems, v. 12, doi: 10.1029/2011GC003751.

Bode, G., 1974, Proceedings of the Deep Sea Drilling Project, *in* Heirtzler, J., Veevers, J., and Robinson, P. eds., Proceedings of the Deep Sea Drilling Project Volume 27, p. 499–502, doi: doi:10.2973/dsdp.proc.27.1974.

Cook-Kollars, J., Bebout, G.E., Collins, N.C., Angiboust, S., and Agard, P., 2014, Subduction Zone Metamorphic Pathway for Deep Carbon Cycling: I. Evidence from HP/UHP Metasedimentary Rocks, Italian Alps: Chemical Geology, doi: 10.1016/j.chemgeo.2014.07.013.

Dean, S.M., McNeill, L.C., Henstock, T.J., Bull, J.M., Gulick, S.P., Austin, J.A., Bangs, N.L., Djajadihardja, Y.S., and Permana, H., 2010, Contrasting decollement and prism propoerties over the Sumatra 2004-2005 earthquake rupture boundary: Science, v. 329, p. 207–210.

Expedition 22 Scientific Party, 1974, Site 211: Deep Sea Drilling Project Site Reports, v. 22, p. 13–36.

Graham, D.W., 2002, Noble gas isotope geochemistry of Mid-Ocean Ridge and Ocean Island Basalts: Characterization of mantl source reservoirs, *in* Porcell, D., Ballentine, C.J., and Wieler, R. eds., Noble Gases in Geochemistry and Cosmochemistry, Washington, DC, Mineralogical Society of America, p. 247–318.

Halldórsson, S.A., Hilton, D.R., Troll, V.R., and Fischer, T.P., 2013, Resolving volatile sources along the western Sunda arc, Indonesia: Chemical Geology, v. 339, p. 263–282, doi: 10.1016/j.chemgeo.2012.09.042.

Hilton, D.R., Fischer, T.P., and Marty, B., 2002, Noble gases and volatile recycling at subduction zones, *in* Porcelli, D., Ballentine, C.J., and Wieler, R. eds., Noble gases in geochemistry and cosmochemistry, v. 47.

Kopp, H., 2013, Invited review paper: The control of subduction zone structural complexity and geometry on margin segmentation and seismicity: Tectonophysics, v. 589, p. 1–16, doi: 10.1016/j.tecto.2012.12.037.

Kopp, H., Fleuh, E.R., Klaeschen, D., Bialas, J., and Reichert, C., 2001, Crustal structure of the central Sunda margin at the onset of oblique subduction: Geophysical Journal International, v. 147, p. 449–474.

Kopp, H., Flueh, E., Petersen, C., Weinrebe, W., Wittwer, A., and Scientists, M., 2006, The

Java margin revisited: Evidence for subduction erosion off Java: Earth and Planetary Science Letters, v. 242, p. 130–142, doi: 10.1016/j.epsl.2005.11.036.

Kopp, H., Hindle, D., Klaeschen, D., Oncken, O., Reichert, C., and Scholl, D., 2009, Anatomy of the western Java plate interface from depth-migrated seismic images: Earth and Planetary Science Letters, v. 288, p. 399–407, doi: 10.1016/j.epsl.2009.09.043.

Kopp, H., and Kukowski, N., 2003, Backstop geometry and accretionary mechanics of the Sunda margin: Tectonics, v. 22, p. n/a-n/a, doi: 10.1029/2002tc001420.

Kraft, K., and Bebout, G.E., 2017, Fate of subducting organic carbon: evidence from HP/UHP metamorphic suites, *in* AGU Fall meeting, New Orleans.

Ludden, J.N., and Gradstein, F.M., 1990, Site 765: Proceedings of the Ocean Drilling Program Initial Reports, v. 123, p. 63–267.

Lüschen, E., Müller, C., Kopp, H., Engels, M., Lutz, R., Planert, L., Shulgin, A., and Djajadihardja, Y.S., 2011, Structure, evolution and tectonic activity of the eastern Sunda forearc, Indonesia, from marine seismic investigations: Tectonophysics, v. 508, p. 6–21, doi: 10.1016/j.tecto.2010.06.008.

Marty, B., Jambon, A., and Sano, Y., 1989, Helium isotopes and CO_2 in volcanic gases of Japan: Chemical Geology, v. 76, p. 25–40.

McNeill, L.C., Dugan, B., and Petronotis, K., 2016, Expedition 362 Scientific Prospectus: International Ocean Discovery Program.

McNeill, L.C., Dugan, B., Petronotis, K.E., and Expedition 362 Scientists, 2017, Site U1480, *in* Proceedings of the International Ocean Discovery Program, v. 362, doi: 10.14379/iodp.proc.362.103.2017.

Olivarez Lyle, A., and Lyle, M.W., 2006, Missing organic carbon in Eocene marine sediments: Is metabolism the biological feedback that maintains end-member climates? Paleoceanography, v. 21, doi: 10.1029/2005pa001230.

Pimm, A.C., 1974, Sedimentology and history of the northeastern Indian Ocean from Late Cretaceous to Recent: Initial reports of the Deep Sea Drilling Project, v. 22, p. 717–803, http://hdl.handle.net/10.2973/dsdp.proc.22.139.1974.

Planert, L., Kopp, H., Lueschen, E., Mueller, C., Flueh, E.R., Shulgin, A., Djajadihardja, Y., and Krabbenhoeft, A., 2010, Lower plate structure and upper plate deformational segmentation at the Sunda-Banda arc transition, Indonesia: Journal of Geophysical Research, v. 115, doi: 10.1029/2009jb006713.

Plank, T., and Ludden, J.N., 1992, Geochemistry of sediments in the Argo Abyssal Plain at

site 765: A continental margin reference section for sediment related recycling in subduction zones: Proceedings of the Ocean Drilling Program, Scientific Results, v. 123, p. 167–189.

Sano, Y., and Marty, B., 1995, Origin of carbon in fumarolic gas from island arcs: Chemical Geology, v. 119, p. 265–274.

Varekamp, J.C., Kreulen, R., Poorter, R.P.E., and van Bergen, M.J., 1992, Carbon sources in arc volcanism, with implications for the carbon cycle: Terra Nova, v. 4.

Supplemental figures

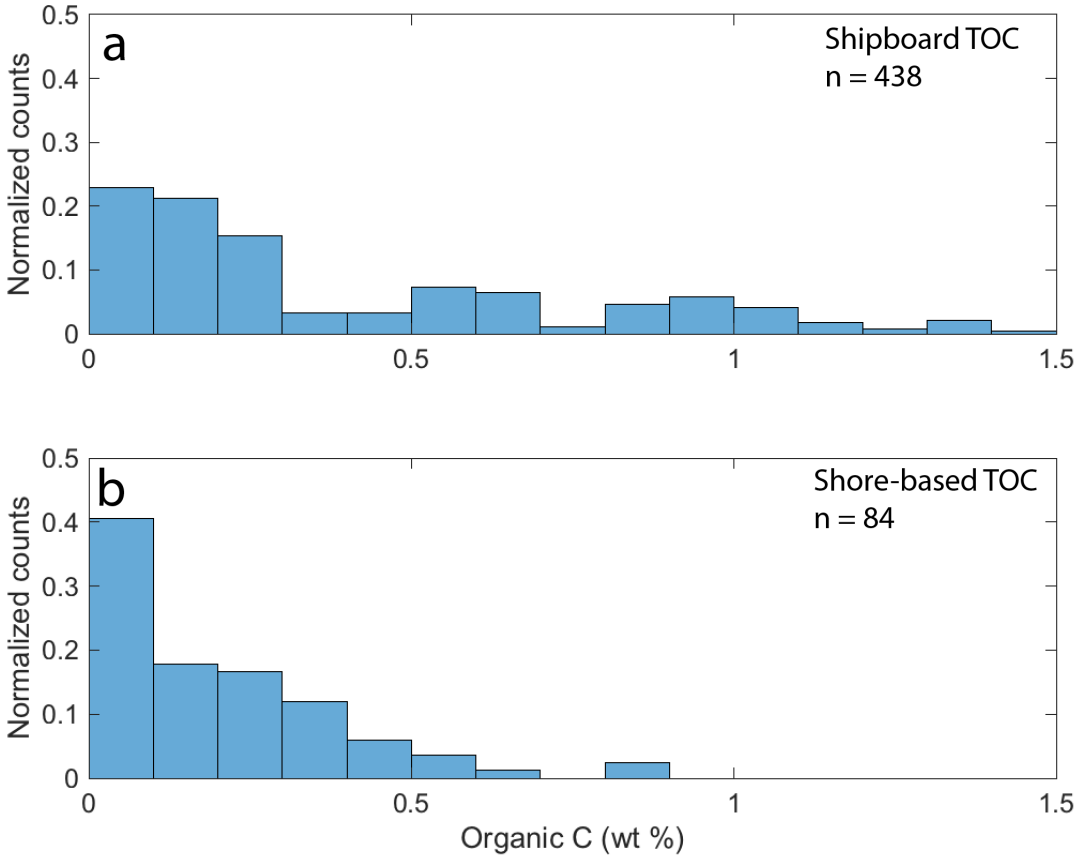

Figure 3.S1. Histograms showing distributions of shipboard (a) and shore-based (b) Total Organic Carbon (TOC) measurements generated for this study from DSDP 211, 213, 260, 261, 262 and ODP 765. Normalized counts represent the fraction of samples that fall within a given range of TOC values. Shipboard values are calculated as the difference between total C, measured by combustion elemental analysis, and carbonate C, measured by coulometry whereas shore-based values represent direct measurements of TOC following acidification to remove carbonate phases. While we were not able to analyze splits of precisely the same samples used for shipboard analyses, the pronounced difference in the distributions and number of data points strongly suggests that shipboard analyses overestimate the true TOC. Indeed, we were unable to reproduce TOC values over 0.86 wt% C with shore-based analyses.

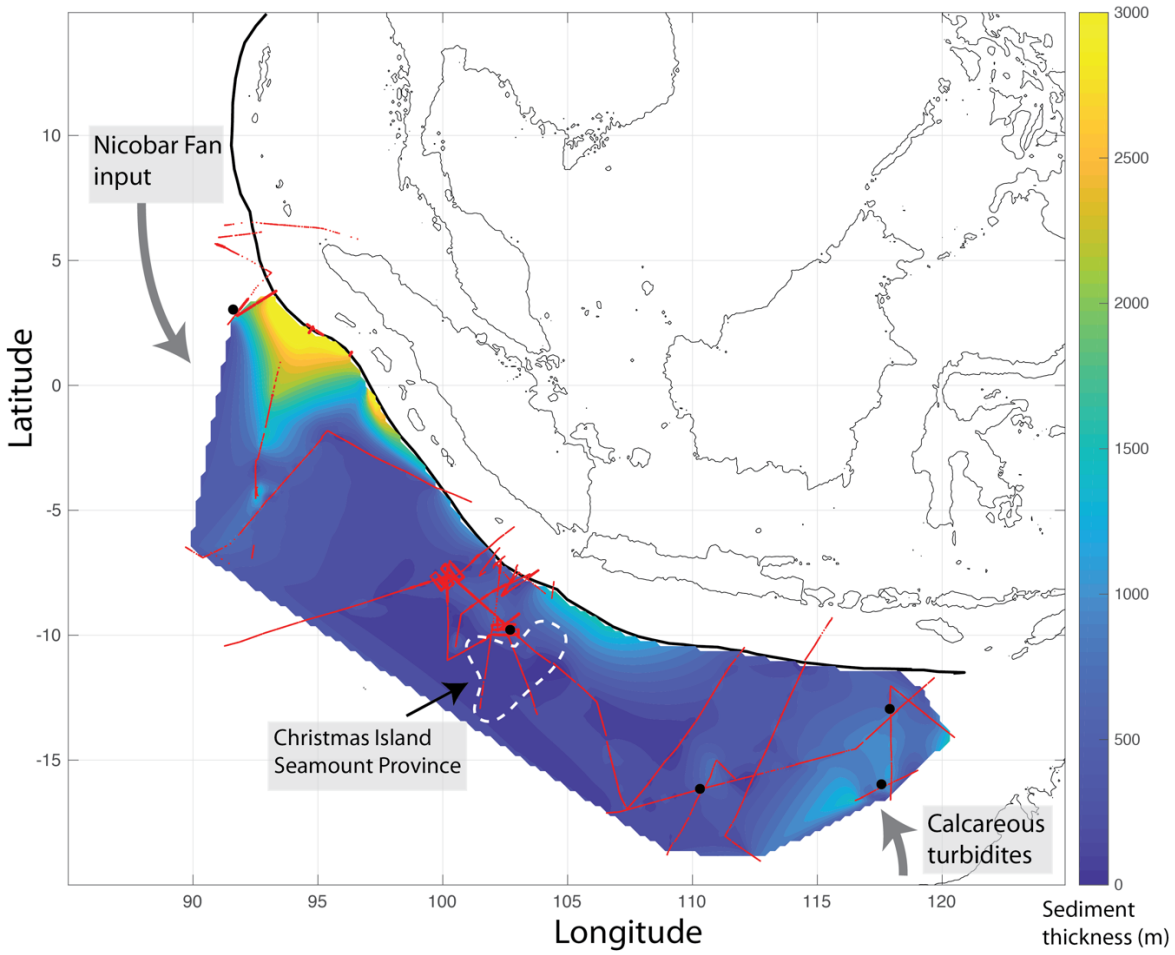

Figure 3.S2. Model of overall sediment thickness model based on seismic picks (small red points) of seafloor and acoustic basement depth. Points outside the interpolated region represent regions where acoustic basement was not reliably imaged and picks could only be made to constrain unit thicknesses. Black points indicate the DSDP/ODP/IODP sites that are labeled in Fig. 1. The color scale saturates at 3 km sediment thickness. Material from the Nicobar Fan (to the northwest) and calcareous turbidites from the Australian margin (to the southeast) are separated by the Christmas Island Seamount Province.

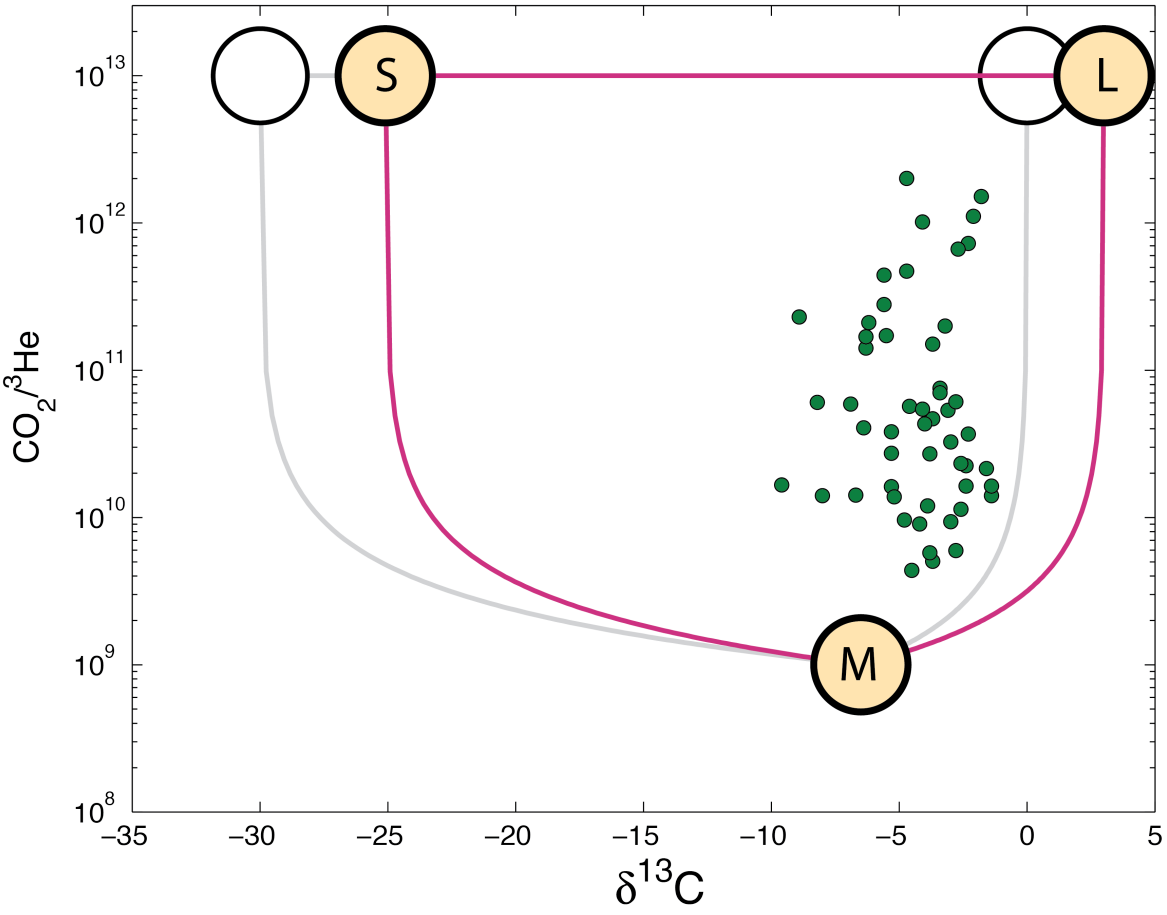

Figure 3.S3. The three-endmember mixing model of Sano and Marty (1995) can be used to infer the provenance of volcanic CO_2 from measured $\delta^{13}C$ and $CO_2/^3He$ ratios in volcanic gases (Halldórsson et al., 2013; Varekamp et al., 1992). Solving a set of linear equations for the fraction of CO_2 from sedimentary carbonate (termed "limestone" in the original reference and represented the L endmember), organic C (termed "sedimentary" and denoted by S), and mantle wedge (M) sources. Open, unshaded circles represent global averages for the S and L endmembers that were used previously, and yellow circles represent values measured for this study. The $CO_2/^3He$ ratio of the mantle wedge is inferred from measurements of Mid-Ocean Ridge Basalt (MORB), but whether these values accurately represent the mantle wedge composition is unclear. For some volcanoes, the results of this mixing model are exceedingly sensitive to the exact $CO_2/^3He$ used.

CHAPTER 4

Looking far from the source: Nicobar Fan records multi-phase ecological change on Indian subcontinent from the late Miocene to Pleistocene

Brian House[1], Kevin Pickering[2], Richard Norris[1]

[1]Scripps Institution of Oceanography 8675 Naga Lane La Jolla CA 92037

[2]Department of Earth Sciences, University College London, WC1E 6BT

Corresponding author: Brian M. House (bhouse@ucsd.edu)

Abstract

Modern grasslands on the Indian subcontinent, in North and South America, and in East Africa appear expanded widely during the late Miocene to earliest Pleistocene, likely in response to increasing aridity. Grasses utilizing the C_4 photosynthetic pathway are more tolerant of high temperatures and dry conditions, and because they induce less C isotope fractionation than plants using the C_3 pathway, the expansion of C_4 grasslands can be traced through the $\delta^{13}C$ of organic matter in soils and terrigenous marine sediments. We present a high-resolution record of the elemental and isotopic composition of bulk organic matter in Nicobar submarine Fan material from IODP Site 1480, off northern Sumatra, to elucidate the timing and pace of the C_3–C_4 plant transition within the ~1.5 x 10^6 km^2 catchment of the Ganges/Brahmaputra river system, which has and continues to supply vast amounts of Himalaya-derived sediments to the Bay of Bengal. Using a multi-proxy approach to correct for the effects of marine organic matter and account for major sources of uncertainty, two distinct phases of C_4 expansion are apparent: a gradual shift from ~8.5–7 Ma and a step-wise transition at ~2.5 Ma. These intervals coincide well with periods of Indian and East Asian monsoon intensification, as well as the expansion of northern hemisphere glaciation at ~2.7 Ma. While our results suggest both periods produced a similar magnitude of grassland expansion, the ~2.5 Ma transition occurred four times as quickly, suggesting that the extent of northern hemisphere glaciation had a particularly profound effect on the climate of South Asia.

1 Introduction

Shortly after 10 Ma, a major paleoclimate transition appears to have led to a synchronous expansion of grasslands on the Indian subcontinent as well as in East Africa and North and South America (e.g. Cerling et al., 1997). Evidence for this comes from the C isotopic composition of tooth enamel (Cerling et al., 1997), paleosol carbonate nodules (Freeman and Colarusso, 2001; Karp et al., 2018; Quade et al., 1989), terrestrial sediments (Vögeli et al., 2017), and terrigenous marine sediments (Freeman and Colarusso, 2001). All of these record a shift toward higher $\delta^{13}C$ values that suggest an expansion of vascular plants utilizing the more complex C_4 photosynthetic pathway rather than the C_3 pathway of woody plants, marine photosynthesizers, and many grasses. Because the C_4 pathway produces a lower degree of C isotopic fractionation, the increase in $\delta^{13}C$ of both bulk organic matter and terrestrial biomarkers is interpreted to reflect the expansion of C_4 plants, most of which are grasses, and are better suited than C_3 plants to warmer and more arid conditions. Therefore, the expansion of C_4 plant coverage in the late Miocene is interpreted to be an indication of increasing aridity (e.g. An et al., 2005; Cerling et al., 1997; Freeman and Colarusso, 2001; Karp et al., 2018; Khim et al., 2019; Morley, 2018; Quade et al., 1989; Scheiter et al., 2012; Zhisheng et al., 2001).

The Indian subcontinent has received particular attention regarding the C_3–C_4 transition in part because of the relationship between grassland expansion and the intensity of monsoon wind patterns. The extreme elevation of the Himalaya and the Tibetan Plateau alters the local atmospheric heat budget to the extent that the predominant winds in summer are southwesterly and transport humid air masses from the Arabian Sea and Bay of Bengal, generating intense rains at the Himalaya front while atmospheric circulation reverses in the winter, causing far more arid conditions. The intensity of monsoonal winds also influences marine productivity, for example by strengthening upwelling off the Arabian Peninsula during the summer monsoon (Kroon et al.,

1991; Prell et al., 1992). Other metrics of monsoon wind intensity like aeolian dust flux and hence magnetic susceptibility, also reflect the intensity of monsoonal circulation patterns, both on the Indian subcontinent as well as in Central and East Asia (Rea et al., 1998).

Terrestrial records of monsoon intensity tend to reflect local conditions, which means they may not be representative of continental-scale ecological shifts (Freeman and Colarusso, 2001; Vögeli et al., 2017). Much of the evidence for grassland expansion has come from the Siwalik paleosols in northern Pakistan and India (Figure 1), and despite efforts to sample throughout the spatial extent of this unit (e.g. Freeman and Colarusso, 2001; Vögeli et al., 2017), extrapolating regional results from a single geologic unit can introduce substantial uncertainty. Other efforts to understand long-term climate evolution on the Indian subcontinent have focused on the elemental and isotopic composition of organic matter in terrigenous sediments of the Indus and Bengal Fans (Freeman and Colarusso, 2001; Karp et al., 2018; Khim et al., 2019; Krishna et al., 2013), which integrate ecological signals over entire river catchments, and can therefore better capture large-scale environmental changes without as much interference from spatially heterogenous variability.

The Bengal-Nicobar Fan system (Figure 1), is uniquely suited to address climate evolution in south Asia because of the largely continuous record of terrigenous sediment flux to the deep sea since 10 Ma and the extremely high sediment accumulation rates (McNeill et al., 2017a, 2017b). We present a high-resolution record of total organic carbon (TOC), the isotopic composition of TOC (expressed in delta units as $\delta^{13}C_{TOC}$), total nitrogen (TN), and major and trace-element composition for a subset of samples from IODP Site 1480, which cored ~1200 m of the Nicobar Fan (McNeill et al., 2017b). Fan deposits at Site 1480 are largely the result sediment gravity flows of Himalaya-sourced material transported via the Ganges/Brahmaputra

river system and therefore incorporate terrigenous organic matter from the combined catchment area. Organic C content was generally < 0.5 wt% and within the range expected for open-ocean sediments, although some horizons contained visible (up to ~1 cm) pieces of organic matter, and the vascular structure of plant fragments was commonly visible in smear slides (McNeill et al., 2017b). Although Site 1480 is ~2000 km from the sediment source in the Bay of Bengal, sediment accumulation rates were commonly higher than at IODP sites on the distal Bengal Fan (Figure 1). Additionally, the Site 1480 record more fully captures sedimentation history since 10 Ma with fewer hiatuses, intervals of bit advancement without coring, and better age constraints than many of the Bengal and Indus Fan sites (sites 1450, 1451, 1455, and 1457; (Expedition 354 Scientists, 2016a, 2016b, 2016c; Khim et al., 2019). Site 1480 therefore presented a unique opportunity to capture a largely continuous record of ecologic and paleoclimate conditions during the past ~10 Ma on the Indian subcontinent.

Our datasets give a unique view of the timing and pace of the C_3–C_4 transition. While previous studies relied primarily on compound-specific isotope analyses of terrestrial plant biomarkers (e.g. Freeman and Colarusso, 2001), we instead relied upon simple analytical techniques to generate a large dataset capable of revealing more subtle temporal trends and reduce the reliance on single measurements. Because the incorporation of organic matter from the marine ecosystem can mimic a shift toward terrestrial C_4 plant cover (Galy et al., 2008), we employed a multi-proxy approach that used mixing models based on $\delta^{13}C$, TOC/TN, and Br/TOC ratios to correct for contributions from marine organic matter. Uncertainty in endmember composition can dramatically limit the utility of mixing models, so we used Monte Carlo simulations using randomly perturbed endmember compositions to place reasonable

quantitative bounds on the contributions of C_4 plants to the terrigenous organic matter through time.

The Site 1480 record suggests two major phases of landscape evolution, a gradual shift between ~8.5–7 Ma, coincident with intensification of Indian summer monsoons (Kroon et al., 1991; Prell et al., 1992), and a second abrupt shift at ~2.5 Ma. Both phases align reasonably well with periods of inferred monsoon intensification, although we infer significant spatial heterogeneity in the timing of the C_3–C_4 transition. While the two phases of C_4 expansion appear similar in magnitude, the second transition was approximately four times faster, suggesting rapid aridification effectively contemporaneous with the major expansion of northern hemisphere ice sheets (Zachos et al., 2001). Our records are consistent with monsoon intensification as a major source of climate change on the Indian subcontinent during the past 10 Myr and give an unusually complete and detailed view of climate evolution on the Indian subcontinent.

2 Methods

2.1 Analytical procedures

The sample set consists of the residues from shipboard carbonate/TOC analyses and additional dedicated samples that were vacuum sealed and kept frozen. The carbonate residues were freeze-dried for 12 hours while additional dedicated samples were dried at 50 C until consecutive weighings indicated no further mass loss. All samples were ground in an agate mortar and pestle. Approximately 10 mg of sediment was weighed into Ag capsules and decarbonated for TOC and $\delta^{13}C$ analyses using aqueous SO_2 (~6–8% by mass). Following dropwise addition of SO_2 solution, the samples were heated to 60 C until dry, at which point

additional SO_2 solution was added. We continued this procedure until a total of ~1.5 mL had been added, representing at least a 100-fold stoichiometric excess of $SO_2/CaCO_3$. Pre-combusted glass pipettes and polypropylene 96 well plates were used to minimize any possibility of contamination with organic matter during decarbonation. The Ag capsules containing the decarbonated sediment samples were sealed in Sn capsules to aid in final conversion of organic C to CO_2 in the elemental analyzer combustion column. Separate sample aliquots of ~40 mg were not subjected to decarbonation and were sealed in Sn capsules for TN analyses.

Prior results (Kennedy et al., 2005) suggested that aqueous SO_2 incompletely decarbonates samples for TOC analysis, but the amount of SO_2 solution added provided a less than stoichiometric ratio of $SO_2/CaCO_3$, so decarbonation should not proceed to completion. Because our samples were likely to contain trace detrital dolomite ($(Ca,Mg)CO_3$), which is resistant to decarbonation, and would artificially raise $\delta^{13}C_{TOC}$ measurements, we tested the decarbonation procedure on a powdered dolomite sample from the Scripps Institution of Oceanography collections. The C content of the untreated dolomite implies an Mg concentration of ~33%, and decarbonation of ~1 mg, far in excess of the amount in our samples, resulted in C concentrations below the analytical detection limit of <10 ug C. We are therefore confident that the decarbonation procedure we used quantitatively removes even unrealistically large amounts of $(Ca,Mg)CO_3$ and is suitable for analyzing TOC and $\delta^{13}C_{TOC}$. Decarbonation with aqueous SO_2 has the added benefit of producing Ca/Mg salts that are not hygroscopic, obviating the need for the rigorous drying procedures required after decarbonation by HCl fumigation.

Analyses of TOC, $\delta^{13}C$ of TOC ($\delta^{13}C_{TOC}$) and TN were conducted at the University of California Santa Cruz Stable Isotope Laboratory. Carbon and nitrogen isotopic and elemental composition was determined by Dumas combustion using a Carlo Erba 1108 elemental analyzer

coupled to a ThermoFinnigan Delta Plus XP isotope ratio mass spectrometer. Analytical precision of internationally calibrated in-house standards is better than 0.2 ‰ for $\delta^{13}C$, which means the $\delta^{13}C$ error bars in Figures 2–5 and 7 would be smaller than the data points. Sample isotopic values are corrected for size, drift and source stretching effects. Carbon and nitrogen elemental composition is estimated based on standards of known elemental composition. Precision of these known compounds is determined to better than 1%, again indicating error bars smaller than data points in Figure 2. All $\delta^{13}C$ values are reported relative to the VPDB C isotope standard.

Major and trace element analyses were conducted on sample aliquots that were washed three times with DI water and centrifuged between washings to ensure seawater-derived bromide would not interfere with sediment Br measurements. The sample aliquots were analyzed by Instrumental Neutron Activation Analysis (INAA) at the Oregon State University Radiation Center. Precision is estimated at ~0.7 ppm at the 2-sigma level for Br, and we also used this value as the detection limit.

1.2 Data treatment

Data were first filtered to address the tendency for samples with low TOC to give low $\delta^{13}C$ values (Figure 2). We established a cutoff of 0.125 wt% C and an overall $\delta^{13}C$ threshold of -28.5 to discard unreliable data while still retaining as many as possible. For Br analyses, we discarded data points for samples with over 400 ppm Cl, which may indicate incomplete removal of seawater Br based on co-variation between Br and Cl for samples with high Cl content. Furthermore, data for which Br concentrations were less than 2 standard deviations from the detection limit were also discarded. These procedures led to 302 measurements of TOC,

$\delta^{13}C_{TOC}$, and TN as well as 28 measurements of Br (and other major/trace elements) that we deemed to be reliable (Tables S1; S2). Only these data were used in further analyses.

Two separate three-endmember mixing models were used to correct the $\delta^{13}C_{TOC}$ values for the influence of marine organic matter and place quantitative bounds on the fraction of organic matter from C_4 plants. Both consisted of a system of linear equations of the form $\boldsymbol{A}f = \boldsymbol{b}$ where $\boldsymbol{A} = \begin{bmatrix} c_{C4}^1 & c_{C3}^1 & c_M^1 \\ c_{C4}^2 & c_{C3}^2 & c_M^2 \\ 1 & 1 & 1 \end{bmatrix}$ with c_j^i equal to the composition of endmember *j* with respect to the elemental/isotopic system *i*, $f = \begin{bmatrix} f_{C4} \\ f_{C3} \\ f_M \end{bmatrix}$ with the fractional contribution f_j from endmember *j*, and $\boldsymbol{b} = \begin{bmatrix} d_1^1 & d_2^1 & \dots \\ d_1^2 & d_2^2 & \dots \\ 1 & 1 & \dots \end{bmatrix}$ with data d_k^i for the measured value of data point *k* with respect to the elemental/isotopic system *i*. A total of 10^4 Monte Carlo simulations were run in which endmember compositions were allowed to vary randomly within normal distributions centered on literature values (e.g. Galy et al., 2008) and/or extreme measured values and with standard deviations encompassing a range of reasonable values (Table 1). The distributions of $\frac{f_{C4}}{f_{C4}+f_{C3}}$ (the fraction of terrigenous organic matter from C_4 plants) are represented in Figure 6, and we generated smoothed curves fitting the data based on the distributions produced by bootstrap resampling of the data and the smoothed values at ages corresponding to those of the data.

3 Results and discussion

3.1 Correcting for marine organic matter inputs

Bulk TOC $\delta^{13}C$ data have been shown to correlate well with C isotope ratios of terrestrial plant biomarkers in Bengal Fan sediments (Freeman and Colarusso, 2001; Valier Galy et al., 2008), suggesting that records of $\delta^{13}C_{TOC}$ (Figure 3) present a reasonable first-order view of landscape evolution and therefore paleoclimate conditions. However, because the $\delta^{13}C$ values of marine organic matter are typically intermediate between those of vascular C_3 and C_4 plant material, a shift toward higher $\delta^{13}C$ values could reflect greater marine organic matter input rather than a true shift toward greater C_4 plant abundance. Attempting to remove the marine organic matter $\delta^{13}C$ signal using only $\delta^{13}C_{TOC}$ results in a mathematically underdetermined system in which the mixing contributions of three endmembers (C_3, C_4 and marine organic matter) cannot be uniquely defined. Because correcting for inputs from marine organic matter offers the potential to place at least quantitative bounds on the C_3/C_4 contributions, we applied a multi-proxy approach to remove or at least minimize the influence of marine organic matter contributions.

The ratio of TOC to total nitrogen (TN) is a widely used metric for the fraction of marine organic matter in marine sediments because while terrestrial organic C preserved in sediment is often N-poor, largely proteinaceous marine organic matter tends to have much greater TN, leading to high TOC/TN ratios for terrigenous and low TOC/TN ratios for marine organic matter (Figure 4). However, TOC/TN as an organic matter provenance proxy suffers from several problems, most notably the potential for inorganic N (primarily as NH_4^+) to adsorb to clay minerals, producing artificially low TOC/TN values (Müller, 1977), and a wide range in particularly the vascular C_3 and C_4 endmember compositions. We relied on three approaches to minimize these effects: (1) a large dataset of $\delta^{13}C$ and TOC/TN (Figure 4), which reduces the importance of individual data that might be influenced by NH_4^+ adsorption, (2) the additional

less common proxy of Br/TOC, and (3) Monte Carlo simulations to reduce the influence of uncertainty in endmember compositions. We chose to use $\delta^{13}C_{TOC}$ as the main proxy for C_3–C_4 transition because the ease of the analytical procedure facilitates the gathering of a large dataset, and indeed, the $\delta^{13}C_{TOC}$ show substantial scatter during nearly all time intervals, which suggests that restricted datasets using a more analytically challenging technique such as compound-specific isotope measurements may not fully reflect the range of isotopic variability.

While we used TOC/TN, measured on all samples, as the main proxy for organic matter provenance, we also analyzed the trace element composition of a subset of samples (Figures 3, 5; Table S2) to use Br/TOC as an additional proxy. The Br/TOC ratio in sediments with predominantly marine organic matter has been shown to far exceed that of sediments rich in terrigenous organic matter (Mayer et al., 2007), presumably due to the incorporation of Br-rich secondary metabolites produced by marine organisms (Gribble, 1998). Therefore, as Mayer et al. (2007) found, we expect a graph of $\delta^{13}C_{TOC}$ and Br/TOC to be consistent with mixing between three extreme endmember compositions, and Figure 5 confirms this, though the marine endmember we infer is not as Br-rich as that identified in continental shelf cores. Because Br/TOC has received less attention than TOC/TN as a tracer of organic matter provenance, we allowed a wide range of endmember compositions (Table 1). Inverting the $\delta^{13}C$ and Br/TOC data produced very similar inferred C_4 plant abundances as we obtained using the $\delta^{13}C$ and TOC/TN system (Figure 6), providing evidence for the utility of Br/TOC ratios in constraining marine organic matter contributions. While the two methods of correcting for marine organic matter contributions are not entirely independent (both rely on $\delta^{13}C_{TOC}$ data), the agreement between the results they produce is encouraging and suggests that our reconstructions of C_4 plant abundance are on robust footing.

We also used Monte Carlo simulations to attempt to limit or at least estimate the uncertainty in C_4 abundance arising from the possible range of endmember composition. Figure 6 shows the results using 10^4 endmember compositions for $\delta^{13}C_{TOC}$, TOC/TN, and Br/TOC taken randomly from normal distributions centered at our estimated endmember compositions and with generous standard deviations (Table 1). Because of the scatter in the resulting data, we used a bootstrapping technique to produce a range and best estimate of a smoothed curve of inferred C_4 landcover (Figure 6). This curve, with confidence intervals predicted through bootstrapping, and (though less clearly) the original inferred C_4 coverage data, show a similar overall trend as the raw $\delta^{13}C_{TOC}$ uncorrected for marine organic matter inputs. Our approach shows the promise of combining voluminous analytically facile data, multiple proxies, and uncertainty estimation techniques to more quantitatively describe geochemical processes.

3.2 Climatic implications of inferred C_3–C_4 transition

Our data suggest that the expansion of C_4 plant coverage in the South Asia was punctuated by two distinct periods of C_4 expansion rather than a consistent gradual shift or single episode as inferred from many terrestrial and marine records (Freeman and Colarusso, 2001; Gupta and Thomas, 2003; Prell et al., 1992; Quade et al., 1989). We infer an initial increase in $\delta^{13}C_{TOC}$ and C_4 fraction between ~8.5–7 Ma, which is earlier than some records suggest (e.g. Bengal Fan $\delta^{13}C$ in Freeman and Colarusso, 2001, $\delta^{13}C$ in Quade et al., 1989) but effectively contemporaneous with inferred intensification of summer monsoon wind patterns from the Indian subcontinent ($\delta^{18}O$ from Quade et al. 1989), Indian Ocean (Gupta and Thomas, 2003; Kroon et al., 1991; Prell et al., 1992), and IODP Site 1143 in the South China Sea (Chen et al. 2003), as well as a shift toward C_4 plant dominance in North America, South America, and East

Africa (Cerling et al., 1997). The second period of C_4 expansion is much more rapid, occurring at ~2.5 Ma, and is not recorded in other records from either terrestrial paleosols or marine sediments from the Bengal Fan. However, sediment records from the Bengal Fan may not fully reflect terrestrial conditions during this time interval as the Nicobar Fan appears to have received a substantially greater fraction of Himalayan-sourced sediment, so Site 1480 data may be more reliable for dating the onset of C_4 expansion (McNeill et al., 2017a). Finally, analyses of terrestrial samples from specific formations like the well-studied Siwalik paleosols (Figure 1) may fail to capture the true onset of a transition that is spatially heterogenous on a continental scale.

The strength of monsoon winds is a fundamental control on aridity on the Indian subcontinent where southwesterly winds in summer bring moisture-laden air from the Arabian Sea and northern Indian Ocean inland. Humid air masses deflected upward by the Himalaya cause extreme precipitation compared to the dry winters in which northeasterly winds provide little moisture. The separate East Asian monsoon system, while not as pronounced, leads to similar intra-annual precipitation patterns in Central and East Asia. Even if intensification of either monsoon system does not lead to an overall increase in annual precipitation, an increase in summer precipitation, particularly with the tradeoff of greater winter aridity, will tend to favor C_4 grasses (An et al., 2005), which are better suited to warm and dry conditions due to their ability to limit water loss during stomatal gas exchange. Additionally, because the C_4 pathway involves a CO_2 preconcentration mechanism, low atmospheric pCO_2/pO_2 will also favor C_4 grassland expansion.

Freeman and Colarusso (2001) proposed a “vegetation mosaic” model in which environments like river floodplains are likely to be particularly sensitive to monsoon intensity as

episodic inundation and desiccation would become more dramatic, favoring C_4 grasses that could resist drier winters. Monsoon intensification is likely, they argue, to have a lesser effect on more mountainous areas not susceptible to periodic flooding, and these environments are therefore more likely to retain C_3 plants. The modern landscape (Galy et al., 2008) and analyses of Siwalik paleosol organic matter from the eastern front of the Himalaya (Vögeli et al., 2017) support spatial heterogeneity in aridity and C_3 and C_4 plant coverage, as do palynological studies (Morley, 2018) and model results based on orographic effects (Boos and Kuang, 2010). Part of the benefit of using terrigenous seafloor sediments such as those of the Nicobar Fan at Site 1480 is that they spatially integrate heterogenous signals over a wide enough area that localized changes are less likely to alter continental-scale interpretations. For example, the ~8.5–7 Ma episode of C_3–C_4 landscape evolution apparent in our data predates the $\delta^{13}C$ shift in carbonate nodules, but is essentially synchronous with the carbonate nodule $\delta^{18}O$ shift as well as a shift in $\delta^{13}C$ of herbivore tooth enamel (Cerling et al., 1997) that would seem to require a prior or concurrent change in the plant community. This suggests that the apparent ~1 Myr. lag between $\delta^{18}O$ and $\delta^{13}C$ increase in carbonate nodules from the northwest of the Siwalik group (Quade et al., 1989) likely represents a local rather than a more widespread feature. Carbon isotope analyses of long-chain n-alkanes also suggest an earlier onset for C_4 expansion in parts of the Siwalik, underscoring the geographic variability of this formation (Freeman and Colarusso, 2001; Vögeli et al., 2017). The scatter in both our $\delta^{13}C$ and inferred C_4 coverage supports the hypothesis that the entire C_3–C_4 transition from ~9 to 2 Ma was patchy, and that local terrestrial samples may not convey the full spatial variability in ecosystem composition (Vögeli et al., 2017).

Additionally, when compared with many studies using organic matter from sands/sandstones, the C_3–C_4 data presented in this study (from muds/mudstones) records a higher-resolution climate-change, including monsoonal, signal. This is because the former data represents a more time-averaged response (as sandy sediments can be stored in "temporary sinks" in river and coastal systems, e.g., in the Himalaya for the order of 100 kyr or longer (Blöthe and Korup, 2013; Gaudemer and Metivier, 1999) such that millennial lag times complicate correlating sedimentary archives to climate forcing. Sandy beds tend to be much thicker than muds/mudstones and represent relatively infrequent events compared with muddy sediment delivery to ocean basins. Sand samples depend on the availability of coarser-grained sediment, especially compared with the abundance of finer-grained sediment. Even though plant material will also be stored with sands, to be incorporated into (relatively infrequent) sediment gravity-flows, plant material is continuously being supplied to ocean basins via several higher-frequency processes such as hyperpycnal flows, nepheloid layers and other plumes of suspended finer-grained sediment from river and coastal environments. Thus, understanding any climate change signals is best achieved through analyzing muddy sediments from the distal parts of the Nicobar Fan. It is, therefore, perhaps unsurprising that many studies of sandy sediments tend not to show clear monsoonal changes.

Uplift of the Himalaya and Tibet has long been proposed as a mechanism for monsoon intensification either through direct orographic effects or by influencing global temperature and latitudinal temperature gradients (e.g. Molnar et al., 1993; Raymo and Ruddiman, 1992). However, because increases in marine productivity and C_4 landcover begin globally ~9 Ma (Cerling et al., 1997; Kroon et al., 1991; Prell et al., 1992), the hypothesis that this initial shift only reflects increasing monsoon intensity on the Indian subcontinent seems problematic.

Furthermore, while phased uplift of the Himalaya and Tibetan Plateau has been proposed as an explanation for monsoon intensification ~8 Ma (Zhisheng et al., 2001), the mechanism by which the Himalaya and Tibet enhance monsoon wind patterns may be more complicated than first thought and may depend on the precise location of uplift (Boos and Kuang, 2010). In a study of sediment provenance in the Indus Fan since ~17 Ma, Clift et al., (2019) conclude that "no simple links can be made between erosion and the development of the South Asian Monsoon, implying a largely tectonic control on Lesser Himalayan unroofing," in accordance with the results of sediment provenance studies by McNeill et al. (2017a).

Records of monsoon intensity in Central Asia, largely from loess plateaux and marine sediments suggest that aridification progressed northward through time as the East Asian monsoon intensified, increasing the difference in seasonal precipitation (Shen et al., 2018, 2017). Our results are also consistent with a general northward expansion of C_4 grasslands during this time: we detect the shift beginning ~8.5 Ma, which coincides with the change in Indian Ocean monsoon intensity inferred from western Siwalik carbonate nodules (Freeman and Colarusso, 2001), but predates the increase in $\delta^{13}C$ of Quade et al. (1989). We propose that increasing seasonality or long-term aridification, regardless of the underlying cause, affected the paleoecology of the lowlands of the Ganges catchment first, and C_4 grasslands then spread to the north, finally reaching the location of the northwest Siwalik sampled by Quade et al. (1989) after ~1.5 Myr. Northward C_4 grassland expansion also appears consistent with the shift toward higher $\delta^{13}C$ of mammal tooth enamel – which indicates a dietary shift to more C_4 grasses – shortly after 10 Ma in northern Pakistan but later in China (Arppe et al., 2015). Additionally, the production rate of North Atlantic Deep Water (NADW) appears to have been strongly variable beginning ~10 Ma (Wright et al., 1991), and the associated changes in heat transport could have

substantially altered the global climate, although whether changes in NADW formation rate caused or resulted from climate changes in the late Miocene is unclear.

The alternative explanation from Cerling et al. (1997) that decreasing atmospheric pCO_2 in the late Miocene was a fundamental driver of global climate change is difficult to reconcile with more recent records indicating relatively low and stable pCO_2 lacking pronounced changes from ~10–8 Ma (Knorr et al., 2011; Pagani et al., 2005). However, despite low pCO_2, the Miocene is known to have been warmer than present (e.g. Knorr et al., 2011), and the combination of a warmer climate along with low pCO_2 would be particularly favorable to C_4 grassland expansion. Finally, expansive wildfires have been proposed as either a cause or result of C_4 grassland expansion (Scheiter et al., 2012), and while records of fire frequency have limited temporal resolution, they appear to agree with the increase in C_4 abundance we infer to have started ~8.5 Ma (Karp et al., 2018). The complexity and multitude of explanations for increasing aridity in South and Central Asia makes us hesitant to definitively attribute the ~8.5–7 Ma shift to a single mechanism, but a consensus appears to be building around the primacy of monsoon intensification (e.g. An et al., 2005), which is consistent with our observations.

The second main feature of both the $\delta^{13}C$ data and inferred C_4 coverage is a sharp increase in $\delta^{13}C_{TOC}$ and C_4 fraction between ~2.5 and 2 Ma, effectively coeval with the major expansion of northern hemisphere glaciation (e.g. Raymo et al., 1989). Similar changes have been recorded in the abundance of marine primary producers thought to be particularly responsive to upwelling intensity (Kroon et al., 1991; Prell et al., 1992) as well as magnetic susceptibility and aeolian dust flux from loess and marine sediment deposits (Figure 7; Rea et al., 1998). Many other records showing increasing aridity beginning ~9–7 Ma on the Indian subcontinent rarely indicate an additional transition at ~2.5 Ma (Cerling et al., 1997; Freeman

and Colarusso, 2001; Karp et al., 2018; Quade et al., 1989). North Pacific Site 885/886 dust flux records (Figure 7), which are thought to predominantly reflect aridity in central Asia and East Asian monsoon wind patterns (e.g. Rea et al., 1998), also show a peak at ~2.5 Ma, suggesting that the Site 1480 record may also reflect ecological evolution outside the Indian subcontinent. While the rapidity of the ~2.5 Ma transition in the Site 1480 record could conceivably arise from a sudden change in sediment provenance rather than true C_4 expansion, zircon age spectra from Site 1480 are inconsistent with major sediment provenance shifts (McNeill et al., 2017a). Furthermore, at Site 1480, sediment from the Ganges catchment exceeds that from the Brahmaputra throughout this time period, which would be consistent with the expectation that organic matter from the Ganges would show an earlier and greater shift toward higher $\delta^{13}C$ values (Galy et al., 2008; Vögeli et al., 2017).

The rapidity of the ~2.5 Ma shift toward greater C_4 plant cover is noteworthy compared to the more gradual shift starting ~8.5 Ma. While we infer C_4 coverage increased from ~20 to ~40% between 8.5 and 7 Ma, the shift at ~2.5 Ma is of similar magnitude (~45 to ~65% coverage) but occurs over about 0.5 Myr. Such a dramatic, effectively stepwise change, demands a similarly abrupt cause and coincides with both the end of a particularly substantial increase in monsoon intensity as well as the major expansion of Northern Hemisphere glaciation, which made South and East Asian climates more arid (Shen et al., 2018, 2017). However, while we find an abundant range in both $\delta^{13}C_{TOC}$ and inferred C_4 plant coverage, our estimates of C_4 fraction agree remarkably well with those of An et al. (2001) based on modeling results assuming multiple episodes of Himalayan uplift and records of East Asian summer monsoon intensity, so we cannot discount the possibilities that regional uplift, a global climate shift, and/or

spatially complex landscape evolution conspired to produce the ecological changes apparent in the Site 1480 record.

4 Conclusions

Altogether, the elemental and isotopic composition of organic matter at Site 1480 gives an unusually complete view of major climate shifts throughout South and East Asia since ~10 Ma. What we infer to be an initial expansion of C_4 plant coverage, likely associated with greater aridity and intensifying monsoons ~8.5–7 Ma, coincides with greater abundance of marine primary producers that thrive with increasing monsoon wind intensity as well as a multi-continental shift toward C_4 grassland coverage (e.g. Cerling et al., 1997). A second episode of C_4 expansion at ~2.5 Ma is of similar magnitude but is four times a rapid, implying a sudden climatic alteration contemporaneous with the expansion of Northern Hemisphere glaciation, a major climatic event whose effects are not detected in many other ecological records from south Asia. The wide array and complexity of potential forcing mechanisms makes drawing definitive conclusions about climate drivers difficult; however, the uniquely detailed record of $\delta^{13}C_{TOC}$ from Site 1480 underscores the potential for both local factors (e.g. monsoon intensification) and global (expansion of northern hemisphere glaciation) ones in causing spatially heterogenous landscape evolution.

Acknowledgements

Participation on IODP Expedition and post-expedition analyses were supported by the United States Science Support Program. Dyke Andreasen and Colin Carney of the University of Santa Cruz Stable Isotope Laboratory provided insight into sample preparation and conducted analyses

of organic matter. Sarah Feakins of the University of Southern California provided helpful discussion regarding sample preparation and data interpretation. All members of the Exp. 362 Scientific Party contributed to sample collection and generation of peripheral datasets. Funding support was provided by United States Science Support Program Post Expedition Award GG009393-01 to BMH.

Chapter 4 has been submitted for publication and may appear in *Earth and Planetary Science Letters* as House, B., Pickering, K., and Norris, R. D. 2019. The dissertation author was the primary investigator and author of this paper.

References

An, Z., Huang, Y., Liu, W., Guo, Z., Clemens, S., Li, L., Prell, W., Ning, Y., Cai, Y., Zhou, W., Lin, B., Zhang, Q., Cao, Y., Qiang, X., Chang, H., Wu, Z., 2005. Multiple expansions of C4 plant biomass in East Asia since 7 Ma coupled with strengthened monsoon circulation. Geology 33, 705–708. https://doi.org/10.1130/G21423.1

Arppe, L., Kaakinen, A., Passey, B., Zhang, Z., Fortelius, M., 2015. Small mammal tooth enamel carbon isotope record of C4 grasses in late Neogene China. Glob. Planet. Change 133, 288–297. https://doi.org/10.1016/j.gloplacha.2015.09.003

Blöthe, J.H., Korup, O., 2013. Millennial lag times in the Himalayan sediment routing system. Earth Planet. Sci. Lett. https://doi.org/10.1016/j.epsl.2013.08.044

Boos, W., Kuang, Z., 2010. Dominant control of the South Asian monsoon by orographic insulation versus plateau heating. Nature 463, 218–223. https://doi.org/10.1038/nature08707

Cerling, T., Harris, J., McFadden, B., Leakey, M., Quade, J., Eisenmann, V., Ehleringer, J., 1997. Global vegetation change through the Miocene/Pliocene boundary. Nature 389, 153–158.

Clift, P.D., Zhou, P., Stockli, D.F., Blusztajin, J., 2019. Regional Pliocene exhumation of the Lesser Himalaya in the Indus drainage. Solid Earth 10, 647–661. https://doi.org/10.5194/se-10-647-2019

Expedition 354 Scientists, 2016a. Site U1450. Proc. Int. Ocean Discov. Progr. 354.

Expedition 354 Scientists, 2016b. Site U1451. Proc. Int. Ocean Discov. Progr. 354.

Expedition 354 Scientists, 2016c. Site U1455. Proc. Int. Ocean Discov. Progr. 354.

Freeman, K.H., Colarusso, L.A., 2001. Molecular and isotopic records of C4 grassland expansion in the late Miocene. Geochim. Cosmochim. Acta 65, 1439–1454.

Galy, V, France-Lanord, C., Lartiges, B., 2008. Loading and fate of particulate organic carbon from the Himalaya to the Ganga-Brahmaputra delta. Geochim. Cosmochim. Acta 72, 1767–1787.

Galy, Valier, François, L., France-Lanord, C., Faure, P., Kudrass, H., Palhol, F., Singh, S.K., 2008. C4 plants decline in the Himalayan basin since the Last Glacial Maximum. Quat. Sci. Rev. 27, 1396–1409. https://doi.org/10.1016/j.quascirev.2008.04.005

Gaudemer, Y., Metivier, F., 1999. Stability of output fluxes of large rivers in South and East Asia during the last 2 million years: implications on floodplain processes. Basin Res. https://doi.org/10.1046/j.1365-2117.1999.00101.x

Gribble, G.W., 1998. Naturally Occurring Organohalogen Compounds. Acc. Chem. Res. 31, 141–152. https://doi.org/10.1021/ar9701777

Gupta, A.K., Thomas, E., 2003. Initiation of Northern Hemisphere glaciation and strengthening of the northeast Indian monsoon: Ocean Drilling Program Site 758, eastern equatorial Indian Ocean. Geology 31, 47–50.

Karp, A., Behrensmeyer, A., Freeman, K.H., 2018. Grassland fire ecology has roots in the late Miocene. Proc. Natl. Acad. Sci. 115, 1230–1235.

Kennedy, P., Kennedy, H., Papadimitriou, S., 2005. The effect of acidification on the determination of organic carbon, total nitrogen and their stable isotopic composition in algae and marine sediment. Rapid Commun. Mass Spectrom. 19, 1063–1068.

Khim, B.-K., Lee, J., Ha, S., Park, J., Pandey, D., Clift, P.D., Kulhanek, D., Steinke, S., Griffith, E., Suzuki, K., Xu, Z., IODP Expedition 355 Scientists, 2019. Variations in $\delta^{13}C$ values of sedimentary organic matter since late Miocene time in the Indus Fan (IODP Site 1457) of the eastern Arabian Sea. Geol. Mag. 1–10. https://doi.org/doi:10.1017/S0016756818000870

Knorr, G., Butzin, M., Micheels, A., Lohmann, G., 2011. A warm Miocene climate at low atmospheric CO2 levels. Geophys. Res. Lett. https://doi.org/10.1029/2011GL048873

Krishna, M.S., Naidu, S.A., Subbaiah, C. V, Sarma, V.V.S.S., Reddy, N.P.C., 2013. Distribution and sources of organic matter in surface sediments of the eastern continental margin of India. J. Geophys. Res. Biogeosciences 118, 1484–1494. https://doi.org/10.1002/2013jg002424

Kroon, D., Steens, T., Troelstra, S., 1991. Onset of Monsoonal related upwelling in the western Arabian Sea as revealed by planktonic foraminifers. Proc. Ocean Drill. Progr. Sci. Results 117.

Mayer, L.M., Schick, L.L., Allison, M.A., Ruttenberg, K.C., Bentley, S.J., 2007. Marine vs. terrigenous organic matter in Louisiana coastal sediments: The uses of bromine:organic carbon ratios. Mar. Chem. 107, 244–254. https://doi.org/10.1016/j.marchem.2007.07.007

McNeill, L.C., Dugan, B., Backman, J., Pickering, K.T., Pouderoux, H.F.A., Henstock, T.J., Petronotis, K.E., Carter, A., Chemale, F., Milliken, K.L., Kutterolf, S., Mukoyoshi, H., Chen, W., Kachovich, S., Mitchison, F.L., Bourlange, S., Colson, T.A., Frederik, M.C.G., Guèrin, G., Hamahashi, M., House, B.M., Hüpers, A., Jeppson, T.N., Kenigsberg, A.R., Kuranaga, M., Nair, N., Owari, S., Shan, Y., Song, I., Torres, M.E., Vannucchi, P., Vrolijk, P.J., Yang, T., Zhao, X., Thomas, E., 2017a. Understanding Himalayan erosion and the significance of the Nicobar Fan. Earth Planet. Sci. Lett. 475. https://doi.org/10.1016/j.epsl.2017.07.019

McNeill, L.C., Dugan, B., Petronotis, K.E., Expedition 362 Scientists, 2017b. Site U1480, in: Proceedings of the International Ocean Discovery Program.

https://doi.org/10.14379/iodp.proc.362.103.2017

Molnar, P., England, P., Martinod, J., 1993. Mantle dynamics, uplift of the Tibetan Plateau, and the Indian Monsoon. Rev. Mineral. Geochemistry 31, 357–396.

Morley, R.J., 2018. Assembly and division of the South and South-East Asian flora in relation to tectonics and climate change. J. Trop. Ecol. 34, 209–234. https://doi.org/10.1017/S0266467418000202

Müller, P.J., 1977. C/N ratios in Pacific deep-sea sediments: Effects of inorganic ammonium and organic nitrogen compounds sorbed by clays. Geochim. Cosmochim. Acta 41, 765–776.

Pagani, M., Zachos, J., Freeman, K.H., Tipple, B., Bohaty, S., 2005. Marked decline in atmospheric carbon dioxide concentrations during the Paleogene. Science (80-.). 309, 600–603. https://doi.org/10.1126/science.1110063

Prell, W.L., Murray, D., Clemens, S., Anderson, D., 1992. Evolution and variability of the Indian Ocean summer monsoon: Evidence from the western Arabian sea drilling program, in: Duncan, R., Rea, D., Kidd, R., von Rad, U., Weissel, J. (Eds.), Synthesis of Results from Scientific Drilling in the Indian Ocean. American Geophysical Union, pp. 447–469.

Quade, J., Cerling, T., Bowman, J., 1989. Development of Asian monsoon revealed by marked ecological shift during the latest Miocene in northern Pakistan. Nature 342, 163–166.

Raymo, M.E., Ruddiman, W.F., 1992. Tectonic forcing of late Cenozoic climate. Nature 359, 117–122.

Raymo, M.E., Ruddiman, W.F., Backman, J., Clement, B.M., Martinson, D.G., 1989. Late Pliocene variation in northern hemisphere ice sheets and North Atlantic deep water circulation. Paleoceanography 4, 413–446.

Rea, D.K., Snoeckx, H., Joseph, L.H., Arbor, A., 1998. Late Cenozoic eolian deposition in the North Pacific: Asian drying, Tibetan uplift, and cooling of the northern hemisphere. Paleoceanography 13, 215–224.

Scheiter, S., Higgins, S., Osborne, C., Bradshaw, C., Lunt, D., Ripley, B., Taylor, L., Beerling, D., 2012. Fire and fire-adapted vegetation promoted C4 expansion in the late Miocene. New Phytol. 195, 653–666. https://doi.org/10.1111/j.1469-8137.2012.04202.x

Shen, X., Wan, S., Colin, C., Tada, R., Shi, X., Pei, W., Tan, Y., Jiang, X., Li, A., 2018. Increased seasonality and aridity drove the C4 plant expansion in Central Asia since the Miocene–Pliocene boundary. Earth Planet. Sci. Lett. 502, 74–83. https://doi.org/10.1016/j.epsl.2018.08.056

Shen, X., Wan, S., France-Lanord, C., Clift, P.D., Tada, R., Révillon, S., Shi, X., Zhao, D., Liu, Y., Yin, X., Song, Z., Li, A., 2017. History of Asian eolian input to the Sea of Japan since

15 Ma: Links to Tibetan uplift or global cooling? Earth Planet. Sci. Lett. https://doi.org/10.1016/j.epsl.2017.06.053

Vögeli, N., Najman, Y., van der Beek, P., Huyghe, P., Wynn, P.M., Govin, G., van der Veen, I., Sachse, D., 2017. Lateral variations in vegetation in the Himalaya since the Miocene and implications for climate evolution. Earth Planet. Sci. Lett. 471, 1–9. https://doi.org/10.1016/j.epsl.2017.04.037

Wright, J.D., Miller, K.G., Fairbanks, R.G., 1991. Evolution of modern deepwater circulation: evidence from the late Miocene Southern Ocean. Paleoceanography 6, 275–290.

Zachos, J., Pagani, M., Sloan, L., Thomas, E., Billups, K., 2001. Trends, rhythyms, and aberrations in global climate 65 Ma to present. Science (80). 292, 686–693.

Zhisheng, A., Kutzbach, J.E., Prell, W.L., Porter, S.C., 2001. Evolution of Asian monsoons and phased uplift of the Himalaya-Tibetan plateau since Late Miocene times. Nature 411.

Figures

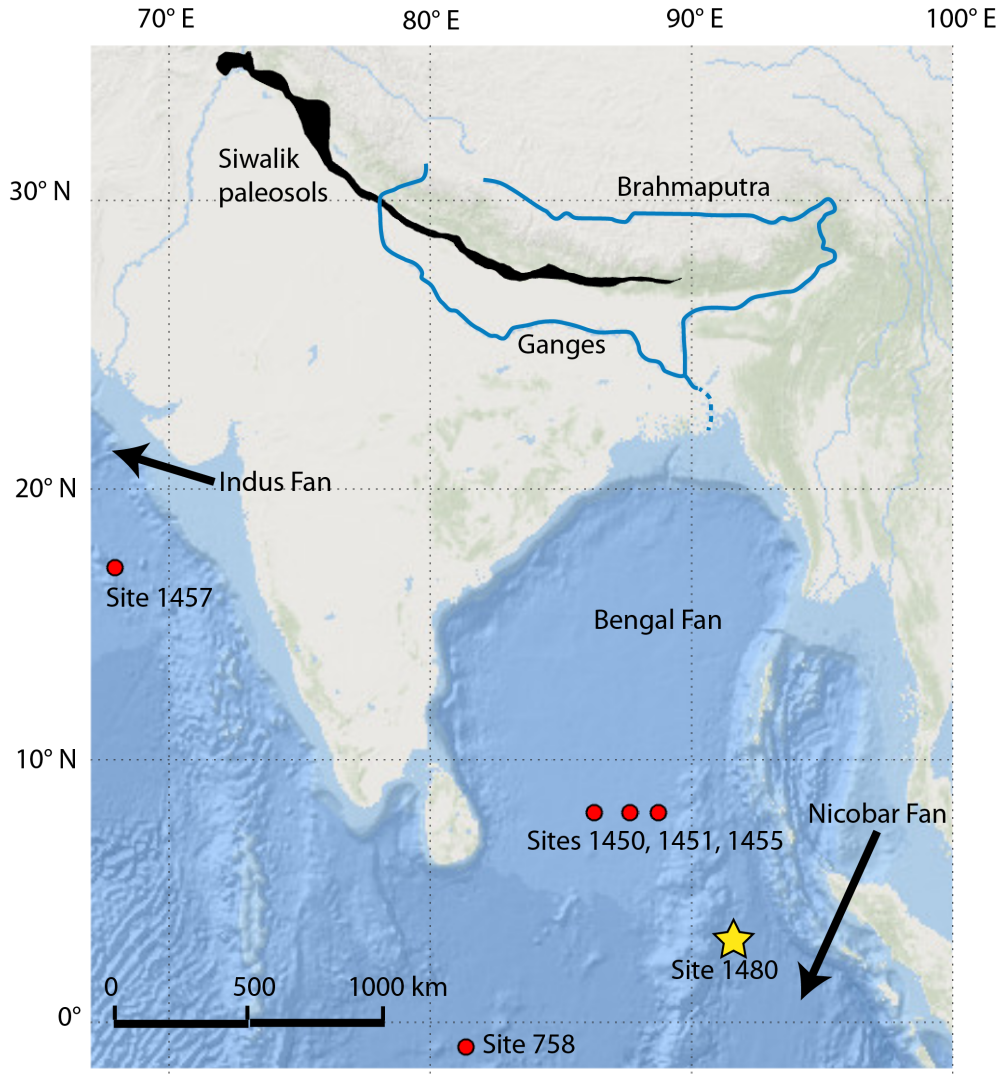

Figure 4.1. Overview map showing the locations of Site 1480 on the Nicobar Fan and sites where other related studies have been conducted. The Ganges and Brahmaputra Rivers transport most of the terrigenous sediment in the Nicobar and Bengal Fans (we have denoted the general position of the river system near the Bay of Bengal as the river delta is complex). Paleosols of the Siwalik group are the most studied terrestrial deposits that provide evidence for the C_3-C_4 shift, though no shift appears to have occurred at the eastern extent of the group, and it captures conditions at the foot of the Himalaya, not farther into the lowlands where C_4 grasses may be expected to first appear (Freeman and Colarusso, 2001).

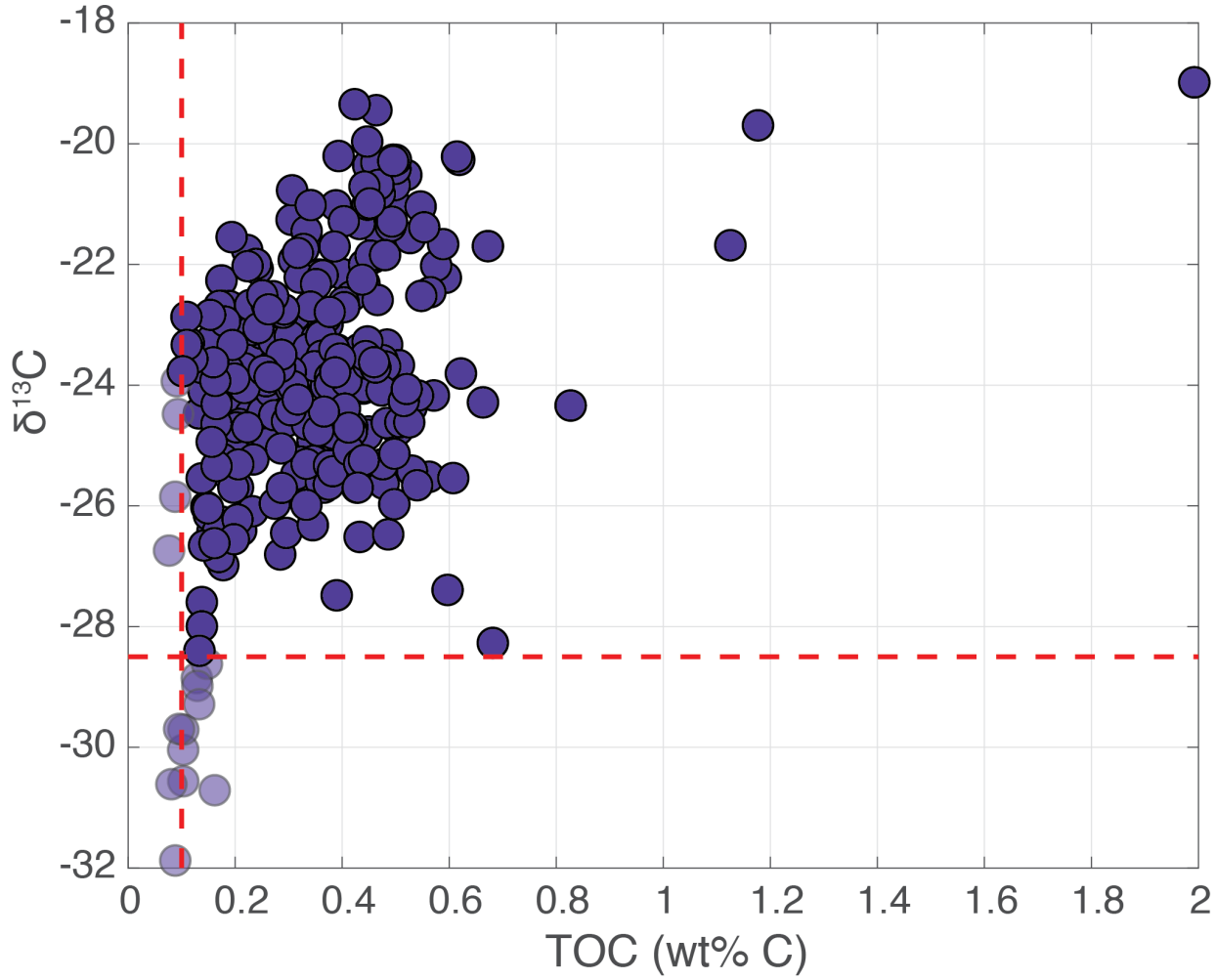

Figure 4.2. Measured $\delta^{13}C_{TOC}$ as a function of TOC in Site 1480 sediments shows a substantial decrease in $\delta^{13}C_{TOC}$ in samples with low TOC. The positions of the red lines indicate the cutoffs used to filter data (Section 3.1); points to the left and below these lines were not used for further analyses.

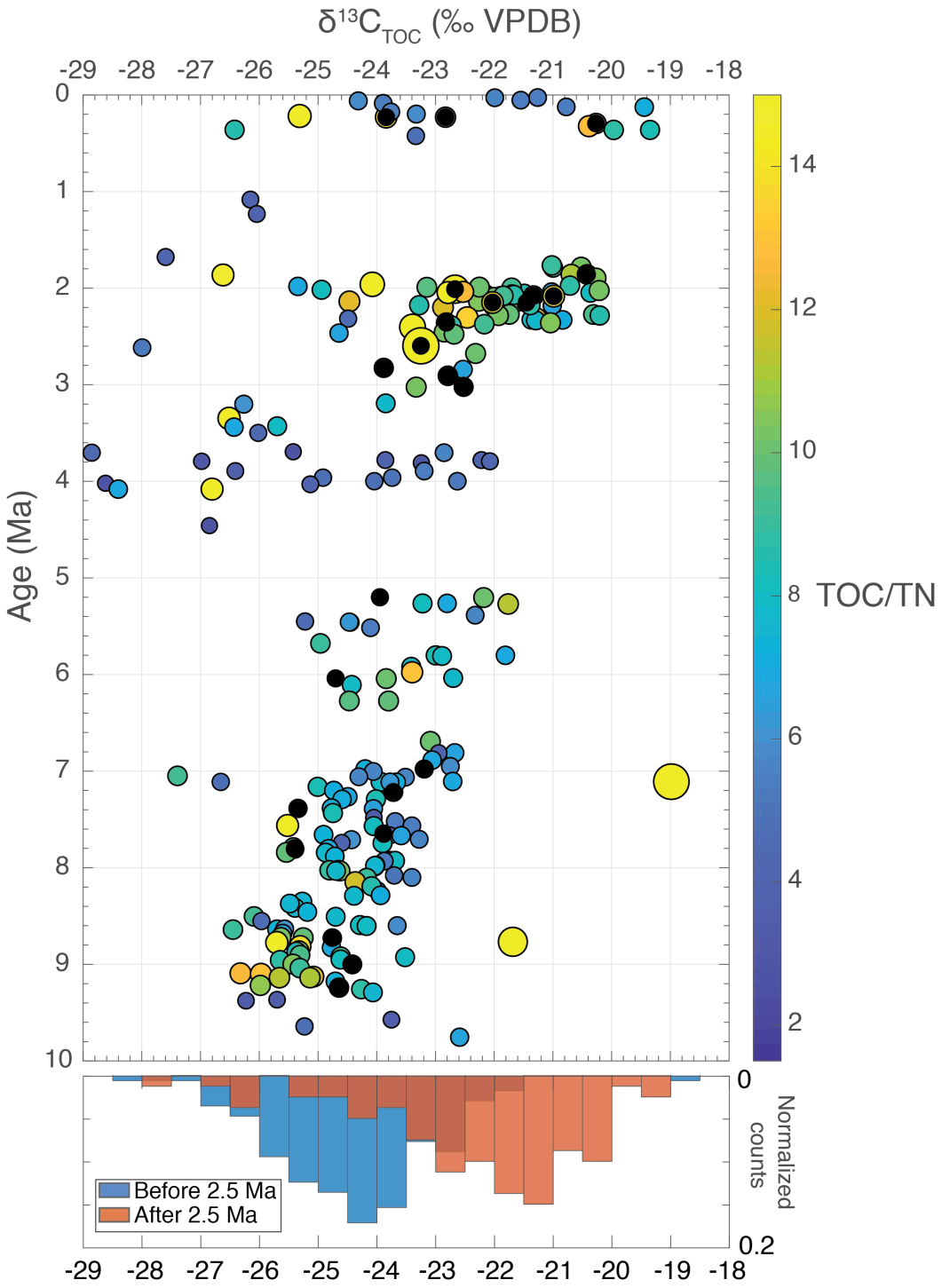

Figure 4.3. Site 1480 $\delta^{13}C_{TOC}$ record for the past 10 Ma data point color denoting TOC/TN ratios and black points indicating the subset of samples chosen for trace element analysis to establish Br/TOC. Heavier $\delta^{13}C$ values (reported as permill with respect to the VPDB standard)

imply either a shift toward more C_4-derived and/or a greater fraction of marine organic matter. The TOC/TN ratio is a proxy for organic matter provenance with ratios below ~5-8 indicating a marine origin and ratios above ~8 indicating a terrestrial source. Data characterized by a high TOC/TN ratio will therefore be more representative of terrestrial conditions and will be subject to a smaller correction when the marine organic matter signal is subtracted (Section 3.1; Figure 6) The marginal histogram shows the difference in frequency of $\delta^{13}C_{TOC}$ before and after the dramatic ~2.5 Ma shift.

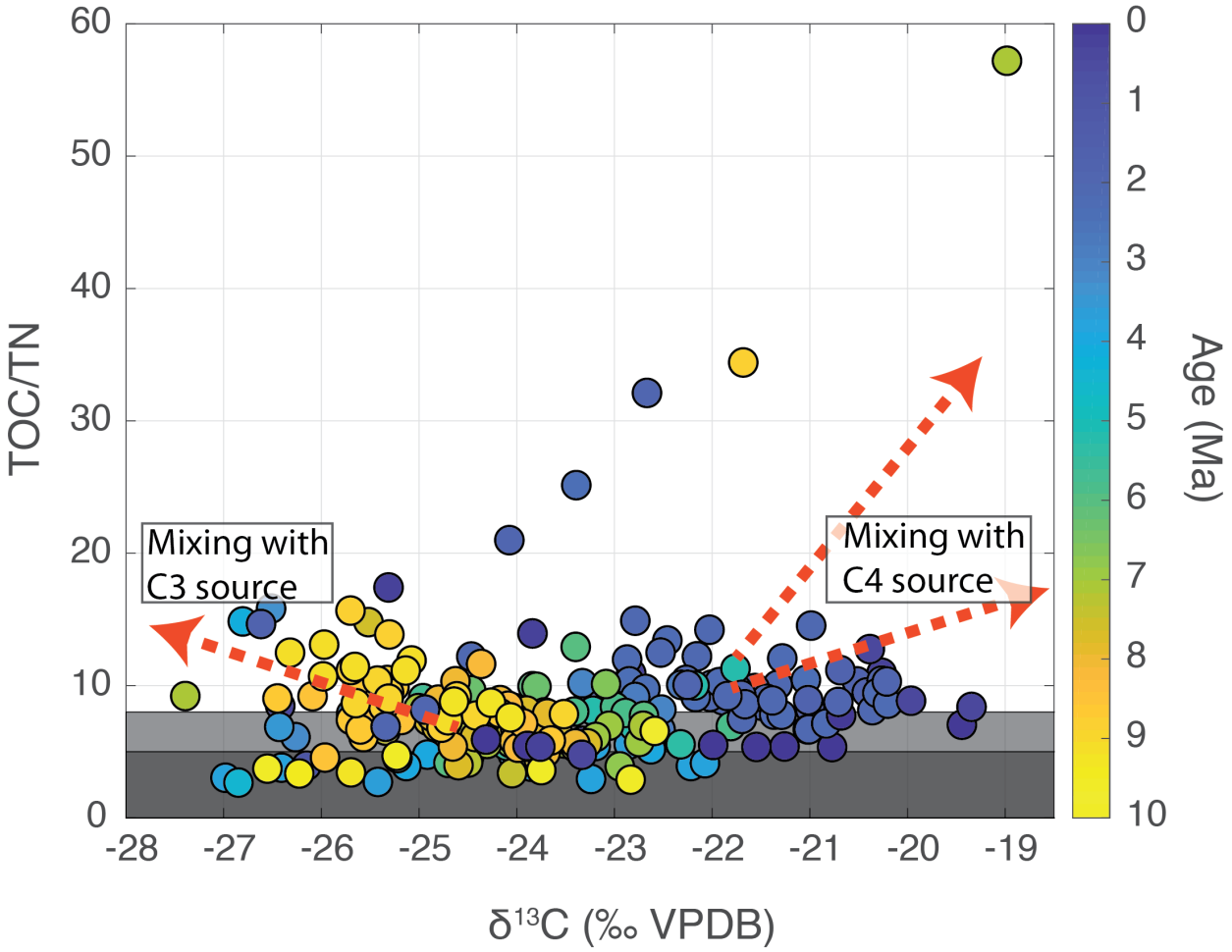

Figure 4.4. $\delta^{13}C_{TOC}$ and TOC/TN data can be largely explained by a mixing model between organic matter from: vascular C_3 plants with high TOC/TN and low $\delta^{13}C$, C_4 plants with high TOC/TN and high $\delta^{13}C$, and marine organic matter with low TOC/TN and intermediate $\delta^{13}C$. Shaded regions indicate the approximate TOC/TN range of <5-8 for marine organic matter and >8 for both C_3 and C_4 terrestrial organic matter. Because of the uncertainty in both the TOC/TN and $\delta^{13}C$ values of the three endmembers, we assumed reasonable values based on this figure and previous work (e.g. Galy et al. 2008) and conducted Monte Carlo simulations in which endmember values were perturbed over a wide range (Table 1) to more fully account for uncertainty introduced when applying the mixing models.

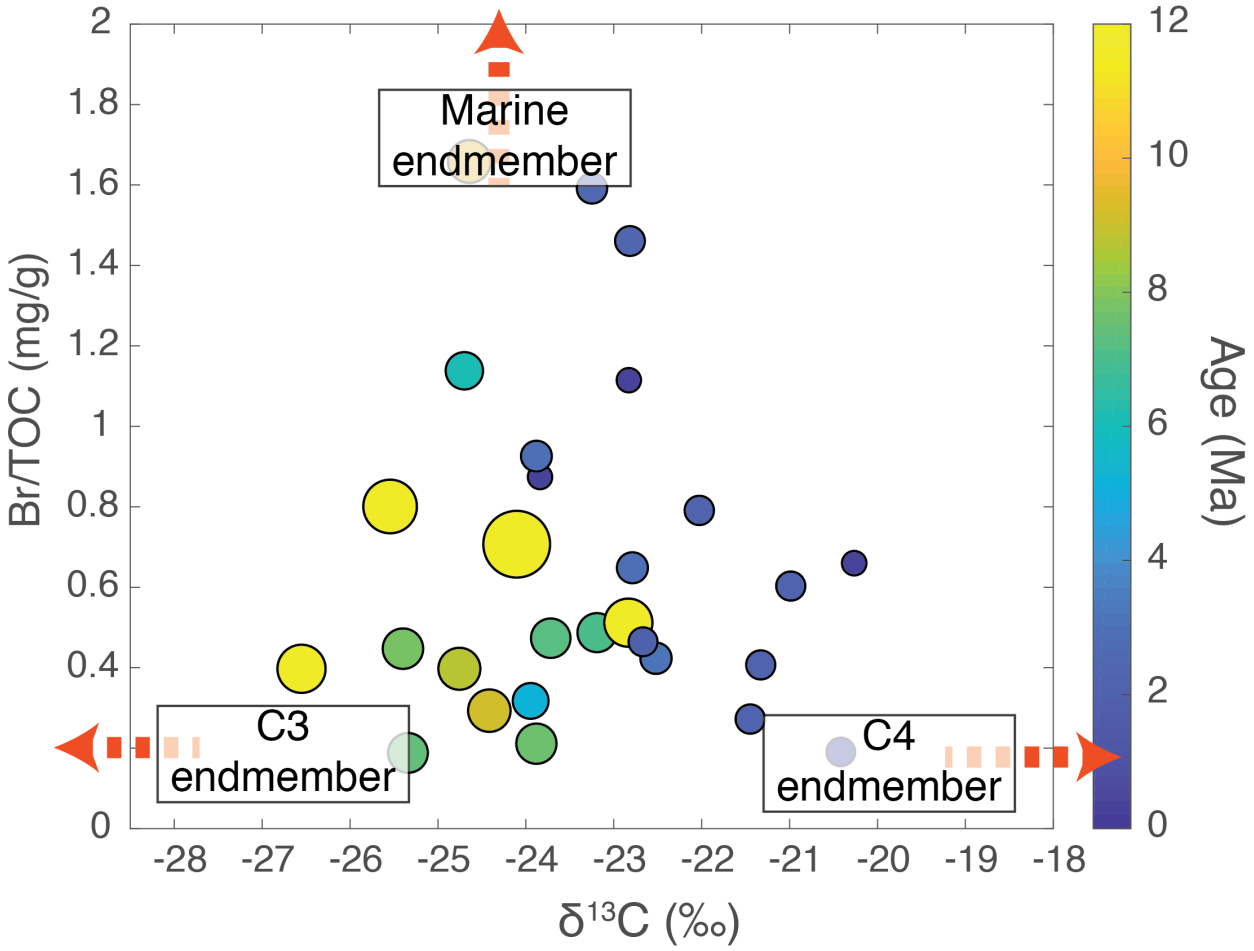

Figure 4.5. $\delta^{13}C_{TOC}$ and Br/TOC for the subset of samples analyzed for major and trace element composition. These data are consistent with the three endmember mixing model introduced by Mayer et al. (2007) in which terrigenous organic matter is characterized by much lower Br/TOC ratios than marine organic matter. These data were used in a separate mixing model based on assumed and previously published endmember values (Mayer et al., 2007) to correct for organic matter contributions and produce quantitative bounds on the fraction of C_4 land cover through time. Using Br/TOC as well as TOC/TN as independent metrics of marine organic matter contributions provides a more robust basis for inferring the composition of terrestrial plant communities through $\delta^{13}C_{TOC}$ in marine sediments. The effects of uncertainties in Br/TOC endmember compositions were estimated using Monte Carlo simulations based on random perturbations in endmember composition (Section 3.1).

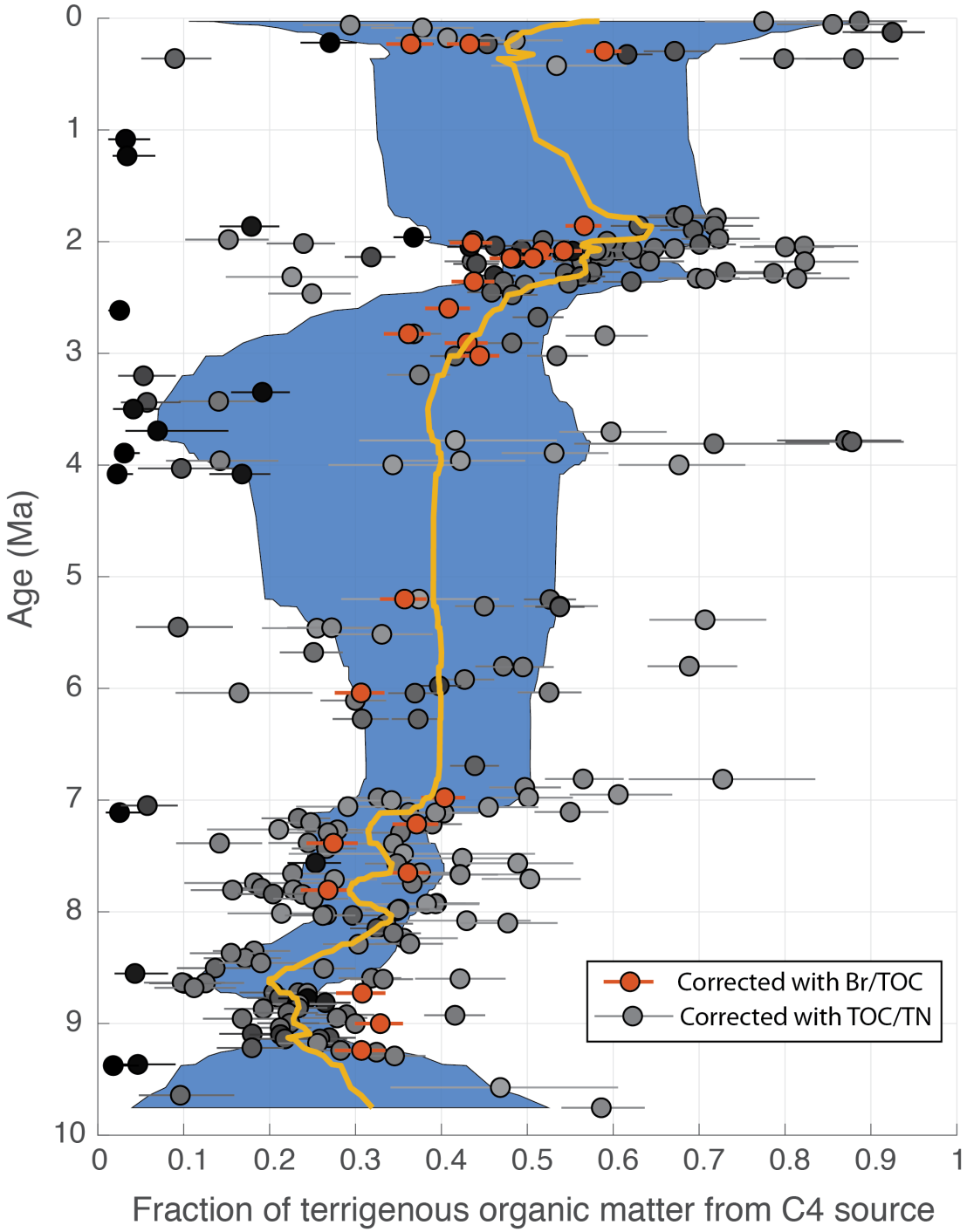

Figure 4.6. Estimated fraction of terrigenous organic matter from C_4 plants through time based on $\delta^{13}C_{TOC}$, TOC/TN, and Br/TOC data from Site 1480. Two separate mixing models using TOC/TN and Br/TOC data respectively were used to minimize the influence of marine organic matter. Data points in grey show the median output from 10^5 Monte Carlo simulations using

random perturbations of TOC/TN and $\delta^{13}C_{TOC}$ endmember compositions while the uncertainty bars represent the interquartile range of simulation outputs. Points in darker grey were inferred to have smaller contributions from marine organic matter and therefore underwent a smaller correction to minimize the influence of marine organic matter. Points in red show C_4 fraction when contributions to the $\delta^{13}C_{TOC}$ data from marine sources were corrected for using Br/TOC, and the error bars represent the interquartile of values based on Monte Carlo simulations. The blue region represents the interquartile range of smoothed curves resulting from random resampling (bootstrapping) of C_4 coverage estimates while the yellow curve is the median of the smoothed curves from bootstrap resampling. Two main periods of C_4 expansion (~8.5-7 and ~2.5 Ma) are apparent, suggesting a multi-phase transition toward greater aridity.

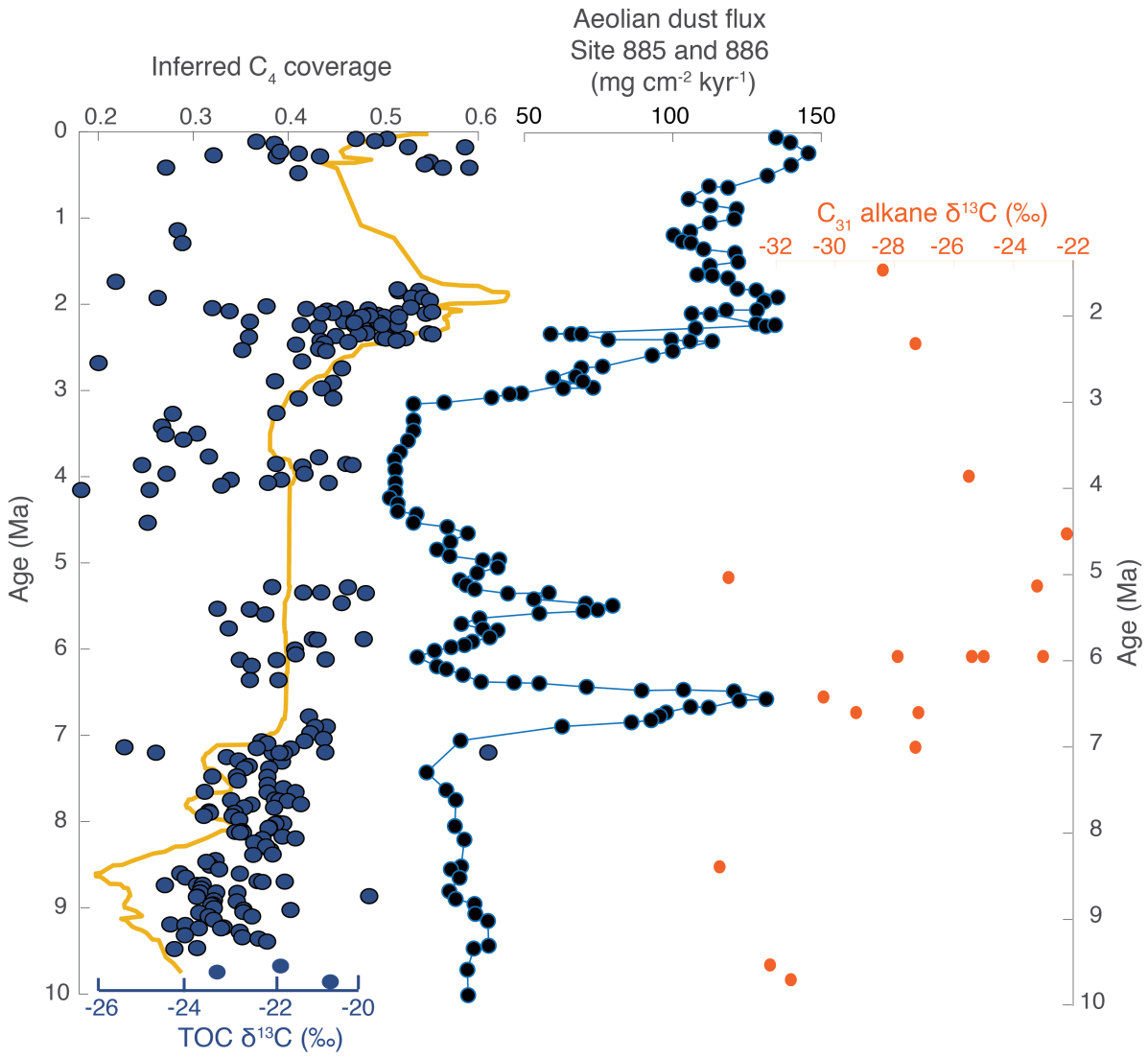

Figure 4.7. Comparison of multiple marine and terrestrial proxies for the C_3-C_4 transition and aridity including Site 1480 $\delta^{13}C_{TOC}$ and median smoothed C_4 coverage (this study), Site 885/886 aeolian dust flux from central Asia (Rea et al., 1998), and $\delta^{13}C$ of 31 C n-alkanes extracted from Siwalik paleosols (Freeman and Colarusso, 2001; Karp et al., 2018). The initial shift inferred from this study appears to pre-date the first spike in dust flux from central Asia, suggesting that the C_3-C_4 transition on the Indian subcontinent may have begun before widespread aridification of central Asia. Low temporal resolution introduces uncertainty into the timing of C_4 expansion from the $\delta^{13}C$ of C_3, though the onset of the transition appears to postdate that implied by the Site 1480 record, suggesting that regions of the Ganges catchment downstream from the northwest Siwalik paleosols may have shifted toward C_4 plant coverage earlier. The sharp ~2.5 Ma increase in C_4 coverage inferred from Site 1480 data agrees well with the timing of the second increase in aeolian dust flux, suggesting this transition was rapid across Asia.

Tables

Table 1. Endmember values and ranges used in mixing models

Endmember	$\delta^{13}C_{TOC}$ (‰ VPDB)	TOC/TN (‰ VPDB)	Br/TOC (parts per thousand)
Terrigenous C_4	-15±1	15±5	1±0.95
Terrigenous C_3	-30±2	15±5	1±0.95
Marine	-24±1	5±3	8±2

Chapter 4 appendix

Table S1. Elemental and isotopic composition of sediment organic matter

Sample ID	Hole	Core	Section	Interval (cm)	Depth (m)	Age (Ma)	TOC (wt% C)	$\delta^{13}C$ (‰ VPDB)	TOC/TN	Br/TOC (mg/g)
7857271	U1480E	1H	1	124-125	1.25	0.03	0.31	-21.3	5.4	
7857311	U1480E	1H	4	138-139	5.74	0.12	0.31	-20.8	5.4	2.1
7860231	U1480E	2H	1	137-138	9.17	0.2	0.23	-23.3	5.8	
7860881	U1480E	2H	2	137-138	10.67	0.23	0.23	-22.8	10.9	1.11
7860881	U1480E	2H	2	137-138	10.67	0.23	0.29	-23.8	13.9	0.87
7861471	U1480E	2H	4	137-138	13.68	0.3	0.5	-20.3	11	0.66
7861571	U1480E	2H	5	113-121	14.97	0.32	0.48	-20.4	12.8	
7861621	U1480E	2H	6	139-140	16.7	0.36	0.16	-26.4	8.5	
7862401	U1480E	3H	3	139-140	21.69	1.08	0.15	-26.2	4	
7862641	U1480E	3H	6	127-129	26.08	1.68	0.14	-27.6	4.2	
7863131	U1480E	4H	1	138-139	28.19	1.78	0.59	-22.2	0	
7863251	U1480E	4H	3	5-6	29.86	1.79	0.5	-21	8.2	
7863361	U1480E	4H	2	57-61	28.89	1.78	0.52	-20.5	10.3	
7863641	U1480E	5H	1	133-134	32.93	1.8	0.1	-30.6	0	
7863991	U1480E	6H	2	84-85	43.43	1.86	0.5	-20.7	11.2	
7864011	U1480E	6H	6	65-66	48.48	1.88	0.08	-30.6	9.2	
7864161	U1480E	6H	2	73-79	43.35	1.86	0.5	-20.4	9.5	0.19
7864591	U1480E	7H	1	16-17	50.77	1.9	0.62	-20.3	10.4	
7864611	U1480E	7H	3	73-74	53.61	1.91	0.09	-31.9	-20.7	
7864621	U1480E	7H	6	129-130	57.88	1.93	0.1	-30	12.5	
7864931	U1480E	8H	1	101-102	61.11	1.95	0.1	-29.7	3.8	
7865291	U1480E	9H	2	1-2	63.21	1.96	0.25	-24.1	21	

Table S1 (cont'd)

Sample ID	Hole	Core	Section	Interval (cm)	Depth (m)	Age (Ma)	TOC (wt% C)	$\delta^{13}C$ (‰ VPDB)	TOC/TN	Br/TOC (mg/g)
7865421	U1480E	9H	5	135-136	69.05	1.99	0.25	-23.1	9.7	
7866721	U1480E	10H	5	137-138	78.57	2.04	0.39	-21	6.7	
7866781	U1480E	10H	6	125-127	79.96	2.05	0.45	-20.4	8.1	
7868761	U1480E	11H	6	85-86	89.05	2.07	0.4	-22.2	12.2	
7868941	U1480E	11H	2	129-130	83.5	2.06	0.47	-21.5	8.5	
7869911	U1480E	12H	1	113-117	91.35	2.08	0.43	-21.3	10.1	0.41
7871681	U1480F	3H	3	130-131	111.1	2.13	0.53	-21.6	9.8	
7871771	U1480F	3H	4	48-52	111.8	2.13	0.17	-22.3	10.4	
7871871	U1480F	3H	4	129-130	112.59	2.14	0.2	-24.5	12.2	
7872251	U1480E	12H	2	126-127	92.96	2.08	0.46	-21.9	8.9	
7872341	U1480E	12H	5	128-129	97.48	2.1	0.44	-22	10.1	
7872511	U1480F	4H	1	28-32	116.6	2.15	0.33	-21.4	9	0.27
7872981	U1480F	4H	2	4-4	117.84	2.15	0.45	-21.9	9.7	
7873271	U1480F	5H	1	129-130	127.09	2.18	0.27	-23.3	8.6	
7873281	U1480F	5H	2	4-5	127.34	2.18	0.58	-22	9.2	
7873291	U1480F	5H	2	63-64	127.94	2.18	0.45	-21	6.7	
7873851	U1480F	5H	1	27-31	126.09	2.17	0.11	-23.3	8.3	
7874761	U1480F	6H	2	116-117	135.56	2.2	0.27	-22.9	12	
7877241	U1480F	12F	1	145-146	162.06	2.27	0.33	-21.7	9.7	
7877281	U1480F	12F	2	24-28	162.36	2.27	0.46	-20.3	9.4	
7877551	U1480F	13F	1	58-62	165.9	2.28	0.11	-22.9	6.8	4.71
7877711	U1480F	13F	1	92-96	166.24	2.28	0.39	-20.2	8.6	
7877761	U1480F	13F	1	124-125	166.55	2.28	0.31	-21.9	10.3	
7878491	U1480F	14F	3	72-73	173.72	2.3	0.56	-22.5	13.4	
7879431	U1480F	15F	2	128-129	176.74	2.31	0.4	-21.3	12	
7879511	U1480F	15F	3	129-130	178.25	2.32	0.23	-24.5	4.6	

Table S1 (cont'd)

Sample ID	Hole	Core	Section	Interval (cm)	Depth (m)	Age (Ma)	TOC (wt% C)	$\delta^{13}C$ (‰ VPDB)	TOC/TN	Br/TOC (mg/g)
7881031	U1480F	16F	3	70-71	183.11	2.33	0.47	-20.8	7.1	
7881741	U1480F	16F	2	123-124	182.13	2.33	0.49	-21.4	7.8	
7882271	U1480F	17F	1	86-87	184.97	2.33	0.49	-21.3	7.8	
7882851	U1480F	19F	1	55-56	194.06	2.36	0.55	-21	10.4	
7882881	U1480F	19F	1	22-26	193.74	2.36	0.2	-22.8	9.5	1.46
7883011	U1480F	21F	3	133-134	207.24	2.4	0.38	-23.4	25.1	
7883221	U1480F	21F	2	32-36	204.74	2.39	0.2	-22.7	8.7	
7884191	U1480F	23F	1	127-128	213.57	2.45	0.31	-22.8	10.3	
7884301	U1480F	23F	2	125-126	215.06	2.47	0.21	-24.6	6.6	
7884321	U1480F	23F	3	120-124	216.52	2.48	0.18	-22.7	9.8	
7884601	U1480F	20F	1	113-114	199.34	2.37	0.36	-22.2	9.1	
7886231	U1480F	27F	1	48-52	231.6	2.6	0.18	-23.2	59.7	1.59
7886301	U1480F	27F	2	134-135	233.94	2.62	0.14	-28	5.2	
7886621	U1480F	29F	1	105-106	241.56	2.68	0.44	-22.3	10.1	
7887111	U1480F	33F	2	92-93	262.32	2.84	0.42	-22.5	6.7	
7887431	U1480F	33F	1	32-36	260.24	2.83	0.14	-23.9	8.5	0.93
7887441	U1480F	35X	1	11-15	270.53	2.91	0.27	-22.8	9.1	0.65
7888481	U1480F	36F	2	45-53	282.09	3	0.09	-24.5	8.6	
7888531	U1480F	37X	1	12-16	284.94	3.02	0.55	-22.5	8.2	0.42
7888611	U1480F	37X	1	40-41	285.2	3.02	0.48	-23.3	10.2	
7889441	U1480F	41F	3	85-86	307.36	3.2	0.18	-26.3	6.1	
7889581	U1480F	41F	2	81-82	306.31	3.19	0.32	-23.8	7.7	
7889931	U1480F	45F	2	75-76	325.86	3.35	0.43	-26.5	15.8	
7889951	U1480F	47F	2	128-129	336.01	3.43	0.21	-25.7	7.9	
7889971	U1480F	47F	3	95-96	337.19	3.44	0.17	-26.4	6.9	
7891221	U1480F	53X	3	96-97	370.38	3.7	0.13	-28.9	4.4	

Table S1 (cont'd)

Sample ID	Hole	Core	Section	Interval (cm)	Depth (m)	Age (Ma)	TOC (wt% C)	$\delta^{13}C$ (‰ VPDB)	TOC/TN	Br/TOC (mg/g)
7891221	U1480F	53X	3	96-97	370.38	3.7	0.16	-22.9	5.5	
7891321	U1480F	53X	2	78-79	369.19	3.69	0.18	-25.4	2.7	
7891721	U1480F	49F	1	138-139	344.69	3.5	0.15	-26	4.3	
7892321	U1480F	54X	2	127-128	379.98	3.78	0.32	-23.9	3.9	
7892321	U1480F	54X	2	127-128	379.98	3.78	0.32	-22.2	3.9	
7892421	U1480F	54X	3	134-135	381.56	3.79	0.18	-27	3	
7892421	U1480F	54X	3	134-135	381.56	3.79	0.24	-22.1	4.1	
7892671	U1480F	54X	5	48-54	383.64	3.81	0.16	-23.2	2.9	
7893731	U1480F	55X	2	128-129	389.78	3.89	0.21	-26.4	3.8	
7893731	U1480F	55X	2	128-129	389.78	3.89	0.3	-23.2	5.4	
7893881	U1480F	55X	5	128-129	394.28	3.96	0.34	-24.9	4.8	
7893881	U1480F	55X	5	128-129	394.28	3.96	0.35	-23.7	4.9	
7893961	U1480F	55X	CC	15-16	396.68	4	0.37	-24	4.8	
7893961	U1480F	55X	CC	15-16	396.68	4	0.4	-22.6	5.2	
7894411	U1480F	56X	1	126-127	398.06	4.02	0.15	-28.6	2.6	0.21
7894681	U1480F	56X	2	44-48	398.76	4.03	0.2	-25.1	3.9	
7894721	U1480F	56X	2	128-129	399.58	4.04	0.13	-29	0	
7894721	U1480F	56X	2	128-129	399.58	4.04	0.17	-22.7	0	
7894921	U1480F	56X	CC	13-14	402.01	4.08	0.13	-28.4	7	
7894921	U1480F	56X	CC	13-14	402.01	4.08	0.28	-26.8	14.8	
7896081	U1480F	59X	1	59-60	426.69	4.46	0.17	-26.8	2.7	
7896091	U1480F	59X	1	128-129	427.38	4.47	0.13	-29.3	2.4	0.85
7896871	U1480F	64X	1	93-97	475.65	5.2	0.36	-22.2	10	
7896921	U1480F	64X	1	43-44	475.13	5.2	0.19	-23.9	4.3	0.32
7897071	U1480F	65X	1	113-114	485.53	5.26	0.35	-23.2	8.1	
7897261	U1480F	67X	CC	14-15	505.33	5.39	0.35	-22.3	5.6	

Table S1 (cont'd)

Sample ID	Hole	Core	Section	Interval (cm)	Depth (m)	Age (Ma)	TOC (wt% C)	$\delta^{13}C$ (‰ VPDB)	TOC/TN	Br/TOC (mg/g)
7897431	U1480F	65X	1	97-101	485.39	5.26	0.29	-22.8	6.9	
7897661	U1480F	65X	CC	9-10	486.52	5.27	0.22	-21.8	11.3	
7897801	U1480F	68X	2	84-85	515.93	5.45	0.18	-25.2	4.5	
7897821	U1480F	68X	3	135-136	517.52	5.46	0.25	-24.5	5.4	
7898311	U1480F	68X	3	74-78	516.93	5.46	0.13	-24.5	6.3	
7898921	U1480F	69X	3	19-20	526.5	5.52	0.27	-24.1	5.5	
7899481	U1480F	72X	CC	36-37	552.87	5.68	0.26	-25	9	
7899611	U1480F	74X	1	111-115	573.03	5.8	0.32	-21.8	6.9	
7899621	U1480F	74X	1	123-124	573.13	5.8	0.37	-23	8.4	
7899781	U1480F	74X	2	74-75	574.14	5.81	0.37	-22.9	7.9	
7900571	U1480F	76X	1	110-111	592.4	5.92	0.39	-23.4	8	
7900641	U1480F	77X	CC	56-57	601.57	5.98	0.34	-23.4	12.9	
7900811	U1480F	78X	1	41-45	611.23	6.04	0.34	-22.7	7.7	
7900891	U1480F	78X	1	107-108	611.88	6.04	0.2	-24.7	4.2	1.14
7900971	U1480F	78X	2	20-21	612.3	6.04	0.34	-23.8	10	
7901411	U1480F	79X	2	94-95	622.95	6.11	0.31	-24.4	7.9	
7901781	U1480F	82X	1	26-27	649.97	6.27	0.3	-23.8	9.9	
7901871	U1480F	82X	1	17-21	649.89	6.27	0.29	-24.5	9.6	
7902681	U1480F	89X	CC	34-35	718.14	6.69	0.23	-23.1	10.1	
7904001	U1480F	91X	1	21-23	737.42	6.81	0.23	-22.7	6.7	
7904041	U1480F	91X	1	58-62	737.8	6.81	0.18	-22.9	3.9	
7904381	U1480F	92X	1	5-6	746.96	6.87	0.12	-23.6	13.5	
7904451	U1480F	92X	2	127-128	749.67	6.89	0.24	-23.1	7	
7907431	U1480F	96X	1	59-60	786.39	7.11	0.14	-26.7	4.8	
7907471	U1480F	96X	1	40-44	786.22	7.11	0.26	-23.9	7.9	
7907531	U1480F	96X	1	18-18	785.98	7.11	1.99	-19	57.2	

Table S1 (cont'd)

Sample ID	Hole	Core	Section	Interval (cm)	Depth (m)	Age (Ma)	TOC (wt% C)	$\delta^{13}C$ (‰ VPDB)	TOC/TN	Br/TOC (mg/g)
7907931	U1480F	98X	CC	29-30	805.6	7.21	0.09	-23.9	7	
7907961	U1480F	98X	CC	34-38	805.66	7.22	0.22	-23.7	8	0.47
7914801	U1480G	2R	1	59-60	760.2	6.95	0.29	-22.7	5.7	
7915791	U1480G	3R	1	103-107	764.65	6.98	0.36	-23.2	6.1	0.49
7915821	U1480G	3R	1	122-123	764.83	6.98	0.37	-24.2	7.3	
7915941	U1480G	3R	4	75-76	768.86	7	0.3	-24.1	5.6	
7916811	U1480G	4R	4	58-59	778.5	7.06	0.36	-23.5	5.6	
7916821	U1480G	4R	2	128-129	776.18	7.05	0.6	-27.4	9.2	
7916951	U1480G	4R	3	134-135	777.75	7.06	0.33	-24.3	5.6	
7917541	U1480G	5R	2	116-117	785.62	7.11	0.4	-22.7	7	
7917661	U1480G	5R	3	110-111	786.99	7.12	0.51	-23.7	7	
7917751	U1480G	5R	3	82-86	786.72	7.11	0.46	-23.8	6.3	
7918521	U1480G	6R	2	65-66	794.7	7.16	0.37	-25	8.3	
7918541	U1480G	7R	CC	6-7	802.57	7.2	0.42	-24.7	7.2	
7919131	U1480G	8R	4	35-36	816.05	7.26	0.27	-24.5	4.2	
7919191	U1480G	8R	4	92-93	816.62	7.27	0.37	-24.5	6.9	
7920011	U1480G	9R	1	42-43	822.33	7.29	0.37	-24.6	7.2	
7920101	U1480G	9R	1	31-35	822.23	7.29	0.37	-24	8.3	
7920211	U1480G	11R	2	102-103	843.4	7.39	0.44	-24.1	6.5	
7920291	U1480G	11R	2	28-32	842.68	7.39	0.43	-25.3	6.6	0.19
7920301	U1480G	11R	1	83-84	842.13	7.38	0.45	-24.8	7.3	
7921251	U1480G	12R	2	46-47	852.97	7.43	0.5	-24.7	8.4	
7921461	U1480G	13R	2	109-110	863.29	7.48	0.22	-24	3.4	
7922551	U1480G	14R	2	64-65	871.86	7.52	0.35	-23.7	5.3	
7923011	U1480G	15R	1	79-80	880.89	7.56	0.56	-25.5	14.8	
7923071	U1480G	15R	2	36-39	881.51	7.57	0.43	-23.4	5.3	

Table S1 (cont'd)

Sample ID	Hole	Core	Section	Interval (cm)	Depth (m)	Age (Ma)	TOC (wt% C)	$\delta^{13}C$ (‰ VPDB)	TOC/TN	Br/TOC (mg/g)
7923171	U1480G	15R	2	109-110	882.24	7.57	0.3	-24.1	8.2	
7924241	U1480G	17R	1	34-38	899.96	7.65	0.47	-23.9	6	0.21
7924351	U1480G	17R	2	78-79	901.7	7.66	0.39	-24.9	7.3	
7924441	U1480G	17R	3	118-119	903.1	7.67	0.3	-23.8	4.5	
7924521	U1480G	17R	4	29-30	903.62	7.67	0.48	-23.6	6.6	
7925591	U1480G	18R	3	3-4	911.88	7.71	0.45	-23.3	5.6	
7925681	U1480G	18R	3	91-92	912.76	7.71	0.4	-24.4	6.1	
7926761	U1480G	19R	1	68-69	919.78	7.74	0.3	-24.6	4	
7926821	U1480G	20R	1	101-102	929.82	7.79	0.53	-25.4	8.5	
7927081	U1480G	19R	2	54-58	920.55	7.75	0.4	-23.9	8.1	
7927631	U1480G	20R	3	135-136	932.93	7.8	0.45	-24.8	6.9	
7927641	U1480G	20R	4	36-40	933.48	7.81	0.46	-25.4	7.3	0.45
7927981	U1480G	21R	3	31-32	941.75	7.84	0.41	-24.9	7.6	
7928121	U1480G	21R	2	118-119	941.17	7.84	0.61	-25.5	9.8	
7929161	U1480G	22R	2	56-57	950.16	7.88	0.38	-24.7	7.2	
7929821	U1480G	23R	1	110-114	959.12	7.92	0.44	-23.8	6.1	
7929861	U1480G	23R	2	62-63	960.09	7.93	0.48	-23.7	7.9	
7930021	U1480G	23R	3	55-56	960.78	7.93	0.38	-23.9	5.4	
7931001	U1480G	24R	2	103-104	970.02	7.97	0.31	-24	6.7	
7931101	U1480G	24R	5	110-111	973.78	7.99	0.4	-24	5.8	
7931291	U1480G	24R	3	105-106	971.27	7.98	0.44	-24	7.6	
7931891	U1480G	25R	1	126-127	978.66	8.01	0.33	-24.7	5.4	
7932111	U1480G	25R	3	115-116	981.22	8.03	0.38	-24.8	8.9	
7932611	U1480G	25R	4	118-119	982.62	8.03	0.48	-24.6	10.3	
7932621	U1480G	25R	CC	5-9	982.79	8.03	0.42	-24.7	7.6	
7933161	U1480G	26R	5	55-56	992.82	8.08	0.28	-23.7	4.9	

Table S1 (cont'd)

Sample ID	Hole	Core	Section	Interval (cm)	Depth (m)	Age (Ma)	TOC (wt% C)	$\delta^{13}C$ (‰ VPDB)	TOC/TN	Br/TOC (mg/g)
7933551	U1480G	26R	3	106-107	990.9	8.07	0.29	-23.5	0	
7934161	U1480G	27R	2	79-80	998.59	8.11	0.57	-24.2	8.9	
7934251	U1480G	27R	1	54-58	997.36	8.1	0.39	-23.4	5.6	
7935171	U1480G	28R	1	104-105	1007.64	8.15	0.53	-24.4	11.6	
7935191	U1480G	30R	1	90-91	1026.91	8.24	0.38	-24	5.3	
7935471	U1480G	29R	1	82-86	1017.14	8.19	0.47	-24.1	8.5	
7936151	U1480G	31R	2	53-54	1037.51	8.29	0.41	-23.9	7.1	
7936201	U1480G	31R	3	69-70	1038.47	8.29	0.41	-24.4	7.7	
7936621	U1480G	32R	5	91-92	1051.51	8.35	0.32	-25.3	7.5	
7937291	U1480G	34R	1	79-80	1065.7	8.42	0.35	-25.4	7.7	
7937401	U1480G	34R	2	64-68	1066.55	8.42	0.39	-27.5	0	0.37
7937601	U1480G	33R	1	83-84	1056.03	8.37	0.31	-25.5	7.5	
7938031	U1480G	36R	1	82-83	1085.22	8.5	0.23	-26.1	9.2	
7938111	U1480G	36R	2	47-51	1085.93	8.51	0.22	-24.7	7.7	
7938281	U1480G	35R	1	44-45	1075.05	8.46	0.42	-25.2	7.4	
7939351	U1480G	37R	2	77-78	1095.74	8.55	0.27	-26	4.6	
7940061	U1480G	38R	1	98-99	1104.78	8.59	0.66	-24.3	8.1	
7940321	U1480G	38R	4	2-3	1106.86	8.6	0.54	-24.2	7.9	
7940511	U1480G	38R	3	0-4	1106.07	8.6	0.45	-23.7	5.9	
7940621	U1480G	39R	1	87-88	1114.38	8.64	0.37	-25.7	7.4	
7940701	U1480G	39R	2	54-55	1115.11	8.64	0.3	-26.4	9	
7940881	U1480G	39R	1	20-24	1113.72	8.63	0.43	-25.6	6.1	
7941281	U1480G	40R	1	48-49	1123.78	8.68	0.36	-25.6	6.7	
7941601	U1480G	41R	1	24-25	1133.24	8.72	0.48	-25.6	10.3	
7941621	U1480G	41R	1	38-39	1133.39	8.72	0.35	-25.3	9.9	
7941871	U1480G	41R	2	8-12	1134.34	8.73	0.36	-24.8	7.2	0.4

Table S1 (cont'd)

Sample ID	Hole	Core	Section	Interval (cm)	Depth (m)	Age (Ma)	TOC (wt% C)	$\delta^{13}C$ (‰ VPDB)	TOC/TN	Br/TOC (mg/g)
7942121	U1480G	42R	1	81-82	1143.51	8.77	0.43	-25.7	11.2	
7942251	U1480G	42R	2	92-93	1144.64	8.78	0.29	-25.7	15.7	
7942421	U1480G	42R	1	12-13	1142.82	8.77	1.13	-21.7	34.4	
7943141	U1480G	43R	1	61-62	1153.11	8.81	0.33	-25.3	13.9	
7943351	U1480G	43R	3	112-116	1155.83	8.83	0.42	-24.8	6.8	
7944341	U1480G	44R	1	103-104	1163.24	8.86	0.38	-25.3	10.4	
7944461	U1480G	44R	3	72-73	1165.09	8.87	0.42	-25.4	8.4	
7945061	U1480G	45R	1	99-100	1172.89	8.9	0.48	-25.3	9.5	
7945241	U1480G	45R	4	54-55	1176.61	8.92	0.51	-24.6	9.2	
7945361	U1480G	45R	5	94-98	1177.71	8.93	0.44	-23.5	7.8	
7945791	U1480G	46R	1	129-130	1182.89	8.95	0.53	-24.6	8.1	
7945871	U1480G	46R	3	0-1	1184.39	8.96	0.37	-25.6	8.7	
7946441	U1480G	47R	2	60-61	1193.41	9	0.38	-25.4	10.4	
7946551	U1480G	47R	3	37-41	1194.03	9	0.3	-24.4	7.7	0.29
7947081	U1480G	48R	1	123-124	1202.24	9.04	0.48	-25.3	9	
7947961	U1480G	49R	4	2-3	1214.2	9.09	0.35	-26.3	12.5	
7948001	U1480G	49R	5	3-4	1215.61	9.1	0.5	-26	13.1	
7948401	U1480G	50R	3	62-63	1224.12	9.14	0.54	-25.7	11.4	
7948411	U1480G	50R	1	122-123	1221.72	9.13	0.41	-25.1	11.9	
7948631	U1480G	50R	3	61-62	1224.11	9.14	0.5	-25.1	11.1	
7949221	U1480G	51R	2	78-82	1232.6	9.18	0.41	-24.7	7.4	
7949301	U1480G	51R	CC	5-6	1233.16	9.18	0.43	-25.3	0	
7950381	U1480G	52R	3	81-82	1241.61	9.22	0.33	-26	10.7	
7950421	U1480G	52R	4	103-104	1242.86	9.22	0.44	-25.2	0	
7951081	U1480G	53R	2	123-124	1247.32	9.24	0.43	-25.7	0	0.2
7951221	U1480G	53R	2	56-60	1246.66	9.24	0.16	-24.6	8.8	1.66

Table S1 (cont'd)

Sample ID	Hole	Core	Section	Interval (cm)	Depth (m)	Age (Ma)	TOC (wt% C)	$\delta^{13}C$ (‰ VPDB)	TOC/TN	Br/TOC (mg/g)
7952141	U1480G	54R	1	43-44	1250.14	9.26	0.52	-24.3	8.7	
7952151	U1480G	54R	4	126-127	1255.32	9.29	0.52	-24.1	7.6	
7952161	U1480G	54R	5	90-91	1256.47	9.37	0.2	-25.7	3.4	
7952211	U1480G	54R	5	106-107	1256.62	9.38	0.2	-26.2	3.4	
7953211	U1480G	55R	1	19-24	1259.62	9.57	0.19	-23.7	3.6	-0.02
7953341	U1480G	55R	3	47-48	1262.38	9.75	0.47	-22.6	6.6	
7953591	U1480G	55R	1	127-128	1260.68	9.64	0.23	-25.2	4.7	
7953921	U1480G	56R	4	143-144	1274.78	12.78	0.2	-26.6	3.7	0.4
7953921	U1480G	56R	4	143-144	1274.78	12.78	0.15	-22.8	2.9	0.51
7954551	U1480G	57R	2	56-57	1280.61	15.44	0.37	-24.4	0	
7954781	U1480G	57R	4	93-97	1283.52	16.77	0.14	-25.5	2.8	0.8
7956701	U1480G	59R	2	72-73	1300.47	24.53	0.16	-30.7	6.3	-0.02
7956701	U1480G	59R	2	72-73	1300.47	24.53	0.09	-25.8	3.4	-0.04
7956781	U1480G	59R	3	109-113	1301.8	25.14	0.08	-26.7	1.9	
7958011	U1480G	60R	1	54-55	1308.55	28.23	0.14	-24.1	3	0.71
7970131	U1480H	1H	1	133-134	1.33	0.03	0.24	-22	5.5	
7970141	U1480H	1H	2	132-133	2.83	0.06	0.17	-24.3	5.9	
7970321	U1480H	1H	2	98-102	2.5	0.05	0.19	-21.5	5.4	
7970511	U1480H	1H	3	100-101	4	0.09	0.2	-23.9	5.4	
7970761	U1480H	2H	1	133-134	5.83	0.13	0.46	-19.4	7	
7970791	U1480H	2H	4	132-133	10.09	0.22	0.21	-25.3	17.4	
7971031	U1480H	2H	3	80-81	8.12	0.18	0.25	-23.8	5.4	
7974051	U1480H	3H	2	133-134	16.77	0.36	0.45	-20	8.9	
7974051	U1480H	3H	2	133-134	16.77	0.36	0.42	-19.3	8.4	
7974151	U1480H	3H	4	131-132	19.64	0.42	0.19	-23.3	4.8	
7975391	U1480H	4H	1	132-133	24.82	1.23	0.15	-26	4	

Table S1 (cont'd)

Sample ID	Hole	Core	Section	Interval (cm)	Depth (m)	Age (Ma)	TOC (wt% C)	$\delta^{13}C$ (‰ VPDB)	TOC/TN	Br/TOC (mg/g)
7975501	U1480H	4H	2	132-133	26.32	1.76	0.34	-21	8.9	
7977001	U1480H	6H	2	91-92	44.45	1.86	0.16	-26.6	14.7	
7977321	U1480H	7H	3	18-19	54.58	1.92	0.1	-29.7	13.6	
7978171	U1480H	8H	3	131-132	65.81	1.97	0.44	-20.7	8.8	
7978181	U1480H	8H	4	133-134	67.34	1.98	0.17	-25.3	6.9	
7978191	U1480H	8H	5	132-133	68.82	1.99	0.44	-22.3	10.1	
7978201	U1480H	8H	6	113-114	70.13	2	0.39	-21.7	9.3	
7979141	U1480H	9H	2	41-45	72.93	2.01	0.26	-22.7	32.1	0.46
7979231	U1480H	9H	3	11-12	74.12	2.02	0.16	-24.9	8.2	
7979291	U1480H	9H	4	12-13	75.62	2.02	0.61	-20.2	10.3	
7979321	U1480H	9H	5	129-130	78.29	2.04	0.27	-22.5	12.5	
7979371	U1480H	9H	6	119-120	79.69	2.05	0.38	-22.8	14.9	
7982821	U1480H	10H	3	133-134	84.84	2.06	0.67	-21.7	7.5	
7984071	U1480H	10H	5	131-132	87.81	2.07	0.59	-21.7	8.6	
7984531	U1480H	11H	1	132-133	91.32	2.08	0.48	-21.8	9.2	
7984721	U1480H	11H	2	114-118	92.66	2.08	0.45	-21	14.5	0.6
7985091	U1480H	16H	1	84-88	116.86	2.15	0.22	-22	14.2	0.79
7985551	U1480H	17H	1	132-133	126.82	2.18	0.55	-21.4	8.9	

Decarbonation test	Total C (wt%)
Dolomite	12.7
Decarbonated dolomite	b.d.l.

Table S2. Select trace element data

Sample ID	Hole	Core	Section	Interval (cm)	Depth (CSF-A m)	Cl	± σ	Br	± σ	I	± σ
7857311	U1480E	1H	4	138-139	5.7	503.56	57.73	6.45	0.35	18.95	2.83
7860881	U1480E	2H	2	137-138	10.7	295.75	78.91	2.52	0.24	-0.39	0.05
7861471	U1480E	2H	4	137-138	13.7	181.05	52.69	3.27	0.25	-0.25	0.03
7864161	U1480E	6H	2	73-79	43.3	-7.48	0.26	0.95	0.18	1.84	1.01
7979141	U1480H	9H	2	41-45	72.9	169.59	38.62	1.20	0.18	-0.22	0.03
7869911	U1480E	12H	1	113-117	91.4	104.56	39.41	1.76	0.23	-0.23	0.03
7984721	U1480H	11H	2	114-118	92.7	356.17	56.71	2.72	0.20	-0.23	0.03
7872511	U1480F	4H	1	28-32	116.6	162.56	43.30	0.91	0.22	-0.22	0.03
7985091	U1480H	16H	1	84-88	116.9	286.38	50.34	1.77	0.16	2.42	0.95
7877551	U1480F	13F	1	58-62	165.9	164.75	41.83	5.14	0.29	-0.18	0.02
7882761	U1480F	18F	3	4-5	191.84	1289.00	79.37	5.44	0.32	-0.25	0.03
7882881	U1480F	19F	1	22-26	193.7	186.83	42.75	2.94	0.21	-0.19	0.02
7886231	U1480F	27F	1	48-52	231.6	-6.65	0.23	2.85	0.22	-0.19	0.02
7887431	U1480F	33F	1	32-36	260.2	233.68	47.05	1.29	0.19	-0.19	0.02
7887441	U1480F	35X	1	11-15	270.5	330.23	49.99	1.76	0.18	2.41	1.16
7888531	U1480F	37X	1	12-16	284.9	187.90	49.20	2.32	0.28	-0.24	0.03
7894411	U1480F	56X	1	126-127	398.1	48.78	49.34	0.31	0.15	-0.20	0.02
7896091	U1480F	59X	1	128-129	427.4	320.36	70.89	1.12	0.22	-0.27	0.03
7896921	U1480F	64X	1	43-44	475.1	186.21	49.90	0.61	0.15	1.75	1.49
7900521	U1480F	76X	1	82-86	592.12	174.47	44.72	1.20	0.21	-0.19	0.02
7900891	U1480F	78X	1	107-108	611.9	102.35	38.62	2.30	0.27	-0.23	0.03
7902231	U1480F	87X	CC	0-1	698.3	-11.88	0.42	0.99	0.14	-0.40	0.05
7915791	U1480G	3R	1	103-107	764.6	82.02	37.26	1.76	0.21	3.00	1.19
7907961	U1480F	98X	CC	34-38	805.7	175.19	47.41	1.03	0.18	1.61	1.21
7920291	U1480G	11R	2	28-32	842.7	-6.92	0.24	0.81	0.13	-0.23	0.03
7924241	U1480G	17R	1	34-38	900	163.05	41.65	1.00	0.23	-0.23	0.03

Table S2. (cont'd)

Sample ID	Hole	Core	Section	Interval (cm)	Depth (CSF-A m)	Cl	± σ	Br	± σ	I	± σ
7927641	U1480G	20R	4	36-40	933.5	98.63	44.19	2.04	0.23	-0.24	0.03
7937401	U1480G	34R	2	64-68	1066.5	85.34	39.34	1.44	0.19	-0.21	0.02
7941871	U1480G	41R	2	8-12	1134.3	51.83	37.63	1.41	0.13	-0.24	0.03
7946551	U1480G	47R	3	37-41	1194	151.98	45.85	0.89	0.14	0.78	1.18
7951221	U1480G	53R	2	56-60	1246.7	-6.43	0.23	2.74	0.25	-0.20	0.02
7951081	U1480G	53R	2	123-124	1247.3	30.33	41.46	0.86	0.23	-0.28	0.03
7953211	U1480G	55R	1	19-24	1259.6	-6.24	0.22	-0.03	0.00	-0.20	0.02
7953921	U1480G	56R	4	143-144	1274.8	-5.05	0.18	0.79	0.26	-0.17	0.02
7954781	U1480G	57R	4	93-97	1283.5	71.11	30.58	1.10	0.15	-0.18	0.02
7956701	U1480G	59R	2	72-73	1300.5	-7.98	0.28	-0.03	0.00	-0.27	0.03
7958011	U1480G	60R	1	54-55	1308.5	-5.78	0.20	1.00	0.25	-0.18	0.02

NOTE: **All values in parts per million (ppm).**

Negative values reflect concentrations below detection limits and indicate Minimum Detectable Concentrations (MDCs).
These should be read as "less than" values.

CHAPTER 5

A helium isotope map and mantle tomography reveal a persistent plume in the Ethiopian and Afar Rifts

Brian M. House[1], James Hammond[2], Derek Keir[3,4], Ryan Gallacher[3,5], David R. Hilton[1†], Paolo Scarsi[6], Tsegaye Abebe[6], Sæmundur A. Halldórsson[1,7], Paterno R. Castillo[1]

[†]Deceased

1. Scripps Institution of Oceanography, University of California San Diego, La Jolla, CA 92093, USA

2. Department of Earth and Planetary Sciences, Birkbeck, University of London, London, UK

3. Ocean and Earth Science, University of Southampton, Southampton, UK

4. Dipartimento di Scienze della Terra, Università degli Studi di Firenze, Florence, Italy

5. Department of Earth and Environmental Sciences, Tulane University, New Orleans, LA, 10 70118, USA

6. Institute of Geosciences and Earth Resources, National Research Council of Italy, 56124 Pisa, Italy

7. Nordic Volcanological Center, Institute of Earth Sciences, University of Iceland, Askja, Sturlugata 7, 101 Reykjavík, Iceland

Corresponding author: Brian M. House (bhouse@ucsd.edu)

Abstract

Two main processes have been proposed for initiating and sustaining magmatic continental rifting: a "passive" mechanism in which decompression melting of the upper mantle supplies the magma, and one in which a deep-rooted mantle plume encourages melt production. While a mantle plume has been implicated in initial rifting of the Arabian, Nubian, and Somalian plates in the northern section of the East Africa Rift System, recent seismic and petrologic studies question the current role of deep mantle upwelling in sustaining melt production and continental rifting. In this study, we compare the spatial distribution of He isotope ratios, a highly sensitive tracer of deep mantle input, with tomographic shear-wave velocity models of the Ethiopian and Afar rifts to show that regions of contemporary deep mantle input correlate well with inferred areas of higher than average partial melt content. The most compelling explanation is that deep mantle input continues to facilitate melting, and that the mantle plume therefore has an ongoing role in rifting, though this role may be subordinate to more passive processes in much of Afar.

1 Main text

Flood basalts emplaced at ~30 Ma on what is now the Ethiopian and Yemen Plateaux (Hofmann et al., 1997; Rooney, 2017) are thought to represent the first volcanic expression of deep mantle upwelling associated with a thermochemically anomalous plume beneath East Africa (Courtillot et al., 2003; Simmons et al., 2007). While deep mantle upwelling may have facilitated initial rifting in East Africa (White and McKenzie, 1989), the estimated upper mantle thermal anomaly of ~100°C and melt formation depth of ~90 km are unusual among other plume-influenced regions – Hawaii and Iceland are inferred to have thermal anomalies

of ~300°C with melting commencing at 100-300 km. Additional seismic and petrologic studies in the Ethiopia and Afar rifts also question the ongoing role of a deep mantle plume in melt generation and continental breakup (Rooney et al., 2005; Rychert et al., 2012). Instead, rifting may be sustained by decompressional melting as the region transitions to an oceanic spreading regime, particularly in Afar. The residual geochemical and thermal signature of a mantle plume could therefore represent "fossil" plume material that stalled beneath the lithosphere and is no longer being renewed (Rooney et al., 2012, 2005; Rychert et al., 2012). Therefore, the extent of continued communication between the shallow and deep mantle is unclear, particularly in light of contrasting studies suggesting plume-enhanced melting still contributes to rifting (Kendall et al., 2005). An extensive set of xenolith and mafic lava samples from Ethiopia and Afar (Figure 1) makes this region an ideal target for combining geochemical data and tomographic velocity models to more fully understanding rifting processes.

He isotope ratios ($^4He/^3He$) are an exceptionally sensitive tracer of deep mantle input in part because they span three orders of magnitude in natural samples. Continental crust averages ~0.05 R_A(Marty et al., 1996) where $R_A = 1.4 \times 10^{-6}$, the ratio in air[4]. A maximum of ~50 R_A has been measured in (extinct) hotspots (Stuart et al., 2003), thought to sample the less degassed deep mantle (Craig and Lupton, 1976; Marty et al., 1996), while upper mantle He sources are characterized by isotope ratios of ~6±1 R_A for the subcontinental lithospheric mantle and ~8±1 R_A for the asthenospheric mantle (Gautheron et al., 2005; Graham, 2002). Therefore He isotope ratios above ~9 R_A in mafic mineral fluid inclusions, which capture magmatic volatiles prior to eruption, typically indicate deep mantle upwelling (Marty et al., 1996). The sensitivity of $^3He/^4He$ ratios to mixing of deep and shallow mantle He reservoirs,

as well as the tendency to decrease over time due to ^{4}He production by alpha decay of U and Th, make He isotope ratios ideal for evaluating the degree of current mantle plume involvement.

2 He isoscape and comparison with velocity models

Our He isotope dataset for the Ethiopian Rift and Afar consists of two parts: new data generated for this study and published data (Beccaluva et al., 2011; Halldórsson et al., 2014; Hopp et al., 2004; Marty et al., 1996, 1993; Medynski et al., 2013; Moreira et al., 1996; Pik et al., 2006; Rooney et al., 2012; Scarsi and Craig, 1996). We combined 86 new reliable analyses of ^{3}He/^{4}He from crushed olivine and clinopyroxene phenocrysts separated from basaltic lavas with 75 reliable measurements from a compilation of literature ^{3}He/^{4}He ratios (see Supplemental Discussion). The final dataset consists of 161 measurements, representing 133 unique sample locations that encompass an area of 500,000 km^2, nearly 95% of which now falls within 100 km of a ^{3}He/^{4}He measurement (Figure 1; Supplemental Discussion). He isotope ratios were interpolated through the MER and Afar to visualize spatial variations and compare them with tomographic velocity models (Figure 2).

One of the strengths of ^{3}He/^{4}He as a tracer of deep mantle input can also be a weakness: addition of small amounts of He from shallow reservoirs can lower the high ^{3}He/^{4}He ratio of a mantle plume before lithogenic tracers like olivine Mg content (Mg#) or Sr isotope ratios show evidence of mixing (Füri et al., 2010; Halldórsson et al., 2014). In the strictest sense then, measured ^{3}He/^{4}He ratios higher than upper mantle/crustal ratios represent a lower bound on the true He isotope ratio of a high ^{3}He/^{4}He mantle plume. However, these values are still useful in that they indicate some contribution from deep mantle He, and He

isotope ratios in modern samples that reach values near the maximum found in continental flood basalts suggest an ongoing connection to the deep mantle that allows plume-derived He to reach the surface relatively quickly and with minimal "contamination" from shallow He reservoirs. Likewise, $^{3}He/^{4}He$ ratios well below upper mantle or lithosphere values indicate old continental crust rich in U and Th, which produce ^{4}He by alpha decay.

Lithogenic tracers of deep mantle input occasionally correlate with He isotope ratios (Marty et al., 1994), but in many cases, $^{3}He/^{4}He$ will reflect shallow contributions not recorded in other element or isotope systems, reducing the utility of independent tracers to evaluate how faithfully $^{3}He/^{4}He$ represents deep mantle input (Halldórsson et al., 2014). We therefore employed several strategies to ensure our interpretations of He isotope ratios are on a robust footing. The lack of a clear trend between $^{3}He/^{4}He$ ratios and He concentrations as well as good agreement between the $^{3}He/^{4}He$ ratios of fluid inclusions in olivine and clinopyroxene grains from the same samples suggests our dataset as a whole retains reliable information on deep mantle He incorporation (see Supplement). We furthermore restricted our interpretations to three broad classes of He isotope ratios: (1) those high enough to be best explained by ongoing plume input, (2) intermediate values suggesting significant incorporation of He from shallow reservoirs, and (3) those low enough to be indicative of radiogenic ^{4}He ingrowth in old continental crust. Because the $^{3}He/^{4}He$ ratios from lithospheric mantle xenoliths show a bimodal distribution with peaks at ~8 and 13 R_A (Figure 3, deep mantle He appears to have infiltrated the lithosphere (Figure 3), indicating the canonical upper mantle $^{3}He/^{4}He$ ratio of 8±1 R_A may not be appropriate for this region. To be conservative, we therefore only considered samples with $^{3}He/^{4}He$ ratios above 15 R_A as

indicative of ongoing deep mantle input, ratios between 7 and 15 R_A to represent primarily upper mantle He, and values << 7 R_A to indicate He derived from old continental crust.

The most notable feature in the He isoscape is an elongate ~400 km region of $^3He/^4He$ values above 13 R_A extending through most of the MER (Figure 2). He isotope ratios within this region reach 19.2 R_A, effectively identical to the putative plume value(Marty et al., 1996). This is strong evidence that deep mantle volatiles continue to traverse the upper mantle and crust rapidly enough to reach the surface with minimal contamination from He reservoirs with lower $^3He/^4He$ ratios. The other well-constrained region with plume-like $^3He/^4He$ is Southeast of Erta Ale volcano in northwestern Afar, where $^3He/^4He$ reaches 15.8 R_A, also indicative of substantial input of deep mantle He. The final prominent feature of the isoscape is a region of highly radiogenic $^3He/^4He$ (minimum of 0.034 R_A) near the Tadjoura Gulf. This ~100 km long region, marked by 3 samples below 2 R_A, implies the existence of residual continental crust old enough to incorporate substantial ^4He from U and Th alpha decay. Aside from the Erta Ale area and this region of radiogenic $^3He/^4He$, He isotope ratios are generally around 11 R_A in Afar, which likely reflects mixing of plume and upper mantle/lithospheric material, consistent with previous models (Deniel et al., 1994; Feyissa et al., 2017).

Using high $^3He/^4He$ from young (Pleistocene to recent) lavas as a tracer of contemporary deep mantle input and two models of upper mantle S-wave velocity (V_s) structure(Gallacher et al., 2016; J O S Hammond et al., 2013) (Figure 2), we can link sustained plume input with regions of partial melt in the upper mantle. Low shear velocities in this region are thought to primarily reflect higher than average partial melt content (Hammond et al., 2013; Keir et al., 2009a), so if a mantle plume continues to influence melt production, we would expect a negative correlation between $^3He/^4He$ and V_s anomalies: that

is, regions of plume-like $^3He/^4He$ should overlap regions of high melt content – and therefore low V_s – and vice versa. Indeed our He isoscape correlates well with 75 km depth relative V_s anomalies imaged with body-wave tomography (Hammond et al., 2013) as well as surface wave-derived absolute V_s values (Gallacher et al., 2016) (Figure 4). A shallow mantle (75 km) depth slice maximizes horizontal resolution and is most likely to reflect surface melt expression. Areas of low shear-wave velocity, reaching a -2% anomaly and ~3.85 km s^{-1}, underlie both the MER and Erta Ale region (Figure 2b) (Gallacher et al., 2016; Hammond et al., 2013) in which many $^3He/^4He$ values exceed 13 R_A, indicative of plume input (Figure 2c; Figure 3). Also the region of what we infer to be continental crust near the Tadjoura Gulf corresponds closely with a high velocity anomaly (δV_s up to 0%) and lies near an area where S-wave receiver functions suggest thicker crust (Hammond et al., 2011).

A more quantitative comparison between $^3He/^4He$ and shear-wave velocities reveals the strength of the spatial (anti) correlation that is qualitatively apparent in Figure 2. We compared the relative and absolute shear-wave velocity models with $^3He/^4He$ values at the 68 locations where samples were collected from young lavas (Figure 2 and Supplemental Discussion) to ensure He isotope ratios would reflect modern mantle conditions. Ordinary least-squares linear regressions of this subset of He isotope measurements and the velocities or velocity anomalies in log-linear space gave R^2 values of 0.6 for the relative velocity model (Hammond et al., 2013), indicating a strong negative correlation (Figure 4a), and 0.4 for the absolute velocity model (Gallacher et al., 2016). Even though the correlation with the absolute velocity model is only moderate, that V_s values alone predict ~40% of the variance in He isotope ratios is encouraging given the extreme sensitivity of He isotope ratios to slight contamination from non-plume sources.

We also conducted Monte Carlo simulations to estimate the statistical significance of the two-dimensional spatial correlation between the He isotope and V_s surfaces (Figure 4; Supplemental Discussion). Because passive rifting, in which melting is predominantly decompressional, samples the chemical heterogeneities of the upper mantle (Agranier et al., 2005), it would be expected to equally sample regions of high and low $^3He/^4He$, meaning that any spatial correlation between $^3He/^4He$ and shear-wave velocities would likely be coincidental. We simulated this process by generating random synthetic He isotope values at the sample locations of young lavas, and constructing 10^5 simulated $^3He/^4He$ datasets for each velocity model suggests at most a ~1% chance that these random values would correlate as well with shear-wave velocities as our data do (Figure 4; Supplemental Discussion).

3 Implications of spatial correlation

Therefore, the most compelling explanation for the overall spatial coherence of $^3He/^4He$ and shear-wave velocities is that continued deep mantle input, supplying He at plume-like $^3He/^4He$ values, is involved in melt production (Castillo et al., 2014). Furthermore, because He is a minor volatile phase, upwelling of deep mantle He – which could be decoupled from bulk material upwelling – implies that other deeply-sourced volatile phases (e.g. CO_2, H_2O) are also introduced into the shallow mantle, which encourages melting (Metrich et al., 2014) and itself could help reconcile the difference in melt content inferred from seismic and magnetotelluric studies (Desissa et al., 2013; Hammond et al., 2010; Pommier and Garnero, 2014). Regional- to continental-scale correlations between inferred areas of low mantle velocity and high $^3He/^4He$ ratios have previously been established (Halldórsson et al., 2014; Harðardóttir et al., 2018; Karlstrom et al., 2013; Newell et al., 2005;

Pik et al., 2006), but this is the first time that an He isoscape has been compared quantitatively with fine-scale tomographic velocity models, and our results highlight the unique insight to be gained from combining geochemical and geophysical datasets.

The spatial coherence of $^{3}He/^{4}He$ values and shear-wave velocities suggests sustained plume involvement throughout the region. However, in Afar, the He isoscape and velocity models suggest competing processes that encourage He isotopic homogenization with possible localized upwelling of deep mantle He near Erta Ale and interaction with residual continental crust near the Gulf of Tadjoura. Previous studies suggest that rather than contemporary deep mantle upwelling, decompressional melting or localized diapiric upwelling from a pervasive region of anomalous composition in the upper mantle account for seismic and geochemical observations in Afar (Civiero et al., 2015; Hammond et al., 2014; Hammond et al., 2013; Rychert et al., 2012). While this material may have originated from a plume, it is now isolated with minimal renewal from the deep mantle. Interpretations of S-wave splitting suggest a general SW-NE flow in the upper mantle (Hammond et al., 2014), which is consistent with (broadly) horizontal sub-lithospheric transport of stalled plume material. The deep mantle He isotope signature of plume material stored in the shallow mantle and cut off from deep mantle renewal would be dampened over time by alpha decay and mixing with upper mantle and/or crustal He characterized by lower $^{3}He/^{4}He$ (Gautheron et al., 2005), leading to lower and possibly more homogenous $^{3}He/^{4}He$ values. While we cannot say precisely how He from the deep mantle becomes mixed with that from shallower sources, geochemical and geodynamic observations are consistent with some combination of He homogenization due to dike injection into the lithosphere and incorporation of He from the geochemically depleted upper mantle.

Mixing of He from narrow dikes in the lithosphere is one method by which plume-derived He can mix with upper mantle and crustal He (Gautheron et al., 2005), and dike injection is thought to accommodate much of the rift-related strain in Afar (Keir et al., 2009b; Kendall et al., 2005). He isotope ratios in mantle xenoliths (Figure 3) support the argument that deep mantle He is now stored in the upper mantle, and petrologic studies indicate melt formation in the lithospheric upper mantle. While He diffusion is slow, it does appears to be rapid enough to mix He between dikes and the lithosphere without the aid of other faster He homogenization processes (see Supplement)

Alternatively, spreading rates in Afar are ~15 mm yr^{-1} compared to ~5 mm yr^{-1} in the MER(Fernandes et al., 2004), so while plume input may be sufficient to accommodate necessary melt extraction rates in the MER, rifting in Afar may demand a rate of melt extraction that cannot be accommodated by plume upwelling alone. Instead, decompressional melting of the asthenospheric mantle, which would be expected to introduce He of ~8 R_A, may supply the remaining melt. Petrologic studies suggest that lavas younger than 9 Ma in Afar arise from mixing between plume and lithospheric or geochemically depleted upper mantle material (Deniel et al., 1994; Feyissa et al., 2017; Rooney et al., 2012), suggesting that $^3He/^4He$ ratios of ~11 R_A through much of Afar likely reflect some mixture of plume (~19 R_A) and upper mantle He. The region of elevated $^3He/^4He$ near Erta Ale may represent localized and persistent deep mantle upwelling distinct from that in the MER (Deniel et al., 1994; Feyissa et al., 2017), which is consistent with P-wave velocity models that indicate a small (~200-400 km diameter) thermal upwelling traversing the 410-660 km transition zone beneath this region (Civiero et al., 2015), suggesting a sustained connection between the deep mantle and surface. These interpretations of the He isoscape and velocity models in Afar suggest that

a mantle plume may no longer play a significant role in melt generation in much of the region, with the notable exception of the area around Erta Ale.

The utility of geochemistry to test geophysical models has recently been questioned (Foulger et al., 2015). However, the striking spatial correlation between the He isoscape and upper mantle shear-wave velocities in the MER and Afar implies that geochemical observations can help ground-truth tomographic velocity models. Furthermore, we show that uniting geochemical and seismic models provides greater geodynamic insight than either could alone, and we propose that a mantle plume still influences melt production – and hence continental breakup – throughout Ethiopia and Afar, but that passive rifting processes accompany plume-mediated melt production in Afar.

Acknowledgements

Our thanks to Dave Stegman for input regarding the geodynamics of slow spreading centers. Hannah Stroud digitized the geologic map of Ethiopia and Afar to identify young lavas based on unit ages, and DK is supported by NERC grant NE/L013932/1. Thanks as well to Richard Norris for advice and insight. This work was supported by the Petrology and Geochemistry program of NSF (EAR-1019489 grant to DRH).

Chapter 5 is in revision for publication and will likely appear in *Nature Geoscience* as House, Brian M., Hammond, James, Keir, Derek, Gallacher, Ryan, Hilton, David R., Scarsi, Paolo, Abebe, Tsegaye, Halldórsson, Sæmundur A., and Castillo, Paterno R., 2019.

References

Agranier, A., Blicherttoft, J., Graham, D., Debaille, V., Schiano, P., Albarede, F., 2005. The spectra of isotopic heterogeneities along the mid-Atlantic Ridge. Earth Planet. Sci. Lett. 238, 96–109. https://doi.org/10.1016/j.epsl.2005.07.011

Beccaluva, L., Bianchini, G., Ellam, R.M., Natali, C., Santato, A., Siena, F., Stuart, F.M., 2011. Peridotite xenoliths from Ethiopia: Inferences about mantle processes from plume to rift settings, in: Beccaluva, L., Bianchini, G., Wilson, M. (Eds.), Volcanism and Evolution of the African Lithosphere. The Geological Society of America, Boulder, CO, pp. 77–104.

Castillo, P.R., Hilton, D.R., HalldÃ³rsson, S.A., 2014. Trace element and Sr-Nd-Pb isotope geochemistry of Rungwe Volcanic Province, Tanzania: implications for a Superplume source for East Africa Rift magmatism. Front. Earth Sci. 2, 1–17. https://doi.org/10.3389/feart.2014.00021

Civiero, C., Hammond, J.O.S., Goes, S., Fishwick, S., Ahmed, A., Ayele, A., Doubre, C., Goitom, B., Keir, D., Kendall, J.M., Leroy, S., Ogubazghi, G., Rümpker, G., Stuart, G.W., 2015. Multiple mantle upwellings in the transition zone beneath the northern East-African Rift system from relative P-wave travel-time tomography. Geochemistry, Geophys. Geosystems 16, 2949–2968. https://doi.org/10.1002/2015gc005948

Courtillot, V., Davaille, A., Besse, J., Stock, J., 2003. Three distinct types of hotspots in the Earth's mantle. Earth Planet. Sci. Lett. 205, 295–308.

Craig, H :(, Lupton, J.E., 1976. Primordial neon, helium, and hydrogen in oceanic basalts. Earth Planet. Sci. Lett. 31, 369–385.

Deniel, C., Vidal, P., Coulon, C., Vellutini, P., Piguet, P., 1994. Temporal evolution of mantle sources during continental rifting: the volcanism of Djibouti (Afar). J. Geophys. Res. 99, 2853–2869.

Desissa, M., Johnson, N.E., Whaler, K.A., Hautot, S., Fisseha, S., Dawes, G.J.K., 2013. A mantle magma reservoir beneath an incipient mid-ocean ridge in Afar, Ethiopia. Nat. Geosci. 6, 861–865. https://doi.org/10.1038/ngeo1925

Fernandes, R.M.S., Ambrosius, B.A.C., Noomen, R., Bastos, L., Combrinck, L., Miranda, J.M., Spakman, W., 2004. Angular velocities of Nubia and Somalia from continuous GPS data: implications on present-day relative kinematics. Earth Planet. Sci. Lett. 222, 197–208. https://doi.org/10.1016/j.epsl.2004.02.008

Feyissa, D.H., Shinjo, R., Kitagawa, H., Meshesha, D., Nakamura, E., 2017. Petrologic and geochemical characterization of rift-related magmatism at the northernmost Main Ethiopian Rift: Implications for plume-lithosphere interaction and the evolution of rift

mantle sources. Lithos 282–283, 240–261. https://doi.org/10.1016/j.lithos.2017.03.011

Foulger, G.R., Panza, G.F., Artemieva, I.M., Bastow, I.D., Cammarano, F., Doglioni, C., Evans, J.R., Hamilton, W.B., Lustrino, B.R.J., Thybo, H., Yanovskaya, T.B., 2015. What lies deep in the mantle below? Eos (Washington. DC). https://doi.org/doi:10.1029/2015EO034319

Füri, E., Hilton, D.R., Halldórsson, S.A., Barry, P.H., Hahm, D., Fischer, T.P., Grönvold, K., 2010. Apparent decoupling of the He and Ne isotope systematics of the Icelandic mantle: The role of He depletion, melt mixing, degassing fractionation and air interaction. Geochim. Cosmochim. Acta 74, 3307–3332. https://doi.org/10.1016/j.gca.2010.03.023

Gallacher, R.J., Keir, D., Harmon, N., Stuart, G., Leroy, S., Hammond, J.O.S., Kendall, J.M., Ayele, A., Goitom, B., Ogubazghi, G., Ahmed, A., 2016. The initiation of segmented buoyancy-driven melting during continental breakup. Nat. Commun. 7. https://doi.org/10.1038/ncomms13110

Gautheron, C., Moreira, M., Allègre, C., 2005. He, Ne and Ar composition of the European lithospheric mantle. Chem. Geol. 217, 97–112. https://doi.org/10.1016/j.chemgeo.2004.12.009

Graham, D.W., 2002. Noble Gas Isotope Geochemistry of Mid-Ocean Ridge and Ocean Island Basalts: Characterization of Mantle Source Reservoirs, in: Porcelli, D., Ballentine, C.J., Wieler, R. (Eds.), Reviews in Mineralogy and Geochemistry. pp. 247–317. https://doi.org/10.2138/rmg.2002.47.8

Halldórsson, S.A., Hilton, D.R., Scarsi, P., Abebe, T., Hopp, J., 2014. A common mantle plume source beneath the entire East African Rift System revealed by coupled helium-neon systematics. Geophys. Res. Lett. https://doi.org/10.1002/2014GL059424

Hammond, J.O.S., Kendall, J.M., Angus, D., Wookey, J., 2010. Interpreting spatial variations in anisotropy: Insights into the Main Ethiopian Rift from SKS waveform modelling. Geophys. J. Int. 181, 1701–1712. https://doi.org/10.1111/j.1365-246X.2010.04587.x

Hammond, J O S, Kendall, J.M., Stuart, G.W., Ebinger, C.J., Bastow, I.D., Keir, D., Ayele, A., Belachew, M., Goitom, B., Ogubazghi, G., Wright, T.J., 2013. Mantle upwelling and initiation of rift segmentation beneath the Afar Depression. Geology 41, 635–638. https://doi.org/10.1130/g33925.1

Hammond, J. O S, Kendall, J.M., Stuart, G.W., Ebinger, C.J., Bastow, I.D., Keir, D., Ayele, A., Belachew, M., Goitom, B., Ogubazghi, G., Wright, T.J., 2013. Mantle upwelling and initiation of rift segmentation beneath the Afar Depression. Geology 41, 635–638. https://doi.org/10.1130/G33925.1

Hammond, J.O.S., Kendall, J.M., Stuart, G.W., Keir, D., Ebinger, C.J., Ayele, A., Belachew,

M., 2011. The nature of the crust beneath the Afar triple junction: Evidence from receiver functions. Geochemistry Geophys. Geosystems 12. https://doi.org/10.1029/2011GC003738

Hammond, J.O.S., Kendall, J.M., Wookey, J., Stuart, G.W., Keir, D., Ayele, A., 2014. Differentiating flow, melt, or fossil seismic anisotropy beneath Ethiopia. Geochemistry, Geophys. Geosystems 15, 1878–1894. https://doi.org/10.1002/

Harðardóttir, S., Halldórsson, S.A., Hilton, D.R., 2018. Spatial distribution of helium isotopes in Icelandic geothermal fluids and volcanic materials with implications for location, upwelling and evolution of the Icelandic mantle plume. Chem. Geol. 480, 12–27. https://doi.org/10.1016/j.chemgeo.2017.05.012

Hofmann, C., Courtillot, V., Feraud, G., Rochette, P., Yirgu, G., Ketefo, E., Pik, R., 1997. Timing of the Ethiopian flood basalt event and implications for plume birth and global change. Nature 389, 838–841.

Hopp, J., Trieloff, M., Altherr, R., 2004. Neon isotopes in mantle rocks from the Red Sea region reveal large-scale plume-lithosphere interaction. Earth Planet. Sci. Lett. 219, 61–76. https://doi.org/10.1016/S0012-821X(03)00691-5

Karlstrom, K.E., Crossey, L.J., Hilton, D.R., Barry, P.H., 2013. Mantle ^{3}He and CO2 degassing in carbonic and geothermal springs of Colorado and implications for neotectonics of the Rocky Mountains. Geology 41, 495–498. https://doi.org/10.1130/g34007.1

Keir, D., Bastow, I.D., Whaler, K.A., Daly, E., Cornwell, D.G., Hautot, S., 2009a. Lower crustal earthquakes near the Ethiopian rift induced by magmatic processes. Geochemistry, Geophys. Geosystems 10, 1–3. https://doi.org/10.1029/2009GC002382

Keir, D., Hamling, I., Ayele, A., Calais, E., Ebinger, C.J., Wright, T.J., Jacques, E., Mohamed, K., Hammond, J.O.S., Belachew, M., Baker, E., Rowland, J., Lewi, E., Bennati, L., 2009b. Evidence for focused magmatic accretion at segment centers from lateral dike injections captured beneath the Red Sea rift in Afar. Geology 37, 59–62. https://doi.org/10.1130/G25147A.1

Kendall, J.M., Stuart, G.W., Ebinger, C.J., Bastow, I.D., Keir, D., 2005. Magma-assisted rifting in Ethiopia. Nature 433, 146–148. https://doi.org/10.1038/nature03161

Marty, B., Appora, I., Barrat, J., Deniel, C., Vellutini, P., Vidal, P., 1993. He, Ar, Sr, Nd and Pb isotopes in volcanic rocks from Afar: Evidence for a primitive mantle component and constraints on magmatic sources. Geochem. J. 27, 219–228.

Marty, B., Pik, R., Gezahegn, Y., 1996. Helium isotopic variations in Ethiopian plume lavas: nature of magmatic sources and limit on lower mantle contribution. Earth Planet. Sci.

Lett. 144, 223–237. https://doi.org/10.1016/0012-821X(96)00158-6

Marty, B., Trull, T., Lussiez, P., Basile, I., Tanguy, J.-C., 1994. He, Ar, O, Sr, and Nd isotope constraints on the origin and evolution of Mount Etna magmatism. Earth Planet. Sci. Lett. 126, 23–39.

Medynski, S., Pik, R., Burnard, P., Williams, A., Vye-Brown, C., Ferguson, D., Blard, P.H., France, L., Yirgu, G., Seid, J.I., Ayalew, D., Calvert, A., 2013. Controls on magmatic cycles and development of rift topography of the Manda Hararo segment (Afar, Ethiopia): Insights from cosmogenic ^{3}He investigation of landscape evolution. Earth Planet. Sci. Lett. 367, 133–145. https://doi.org/10.1016/j.epsl.2013.02.006

Metrich, N., Zanon, V., Creon, L., Hildenbrand, A., Moreira, M., Marques, F.O., 2014. Is the "Azores Hotspot" a Wetspot? Insights from the Geochemistry of Fluid and Melt Inclusions in Olivine of Pico Basalts. J. Petrol. 55, 377–393. https://doi.org/10.1093/petrology/egt071

Moreira, M., Valbracht, P.J., Staudacher, T., Allègre, C.J., 1996. Rare gas systematics in RedSea ridge basalts. Geophys. Res. Lett. 23, 2453–2456.

Newell, D.L., Crossey, L.J., Karlstrom, K.E., Fischer, T.P., Hilton, D.R., 2005. Continent-scale links between the mantle groundwater systems of the western United States: evidence from travertine springs and regional He isotope data. GSA Today 15, 4–10. https://doi.org/10.1130/1052-5173(2005)015<4:CSLBTM>2.0.CO;2

Pik, R., Marty, B., Hilton, D.R., 2006. How many mantle plumes in Africa? The geochemical point of view. Chem. Geol. 226, 100–114.

Pommier, A., Garnero, E.J., 2014. Petrology-based modeling of mantle melt electrical conductivity and joint interpretation of electromagnetic and seismic results. J. Geophys. Res. Solid Earth 119, 4001–4016. https://doi.org/10.1002/

Rooney, T.O., 2017. The Cenozoic magmatism of East-Africa: Part I — Flood basalts and pulsed magmatism. Lithos 286–287, 264–301. https://doi.org/10.1016/j.lithos.2017.05.014

Rooney, T.O., Furman, T., Yirgu, G., Ayalew, D., 2005. Structure of the Ethiopian lithosphere: Xenolith evidence in the Main Ethiopian Rift. Geochim. Cosmochim. Acta 69, 3889–3910. https://doi.org/10.1016/j.gca.2005.03.043

Rooney, T.O., Hanan, B.B., Graham, D.W., Furman, T., Blichert-Toft, J., Schilling, J.G., 2012. Upper Mantle Pollution during Afar Plume-Continental Rift Interaction. J. Petrol. 53, 365–389. https://doi.org/10.1093/petrology/egr065

Rychert, C.A., Hammond, J.O.S., Harmon, N., Michael Kendall, J., Keir, D., Ebinger, C.,

Bastow, I.D., Ayele, A., Belachew, M., Stuart, G., 2012. Volcanism in the Afar Rift sustained by decompression melting with minimal plume influence. Nat. Geosci. 5, 406–409. https://doi.org/10.1038/ngeo1455

Scarsi, P., Craig :(, 1996. Helium isotope ratios in Ethiopian Rift basalts. Earth Planet. Sci. Lett. 144, 505–516.

Simmons, N.A., Forte, A.M., Grand, S.P., 2007. Thermochemical structure and dynamics of the African superplume. Geophys. Res. Lett. 34, 1–5. https://doi.org/10.1029/2006GL028009

Stuart, F.M., Lass-Evans, S., Fitton, J.G., Ellam, R.M., 2003. High $^{3}He/^{4}He$ ratios in picritic basalts from Baffin Island and the role of a mixed reservoir in mantle plumes. Nature 424, 57–59.

White, R., McKenzie, D., 1989. Magmatism at rift zones: the generation of volcanic continental margins and flood basalts. J. Geophys. Res. 94, 7685–7729.

Figures

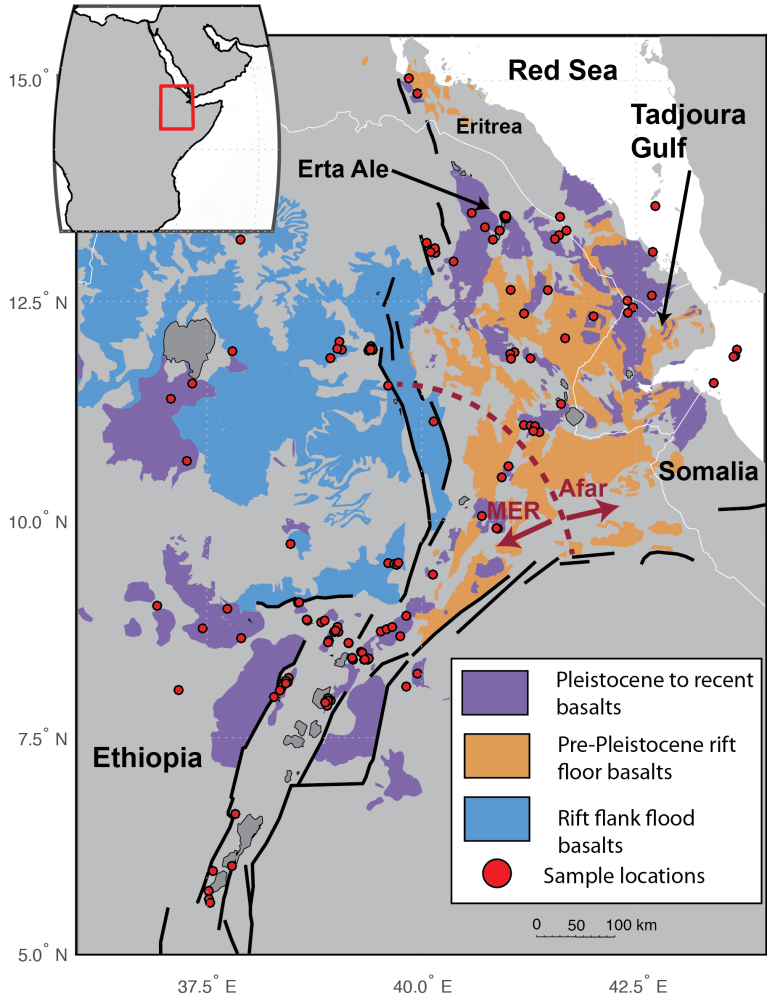

Figure 5.1. Overview map of major basaltic volcanic deposits grouped by age in Ethiopia and Afar and rift-zone bounding faults after Merla et al. (1973). Purple regions represent mafic lavas of Pleistocene to recent ages, orange unit represents older rift basalts, and blue unit represents rift-flank flood basalts. Red points indicate all sample locations used to construct the He isoscape, and dark red arc indicates the operational boundary between the Main Ethiopian Rift (MER) and Afar used in this paper. The total $^{3}He/^{4}He$ database consists of 161 reliable data points representing 133 unique locations. The subset of 68 samples that could be positively identified as coming from Pleistocene to recent lavas (purple) was used in quantitative comparisons between $^{3}He/^{4}He$ and tomographic velocities.

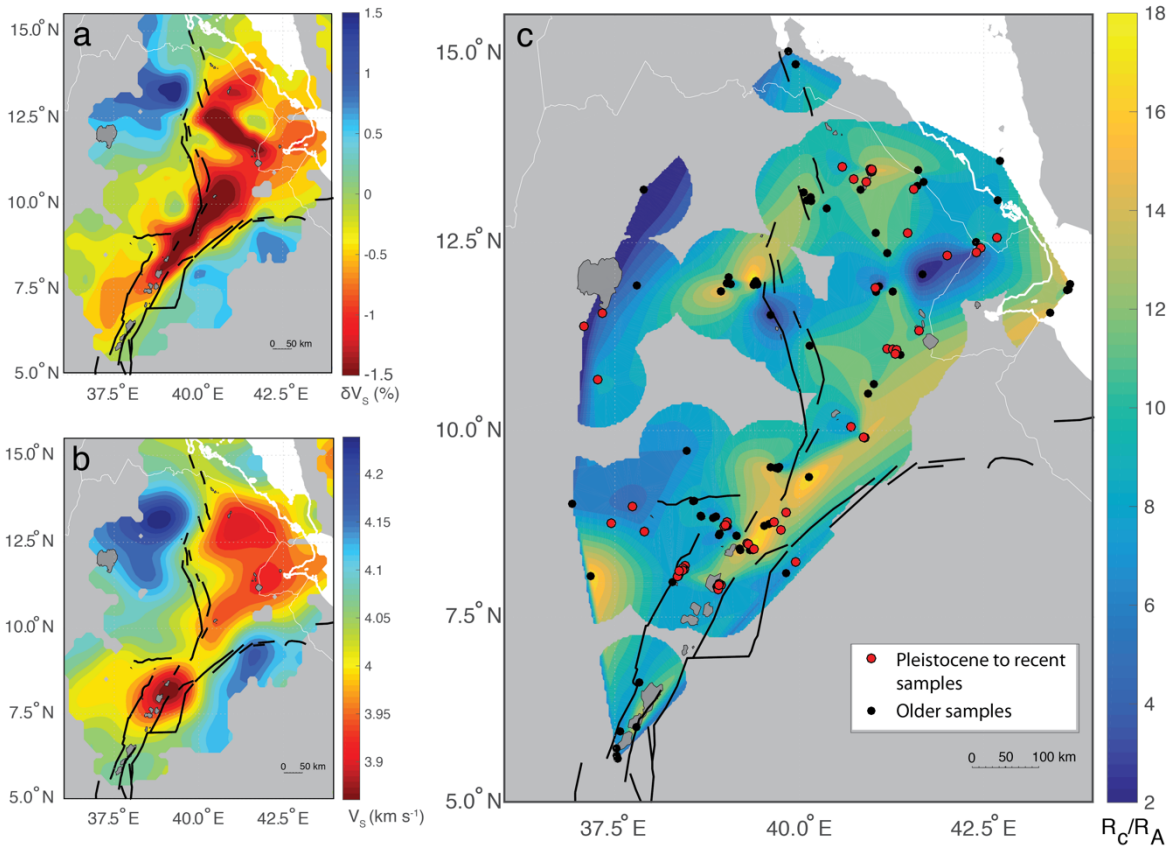

Figure 5.2. (a) 75 km depth slice of relative shear velocity (δV_s) from body-wave tomography (Hammond, et al. 2013), (b) absolute V_s averaged between 40 and 132 km from surface wave tomographic model (Gallacher et al. 2016), and (c) isoscape of all $^3He/^4He$ data deemed reliable (see Supplemental Discussion). The color scale saturates at 18 RA. To minimize the influence of numerical artifacts during the interpolation of $^3He/^4He$ data, we have greyed-out isoscape regions that are greater than 75 km from a He isotope measurement (see Supplemental Discussion). Locations of samples taken from Pleistocene to recent lavas are shown in red and other sample locations in black. In all panels, the main rift boundary faults are shown with thick black lines.

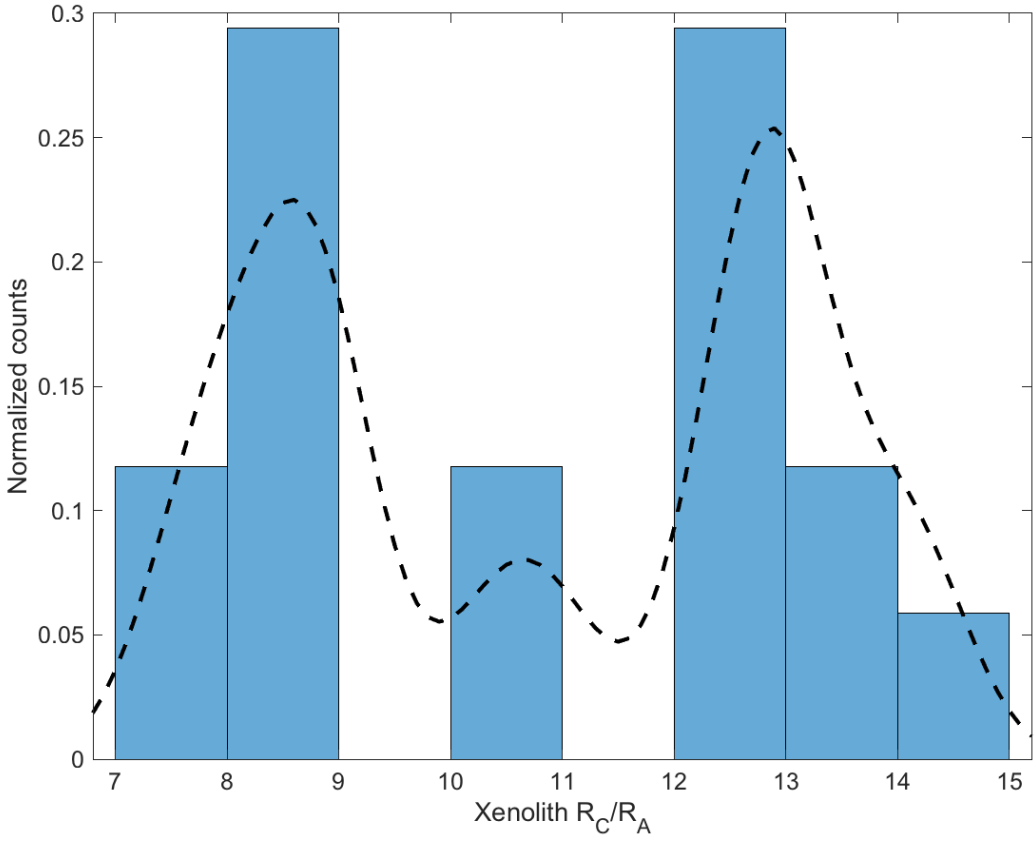

Figure 5.3. Histogram of He isotope ratios of mantle lithosphere xenoliths (blue) show a distinct bimodal distribution emphasized by a probability density function estimated from the data (black dotted line).
The peak centered around 8 R_A matches the global value for the geochemically depleted upper mantle, while the peak centered at ~12-13 R_A shows that the mixing of plume (~19 R_A) and upper mantle He is pervasive, supporting the interpretation that melting of the upper mantle without sustained deep mantle He input would give $^3He/^4He$ values between ~8 and 15 R_A.

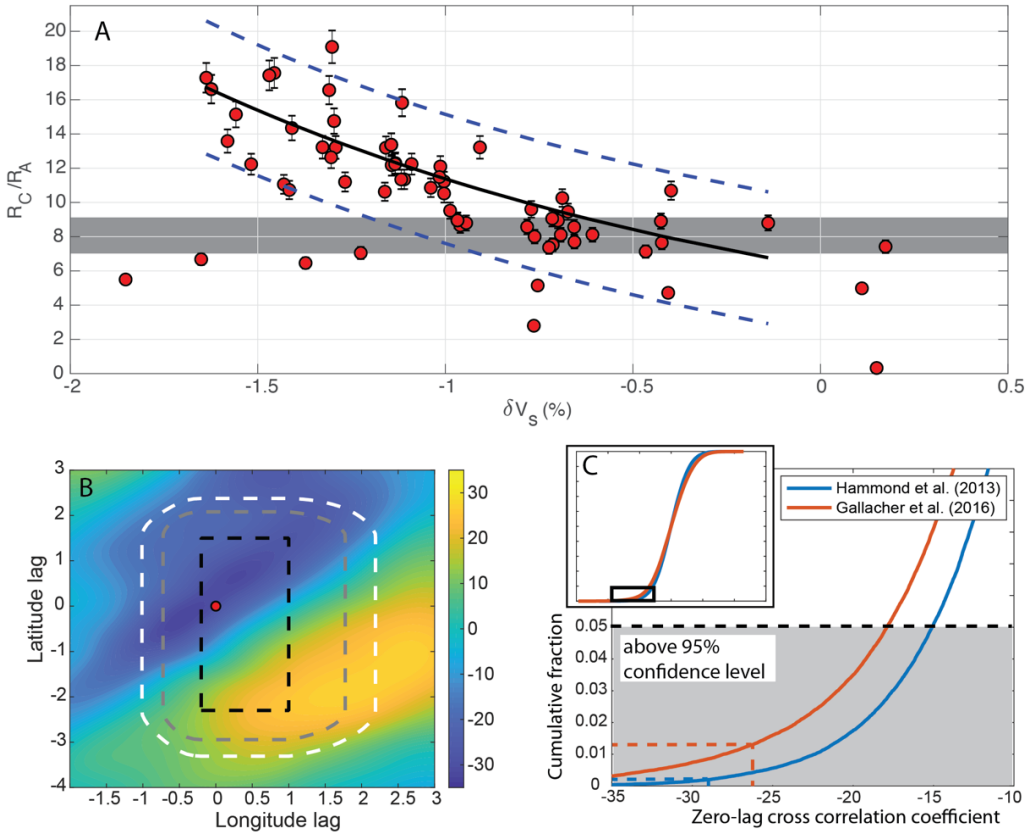

Figure 5.4. (a) comparison of 3He/4He and δVs values at He isotope sample locations, (b) contour plot of 2D cross correlation coefficients between He isotope surface and δVs model, and (c) results of Monte-Carlo simulations of zero lag cross-correlation coefficients between synthetic He isotope distributions and the velocity models of Hammond et al. (2013) and Gallacher et al. (2016). Black curve in (a) is the exponential least-squares best fit curve of $^3He/^4He$ greater than depleted upper mantle values (shaded region) and δV_s. Error bars show estimated two-sigma uncertainty, and dotted blue lines represent 95% confidence interval for curve of best fit. In (b), the red point shows the location of zero lag in both latitude and longitude (i.e. He isotope surface and δV_s latitude and longitude aligned), and the fact that this point is near a minimum in the correlation coefficients indicates a strong negative correlation between $^3He/^4He$ and δV_s values. The rectangle in black represents the latitude and longitude lag values that result in full overlap between $^3He/^4He$ and δV_s surfaces, while the region within the grey curve represents 95% overlap, and that within the white curve represents 90% overlap. In (c), the results of 10^5 Monte-Carlo simulations (see Supplemental Discussion) using synthetic random He isotope distributions are compared with two velocity models to establish a full cumulative distribution function (inset) of the zero lag cross correlation coefficients. The black rectangle shows the region of enlargement, and dotted vertical lines indicate the values of the correlation coefficients using our dataset. Both velocity models give results well within the 95% confidence interval (shaded region).

Chapter 5 Appendix

1. Methods

1.1 Sample selection, preparation, and analysis

New data were generated by crushing olivine and/or clinopyroxene phenocrysts separated from porphyritic lavas either collected during a 2011-2012 field campaign or provided by P. Scarsi from the University of Pisa collection. All samples were from the Ethiopian Rift, Afar, or the rift flank basalts on the northern Ethiopian Plateau. Samples were prepared and analyzed according to standard procedures that are presented in detail elsewhere (Shaw et al., 2006). To summarize, phenocrysts of olivine or clinopyroxene (cpx) were separated under a binocular microscope before ultrasonication in a 1:1 methanol:acetone bath. Samples were repicked following sonication to minimize adhering matrix and were loaded into online crushers and pumped to ultra-high vacuum overnight before being crushed in vacuo preferentially release He from fluid inclusions while minimizing liberation of lattice-hosted He (which can reflect either radiogenic or cosmogenic influence; Scarsi, 2000). Previous stepwise crushing experiments (Hilton et al., 2011, 1995, 1993) and comparisons between crushing and heating of samples suggest minimal lattice bound radiogenic ^{4}He and cosmogenic ^{3}He release during crushing (Hilton et al., 1993; Marty et al., 1996; Medynski et al., 2013).

A series of gas purification steps were employed to remove H_2O, CO_2, and other active gases. He and Ne were captured on a cryogenic charcoal trap held below 20 K; He was subsequently released at 35 K, and the $^{3}He/^{4}He$ ratio was measured using electron multiplier (for ^{3}He) and Faraday cup (^{4}He) detectors on a MAP-215 noble gas mass spectrometer.

Following He analysis, Ne was released at 90 K and the $^{4}He/^{20}Ne$ ratio was used to monitor for leaks and to correct for minor air contamination.

Full procedural blanks were measured prior to the crushing of each sample and crushing was initiated only when blanks were below ~3 x 10^{-10} cm^3 STP He (~1.2 x 10^{-14} mol He) or showed repeatability within the level of analytical uncertainty between at least two repeated full procedural blanks. The maximum level for which a sample was run was 6.8 x 10^{-10} cm^3 STP He (2.8 x 10^{-14} mol He) after three full procedural blanks agreed within analytical uncertainty. The magnitude of the He blank and He amount analyzed for each sample were compared as one selection criterion to test data reliability (see Section 2.2).

2. Data

2.1 Data handling

All published He isotope measurements from the rectangular region extending NE from 5 N, 36 E to 15.5 N, 44 E, covering the Ethiopian Rift, rift flank flood basalts, Afar, and select samples from the Red Sea and Gulf of Aden spreading centers were compiled from the dataset in (Halldórsson et al., 2014) using previously published data (Beccaluva et al., 2011; Halldórsson et al., 2014; Hopp et al., 2004; Marty et al., 1996, 1993; Medynski et al., 2013; Moreira et al., 1996; Pik et al., 2006; Rooney et al., 2012; Scarsi and Craig, 1996). This set of 155 $^{3}He/^{4}He$ measurements was screened for data reliability and assigned confidence levels based on selection criteria presented in Section 2.2 below. Of the 155 published measurements, 75 made on phenocrysts separated from lavas were deemed to be reliable (confidence level 1), and these were incorporated in the isoscape presented in Figure 2 of the

main text. An additional 108 new analyses were reduced to 86 deemed reliable by more restrictive selection criteria (see Section 2.2).

We use quadrature uncertainty propagation to estimate the standard deviation of R_C/R_A values reported. Our estimations of uncertainty, presented in Table 2 as twice the standard deviation, incorporate analytical uncertainty from the measurement of our reference standard (SIO pier air, $R/R_A = 1$), full procedural blanks, and samples. Due to the inherent difficulties in measuring isotope ratios involving scarce species like ^3He (Coath et al., 2013; Ogliore et al., 2011), we are confident our approach gives reasonable estimates of analytical uncertainty. When not specified in published data, uncertainties were assumed to be at the one sigma level and were therefore doubled before the selection criteria were applied.

It is important to note that analytical uncertainty estimates for new and literature data reflect only the uncertainty in $^3He/^4He$ measurement and not how representative a sample may be of the original He source. For example, the extremely low $^3He/^4He$ associated with highly radiogenic sources are typically accompanied by correspondingly low absolute uncertainties, such as 0.009 ± 0.0037 R_A for sample E253 (Medynski et al., 2013). However, this sample is clearly dominated by radiogenic He, which has overwhelmed any initial deep mantle $^3He/^4He$ signature, making this value unrepresentative of the underlying mantle source. Such data are retained for the construction of the isoscape but are excluded from further discussion of mantle volatile composition.

2.2 Selection Criteria

Figure 1 presents the selection criteria used to evaluate the reliability of previously published (1a) and new (1b) data. The stricter selection criteria applied to new data, for

which more information is available, led us to include new data of confidence levels 1 and 2 in construction of the isoscape and subsequent interpretations. Data from the literature database with confidence level 1 were combined with these new data to construct an exhaustive collection of reliable measurements. When references gave a range of sample masses analyzed instead of a mass for each sample, the lower bound of the mass range was chosen to generate a conservative estimate of the amount of He analyzed.

2.4 Integrity of He isotope measurements

Monitoring the $^{4}He/^{20}Ne$ ratio is a standard method by which potential air contamination, either from small pockets of trapped air in phenocrysts or from vacuum leaks induced by the mechanical stress of crushing, can be evaluated. We adopt a modified air-correction method to account for ^{20}Ne abundance above blank levels during crushing (Halldórsson et al., 2014). When ^{20}Ne levels in the full procedural blanks were higher than in the corresponding samples, we disregarded the air correction ($X = \infty$ due to a blank-corrected $^{4}He/^{20}Ne$ ratio of 0 in the sample) as this provided the best agreement between three replicates of C-426 olivines. X values listed as N.A. in the above tables indicate samples for which the air correction was unnecessary.

The most reliable method by which the fidelity of bulk sample sets can be assessed is the comparison of He concentration and R_C/R_A value (Halldórsson et al., 2014; Hilton et al., 2011). The lack of a clear trend in R_C/R_A values at either high or low He concentrations (Figure S2) suggests that samples in our dataset are not being substantially affected by addition to, or removal of, original He. Pre- or post-eruptive addition of radiogenic He is likely to lead to high He concentrations associated with low R_C/R_A values. If this process

were widespread, it would manifest as a significant trend toward lower R_C/R_A values at high He concentrations, which is not apparent from Figure S2. Alternatively degassing of magmatic volatiles and contamination can lead to a trend toward lower R_C/R_A values at low [He] as loss of He with a deep mantle signature makes the isotopic ratio of the residual He more sensitive to incorporation of small amounts of upper mantle/lithospheric He (Hopp et al., 2004). However, such a trend is not apparent from the plot of the bulk dataset in Figure S2. Plots of [He] vs. R_C/R_A were prepared for data from each reference (not shown) to elucidate any trends or biases that may indicate the measured He isotope ratios are not representative of the parental He and instead reflect $^3He/^4He$ modification. No trends are apparent in any of the datasets, providing one line of evidence that the data – considered on the whole – represent the parental He source rather than alteration artifacts.

The degree to which fluid inclusions reflect the parental volatile source can additionally be evaluated by comparing olivine and cpx $^3He/^4He$ ratios and [He] (figure S3). Fluid inclusions in olivine often represent the first fraction of volatiles trapped as a melt cools and are also less susceptible to later overprinting by other He sources, frequently making them a more reliable record of original melt composition (Hilton et al., 1995). Therefore, the relationship between the volatiles in olivine and cpx can be used to further evaluate how well the measured He represents the pristine parental source. The distribution of all [He] and R_C/R_A values from fluid inclusions in olivine and cpx are indistinguishable at the 95 % confidence level ($p = 0.35$; $df = 50.7$ for R_C/R_A and $p = 0.26$; $df = 32.2$ for [He] from two-sample unpaired t-test) suggesting the dataset as a whole is likely more reflective of parental volatile composition than modification processes.

Additionally, Figure S3 compares R/R_A values measured in olivine and cpx phenocrysts to the 1:1 line expected if all fluid inclusions in both phases incorporated He from the same source and experienced no subsequent He isotopic alteration. While $^3He/^4He$ ratios are frequently higher for olivine than cpx, they tend to agree reasonably well, suggesting that major alterations in He isotope ratio and [He] are not occurring either between the time of olivine and cpx formation in the melt or post-eruptively due to radiogenic ingrowth or He loss, both processes that would preferentially lower the cpx $^3He/^4He$ ratio (Hilton et al., 1995).

Finally, the [He], $^3He/^4He$ trajectories of coexistent olivine and cpx are shown in Figure S4 as a final method of evaluating data integrity. Because radiogenic in-growth and shallow (low R_C/R_A) He incorporation during magmatic stalling would be expected to lead to higher [He] and lower $^3He/^4He$ ratios for cpx phenocrysts compared to olivine, we focus on those pairs that show a negative trajectory from olivine to cpx. In Figure S4b we have relocated the olivine measurements to the origin and now consider only the differences in [He] and $^3He/^4He$ between olivine and cpx He measurements (the [He] and $^3He/^4He$ distance). This diagram makes the olivine-to-cpx trajectories clearer and emphasizes a strong negative trajectory for five samples. Of these, two (R-Eth-177A and R-Eth-122B) are from the rift flank flood basalts, and one (B-390) is from near the region of exceptionally low $^3He/^4He$ ratio in Afar (see Figure 2). Because the rift flank basalts formed around 30 Ma, they have had ample time for radiogenic ingrowth of ^4He from U and Th decay, and because these two elements are more easily incorporated into the cpx lattice, their decay would be expected to disproportionally affect cpx He measurements. Melting experiments of crushed powder residues from this region released up to 1250 x 10^{-9} cm^3 STP/g at a $^3He/^4He$ of ~0.009 R_A, indicating substantial accumulation of lattice-sited radiogenic ^4He (Marty et al., 1996). The

strong negative trajectory of sample B-390 near the inferred region of relict continental lithosphere in Afar is consistent with incorporation of radiogenic He, which would be expected to alter the [He] and $^3He/^4He$ ratio of cpx relative to those of olivine (Füri et al., 2011).

2.5 Xenolithic evidence for plume modification of lithospheric $^3He/^4He$

Published $^3He/^4He$ from xenoliths shows a distinct bimodal trend with one peak centered around the canonical upper mantle average of ~8 Ra and a second distinct peak at ~13 Ra and only one sample between 8 and 13 Ra (Figure 3). We take the peak at ~13 Ra as strong evidence that upper mantle and lithospheric He has been modified by input of plume He with $^3He/^4He$ ratio above 13 Ra, but the peak at ~8 Ra indicates that some regions of the upper mantle and lithosphere may persist largely unmodified by deep He input. This suggests spatially heterogeneous mixing of He from deep and shallow sources and therefore that $^3He/^4He$ above the upper mantle average of ~8 Ra may not necessarily provide conclusive evidence of modern plume input. Rather, ratios up to ~13 Ra may result from decompressional melting of the plume-modified upper mantle/lithosphere.

The diffusion of He through mineral lattices is likely to be much slower than other processes such as grain-boundary channelization and hydrothermal circulation, which leads to $^3He/^4He$ ratios up to 16 R_A in hydrothermal samples indicative of rapid, fluid-mediated transport of deep mantle He (Craig, 1977). Estimating the length scales of He diffusion through olivine should therefore give a lower bound on the extent to which He from dikes and the surrounding lithosphere may be homogenized. Using He diffusion parameters in olivine (Wang et al., 2015) and inferred upper mantle temperatures (Armitage et al., 2015; Rooney et

al., 2011), we estimate that, barring dramatic differences in dike and lithosphere He concentrations, diffusion through the olivine lattice would mix He over at least ~30 m in 30 Myr. ($\tau = t^2/D$ where τ is the characteristic length-scale of diffusion, t is the time diffusion is allowed to operate, and D is the temperature-dependent diffusivity). This distance while small, is more than an order of magnitude greater than the estimated half-width of recent dikes (Keir et al., 2009). Indeed, a cluster of lithospheric xenoliths yield $^3He/^4He$ ratios around ~13 R_A (Halldórsson et al., 2014; Scarsi and Craig, 1996), intermediate between deep and upper mantle values, providing evidence for the incorporation of plume He in the lithosphere (see Figure S6).

2.6 Construction of isoscape

A grid with 0.05° (~5 km) latitude and longitude spacing throughout the region of interest was used to interpolate He isotope data using a natural neighbor interpolation scheme. This process has the benefit of relaxing the surface to a regional mean outside the neighborhood of peaks or valleys in the data so that extrema do not dominate in regions with poor data coverage. To minimize interpolation into such poorly constrained regions – which is critical to maximize the integrity of the surface – grid points greater than 75 km from a data point are excluded from Figure 2. Because fluid inclusion He isotope ratios are, sensu stricto, a lower bound on the true parental isotope ratio, when coexistent olivine and clinopyroxene were both analyzed, the higher ratio (typically from olivine) was used to constrain the isoscape. Comparisons between $^3He/^4He$ ratios generated from olivine and coexistent clinopyroxene are discussed in Section 2.4. He isotope ratios from xenoliths were excluded during construction of the isoscape and subsequent comparison with Vs structure since the

processes that may have modified the lithospheric $^{3}He/^{4}He$ (see Section 2.5) may cause xenolithic $^{3}He/^{4}He$ to be less representative of true mantle structure than phenocrystic $^{3}He/^{4}He$.

2.7 Spatial coverage

Addition of the 86 new reliable data points to the literature database of 75 values dramatically improves the spatial density of He isotope ratios measured in the MER and Afar. Distance testing was conducted using the He isotope interpolation grid with latitude and longitude intervals of 0.05° to determine the distance of each grid point from the nearest point at which a He isotope measurement exists. An empirical cumulative distribution function generated from this process indicates that, for the combined set of new and literature data, 50% of the grid points lie within ~40 km of a He isotope measurement and 95% lie within ~100 km. Separate coverage analyses calculated for published data and the complete dataset (published and new) are summarized in Figure S5.

2.8 Age cutoff for samples compared to seismic velocities

We only consider samples from Pleistocene to Recent basalts for comparison with seismic velocities to avoid comparing samples that may have been displaced after eruption or may not represent modern mantle structure. Geodetically determined rifting rates for Ethiopia and Afar vary from ~5 mm/yr in the Main Ethiopian Rift to ~15 mm/yr in Afar based on rotation pole location and rotation rate for the Nubian and Somalian plates (Fernandes et al., 2004). Therefore, lavas erupted in the earliest Pleistocene would be expected to be displaced from their location of eruption by no more than ~12 km in the Main Ethiopian Rift and up to

~ 35 km in Afar, distances that are minor considering the imperfect spatial resolution of the interpolated regions of the He isoscape. Furthermore the "African Superplume" appears to be associated with SW to NE upper mantle flow (Hammond et al., 2014), and assuming a reasonable upper mantle velocity of 30 mm yr^{-1} implies a maximum displacement of ~70 km along the strike of the rift since 2.33 Ma. If the rift-perpendicular displacement of (the oldest) lavas from their location of eruption and sub-lithospheric translation of upper mantle material substantially affected our spatial comparisons of He isotope ratios and S-wave velocities, we would expect to see the He isotope anomalies elongated in the direction of spreading and generally be sited to the southwest of velocity anomalies. These processes may account for the slight spatial disjunction of δVs and $^3He/^4He$ at Erta Ale and the inferred block of remnant continental crust to the northwest of the Tadjoura Gulf. However, the reasonably good spatial correlation of relative velocity and $^3He/^4He$ in the Debre-Zeyit fault zone, which is nearly perpendicular to the spreading axis in the MER suggests that our Pleistocene age cutoff does not substantially bias our spatial comparisons.

For samples displaying clearly radiogenic $^3He/^4He$ (below the sub-continental lithospheric mantle average of ~6 R_A), we relax the age constraint to include lavas erupted within the last ~5 My. since these lavas are unlikely to represent mantle structures that may evolve over time. Instead these samples, most of which are centered in the region of low $^3He/^4He$ near the Tadjoura Gulf, trace the extent of continental crust capable of substantially lowering $^3He/^4He$. Such crustal blocks within the current region of rifting are likely to be remnants from initial rifting and therefore are long-lasting features that would be expected to influence upper mantle seismic velocities on similarly long timescales. Therefore, the greatest concern with these samples is that rift-related extension may have displace them from

their place of eruption, but even assuming a regional maximum of 15 mm/yr of extension, these samples would be displaced by a maximum of ~75 km over 5 My., or approximately half the diameter of the high δVs region near the Tadjoura Gulf. This offset would therefore not be substantial enough to alter the overall spatial correlation of $^{3}He/^{4}He$ and δVs.

2.9 Spatial correlation between He isoscape and seismic velocity anomalies

We employed two methods to establish a correlation between He isotope measurements and seismic velocity anomaly values: 1) comparison of both values at points where He data were measured, and 2) an evaluation of the goodness-of-fit between the He isotope and Vs/δVs surfaces using Monte Carlo simulations with random He isotope data. The first method reveals a clear correlation between $^{3}He/^{4}He$ values and their corresponding shear-wave velocities, established by interpolating the already densely-sampled velocity surfaces to the precise locations of He samples from young lavas. In the first approach, we fit a generic exponential decay function of the form ae^{-bx} (where a and b are empirically fit constants and x is the $^{3}He/^{4}He$ ratio) to the data because $^{3}He/^{4}He$ ratios should never equal zero, regardless of seismic velocity. Fitting the data with other functions such polynomial or rational functions did not greatly change the degree of fit. The limitation of this technique, however, is that it loses information about the spatial distribution of $^{3}He/^{4}He$ ratios and shear-wave velocities.

We therefore also conducted a cross-correlation analysis of the two surfaces, the results of which appear in Figure 3 for the Hammond et al. (2013) relative velocity model. Both He isotope and shear-wave velocity values were first normalized by subtracting the mean value and dividing by the range of the mean-subtracted values to give values between 0

and 1. The global minimum near zero lag in both the x and y (longitude and latitude) directions indicates that the two surfaces are well correlated with high $^{3}He/^{4}He$ ratios corresponding to low δVs values and vice versa. We then estimated the chances of obtaining a zero-lag cross-correlation coefficient at least as great in magnitude as what our datasets show by Monte Carlo simulations using random synthetic He isotope datasets. For each of 10^5 iterations, He isotope ratios were randomly chosen using the probability density function empirically defined by our measured values and assigned to the same locations as values in our dataset. The empirical probability distribution generated from this simulation (Figure 3) suggests that the odds of a random He isotope dataset giving a zero-lag cross correlation coefficient at least as great in magnitude as the value for our datasets is ~1%. We are therefore comfortable asserting that the degree of spatial correlation between our two datasets well exceeds the 95% confidence interval typically used to define statistical significance.

References

Armitage, J.J., Ferguson, D.J., Goes, S., Hammond, J.O.S., Calais, E., Rychert, C.A., Harmon, N., 2015. Upper mantle temperature and the onset of extension and break-up in Afar, Africa. Earth Planet. Sci. Lett. 418, 78–90. https://doi.org/10.1016/j.epsl.2015.02.039

Beccaluva, L., Bianchini, G., Ellam, R.M., Natali, C., Santato, A., Siena, F., Stuart, F.M., 2011. Peridotite xenoliths from Ethiopia: Inferences about mantle processes from plume to rift settings, in: Beccaluva, L., Bianchini, G., Wilson, M. (Eds.), Volcanism and Evolution of the African Lithosphere. The Geological Society of America, Boulder, CO, pp. 77–104.

Coath, C.D., Steele, R.C., Lunnon, W.F., 2013. Statistical bias in isotope ratios. J. Anal. At. Spectrom. 28, 52–58.

Craig, H:(, 1977. Isotope Geochemistry and Hydrology of Geothermal Waters in the Ethiopian Rift Valley, Technical Report prepared for the United Nations Development Program and the Ethiopian Government. Scripps Institution of Oceanography.

Fernandes, R.M.S., Ambrosius, B.A.C., Noomen, R., Bastos, L., Combrinck, L., Miranda, J.M., Spakman, W., 2004. Angular velocities of Nubia and Somalia from continuous GPS data: implications on present-day relative kinematics. Earth Planet. Sci. Lett. 222, 197–208. https://doi.org/10.1016/j.epsl.2004.02.008

Füri, E., Hilton, D.R., Murton, B.J., Hémond, C., Dyment, J., Day, J.M.D., 2011. Helium isotope variations between Réunion Island and the Central Indian Ridge (17°–21°S): New evidence for ridge–hot spot interaction. J. Geophys. Res. 116. https://doi.org/10.1029/2010jb007609

Halldórsson, S.A., Hilton, D.R., Scarsi, P., Abebe, T., Hopp, J., 2014. A common mantle plume source beneath the entire East African Rift System revealed by coupled helium-neon systematics. Geophys. Res. Lett. https://doi.org/10.1002/2014GL059424

Hammond, J.O.S., Kendall, J.M., Wookey, J., Stuart, G.W., Keir, D., Ayele, A., 2014. Differentiating flow, melt, or fossil seismic anisotropy beneath Ethiopia. Geochemistry, Geophys. Geosystems 15, 1878–1894. https://doi.org/10.1002/

Hilton, D.R., Barling, J., Wheller, G.E., 1995. Effect of shallow-level contamination on the helium isotope systematics of ocean-island lavas. Nature 373, 330–333.

Hilton, D.R., Halldórsson, S.A., Barry, P.H., Fischer, T.P., de Moor, J.M., Ramirez, C.J., Mangasini, F., Scarsi, P., 2011. Helium isotopes at Rungwe Volcanic Province, Tanzania, and the origin of East African Plateaux. Geophys. Res. Lett. 38, n/a-n/a. https://doi.org/10.1029/2011gl049589

Hilton, D.R., Hammerschmidt, K., Teufel, S., Friedrichsen, H., 1993. Helium isotope characteristics of Andean geothermal fluids and lavas. Earth Planet. Sci. Lett. 120, 265–282.

Hopp, J., Trieloff, M., Altherr, R., 2004. Neon isotopes in mantle rocks from the Red Sea region reveal large-scale plume-lithosphere interaction. Earth Planet. Sci. Lett. 219, 61–76. https://doi.org/10.1016/S0012-821X(03)00691-5

Keir, D., Hamling, I., Ayele, A., Calais, E., Ebinger, C.J., Wright, T.J., Jacques, E., Mohamed, K., Hammond, J.O.S., Belachew, M., Baker, E., Rowland, J., Lewi, E., Bennati, L., 2009. Evidence for focused magmatic accretion at segment centers from lateral dike injections captured beneath the Red Sea rift in Afar. Geology 37, 59–62. https://doi.org/10.1130/G25147A.1

Marty, B., Appora, I., Barrat, J., Deniel, C., Vellutini, P., Vidal, P., 1993. He, Ar, Sr, Nd and Pb isotopes in volcanic rocks from Afar: Evidence for a primitive mantle component and constraints on magmatic sources. Geochem. J. 27, 219–228.

Marty, B., Pik, R., Gezahegn, Y., 1996. Helium isotopic variations in Ethiopian plume lavas: nature of magmatic sources and limit on lower mantle contribution. Earth Planet. Sci. Lett. 144, 223–237.

Medynski, S., Pik, R., Burnard, P., Williams, A., Vye-Brown, C., Ferguson, D., Blard, P.H., France, L., Yirgu, G., Seid, J.I., Ayalew, D., Calvert, A., 2013. Controls on magmatic cycles and development of rift topography of the Manda Hararo segment (Afar, Ethiopia): Insights from cosmogenic 3He investigation of landscape evolution. Earth Planet. Sci. Lett. 367, 133–145. https://doi.org/10.1016/j.epsl.2013.02.006

Moreira, M., Valbracht, P.J., Staudacher, T., Allègre, C.J., 1996. Rare gas systematics in RedSea ridge basalts. Geophys. Res. Lett. 23, 2453–2456.

Ogliore, R.C., Huss, G.R., Nagashima, K., 2011. Ratio estimation in SIMS analysis. Nucl. Instruments Methods Phys. Res. B 269, 1910–1918.

Pik, R., Marty, B., Hilton, D.R., 2006. How many mantle plumes in Africa? The geochemical point of view. Chem. Geol. 226, 100–114.

Rooney, T.O., Hanan, B.B., Graham, D.W., Furman, T., Blichert-Toft, J., Schilling, J.G., 2012. Upper Mantle Pollution during Afar Plume-Continental Rift Interaction. J. Petrol. 53, 365–389. https://doi.org/10.1093/petrology/egr065

Rooney, T.O., Herzberg, C., Bastow, I.D., 2011. Elevated mantle temperature beneath East Africa. Geology 40, 27–30. https://doi.org/10.1130/g32382.1

Scarsi, P., 2000. Fractional extraction of helium by crushing of olivine and clinopyroxene phenocrysts: Effects on the $^{3}He/^{4}He$ measured ratio. Geochim. Cosmochim. Acta 64, 3751–3762.

Scarsi, P., Craig, H:(, 1996. Helium isotope ratios in Ethiopian Rift basalts. Earth Planet. Sci. Lett. 144, 505–516.

Shaw, A.M., Hilton, D.R., Fischer, T.P., Walker, J.A., de Leeuw, G.A.M., 2006. Helium isotope variations in mineral separates from Costa Rica and Nicaragua: Assessing crustal contributions, timescale variations and diffusion-related mechanisms. Chem. Geol. 230, 124–139. https://doi.org/10.1016/j.chemgeo.2005.12.003

Wang, K., Brodholt, J., Lu, X., 2015. Helium diffusion in olivine based on first principle calculations. Geochim. Cosmochim. Acta 156, 145–153. https://doi.org/10.1016/j.gca.2015.01.023

Supplemental figures

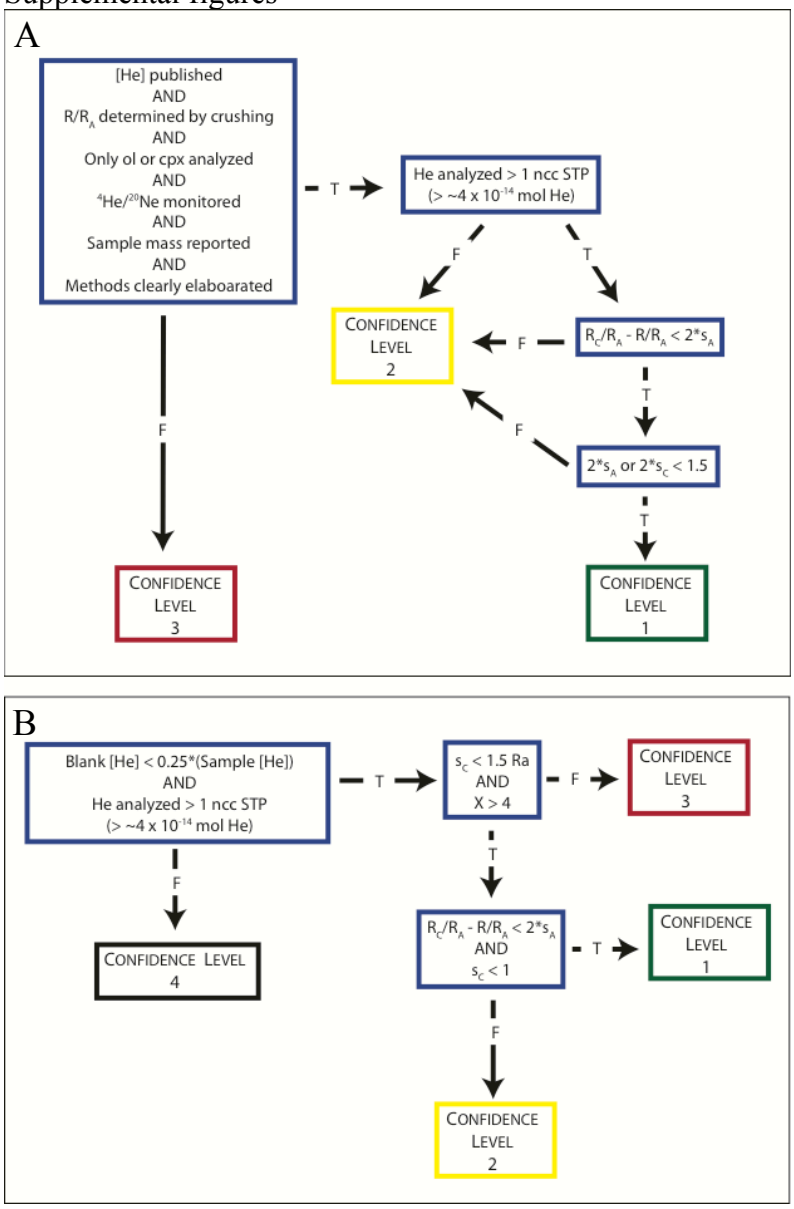

Figure 5.S1. Selection criteria flowcharts for previously published (A) and new data (B). Arrows indicate if given criterion/criteria is/are true (T) or false (F). Abbreviations used: [He]: He concentration; R/R_A: raw $^3He/^4He$ ratio before air correction; R_C/R_A: $^3He/^4He$ ratio after air correction; s_a: standard error of R/R_A; s_c: standard error of R_C/R_A.

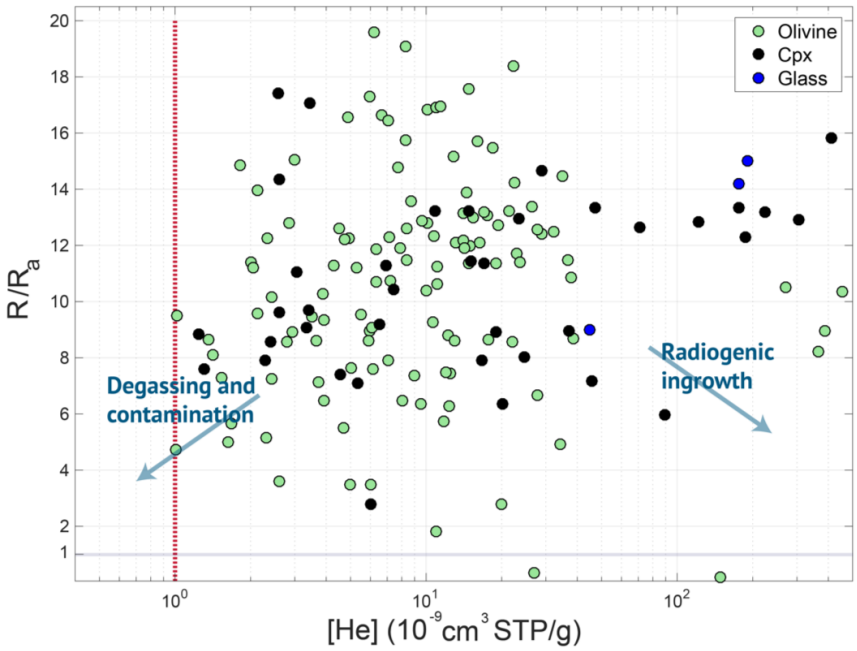

Figure 5.S2. Trends in the He isotope ratio vs. [He] plot can reveal processes altering He isotope ratios making them unrepresentative of parental volatile composition. Radiogenic in-growth of ^{4}He is likely to lead to low R/R_A values associated with high [He] (negative slope at high [He]) while degassing of magmatic volatiles is likely to lead to low R/R_A values at low [He] (positive slope) due to the susceptibility of low [He] materials to shallow He incorporation.

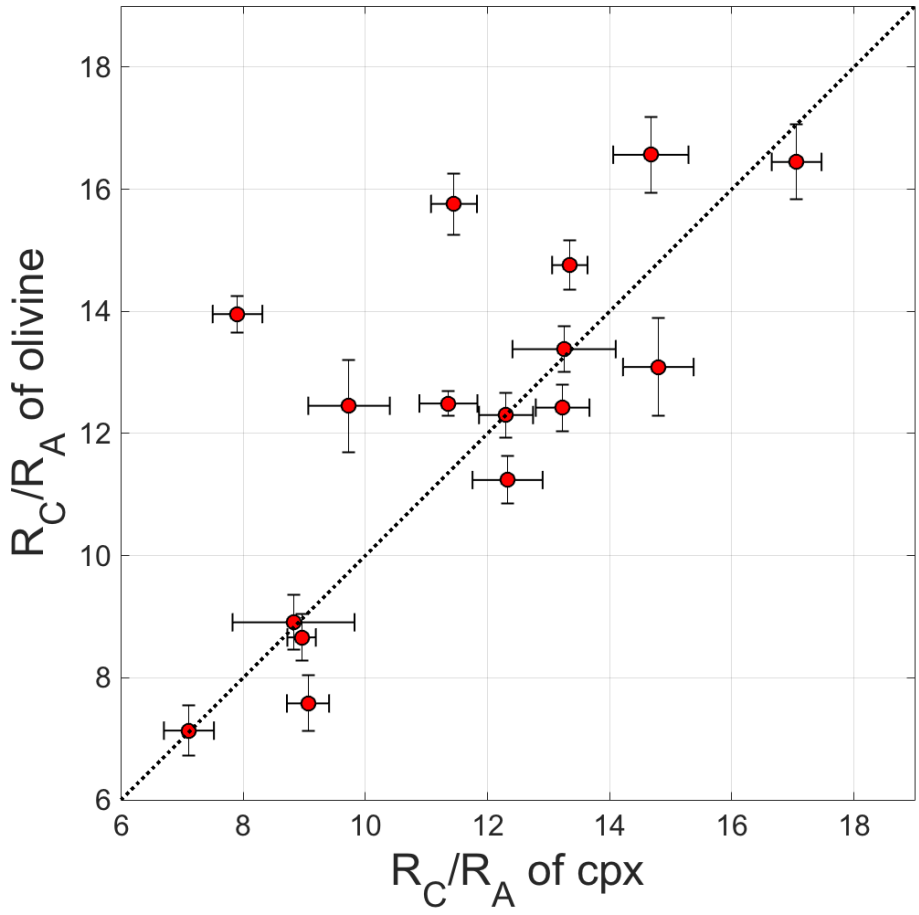

Figure 5.S3. Comparison of R_C/R_A values from olivine and cpx phenocrysts. Points would be expected to fall on dotted 1:1 line if no He alteration processes occurred that affected cpx preferentially. Most samples fall near this line, and the majority that do not show higher R_C/R_A in olivine phenocrysts as expected. The maximum R_C/R_A value for each sample location was used to construct the isoscape since He isotope measurements are a lower bound on the true parental He isotope ratio.

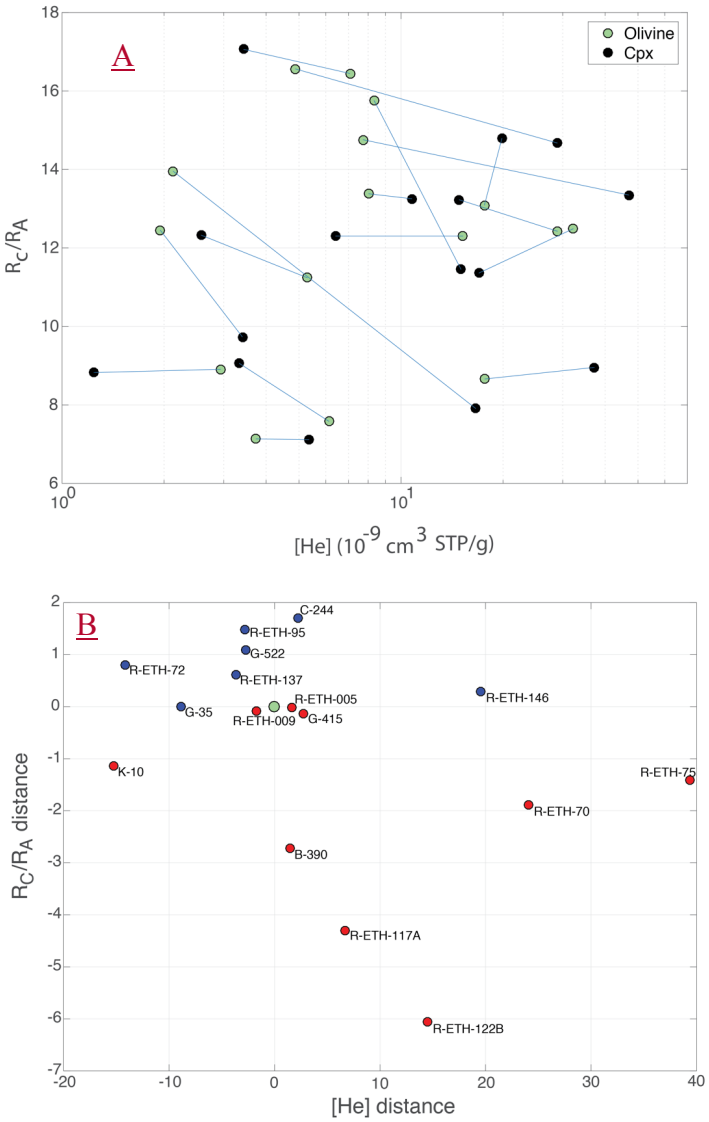

Figure 5.S4. Visual representations of $^3He/^4He$ and [He] from coexistent olivine and cpx phenocrysts showing (A) the measurements of the two phases connected by lines to indicate the olivine-to-cpx trajectories shown in (B) where the olivine $^3He/^4He$ and [He] have all been relocated to the origin (green point) and the difference in R_C/R_A and [He] between the olivine and cpx phases are now plotted. Blue points indicate positive R_C/R_A distance ($^3He/^4He$ higher in cpx than olivine), and red points indicate negative R_C/R_A distance ($^3He/^4He$ lower in cpx than olivine). The points in the lower right quadrant show evidence of coupled degassing and shallow He assimilation or radiogenic ingrowth (see text for further discussion).

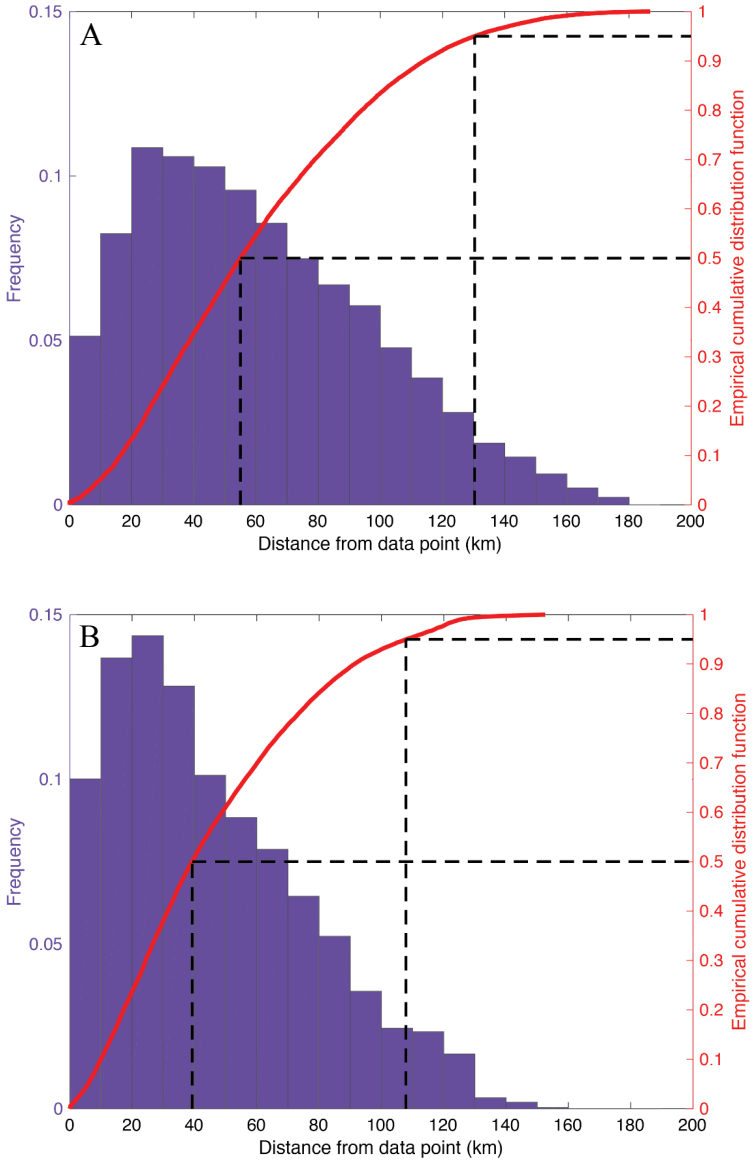

Figure 5.S5. Histograms (purple) and empirical cumulative distribution functions (red) of the distance between each isoscape grid point and the nearest He isotope analysis location for the literature dataset (A) and full dataset including new analyses (B). Both A and B have the same axes. The increase in spatial coverage with the addition of our He isotope contribution is dramatic.

Table S1. Literature $^{3}He/^{4}He$ data compilation

Data source	Sample	Lat (°)	Lon (°)	R/R_A	R_C/R_A	$2*\sigma(R_C/R_A)$	[He] (10^{-9} cm^3 STP/g)	Phase	Mass (g)	He analyzed (10^{-9} cm^3 STP)	Confidence Level
Beccaluva et al. (2011)											
	Injibara-xenolith	*11.02*	*36.91*	*6.9*	*n.d*	*2*	*n.d*	*Ol-X*	*n.d*	*n.d*	*3*
	Injibara-xenolith	*11.02*	*36.91*	*7.3*	*n.d*	*0.8*	*n.d*	*Ol-X*	*n.d*	*n.d*	*3*
	Injibara-xenolith	*11.02*	*36.91*	*7.5*	*n.d*	*1*	*n.d*	*Ol-X*	*n.d*	*n.d*	*3*
	Injibara-xenolith	*11.02*	*36.91*	*7.8*	*n.d*	*0.8*	*n.d*	*Ol-X*	*n.d*	*n.d*	*3*
	Injibara-xenolith	*11.02*	*36.91*	*8.6*	*n.d*	*3.4*	*n.d*	*Ol-X*	*n.d*	*n.d*	*3*
	Injibara-xenolith	*11.02*	*36.91*	*8.9*	*n.d*	*3.2*	*n.d*	*Ol-X*	*n.d*	*n.d*	*3*
	Dedessa-xenolith	*8.67*	*36.17*	*6.6*	*n.d*	*1.6*	*n.d*	*Ol-X*	*n.d*	*n.d*	*3*
Halldorsson et al (2014)											
	H-186	*11.26*	*41.64*	*n.d.*	*n.d.*	*n.d.*	*0.11*	*Ol-X*	*0.2733*	*0.03*	*2*
	H-91	*11.28*	*41.64*	*n.d.*	*n.d.*	*n.d.*	*b.d.l.*	*Px-X*	*0.3163*	*b.d.l.*	*2*
	Zu-15-A	*14.85*	*39.95*	*5.50*	*7.13*	*0.52*	*0.49*	*Ol*	*0.3056*	*0.15*	*2*
	G-124	13.45	40.98	12.29	12.3	0.54	187.00	Cpx-X	0.2919	54.59	1
	G-123	13.45	40.98	12.90	12.9	0.34	306.00	Cpx-X	0.5779	176.84	1

Table S1 (cont'd)

Data source	Sample	Lat (°)	Lon (°)	R/R_A	R_C/R_A	$2*\sigma(R_C/R_A)$	[He] (10^{-9} cm^3 STP/g)	Phase	Mass (g)	He analyzed (10^{-9} cm^3 STP)	Confidence Level
	G-122	13.45	40.98	13.16	13.19	0.44	224.00	Cpx-X	0.4659	104.36	1
	C-244	13.45	40.98	12.50	12.73	0.56	19.29	Cpx-X	0.6219	193.26	1
	G-116	13.44	40.98	13.91	13.93	0.46	321.00	Cpx-X	0.5254	168.65	1
	G-114	13.44	40.98	12.78	12.82	0.42	122.00	Cpx-X	0.6626	80.84	1
	K-12	13.25	41.60	11.86	11.97	0.46	14.98	Ol	0.4107	6.15	1
	Assab	13.07	42.68	12.93	12.95	0.54	23.40	Cpx-X	0.473	11.07	1
	Assab-585	13.07	42.68	8.67	8.69	0.36	38.50	Ol-X	0.5047	19.43	1
	ASSAB_3-G-18-A	13.07	42.68	8.57	8.93	0.48	19.01	Cpx-X	0.6165	11.72	1
	ASSAB_3-G-18-A	13.07	42.68	8.57	8.97	0.42	389.24	Ol-X	0.4965	193.26	1
	TF-298	12.57	42.68	6.70	7.9	0.22	2.28	Cpx-X	0.5141	1.17	1
	TF-299	*12.57*	*42.68*	*n.d.*	*n.d.*	*n.d.*	*0.11*	*Px-X*	*0.6048*	*0.07*	*2*
	TF-140	12.45	43.44	10.36	10.37	0.2	453.00	Ol-X	0.5052	228.86	1
	TF-136	12.45	43.45	8.18	8.21	0.2	366.00	Ol-X	0.3658	133.88	1
	R-ETH-121	11.95	39.40	16.83	16.84	0.56	10.17	Ol	0.7375	7.50	1
	R-ETH-120	11.94	39.38	18.33	18.38	0.88	22.23	Ol	0.7552	16.79	1
	R-ETH-105	11.02	36.91	7.59	7.59	0.54	1.30	Cpx-X	1.0738	1.40	1
	R-ETH-105	*11.02*	*36.91*	*10.94*	*10.94*	*1.24*	*0.32*	*Ol*	*0.6104*	*0.20*	*2*

Table S1 (cont'd)

Data source	Sample	Lat (°)	Lon (°)	R/R_A	R_C/R_A	$2*\sigma(R_C/R_A)$	[He] (10^{-9} cm^3 STP/g)	Phase	Mass (g)	He analyzed (10^{-9} cm^3 STP)	Confidence Level
	ETS-145	*9.07*	*38.73*	*8.40*	*8.4*	*0.4*	*1.64*	*Ol*	*0.462*	*0.76*	*2*
	ETS-264-9	*11.02*	*36.91*	*n.d.*	*n.d.*	*n.d.*	*b.d.l.*	*Ol*	*0.721 3*	*b.d.l.*	*2*
	ETS-264-19	*11.02*	*36.91*	*n.d.*	*n.d.*	*n.d.*	*b.d.l.*	*Ol*	*0.665*	*b.d.l.*	*2*
	ETS-264-20	*11.02*	*36.91*	*n.d.*	*n.d.*	*n.d.*	*b.d.l.*	*Ol*	*0.802 7*	*b.d.l.*	*2*
	ETS-178	9.02	36.92	5.75	5.75	0.22	11.76	Ol	0.610 1	7.17	1
	Bt-001	8.85	38.67	9.07	9.34	0.52	3.91	Ol	0.522 8	2.04	1
	ETS-162	8.76	37.45	7.58	7.65	0.46	5.05	Ol	0.587 5	2.97	1
	R-ETH-149	8.62	38.92	13.16	13.22	0.52	21.39	Ol	0.604 2	12.92	1
	R-ETH-026	*5.72*	*37.44*	*0.47*	*0.45*	*0.1*	*1.86*	*Ol-X*	*0.831 8*	*1.55*	*2*
	D-88	*13.50*	*40.58*	*n.d.*	*n.d.*	*n.d.*	*0.10*	*Px-X*	*0.403 5*	*0.04*	*2*
Marty et al. (1993)											
	PV299	*12.47*	*43.23*	*12.9*	*13.3*	*1.9*	*1.60*	*Ol*	*0.504*	*0.81*	*2*
	PP749	*12.46*	*42.43*	*14.5*	*14.9*	*3.5*	*0.56*	*Ol*	*0.523 8*	*0.29*	*2*
	PV137	12.43	42.46	9.6	9.6	0.2	28.00	Px	0.541	15.15	1
	PP693#1	*12.37*	*42.40*	*9.7*	*10.1*	*1.1*	*2.68*	*Ol*	*0.275 1*	*0.74*	*2*
	PP693#2	*12.37*	*42.40*	*9.9*	*10.1*	*1.9*	*2.24*	*Ol*	*0.560 5*	*1.25*	*2*
	PP693#3	12.37	42.40	2.8	2.8	0.4	19.90	Ol	0.344 4	6.85	1
	DR1-3	11.95	43.67	15.0	15	0.3	191.00	Glass	0.500 8	95.65	1

Table S1 (cont'd)

Data source	Sample	Lat (°)	Lon (°)	R/R_A	R_C/R_A	$2*\sigma(R_C/R_A)$	[He] (10^{-9} cm^3 STP/g)	Phase	Mass (g)	He analyzed (10^{-9} cm^3 STP)	Confidence Level
	103-1	11.88	43.65	14.2	14.2	0.2	176.00	Glass	0.1699	29.90	1
	PV353	*11.53*	*42.52*	*6.8*	*7*	*3.1*	*0.69*	*Ol*	*0.5357*	*0.37*	*2*
Marty et al. (1996)											
	E160-xenolith	*13.58*	*42.72*	*7.7*	*8*	*0.6*	*0.60*	*Ol*	*0.5*	*0.30*	*2*
	E18P-xenolith	13.58	42.72	8.5	8.6	0.2	13.00	Ol	0.5	6.50	1
	C230	13.45	40.98	11.7	12.3	0.4	7.10	Ol	0.5	3.55	1
	E98	13.20	37.89	0.034	0.035	0.01	18.00	Px	0.5	9.00	1
	E12	12.33	42.00	3.4	3.5	0.2	6.00	Ol	0.5	3.00	1
	E159	*12.13*	*37.78*	*5.3*	*8.2*	*0.2*	*11.00*	*Ol*	*0.5*	*5.50*	*2*
	E260	12.08	41.67	0.18	0.18	0.06	148.00	Ol	0.5	74.00	1
	E39	11.99	39.41	19.6	19.6	0.4	6.20	Ol	0.5	3.10	1
	E109	11.96	39.39	3.6	3.6	0.4	2.60	Ol	0.5	1.30	1
	E38	11.96	39.40	12.6	12.6	1	4.50	Ol	0.5	2.25	1
	E40	*11.96*	*39.40*	*13.0*	*n.d*	*n.d*	*0.40*	*Ol*	*0.5*	*0.20*	*2*
	E254	*11.95*	*41.06*	*0.4*	*0.4*	*0.24*	*0.02*	*Ol*	*0.5*	*0.01*	*2*
	E37	11.95	39.07	3.2	3.2	0.2	22.00	Px	0.5	11.00	1
	E253	11.92	41.08	0.009	0.009	0.0074	45.00	Ol	0.5	22.50	1
	E252	11.90	41.03	5.4	5.5	0.2	4.70	Ol	0.5	2.35	1
	E256	*11.90*	*41.10*	*1.7*	*1.76*	*0.6*	*0.52*	*Ol*	*0.5*	*0.26*	*2*
	102-2	11.87	43.63	8.8	9	0.2	45.00	Glass	0.5	22.50	1
	E31	*11.54*	*39.61*	*2.3*	*2.4*	*0.4*	*1.93*	*Px*	*0.5*	*0.96*	*2*
	E31	11.54	39.61	1.81	1.8	0.08	11.00	Ol	0.5	5.50	1
	E50	11.39	37.08	0.34	0.33	0.02	27.00	Ol	0.5	13.50	1
	E154	*10.95*	*36.79*	*7.9*	*8*	*0.8*	*0.83*	*Ol*	*0.5*	*0.42*	*2*
	E156	*10.95*	*36.50*	*9.1*	*9.9*	*0.4*	*2.00*	*Ol*	*0.5*	*1.00*	*2*
	E275	8.83	38.83	10.3	10.4	0.2	10.00	Ol	0.5	5.00	1
	E273	8.72	39.03	3.5	3.5	0.4	5.00	Ol	0.5	2.50	1
	E266	8.67	39.75	13.1	13.2	0.4	17.00	Ol	0.5	8.50	1
	E268	8.40	39.20	16.5	16.9	0.4	11.00	Ol	0.5	5.50	1
	E270	8.40	39.33	7.5	7.5	0.2	12.00	Ol	0.5	6.00	1

Table S1 (cont'd)

Data source	Sample	Lat (°)	Lon (°)	R/R_A	R_C/R_A	$2*\sigma(R_C/R_A)$	[He] (10^{-9} cm^3 STP/g)	Phase	Mass (g)	He analyzed (10^{-9} cm^3 STP)	Confidence Level
	E271	8.40	39.37	15.6	15.7	0.4	16.00	Ol	0.5	8.00	1
Medynski et al. (2013)											
	Bodo	*12.51*	*40.49*	*9.9*	*n.d*	*n.d*	*n.d*	*Ol*	*0.3*	*n.d*	*3*
	Bodo	*12.51*	*40.49*	*9.9*	*n.d*	*n.d*	*n.d*	*Px*	*0.3*	*n.d*	*3*
	Yem-1	*12.51*	*40.53*	*8*	*n.d*	*n.d*	*n.d*	*Px*	*0.3*	*n.d*	*3*
	Yem-6	*12.51*	*40.52*	*12.2*	*n.d*	*n.d*	*n.d*	*Px*	*0.3*	*n.d*	*3*
	Yem-6	*12.51*	*40.52*	*12.2*	*n.d*	*n.d*	*n.d*	*Ol*	*0.3*	*n.d*	*3*
	Gab-I	*12.50*	*40.51*	*10.9*	*n.d*	*n.d*	*n.d*	*Ol*	*0.3*	*n.d*	*3*
	Gab-C3	*12.48*	*40.54*	*10.9*	*n.d*	*n.d*	*n.d*	*Px*	*0.3*	*n.d*	*3*
	Gab-D4	*12.43*	*40.53*	*13.3*	*n.d*	*n.d*	*n.d*	*Px*	*0.3*	*n.d*	*3*
	Gab-D4	*12.43*	*40.53*	*13.3*	*n.d*	*n.d*	*n.d*	*Ol*	*0.3*	*n.d*	*3*
	Bad-3A	*12.41*	*40.35*	*11.4*	*n.d*	*n.d*	*n.d*	*Ol*	*0.3*	*n.d*	*3*
	Bad-2A	*12.41*	*40.35*	*11.4*	*n.d*	*n.d*	*n.d*	*Ol*	*0.3*	*n.d*	*3*
	Bad-5	*12.38*	*40.32*	*10.5*	*n.d*	*n.d*	*n.d*	*Ol*	*0.3*	*n.d*	*3*
	Bad-5	*12.38*	*40.32*	*10.5*	*n.d*	*n.d*	*n.d*	*Px*	*0.3*	*n.d*	*3*
	Boha	*12.32*	*40.31*	*9.7*	*n.d*	*n.d*	*n.d*	*Ol*	*0.3*	*n.d*	*3*
	Boha	*12.32*	*40.31*	*5*	*n.d*	*n.d*	*n.d*	*Px*	*0.3*	*n.d*	*3*
	Yem-10	*12.30*	*40.32*	*10.9*	*n.d*	*n.d*	*n.d*	*Ol*	*0.3*	*n.d*	*3*
	Gab-F	*12.29*	*40.33*	*13*	*n.d*	*n.d*	*n.d*	*Ol*	*0.3*	*n.d*	*3*
	Gab-F	*12.29*	*40.33*	*13*	*n.d*	*n.d*	*n.d*	*Px*	*0.3*	*n.d*	*3*
	Gab-G4	*12.29*	*40.32*	*10*	*n.d*	*n.d*	*n.d*	*Ol*	*0.3*	*n.d*	*3*
	Gab-G4	*12.29*	*40.32*	*5.7*	*n.d*	*n.d*	*n.d*	*Px*	*0.3*	*n.d*	*3*
	Dikika	*12.29*	*40.33*	*8.4*	*n.d*	*n.d*	*n.d*	*Ol*	*0.3*	*n.d*	*3*
Moreira et al. (1996)											
	DRI-3	11.57	43.40	14.73	14.73	0.34	1490.00	Glass	0.63	938.70	1
Pik et al. (2006)											
	E216	*14.25*	*39.34*	*4.4*	*n.d*	*0.2*	*10.00*	*Ol*	*n.d*	*n.d*	*3*

Table S1 (cont'd)

Data source	Sample	Lat (°)	Lon (°)	R/R_A	R_C/R_A	$2*\sigma(R_C/R_A)$	[He] (10^{-9} cm^3 STP/g)	Phase	Mass (g)	He analyzed (10^{-9} cm^3 STP)	Confidence Level
	PM252	*13.25*	*38.19*	*11.3*	*n.d*	*0.4*	*7.80*	*Ol*	*n.d*	*n.d*	*3*
	E38	*11.96*	*39.40*	*16.4*	*n.d*	*1*	*1.80*	*Ol*	*n.d*	*n.d*	*3*
	DR14	*11.53*	*42.52*	*15*	*n.d*	*0.6*	*0.90*	*Ol*	*n.d*	*n.d*	*3*
	AD67	*11.36*	*37.11*	*8.1*	*n.d*	*0.4*	*3.80*	*Ol*	*n.d*	*n.d*	*3*
	60–98	*10.97*	*39.49*	*6*	*n.d*	*0.2*	*19.00*	*Ol*	*n.d*	*n.d*	*3*
	AD70	*9.80*	*38.59*	*7*	*n.d*	*0.2*	*32.00*	*Ol*	*n.d*	*n.d*	*3*
	63–98	*8.03*	*38.72*	*7.7*	*n.d*	*0.6*	*3.10*	*Ol*	*n.d*	*n.d*	*3*
Rooney et al. (2012)											
	WFB-N-14	9.51	39.61	15.12	n.d	0.6	3.10	Ol	0.8714	2.70	1
	WFB-N-21	9.50	39.68	12.82	n.d	0.52	6.40	Ol	0.5378	3.44	1
	WFB-1036	9.49	39.71	12.16	n.d	0.48	8.00	Ol	0.6314	5.05	1
	WFB-1027	9.48	40.20	12.66	n.d	1.96	0.70	Ol	0.4286	0.30	2
	DZ-1007	8.72	38.99	8.66	n.d	0.28	11.00	Ol	0.7446	8.19	1
	DZ-1008	8.72	38.98	8.8	n.d	0.32	11.00	Ol	0.5815	6.40	1
	DZ-1014	8.60	38.91	5.61	n.d	0.68	1.70	Cpx	0.5981	1.02	1
	DZ-1009	8.59	39.15	8.3	n.d	0.8	2.60	Ol	0.4421	1.15	1
	BJ-1053	8.19	38.45	7.7	n.d	0.48	4.90	Cpx	0.541	2.65	1
	BJ-1043	8.14	38.44	8.11	n.d	0.72	2.60	Ol	0.4304	1.12	1
	BJ-1045	8.06	38.36	7.53	n.d	0.32	14.00	Cpx	0.42	5.88	1
	BJ-1045	8.06	38.36	7.52	n.d	0.6	4.20	Ol	0.4224	1.77	1

Table S1 (cont'd)

Data source	Sample	Lat (°)	Lon (°)	R/R_A	R_C/R_A	$2*\sigma(R_C/R_A)$	[He] (10^{-9} cm^3 STP/g)	Phase	Mass (g)	He analyzed (10^{-9} cm^3 STP)	Confidence Level
Scarsi and Craig (1996)											
	Zu-29	15.02	39.85	6.27	*n.d*	0.4	12.42	Ol	2.66	33.04	1
	Zu-21	14.85	39.95	8.58	*n.d*	0.4	22.09	Ol+Cpx	3.35	74.00	1
	Zu-66	14.85	39.95	8.63	*n.d*	0.4	1.36	Ol+Cpx	3.88	5.28	1
	ZU-68	14.85	39.95	9.08	*n.d*	0.4	6.07	Ol+Cpx	2.66	16.15	1
	C-242	13.47	40.96	11.35	*n.d*	0.4	14.80	Ol+Cpx	3.51	51.95	1
	C-230	13.45	40.98	12.08	*n.d*	0.4	13.13	Ol	2.01	26.39	1
	G-112	13.44	40.98	12.78	*n.d*	0.4	10.17	Ol+Cpx	2.66	27.05	1
	G-113	13.44	40.98	11.85	*n.d*	0.4	6.33	Ol+Cpx	2.8	17.72	1
	G-114	13.44	40.98	12.86	*n.d*	0.4	9.67	Ol	3.78	36.55	1
	G-115	13.44	40.98	13.37	*n.d*	0.4	26.50	Ol-X	3.17	84.01	1
	G-115	13.44	40.98	13.35	*n.d*	0.4	176.93	Cpx-X	3.05	539.64	1
	G-116	13.44	40.98	14.24	*n.d*	0.4	22.56	Ol-X	3.66	82.57	1
	C-201	13.44	40.97	12.18	*n.d*	0.4	14.14	Ol	3.16	44.68	1
	G-111	13.20	40.83	11.41	*n.d*	0.4	23.70	Ol	2.97	70.39	1
	B-12	13.06	42.69	8.12	*n.d*	0.4	1.41	Ol+Cpx	2.19	3.09	1
	D-170	13.05	40.16	12.34	*n.d*	0.4	10.74	Ol	3.38	36.30	1
	H-9	*11.28*	*41.64*	*12.16*	*n.d*	*0.4*	*0.29*	*Ol+Cpx*	*2.24*	*0.65*	*2*
	H-275	11.09	41.19	11.23	*n.d*	0.4	11.06	Ol	2.04	22.56	1
	H-249	11.01	41.37	11.89	*n.d*	0.4	14.20	Ol	2.44	34.65	1
	H-355	10.62	41.01	10.73	*n.d*	0.4	7.18	Ol	2.12	15.22	1
	H-23	10.05	40.70	6.68	*n.d*	0.4	27.76	Ol+Cpx	3.18	88.28	1
	RV-199	8.85	38.87	5.15	*n.d*	0.4	2.31	Ol	2.84	6.56	1

Table S1 (cont'd)

Data source	Sample	Lat (°)	Lon (°)	R/R_A	R_C/R_A	$2*\sigma(R_C/R_A)$	[He] (10^{-9} cm^3 STP/g)	Phase	Mass (g)	He analyzed (10^{-9} cm^3 STP)	Confidence Level
	RV-84	8.42	39.19	13.88	*n.d*	0.4	14.50	Ol	2.33	33.79	1
	RV-95	8.42	39.19	15.46	*n.d*	0.4	18.35	Ol+Cpx	2.43	44.59	1
	5.030089	8.24	39.95	7.42	*n.d*	0.4	4.53	Cpx-X	2.06	9.33	1
	RV-131	8.12	38.37	9.46	*n.d*	0.4	3.52	Ol	3.3	11.62	1
	2.030079	8.09	39.82	6.37	*n.d*	0.4	9.51	Ol	3.02	28.72	1
	RV-351	8.05	37.17	16.96	*n.d*	0.4	11.44	Ol	2.58	29.52	1
	RV-136	7.97	38.28	7.37	*n.d*	0.4	8.97	Ol+Cpx	2.24	20.09	1
	RV-214	7.93	38.94	11.2	*n.d*	0.4	2.04	Ol	3.02	6.16	1
	RV-73	7.87	38.90	7.05	n.d	0.4	0.61	Ol	2.55	1.56	1
	RV-197	6.62	37.83	7.9	*n.d*	0.4	7.08	Ol	2.71	19.19	1
	RV-172	*6.56*	*38.48*	*4.63*	*n.d*	*0.4*	*0.77*	*Ol-X*	*1*	*0.77*	*2*
	RV-165	5.96	37.57	6.37	n.d	0.4	0.87	Ol+Cpx	3.79	3.30	1
	RV-143	5.73	37.52	7.29	*n.d*	0.4	1.54	Ol+Cpx	3.06	4.71	1
	3G-16	13.07	42.68	8.6	*n.d.*	0.4	5.90	Ol-X	1	5.90	1

Table S1. Literature He isotope data from lavas and xenoliths within the region of interest. Confidence levels assigned using the below selection criteria. Confidence levels for data were assigned based on the selection criteria discussed in section 2.2, and samples with confidence levels of 2 or 3, which were deemed unreliable and therefore were not included in isoscape construction, are italicized. When $^3He/^4He$ ratio was reported as R/R_A but $^4He/^{20}Ne$ was monitored, $^3He/^4He$ value was interpreted to be R_C/R_A, and when a range of masses was given for samples, the minimum value was chosen to calculate a conservative amount of He analyzed. Phases analyzed are abbreviated as Ol (olivine), Cpx (clinopyroxene), Px (unspecified pyroxene, assumed to be cpx). Xenolith samples are designated with an X following the phase. Additional abbreviations: n.d.: no data; b.d.l.: below detection level. The conversion factor between the given [He] units of 10^{-9} cm^3 STP and the units of 10^{-14} mol He given in other sources is approximately 4.1.

Table S2. New $^{3}He/^{4}He$ data generated for this study

Region	Sample	Lat (°)	Lon (°)	R/R_A	X	R_C/R_A	$2*\sigma(R/R_A)$	$[^{4}He]$ (10^{-9} cm^3 STP/g)	Phase	Mass (g)	He analyzed (10^{-9} cm^3 STP)	Confidence Level
Unknown location												
	K-10	N/A	N/A	12.3	72.3	12.5	0.21	32.25	Ol	1.0060	32.44	1
	K-10	N/A	N/A	11.2	49.7	11.4	0.48	16.96	Cpx	1.0005	16.97	1
Afar												
	Zu-15	*14.85*	*39.95*	*9.6*	*7.3*	*11.0*	*1.41*	*0.91*	*Cpx*	*0.9030*	*0.82*	*4*
	F-28	*14.8111*	*40.2814*	*24.4*	*N/A*	*24.4*	*5.90*	*0.44*	*Ol*	*1.0043*	*0.44*	*4*
	ET-71/10	13.5022	40.5822	8.0	N/A	8.0	0.51	24.54	Cpx	0.4941	12.12	1
	C-227	13.4669	40.9819	12.5	17.4	13.1	0.32	14.05	Ol	0.9816	13.79	2
	C-244	13.4669	40.9819	12.9	79.6	13.1	0.80	17.62	Ol	0.6974	12.28	1
	C-244	13.4669	40.9819	15.8	278.0	15.8	0.22	411.41	Cpx	0.3215	132.27	1
	C-172	13.4642	40.9756	10.3	9.6	11.3	0.29	18.90	Ol	0.9596	18.14	2
	K-32	13.4584	41.6106	11.7	942.0	11.7	0.25	22.86	Ol	0.8491	19.41	1
	C-169	13.45	40.9836	12.0	38.5	12.2	0.62	4.92	Ol	0.9937	4.89	1
	D-133	*13.4158*	*40.7339*	*14.2*	*2.5*	*22.7*	*1.14*	*3.33*	*Ol*	*0.6409*	*2.13*	*3*
	F-73	*13.3761*	*40.5692*	*22.2*	*N/A*	*22.2*	*5.10*	*0.44*	*Ol*	*0.7200*	*0.32*	*4*
	F-78	*13.349*	*40.142*	*11.3*	*4.3*	*14.4*	*1.65*	*0.85*	*Ol*	*0.5432*	*0.46*	*4*
	G-72	13.3404	40.7367	12.2	N/A	12.2	0.59	2.33	Ol	0.5132	1.20	1
	G-415	13.3025	40.9072	12.6	N/A	12.6	0.88	8.38	Ol	0.8626	7.23	1
	G-415	13.3025	40.9072	13.1	77.3	13.2	0.84	10.80	Cpx	1.0905	11.78	1
	Ottonello Afar Ethiopia	13.3022	41.6844	7.1	173.2	7.2	0.20	45.65	Cpx	0.6484	29.60	1

Table S2 (cont'd)

Region	Sample	Lat (°)	Lon (°)	R/R_A	X	R_C/R_A	$2*\sigma(R/R_A)$	$[^4He]$ (10^{-9} cm^3 STP/g)	Phase	Mass (g)	He analyzed (10^{-9} cm^3 STP)	Confidence Level
	K-2	13.2067	41.5514	10.5	251.8	10.5	0.32	269.34	Ol	0.9622	259.16	1
	K-35	13.1636	40.0583	12.5	216.3	12.6	0.34	27.84	Ol	1.0552	29.38	1
	G-35	13.1006	40.1528	13.0	N/A	13.0	0.76	15.40	Ol	1.0305	15.87	1
	G-35	13.1006	40.1528	11.3	N/A	11.3	0.82	6.90	Cpx	1.0299	7.11	1
	B-176	*13.0664*	*42.6767*	*2.6*	*N/A*	*2.6*	*1.02*	*0.64*	*Ol*	*0.7462*	*0.48*	*4*
	K-42	13.0592	40.1028	11.6	45.8	11.9	0.39	7.91	Ol	1.0482	8.29	1
	K-8	12.9528	40.3708	9.2	179.9	9.3	0.46	10.67	Ol	0.6799	7.25	1
	C-143	*12.9092*	*40.5661*	*6.5*	*3.7*	*8.6*	*2.38*	*0.48*	*Cpx*	*0.7888*	*0.38*	*4*
	C-145	*12.8997*	*40.5686*	*7.8*	*2.4*	*12.7*	*2.49*	*0.47*	*Cpx*	*0.6003*	*0.28*	*4*
	C-321	12.6289	41.0356	11.5	556.0	11.5	0.82	8.34	Ol	0.6398	5.34	1
	C-426	12.6269	41.4683	10.7	N/A	10.7	0.62	6.34	Ol	0.8813	5.59	1
	C-426	12.6269	41.4683	10.3	N/A	10.3	0.51	4.50	Ol	0.5129	2.31	1
	C-426	12.6269	41.4683	10.5	N/A	10.5	0.73	4.54	Ol	0.7310	3.32	1
	C-426	*12.6269*	*41.4683*	*20.5*	*2.9*	*30.9*	*6.13*	*0.46*	*Cpx*	*0.8108*	*0.37*	*4*
	TF-308	12.5658	42.6791	7.0	4.9	8.6	0.87	2.41	Cpx	0.9990	2.41	2
	B-390	12.5067	42.3958	10.2	N/A	10.2	0.56	2.44	Ol	0.8763	2.14	1
	B-390	12.5067	42.3958	9.5	54.3	9.7	0.67	3.42	Cpx	0.6247	2.13	1
	TF-105A	*12.4131*	*40.3114*	*8.1*	*67.4*	*8.2*	*1.01*	*1.44*	*Cpx*	*0.6895*	*0.99*	*4*
	G-522	12.3608	41.1917	11.1	84.7	11.2	0.39	5.31	Ol	0.9275	4.93	1
	G-522	12.3608	41.1917	9.3	26.2	9.6	0.70	2.59	Cpx	0.8787	2.28	1
	S-6	11.8511	41.2664	10.9	6.4	12.8	0.48	2.85	Ol	0.6375	1.82	2
	S-165	11.8472	41.0397	9.4	47.1	9.6	0.75	2.14	Ol	0.8961	1.92	1
	H-113	11.3317	41.6225	10.6	N/A	10.6	0.37	11.09	Ol	0.7442	8.25	1
	H-295	11.1317	40.1389	11.1	63.7	11.3	0.86	4.30	Ol	0.8507	3.66	1
	H-282	11.0833	41.2667	11.8	32.6	12.1	0.49	16.30	Ol	0.6578	10.72	1

Table S2 (cont'd)

Region	Sample	Lat (°)	Lon (°)	R/R_A	X	R_C/R_A	$2*\sigma(R/R_A)$	[^{4}He] (10^{-9} cm^3 STP/g)	Phase	Mass (g)	He analyzed (10^{-9} cm^3 STP)	Confidence Level
	H-233	11.0767	41.3186	11.4	248.1	11.5	0.30	36.72	Ol	0.6457	23.71	1
	H-251	11.0225	41.3003	10.8	857.0	10.9	0.41	37.73	Ol	0.6674	25.18	1
	H-382	10.4931	40.9317	14.4	423.3	14.4	0.59	34.82	Ol	0.6762	23.55	1
	H-387	10.4569	40.9269	14.5	2.5	23.4	0.79	3.20	Ol	0.6348	2.03	2
	H-47	*9.9889*	*40.5419*	*8.1*	*N/A*	*8.1*	*1.28*	*0.89*	*Ol*	*0.5902*	*0.53*	*4*
	H-37	9.9094	40.8708	10.4	14.5	11.1	0.42	3.05	Cpx	0.6219	1.90	1
	H-33	9.905	40.8861	12.8	8.5	14.3	1.03	2.60	Cpx	0.6598	1.71	2
Main Ethiopian Rift												
	R-ETH-132	9.3783	40.1304	17.5	192.6	17.6	0.38	14.80	Ol	0.6835	10.11	1
	R-ETH-001	9.0591	38.5738	9.0	48.0	9.2	0.27	6.54	Cpx	0.5015	3.28	1
	R-ETH-002	*9.0556*	*38.56*	*8.0*	*5.7*	*9.5*	*0.58*	*1.02*	*Ol*	*0.5152*	*0.52*	*4*
	R-ETH-004	*8.9842*	*37.7372*	*4.0*	*4.9*	*4.7*	*0.83*	*1.01*	*Ol*	*0.5155*	*0.52*	*4*
	R-ETH-133	8.9039	39.8206	13.5	150.1	13.6	0.61	8.75	Ol	0.6582	5.76	1
	R-ETH-009	8.8598	38.6618	8.7	45.1	8.9	0.45	2.94	Ol	0.5279	1.55	1
	R-ETH-009	8.8598	38.6618	7.7	6.9	8.8	1.00	1.24	Cpx	0.3380	0.42	1
	R-ETH-148	*8.7999*	*39.0747*	*13.6*	*10.4*	*14.9*	*2.14*	*0.48*	*Ol*	*0.5628*	*0.27*	*4*
	R-ETH-147	8.7762	39.019	9.5	130.7	9.5	0.31	5.48	Ol	0.7286	3.99	1
	R-ETH-136	8.7754	39.6567	12.1	108.4	12.2	0.36	4.74	Ol	0.5637	2.67	1

Table S2 (cont'd)

Region	Sample	Lat (°)	Lon (°)	R/R_A	X	R_C/R_A	$2*\sigma(R/R_A)$	$[^4He]$ (10^{-9} cm^3 STP/g)	Phase	Mass (g)	He analyzed (10^{-9} cm^3 STP)	Confidence Level
	R-ETH-137	8.75	39.5903	16.1	45.3	16.4	0.61	7.07	Ol	0.6503	4.60	1
	R-ETH-146	8.7347	38.9978	8.6	236.8	8.7	0.38	17.65	Ol	0.7719	13.63	1
	R-ETH-146	8.7347	38.9978	8.8	49.9	9.0	0.23	37.19	Cpx	0.9920	36.89	1
	R-ETH-137	8.7246	39.5239	16.4	23.0	17.1	0.41	3.43	Cpx	0.9997	3.43	1
	R-ETH-141	8.5934	39.1471	6.3	26.3	6.5	0.35	3.94	Ol	0.4914	1.93	1
	R-ETH-143	8.4898	39.293	16.0	26.9	16.6	0.35	6.65	Ol	0.6498	4.32	1
	R-ETH-140	8.4791	39.3085	16.8	35.6	17.3	0.65	5.95	Ol	0.5647	3.36	1
	R-ETH-139	8.4134	39.3844	17.2	63.8	17.4	0.38	2.56	Cpx	0.6834	1.75	1
	R-ETH-144	8.4023	39.3377	15.1	387.4	15.1	0.46	12.89	Ol	0.5056	6.52	1
	R-ETH-97B	8.1566	38.4169	8.3	34.4	8.6	0.33	2.80	Ol	0.6462	1.81	1
	R-ETH-91	8.1276	38.4506	8.6	2.6	13.3	0.81	2.64	Ol	0.8277	2.18	2
	R-ETH-92	8.1269	38.418	10.1	52.4	10.3	0.31	3.89	Ol	0.6973	2.71	1
	R-ETH-96	8.0988	38.38	8.8	47.1	8.9	0.45	5.96	Ol	1.0287	6.13	1
	R-ETH-95	8.0462	38.3484	7.4	48.9	7.6	0.46	6.13	Ol	0.5441	3.34	1
	R-ETH-95	8.0462	38.3484	8.8	27.8	9.1	0.34	3.33	Cpx	0.9960	3.32	1
	R-ETH-72	7.9553	38.907	12.3	144.3	12.4	0.38	28.97	Ol	0.5444	15.77	1
	R-ETH-72	7.9553	38.907	11.9	9.5	13.2	0.44	14.84	Cpx	1.0562	15.67	2
	R-ETH-70	7.9449	38.9132	16.1	35.2	16.6	0.62	4.87	Ol	0.6258	3.05	1
	R-ETH-70	7.9449	38.9132	14.1	25.4	14.7	0.62	28.93	Cpx	0.4525	13.09	1
	RV-70	*7.9449*	*38.9132*	*16.7*	*1.2*	*117.0*	*31.80*	*0.11*	*Ol*	*0.5219*	*0.06*	*4*

Table S2 (cont'd)

Region	Sample	Lat (°)	Lon (°)	R/R_A	X	R_C/R_A	$2*\sigma(R/R_A)$	[^{4}He] (10^{-9} cm^3 STP/g)	Phase	Mass (g)	He analyzed (10^{-9} cm^3 STP)	Confidence Level
	R-ETH-75	7.9289	38.9084	14.7	258.5	14.8	0.40	7.73	Ol	0.4706	3.64	1
	R-ETH-75	7.9289	38.9084	12.8	22.0	13.3	0.29	47.08	Cpx	1.0312	48.55	1
	R-ETH-80	7.9092	38.8775	12.2	28.8	12.6	0.25	71.26	Cpx	1.1615	82.77	1
	R-ETH-80	7.9092	38.8775	19.6	572.8	19.7	3.12	76.17	Ol	0.6344	48.32	3
	R-ETH-79	7.9063	38.8766	19.0	376.4	19.1	0.25	8.30	Ol	0.5409	4.49	1
	ET-75/5	6.0181	37.7908	14.9	N/A	14.9	1.33	1.82	Ol	0.6130	1.11	2
	R-ETH-15	*5.6337*	*37.5236*	*46.1*	*1.9*	*98.1*	*9.51*	*0.24*	*Ol*	*0.5221*	*0.12*	*4*
	R-ETH-19	5.6337	37.5236	6.2	31.9	6.3	0.13	20.23	Cpx	1.0516	21.27	1
	R-ETH-22	5.5934	37.5358	7.3	56.6	7.4	0.16	12.51	Ol	0.3881	4.86	1
	R-ETH-21	5.5931	37.5371	4.8	35.4	4.9	0.11	34.21	Ol	0.5046	17.26	1
Ethiopian Plateau												
	R-ETH-119A	12.041	39.0413	9.7	6.1	11.4	0.32	2.01	Ol	0.6550	1.32	2
	R-ETH-125	11.9646	39.4213	8.4	30.5	8.6	0.37	3.67	Ol	0.5250	1.93	1
	R-ETH-118	11.9608	39.0165	14.3	18.3	15.0	0.54	2.99	Ol	0.4846	1.45	1
	R-ETH-128	11.9556	39.4294	10.3	100.6	10.4	0.30	7.45	Cpx	0.7708	5.74	1
	R-ETH-124	11.9543	39.4105	6.8	12.9	7.2	0.38	2.41	Ol	0.5280	1.27	1
	R-ETH-122B	11.9514	39.4044	13.6	39.5	14.0	0.30	2.13	Ol	0.8465	1.80	1
	R-ETH-122B	11.9514	39.4044	7.9	295.5	7.9	0.41	16.62	Cpx	1.0477	17.41	1
	R-ETH-129	11.9454	39.4299	2.7	28.7	2.8	0.13	6.02	Cpx	0.6981	4.20	1

Table S2 (cont'd)

Region	Sample	Lat (°)	Lon (°)	R/R_A	X	R_C/R_A	$2*\sigma(R/R_A)$	[^{4}He] (10^{-9} cm^3 STP/g)	Phase	Mass (g)	He analyzed (10^{-9} cm^3 STP)	Confidence Level
	R-ETH-112	*11.932*	*37.7964*	*5.3*	*15.1*	*5.6*	*0.29*	*1.68*	*Ol*	*0.5182*	*0.87*	*4*
	R-ETH-117A	11.8542	38.9368	15.7	895.1	15.8	0.50	8.33	Ol	0.5612	4.67	1
	R-ETH-117A	11.8542	38.9368	11.2	39.7	11.5	0.38	15.03	Cpx	0.6444	9.69	1
	R-ETH-111	11.5644	37.3289	4.9	41.6	5.0	0.42	1.63	Ol	0.7302	1.19	1
	R-ETH-103	10.8463	37.0262	10.7	16.7	11.3	0.52	0.81	Ol	0.6581	0.53	1
	R-ETH-102	10.68	37.2664	8.8	170.4	8.8	0.16	12.29	Ol	0.6419	7.89	1
	ET-75-27	*9.8917*	*38.3272*	*10.3*	*1.7*	*23.6*	*1.33*	*0.97*	*Cpx*	*0.6688*	*0.65*	*4*
	ET-71/108A	9.7297	38.4725	6.5	N/A	6.5	0.43	8.06	Ol	1.0658	8.59	1
	ET-71/8	9.5133	39.7272	5.9	83.1	6.0	0.14	89.53	Cpx	0.6006	53.77	1
	R-ETH-005	8.648	37.8986	7.1	119.1	7.1	0.42	3.73	Ol	0.5186	1.94	1
	R-ETH-005	8.648	37.8986	6.2	6.9	7.1	0.41	5.36	Cpx	0.5060	2.71	2
	R-ETH-006	*8.5671*	*37.944*	*5.2*	*1.8*	*10.5*	*2.20*	*0.31*	*Ol*	*0.5256*	*0.16*	*4*

Table S2. New data generated for this study. All samples were phenocrysts separated from mafic basaltic lavas. Italicized rows indicate data disregarded from further consideration (confidence levels 3 and 4 based on selection criteria described in section 2.2). Data are listed N to S by region. X values of N/A indicate that the corresponding blank produced a higher amount of ^{20}Ne than the sample, and there was no need to correct for air contamination[18]. The conversion factor between the given [He] units of 10^{-9} cm^3 STP and the units of 10^{-14} mol He given in other sources is approximately 4.1.